Reactivity and Thermochemistry of Gaseous Iron Compounds of Different Valency

von Diplom-Chemikerin Susanne Bärsch
aus Magdeburg

Vom Fachbereich 5
- Chemie-
der Technischen Universität Berlin
zur Erlangung des akademischen Grades

Doktor der Naturwissenschaften
- Dr. rer. nat. -
genehmigte Dissertation

Promotionsausschuß:
Vorsitz: Professor Dr. Reinhard Schomäcker
Berichter: Professor Dr. Dr. h.c. Helmut Schwarz
Berichter: Professor Dr. Ralf Steudel

Tag der mündlichen Prüfung: 20. Juni 2000

Berlin, 2000
D83

Kurzzusammenfassung

Bärsch, Susanne:

Reactivity and Thermochemistry of Gaseous Iron Compounds of Different Valency

In der vorliegenden Arbeit werden Untersuchungen zur Reaktivität und Thermochemie von Übergangsmetallverbindungen des Eisens, sowie der Aktivierung von organischen Substraten durch "nackte" Eisen- und Cobalt-Kationen durchgeführt. Dabei werden theoretische Ansätze sowie massenspektrometrische Methoden verwendet. Die verschiedenen experimentellen Techniken ergänzen sich hierbei, so daß die untersuchten Systeme unter unterschiedlichen Gesichtspunkten betrachtet werden können.

Kapitel 3 beschäftigt sich mit den Reaktionen und der Thermochemie von Eisen-Oxo und Eisen-Hydroxo Verbindungen. Dabei stehen (i) die Untersuchung des Sauerstoffaustausches von FeO^+ und $FeOH^+$ mit $H_2{}^{18}O$, (ii) die Untersuchung der drei $[Fe,O_2,H_2]^+$-Isomere sowie der entsprechenden Dikationenspezies und (iii) die Bestimmung der vertikalen und adiabatischen Ionisierungsenergien der betrachteten $FeO_mH_n^+$-Teilchen im Mittelpunkt.

In Kapitel 4 werden die adiabatischen und vertikalen Elektronentransferprozesse in Eisenchloriden untersucht. Die Bestimmung der vertikalen Redoxeigenschaften der $FeCl_m^n$-Teilchen (m = 1 - 4, n = -1, 0, 1, 2) erfolgt mittels *charge-stripping*, *charge-reversal*, *charge-exchange* und *neutralization-reionization* Massenspektrometrie. Die korrespondierenden adiabatischen Redoxeigenschaften werden durch die Kombination von experimentellen Daten und quantenchemischen Rechnungen bestimmt.

In Kapitel 5 wird die Aktivierung von Wasserstoff und Methan durch Eisensulfid-Kationen beschrieben. Beide Reaktionen werden im Guided-Ion-Beam- und Fourier-Transform-Ionen-Cyclotron-Resonanz-Massenspektrometer sowie durch quantenchemische Rechnungen untersucht. Die Aktivierung beider Substrate erfolgt über eine 1,2-Insertion des FeS^+ in eine σ-Bindung des Substrates unter Spin-Inversion von der Sextett- zur Quartett-Potentialfläche wobei als Hauptprodukt die Bildung von Fe^+ unter Einbau des Schwefelatoms in die aktivierte Bindung des Substrates beobachtet wird.

Den letzten thematischen Schwerpunkt stellt in Kapitel 6 die Aktivierung von organischen Substraten durch verschiedene Übergangsmetalle am Beispiel von Ethylsilan dar. Es zeigt sich experimentell, daß die im Periodensystem "benachbarten" Übergangsmetalle Cobalt und Eisen bei der Aktivierung von Ethylsilan deutlich unterschiedliche Produkte bilden, während die Reaktionen aber nach ähnlichen Mechanismen ablaufen.

Zusammenfassung

Bärsch, Susanne:

Reactivity and Thermochemistry of Gaseous Iron Compounds of Different Valency

Die vorliegende Arbeit beschäftigt sich mit Untersuchungen zur Reaktivität und Thermochemie von Eisen-Ligand-Komplexen, sowie mit der Aktivierung von organischen Substraten durch "nackte" Eisen- und Cobalt-Kationen. Dabei kommen quantenchemische Methoden und verschiedene massenspektrometrische Techniken zur Anwendung. Die untersuchten Eisenkomplexe sind Gasphasen-Modellsysteme sowohl für industrielle Anwendungen, z.B. in der Katalyse und bei Korrosionsprozessen, als auch für biologische Katalysesysteme. Die Arbeit gliedert sich in sieben Kapitel, wobei die vier Hauptkapitel von einer einleitenden Betrachtung (Kapitel 1), einer Vorstellung der verwendeten Methoden (Kapitel 2), sowie einer zusammenfassenden Schlußbetrachtung (Kapitel 7) eingerahmt werden.

Kapitel 3 beschäftigt sich mit der Chemie von Eisen-Oxo- und Eisen-Hydroxo-Verbindungen. Im Mittelpunkt des Interesses steht dabei zunächst die Frage, warum der Sauerstoffaustausch von FeO^+ mit $H_2{}^{18}O$ experimentell deutlich langsamer verläuft als bei $FeOH^+$, wobei zwei in diesem Zusammenhang in Frage kommende Reaktionsmechanismen untersucht werden. Der erste Mechanismus besteht aus einer ($FeOH^+ + H_2O$) bzw. zwei ($FeO^+ + H_2O$) 1,3-Wasserstoff-Wanderungen von einem Sauerstoffatom zum anderen, das Eisen ist dabei nicht direkt in die O–H Aktivierung involviert. Im zweiten Mechanismus wird jede dieser 1,3-Wasserstoff-Wanderungen durch zwei 1,2-Wasserstoff-Wanderungsschritte ersetzt, wobei intermediär Eisen-Wasserstoff-Bindungen gebildet werden. Beide Mechanismen werden unter Einbeziehung der möglichen *low-spin* und *high-spin* Zustände betrachtet. Der 1,3-Wanderungsmechanismus entlang der entsprechenden *high-spin* Potentialfläche ist dabei deutlich bevorzugt, was auf die Stabilität der Oxidationsstufen Fe(II) und Fe(III) der Intermediate im Gegensatz zu den weniger stabilen, hochvalenten Fe(IV) und Fe(V) Intermediaten entlang des 1,2-Wanderungsmechanismus zurückgeführt wird. Neben den Intermediaten der Reaktion von FeO^+ und H_2O, nämlich $FeO(H_2O)^+$ und $Fe(OH)_2{}^+$, existiert noch ein drittes Isomer der Zusammensetzung $[Fe,O_2,H_2]^+$, der Eisen-Wasserstoffperoxid-Komplex $Fe(H_2O_2)^+$. Dieser wird im zweiten Teil von Kapitel 3 genauer untersucht. Auf der Monokationen-Potentialfläche sind die Quartett- und Sextett-Koordinationskomplexe des Wasserstoffperoxids an Eisen deutlich weniger stabil ist als die beiden anderen $[Fe,O_2,H_2]^+$-

Isomere und gehen daher leicht in diese über (Quartett-Komplex) bzw. dissoziieren in $FeOH^+$ + OH (Sextett-Komplex). Auf der Dikationen-Potentialfläche dagegen wird die Reihenfolge der Stabilitäten der drei $[Fe,O_2,H_2]^+$-Isomere umgekehrt: $Fe(H_2O_2)^{2+}$ entspricht der stabilsten zweifach geladenen Spezies mit einer formalen Oxidationsstufe von Fe(II). Die formalen Fe(IV)-Spezies $FeO(H_2O)^{2+}$ und $Fe(OH)_2{}^{2+}$ sind dagegen energetisch ungünstiger, was auf die geringere Stabilität der Oxidationsstufe Fe(IV) gegenüber Fe(II) zurückgeführt wird. Im letzten Teil von Kapitel 3 wird die Thermochemie der zuvor beschriebenen Teilchen mit einem kombinierten massenspektrometrischen und theoretischen Ansatz untersucht. Die Ionisierungsenergien von Fe^+, FeO^+, $FeOH^+$, $Fe(H_2O)^+$, den verschiedenen $[Fe,O_2,H_2]^+$-Isomeren, $(H_2O)FeOH^+$, und $Fe(H_2O)_2{}^+$ werden bestimmt. Am Beispiel der Ionisierungsenergien von Fe^+ versus $Fe(H_2O)^+$, FeO^+ versus $FeO(H_2O)^+$ und $FeOH^+$ versus $FeOH(H_2O)^+$ wird der Einfluß des Liganden H_2O auf die Ionisierungsenergien untersucht. Dabei zeigt sich, das die Addition von Wassermolekülen die zweite Ionisierungsenergie von Eisenverbindungen um etwa 1.6 eV verringert.

Ebenfalls durch Kombination von massenspektrometrischen und quantenchemischen Ansätzen werden in Kapitel 4 die adiabatischen und vertikalen Elektronentransferprozesse in Eisenchloriden untersucht. Obwohl die Kenntnis der Redoxeigenschaften von Eisenchloriden für das Verständnis verschiedener geochemischer Prozesse, aber auch bei der Untersuchung von Korrosionsprozessen und im Bereich der Elektronikindustrie beim Ätzen von Leiterplatten von großer Bedeutung ist, ist dies eine der ersten zusammenfassenden und vergleichenden Studien aller massenspektrometrisch zugänglichen $FeCl_m{}^n$-Ionen.

In Kapitel 5 wird die Aktivierung von Wasserstoff und Methan durch Eisensulfid-Kationen beschrieben. Beide Reaktionen werden mit verschiedenen experimentellen Methoden und quantenchemischen Rechnungen umfassend untersucht. Bei der Aktivierung von Wasserstoff durch FeS^+ werden drei ionische Produkte experimentell detektiert, Fe^+, FeH^+ und $FeSH^+$. Die Beobachtung aller drei Produkte bestätigt den berechneten Reaktionsweg, der eine 1,2-Insertion des Eisensulfid-Kations in die H–H Bindung unter Spin-Inversion von der Sextett- zur Quartett-Potentialfläche vorhersagt. Das Hauptprodukt der H_2-Aktivierung ist das Fe^+-Kation unter Bildung von H_2S als Neutralteilchen, das heißt, das Schwefelatom des aktivierenden Teilchens wird in das Substrat eingebaut. Die Aktivierung von CH_4 verläuft ähnlich, ist aber aufgrund der größeren Anzahl von möglichen Produkten und Reaktionswegen erheblich komplexer. Auch hier findet zunächst eine 1,2-Insertion des FeS^+-Kations in eine C–H-Bindung statt. Diese verläuft regioselektiv unter Bildung einer S–H- und einer Fe–C- Bindung, so daß ein Intermediat der Struktur $CH_3–Fe–SH^+$ entsteht. Auch bei der

Methanaktivierung ist das Hauptprodukt Fe^+, in Analogie zum FeS^+/H_2-System. Die Bildung des dazugehörigen Neutralteilchens, CH_3SH, ist dabei ein interessantes Beispiel für eine Methanoxidation in der Gasphase. Die Reaktionswege für die Substrate H_2 und CH_4 weisen Gemeinsamkeiten auf, die sich auf σ-Bindungsaktivierungen an weiteren unpolaren Substraten übertragen lassen, z.B. an höheren Alkanen.

Den letzten thematischen Schwerpunkt stellt in Kapitel 6 die Aktivierung von organischen Substraten durch verschiedene Übergangsmetalle am Beispiel von Ethylsilan dar. Es zeigt sich experimentell, das die im Periodensystem benachbarten Übergangsmetalle Cobalt und Eisen bei der Aktivierung von Ethylsilan deutlich unterschiedliche Produkte bilden. Es stellt sich die Frage, inwieweit die verschiedene elektronische Struktur der Übergangsmetalle "nur" eine unterschiedliche Energetik der Intermediate und Übergangszustände entlang der Reaktionskoordinate hervorruft, oder ob durch die Variation des Metalls völlig andere Reaktionswege zu den Produkten offenstehen. In den Rechnungen werden ähnliche Mechanismen für beide Übergangsmetalle gefunden, d.h. der Verlust von Methan ist auf eine C–C Insertion als ersten Reaktionsschritt zurückzuführen, während die Bildung von SiH_4 auf eine primäre Insertion in die C–Si Bindung zurückzuführen ist. Beim Vergleich der Reaktionswege die über eine primäre C(1)–H oder C(2)–H Aktivierung zum Verlust von H_2 führen, zeigen beide Metalle eine deutliche Präferenz für den Reaktionsweg der C(1)–H Insertion. Für Cobalt belegen Experimente mit deuteriertem Ethylsilan ($C_2H_5SiD_3$) zusätzlich, das der Verlust von H_2 noch über einen weiteren Reaktionsweg erfolgt, nämlich die primäre Aktivierung von Si–H-Bindungen. Diese kann für das Eisen-System aufgrund der experimentellen Befunde ausgeschlossen werden. Zusammenfassend zeigen die Rechnungen zur Aktivierung von Ethylsilan durch Fe^+ und Co^+, daß sich beide Metalle in ihren Reaktionsmechanismen ähnlicher sind, als es die unterschiedlichen experimentellen Produktverteilungen zunächst vermuten lassen. Die beobachteten experimentellen Unterschiede sind daher eher das Resultat von Änderungen in der Energetik der Übergangszustände, als daß sie auf einem unterschiedlichem mechanistischem Verhalten der beiden Metalle beruhen.

Danksagung

Die vorliegende Arbeit entstand in der Zeit von Januar 1997 bis Mai 2000 am Institut für Organische Chemie der TU Berlin. Meinem Doktorvater, Herrn Professor Dr. Dr. h.c. Helmut Schwarz, danke ich an dieser Stelle für die Überlassung des Themas, für viele Anregungen und Diskussionen, für das in mich gesetzte Vertrauen und für die finanzielle Unterstützung meiner Arbeit. Herrn Professor Dr. Peter B. Armentrout bin ich dankbar für die Gelegenheit, während meines Forschungsaufenthaltes an der University of Utah an seinem Guided-Ion-Beam-Massenspektrometer zu arbeiten. Weiterhin danke ich Herrn Professor Dr. Ralf Steudel für die Übernahme des Koreferates.

Mein besonderer Dank gilt weiterhin Herrn Dr. Detlef Schröder für die Einführung in die Massenspektrometrie und Gasphasenchemie sowie für ungezählte Ideen, stimulierende Diskussionen und seine stete Hilfsbereitschaft. Herrn Dr. Weiske danke ich für die Wartung der Spektrometer und die Betreuung des NT-Computernetzwerkes, ebenso Herrn Dipl.-Chem. Martin Diefenbach für die Betreuung des Unix/Linux-Clusters und Herrn Dr. Thomas Steinke vom Konrad-Zuse-Zentrum Berlin (ZIB) für seine tatkräftige Unterstützung bei den Rechnungen auf den Großrechnern des ZIB. Meinen Kollegen Dr. Georg Hornung und Dr. Ilona Kretzschmar danke ich für die gute Zusammenarbeit im Rahmen gemeinsamer Projekte. Allen Mitgliedern des Arbeitskreises möchte ich an dieser Stelle ganz herzlich für die angenehme Arbeitsatmosphäre und die ständige Diskussionsbereitschaft bei fachlichen Problemen danken.

Meiner Familie, meinem Lebensgefährten und meinen Freunden danke ich sehr herzlich für die Unterstützung und den Zusammenhalt, der mir in den manchmal auch schwierigen Phasen meiner Ausbildung immer wieder geholfen hat, nach vorne zu schauen und das Ziel nicht aus den Augen zu verlieren.

Table of Contents

1 Introduction

Organometallic chemistry constitutes one of the most strongly growing areas in modern chemistry since transition-metal complexes have been recognized as very versatile and useful reagents some fourty years ago.[1] Some general fields of application of transition-metal chemistry are sketched in Figure 1-1.

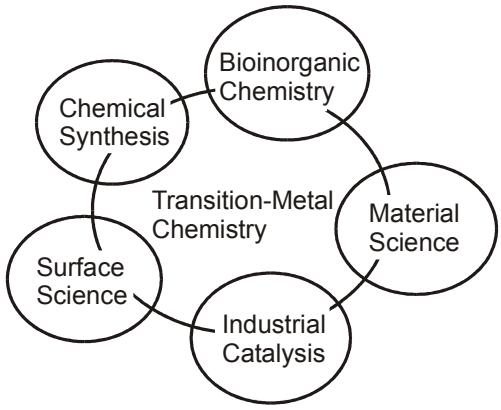

Figure 1-1: Applications of transition-metal chemistry.

Among the numerous organometallic complexes, the importance of iron-complexes can hardly be overrated. Iron-complexes are used as stoichiometric reagents and protecting groups in chemical synthesis; a well-known example is the use of $Fe(CO)_3$-moieties for the protection of 1,3-dienes.[2] Other applications concern the catalysis of industrial processes,[3] for example, the Fischer-Tropsch synthesis of gasoline with an iron-oxide catalyst. This process is still used in several countries, e.g. the United States and South-Africa, the latter being the world's leading applicant of this process.[4] Last but not least, iron is one of the most important elements in bioinorganic chemistry.[5] Thus, iron-based metalloenzymes catalyze a large variety of reactions including dehydrogenations, oxidative and other couplings, and many enzymes contain iron-oxo or iron-sulfido species as reactive centers. An important example for enzymes containing reactive iron-oxo units is cytochrome P-450, this class of enzymes is able to oxidatively activate C–H bonds in a large variety of organic substrates.[6] In contrast, enzymes containing iron-sulfur reactive sites mainly catalyze electron transfer reactions. The above examples show that iron-complexes exhibit a large variety of structural, chemical, and physical properties which can be traced back to the electronic configuration of transition-metals in general. In atomic Fe^+, for example, the valence space (consisting of the 3d, 4s, and 4p orbitals) is only partially occupied with seven electrons leading to a $3d^6 4s^1$ valence

configuration in the Fe^+ (^6D) ground-state and a low lying $3d^7\ 4s^0$ state, Fe^+ (^4F). The partial occupation of the orbitals assigns both, electron donor and electron acceptor properties to the transition metals; in addition, a large number of oxidation states, electronic configurations, and coordination motifs are conceivable. Moreover, ligands can dramatically modulate the reactivity of the transition-metal species.[7] Organometallic reactions therefore involve a large number of unknown parameters needed for (i) a detailed understanding of elementary steps underlying macroscopic reaction mechanisms and (ii) the determination of the thermochemistry of the species involved.

A simple and straightforward approach to obtain this knowledge is provided by the investigation of small model systems in the gas phase. Here, the complexity of the system is dramatically reduced to the structural units which are believed to be crucial for the reaction under study.[8] Strong benefits of this method result not only from the use of simplified models but particularly from the absence of obscuring effects, such as counterions, solvent- and bulk effects. Thus, gas-phase approaches allow to uncover the intrinsic chemical and physical properties of "bare" and ligated transition-metal species. In addition, systematic variations of just one parameter, e.g., the charge or the number and size of ligands attached to the metal, may model the relevance of the metal-environment in solution. It is important to note in this context that for the "naked" transition-metals or singly ligated transition-metal complexes investigated, the presence of net charges and vacant coordination sites as well as the absence of a moderating environment render these gas-phase species much more reactive than their counterparts in solution. Therefore, gas-phase studies cannot mimic en detail the exact solution-phase mechanisms for the processes and kinetic data observed; yet they do provide information on reactivity patterns, possible intermediates, and the role of ligands, which is difficult - if not impossible - to be obtained by other methods.

In this Thesis, mass-spectrometric experiments and quantum-chemical calculations are employed as they conveniently complement each other. Experimentally, there exist powerful techniques allowing detailed insight into certain parts of a potential-energy surface (PES) and/or the thermochemistry of species involved. The complete characterization of reaction paths, however, is a task reserved to the computational chemist. Computational chemistry has already gone far beyond experimental benchmark studies, and many examples are known, where theory has contributed to a more complete understanding of reaction mechanisms.[9] Especially density-functional theory, as a reasonably reliable and cost-efficient method, has gained more and more importance in that respect.[10] The work presented here combines both approaches in order to answer some fundamental and intriguing questions in the chemistry of

iron which are, for example, relevant in catalytic processes, redox-reactions, and corrosion phenomena. In Chapter 3, for instance, the redox-chemistry of iron oxides and iron hydroxides is investigated. Both types of species are common intermediates in industrial and biological catalytic cycles as well as in corrosion processes. Therefore, a high interest exists in the characterization of these species and their redox-properties. The current work specifically unravels the reactions mechanism of these species with water and in addition provides a very detailed data base for the thermochemistry of possible intermediates. Chapter 4 is related to the Chapter 3 as it presents the redox-chemistry of the iron chlorides $FeCl_m^n$ (m = 1 - 3; n = -1, 0, +1, +2), where the chlorine ligands are formally considered as being isoelectronic to the hydroxy ligands. The investigation comprises both, high-energy collision experiments and *ab initio* calculations. For the first time, these data provide a comprehensive data base of the redox thermochemistry of iron chlorides in different charge states; these species are important as single-electron oxidants and, in analogy to iron-oxo and -hydroxo species, play an important role in corrosion processes as well.

In Chapter 5, the focus is set on the reactivity of the FeS^+ cation, which is quite an interesting model for potential iron-sulfide catalysts; in addition it may serve as a very simplified model for the reactive sites of some biological catalysts, i.e., hydrogenases, nitrogenases, sulfite reductase and aldehyde oxidases. As becomes obvious further below, the activation of H_2 and CH_4 by FeS^+ as studied in this Thesis provides a formidable challenge for the interaction of mass-spectrometric and computational approaches. The results of the investigation of the two model reactions provides detailed insight into the mechanism of the elementary steps of FeS^+-mediated σ-bond activations.

In Chapter 6, the focus of this Thesis changes somewhat. While up to this point the chemical and physical properties of ligated iron compounds are investigated, the last chapter compares the different reactivities observed in the activation of organic substrates by different transition metals. For this purpose, the potential-energy surfaces for the activations of ethylsilane by "naked" Co^+ and Fe^+ ions are investigated using density functional theory. Interestingly, although both metals are neighbors in the periodic table of elements, they exhibit very different product-branching ratios in the activation of some organic substrates.

References

[1] a) J. L. Coleman, L. S. Hegedus, J. R. Noton, R. G. Finke *Principles and Applications of Transition-Metal Chemistry*, University Science Books, Mill Valley, **1987**. b) C. Elschenbroich, A. Salzer *Organometallics*, VCH, Weinheim, **1992**.

[2] a) L. S. Hegedus *Organische Synthesen mit Übergangsmetallen*, VCH, Weinheim, **1995**. b) M. Schlosser (Ed.) *Organometallics in Synthesis*, VCH, Weinheim, **1995**. c) M. Beller, C. Bolm (Eds.) *Transition Metals for Organic Synthesis*, VCH, Weinheim, **1998**.

[3] a) B. Cornils, W. A. Herrmann (Eds.) *Applied Homogeneous Catalysis with Organometallic Compounds*, VCH, Weinheim, **1996**. b) G. Ertl, H. Knötzinger, J. Weitkamp (Eds.) *Handbook of Heterogeneous Catalysis*, VCH, Weinheim, **1997**.

[4] Zeus Development Corp. *Remote Gas Strategies Newsletter*, Dez. **1997**, p. 1 and p. 10; Oct. **1997**, p.11; and Dez. **1998**, p.1. For further information on the newsletter, see: www.remotegasstrategies.com. A comprehensive survey of the Fischer-Tropsch process and the companies by which it is applied, can be found at http://www.netservice.no/fischer-tropsch/.

[5] a) K. Mathews, K. E. van Holde *Biochemistry*, Benjamin/Cummings, Redwood City **1990**. b) W. Kaim, B. Schwederski *Bioanorganische Chemie*, Teubner, Stuttgart **1991**. c) H. Sigel, A. Sigel (Eds.) *Metal-Ions in Biological Systems*, Vol. 30, Dekker, New York, **1994**. d) S. J. Lippard, J. M. Berg *Principles of Bioinorganic Chemistry*, University Science Books, Mill Valley **1994**. e) J. Huheey, E. Keiter, R. Keiter *Anorganische Chemie*, Chapter 19, Walter de Gruyter, Berlin **1995**.

[6] (a) P. R. Ortiz de Montellano (Ed.), *Cytochrome P-450; Structure, Mechanism, and Biochemistry*, Plenum-Press, New York, **1995**. (b) W.-D. Woggon, *Top. Curr. Chem.*, Springer-Verlag, Berlin, **1996**. (c) M. Sono, M. P. Roach, E. D. Coulter, J. H. Dawson *Chem. Rev.* **1996**, *96*, 2841.

[7] (a) A. Padwa, D. J. Austin, A. T. Price, M. A. Semones, M. P. Doyle, M. N. Protopopova, W. R. Winchester, and A. Tran *J. Am. Chem. Soc.* **1993**, *115*, 8669. (b) D. Schröder, H. Schwarz *J. Organomet. Chem.* **1995**, *504*, 123. (c) H. H. Cornehl, R. Wesendrup, M. Diefenbach, H. Schwarz *Chem. Eur. J.* **1997,** *3*, 1083. (d) C. X. Young, Q. Chen, S. K. Poehlein, B. S. Freiser *Rap. Comm. in Mass Spectrom.* **1999**, *13*, 645.

[8] a) P. B. Armentrout *Ann. Rev. Phys. Chem.* **1990**, *41*, 313. b) J. A. Martinho-Simões, J. L. Beauchamp *Chem. Rev.* **1990**, *90*, 629. c) K. Eller, H. Schwarz Chem. Rev. 1991, 91, 1121. d) B. S. Freiser *Acc. Chem. Res.* **1994**, *27*, 353. e) D. Schröder, H. Schwarz *Angew. Chem.* **1995**, *107*, 2023; *Angew. Chem. Int. Ed. Engl.* **1995**, *34*, 1973. f) B. S. Freiser *J. Mass Sprectrom.* **1996**, *31*, 703.

[9] P. v. R. Schleyer, N. L. Allinger, T. Clark, J. Gasteiger, P. A. Kollmann, H. F. Schafer III, P. R. Schreiner (Eds.) *The Encyclopedia of Computational Chemistry*, Wiley, Chichester, **1998**.

[10] W. Koch, M. C. Holthausen *A Chemists Guide to Density Functional Theory*, Wiley-VCH, Weinheim, **2000**.

2 Experimental and Theoretical Details

Several mass-spectrometric techniques and theoretical methods have been applied in this Thesis for the evaluation of the intrinsic reactivity of organometallic species. These techniques probe the potential-energy surface (PES) at different points as shown in Scheme 2-1, thus yielding complementary results and providing a more detailed understanding of the reaction under study than any of the applied techniques would provide in its own.

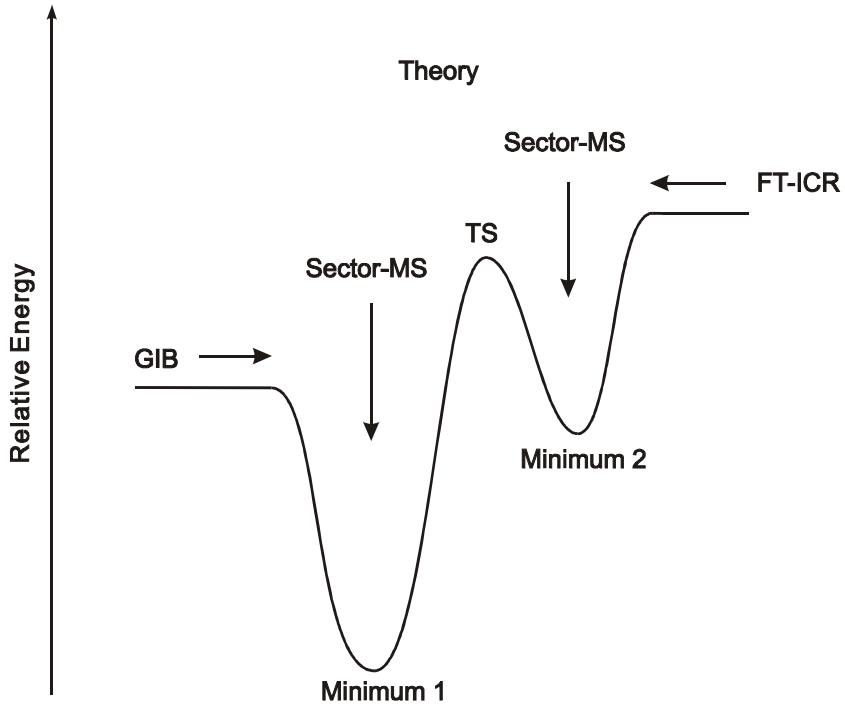

Scheme 2-1: A hypothetical PES and the techniques by which parts of the PES can be assessed.

In Scheme 2-1, theory refers to the Hartree-Fock/Density-functional theory (HF/DFT) hybrid functional B3LYP. Theory in general allows to determine the energetic demand of reaction paths and the geometries of involved stationary states, i.e. minima, transition structures, and higher-order saddle points; furthermore, transition pathways may be calculated via internal reaction coordinate (IRC) calculations. Thus, theory gives an overview of the "full" PES and comparison of these results with experimental data serves both, the understanding of reaction mechanisms as well as the design of new experiments. Examples for this type of study can be found in Chapters 3, 5, and 6.

In Scheme 2-1, the Fourier-transform ion-cyclotron resonance (FT-ICR) mass spectrometry approach is used to monitor the kinetics of exothermic, bimolecular reactions; with respect to the above hypothetical PES, this means that the reaction is monitored starting

from the right-hand side. FT-ICR MS experiments are applied for three purposes, (i) the mere occurrence or non-occurrence of a ligand-exchange reaction allows to bracket bond dissociation energies of metal-ligand complexes, (ii) rate constants of bimolecular reactions can be determined, and (iii) in some more fortunate cases, also chemical equilibria may be studied and equilibrium constants can be derived. A more detailed description of FT-ICR mass spectrometry is found in Chapter 2.2.

In contrast, the guided-ion beam (GIB) mass spectrometry approach in Scheme 2-1 is a means to investigate the energy dependence of endothermic ion-molecule reactions, i.e. to monitor the reaction from left to right (see Section 2.3). The third experimental approach in Scheme 2-1 utilizes a four-sector mass spectrometer (Section 2.4) in order to probe the unimolecular or collision-induced reactivity of certain minima on the PES by choosing a suitable precursor species to enter the PES at this particular point. Next, a summary of the above mentioned theoretical and experimental approaches is presented. For more detailed descriptions of the instruments and methodologies the reader is referred to the references given below.

2.1 Computational Details

The theoretical background of computational chemistry is outlined in many quantum chemical text books, book chapters, and proceedings.[1-3] Therefore, only a summary of the theoretical background of the applied theoretical methods is given in this Thesis. The goal of the computational chemist is the accurate description of chemical systems by means of quantum chemical methods. While this procedure works quite well for main-group elements, computations of transition-metal containing species represent one of the major challenges for todays computational methods.[4]

Basics. Given a system composed of nuclei and electrons, computational chemistry in principle may attempt to calculate the following features:

(i) the geometrical arrangements of the nuclei that correspond to stable molecules,

(ii) the relative energies of these stable species,

(iii) their physical properties, e.g., dipole moments, polarizabilities, IR- and Raman-frequencies etc.,

(iv) the transformation of a stable molecule into another, which requires the calculation of first-order saddle points (transition structures) and transition pathways via IRC calculations.

All quantum chemical calculations are based on the universal Schrödinger equation (Equation 2-1),

$$H\Psi(R,x,t) = E\Psi(R,x,t) \qquad \text{Equation 2-1}$$

where the Hamiltonian operator H operates on a wave function Ψ, thus calculating the total energy E of the system. In a system of nuclei and electrons Ψ depends on the spatial and spin coordinates of the electrons, x, the spatial coordinates of the nuclei, R, and the evolution of Ψ with time t. The Hamiltonian operator involves five different contributions, i.e., the kinetic energy of the electrons, the kinetic energy of the nuclei, the Coulomb attraction between electrons and nuclei, as well as the electron-electron and nucleus-nucleus repulsion.

Although the analytical solution of Equation 2-1 is only possible for one-electron systems, in principle numeric solutions are available for any system. As this would be a very time consuming procedure, two important simplifications are used to reduce computational demands such that todays computational resources are sufficient to deal with reasonably large systems including those containing transition metals. (i) For the description of non-dynamic phenomena, the Hamiltonian operator is independent of time and the time dependence of the wave function Ψ may be separated out as a factor, thus yielding the time-independent Schrödinger-equation (Equation 2-2).

$$H\Psi(R,x) = E\Psi(R,x) \qquad \text{Equation 2-2}$$

(ii) The second assumption used is the so-called Born-Oppenheimer approximation.[5] With the idea behind that the motion of the nuclei is much slower than the motion of the electrons, the nuclei are assumed to be fixed and the electrons may be viewed as if moving in a static field formed by the nuclei. This results in the formulation of the electronic Schrödinger-equation (Equation 2-3).

$$H_e\Psi_e(x) = E_e\Psi_e(x) \qquad \text{Equation 2-3}$$

The Hartree-Fock method. The Hartree-Fock approach[6] is the least time consuming *ab initio* method used to solve Equation 2-3 for a given system, and it forms the basis for many higher correlated *ab initio* methods. Therefore, a short introduction of the Hartree-Fock

approach will be given, followed by a summary of the basics of density functional theory and the HF/DFT hybrid functionals.

Despite all approximations introduced already, the exact analytic solution of the electronic Schrödinger equation is only possible for one-electron systems due to the electron-electron repulsion term, which renders Equation 2-3 inseparable for many-electron systems. In this context, an exact wave function cannot be obtained; instead, an approximate wave function may be formulated as the so-called Hartree-product, reducing the N-electron wave function into N one-electron functions, the so-called spin orbitals (Equation 2-4). Each one-electron function depends on the spatial- and spin coordinates of the corresponding electron.

$$\Psi_e(x_1, x_2, \ldots, x_N) = X_1(x_1)X_2(x_2)\ldots X_N(x_N) \qquad \text{Equation 2-4}$$

The Hartree-product as such is a non-correlated wave function; a model in which the electrons are absolutely independent and where no interaction between the electrons occurs. Thus, the Hartree-product does not obey the quantum-mechanically postulated Pauli-antisymmetry principle. In order to obey this principle, the wave function $\Psi_e(x)$ is formulated as a single Slater determinant Φ, which is the antisymmetrized product of N one-electron functions $X_i(x_i)$, Equation 2-5.

$$\Psi_e(x) \cong \frac{1}{\sqrt{n!}} \begin{vmatrix} X_1(x_1) & \ldots & X_n(x_1) \\ \vdots & \ddots & \vdots \\ X_n(x_1) & \cdots & X_n(x_n) \end{vmatrix} = \Phi \qquad \text{Equation 2-5}$$

A solution of the electronic Schrödinger-equation may then be obtained by applying a self-consistent field (SCF)-procedure, which relies on the validity of the variational principle, stating that any approximate wave function has an energy above or equal to the exact energy, where equality only holds when the wave function is indeed exact. The solution of the one N-electron equation (Equation 2-3) may then be repatriated to the solution of N one-electron equations according to Equation 2-6.

$$F(r_i)X_i(x_i) = \varepsilon_i X_i(x_i) \qquad \text{Equation 2-6}$$

In Equation 2-6, $F(r_i)$ is the Fock-operator, an effective one-electron operator describing the kinetic energy of an electron, and the attraction to all nuclei (h_i) as well as the averaged repulsion to all other electrons, formulated as the average potential created by N-1 electrons

which is experienced by the N[th] electron (Equation 2-7). In Equation 2-7, J_j and K_j are the Coulomb and exchange integrals. The set of spin orbitals $X_i(x_i)$ that describes the above system best is obtained by using a trial wave function and solving Equation 2-6 in an iterative manner.

$$F_i = h_i + \sum_j^N (J_j - K_j) \qquad \text{Equation 2-7}$$

While the HF approach often yields reasonably geometries, the total and relative energies obtained with this method exhibit huge errors. This is due to the fact that HF neglects the incorporation of electron-electron interaction, i.e. electron correlation. More sophisticated *ab initio* methods try to include electron correlation, these methods are not applied in the work presented here and the interested reader is referred to some computational chemistry textbooks,[1] giving overviews on these topics. Here, we will continue with a short discussion of density functional theory.[7,8]

Density Functional Theory. The basic notion of density functional theory is given by the theorem of Hohenberg and Kohn, who showed in 1964 that the ground-state energy of an electronic system is uniquely determined by its charge density $\rho(r)$.[9] Thus, it should be possible to find a functional $F(\rho)$ plus an additive, constant external potential generated by the nuclei $V(\rho)$ to afford the ground-state energy of the system $E(\rho)$; Equation 2-8.

$$E(\rho) = F(\rho) + \int \rho(r) V(r) dr \qquad \text{Equation 2-8}$$

However, this statement does not answer the question of the form of $F(\rho)$, and several classes of density functionals are used nowadays. The first step towards "applicable DFT" as a tool in chemistry was made by Kohn and Sham,[10] who developed a set of one particle eigenvalue equations incorporating both $F(\rho)$ and $V(\rho)$ in an effective one-electron Hamilton operator.

$$h_{KS}\Phi(r_1) = \left[-\frac{1}{2}\Delta + \sum_A \frac{Z_A}{|R_A - r_1|} + \int \frac{\rho(r_2)}{|r_1 - r_2|} + V_{XC}(r) \right] \Phi(r_1) = \varepsilon_1 \Phi(r_1) \qquad \text{Equation 2-9}$$

with $V_{XC} = \dfrac{\partial E_{XC}(\rho[r])}{\partial \rho}$

In this formulation, which is exact and does not contain any approximations so far, the first term of the Hamiltonian operator describes the kinetic energy of a system of N non-interacting electrons of the same density as the actual system. The second and third term account for the nuclei-electron and electron-electron Coulomb interactions, and V_{XC} is the exchange-correlation potential, which incorporates the non-classical exchange and correlation interactions as well as the effect of non-classical electron interaction. Nevertheless, Equation 2-9 constitutes one major problem: although it is exact (in contrast to the previously described Hartree-Fock approach), the correct functional for the description of the exchange-correlation energy E_{XC} is unknown.

Most problems with the determination of E_{XC} arise from the inhomogeneous charge density of molecular systems. Therefore, it seems straightforward to neglect the latter and assume a homogeneous electron gas, where the electron density in the system is either constant or varies very slowly with position. Thus, the exchange-correlation energy E_{XC} may be expressed as a function of the local exchange-correlation energy ε_{XC} per particle (Equation 2-10).

$$E_{XC}^{LDA} = \int \rho(r)\varepsilon(\rho[r])dr \qquad \text{Equation 2-10}$$

This is referred to as local density approximation (LDA). However, as the real electron distribution in molecules is sometimes far from being uniform, LDA-functionals have lots of shortcomings. Indeed, the most severe one is the notorious overbinding encountered in the calculation of bond dissociation energies.[7b,11]

Gradient corrected functionals have been developed to overcome the pitfalls of LDA. A very successful approach considers the gradient of the charge density as a correction to the LDA approach according to Equation 2-11.

$$E_{XC}^{NL} = \int \rho\varepsilon_{XC}(\rho)dr \cdot F(\rho;\nabla\rho) \qquad \text{Equation 2-11}$$

Using the gradient corrections, the disadvantages of the LDA approach can be cured to some extent. The most commonly used gradient-corrected functionals have been developed by Becke (B), Perdew (P), Lee, Yang, and Parr (LYP), and Perdew and Wang (PW).[12]

Becke's name is also inevitably connected to another type of functionals, the HF/DFT-hybrid functionals.[13] Here, mixing of the exact Hartree-Fock exchange with DFT exchange and correlation energies leads to very different and yet very successful HF/DFT-hybrid

functionals. One of the most commonly used of these functionals is Becke's 3-parameter functional (B3; Equation 2-12).

$$E_{XC} = 0.2E_X^{HF} + 0.8E_X^{LDA} + 0.72E_X^B + 1.0E_C^{LDA} + 0.81E_C^{NL} \qquad \text{Equation 2-12}$$

Implementing the LYP functional for E_C^{NL} in Equation 2-12, results in the formulation of the popular B3LYP functional which was employed throughout the present Thesis.[14] Despite its approximations, the B3LYP functional is a reliable and powerful tool in computational chemistry. It offers cost-efficient and in many cases also surprisingly good results in the calculation of many molecular systems. Cost efficiency is reached because computing time for the B3LYP approach scales only with N^4 (with N being the number of primitive basis functions) as compared to a scaling of at least N^7 in post-HF *ab initio* approaches, as for instance CCSD(T).

During the last years, the applicability of B3LYP towards systems containing transition metals has been exploited - again, often but not always, with surprisingly good results.[8] Even models for large bioinorganic molecules, as for instance P450, have been investigated computationally.[15] Moreover, investigations on small iron compounds have been shown to provide reasonably accurate energetics.[16-19] Generally, we assign an error of ± 6 kcal/mol to the energies obtained from calculations which has been derived from comparison of computational reaction enthalpies with literature thermochemistry.[16]

However, some notorious shortcomings of B3LYP remain, which have to be taken into account in the interpretation of the calculated data, i.e. the tendency to overestimate bond dissociation energies[20] and the occurrence of large errors in the calculation of atoms.[21] Especially the latter represents a major problem as will be described for the example of the iron cation next. The B3LYP method only poorly describes the low-spin/high-spin separation in transition-metal atoms. This behavior is attributed to a bias of $3d^n$ over $3d^{n-1}4s^1$ configurations, leading to an artificial preference for the low spin $3d^n$ species.[21-23] Thus, the B3LYP/6-311+G* level of theory predicts Fe^+ (^4F) to be 4.1 kcal mol^{-1} more stable than Fe^+ (^6D), while according to spectroscopy the Fe^+ cation has a ^6D ground-state with a $3d^64s^1$ configuration which is 5.8 kcal mol^{-1} lower in energy compared to Fe^+ (^4F).[24] The ambiguous ground-state assignment of atomic ions leads to increased uncertainties in the computed bond dissociation energies of $M(L)^+$ complexes (L = ligand). In an attempt to circumvent this problem, if possible the computed energies of ligand exchange reactions ($M(L)^+ + L' \rightarrow M(L')^+ + L$) are used for the assignment of bond dissociation energies in this Thesis.

Program Packages, Basis Sets, and Spin-Contamination of Wave-Functions. Nowadays, the computational chemist may choose between several program packages, which are either commercially available (for instance Gaussian)[25] or are given away as freeware within the computational chemistry community (i.e. Molpro,[26] ADF,[27] GAMESS[28] and others). In this Thesis, the Gaussian94 program package is employed. In contrast to some of the other computational chemistry programs, Gaussian offers user-friendly input- and output routines. However, this is achieved at the expense of less control over orbital occupations and thus less control over the wave functions. For many higher correlated *ab initio* methods this represents a major drawback; however, due to the definition of DFT, the concept of spin-orbitals is less important here and poor control over the wave function does not constitute a major problem in DFT calculations of polyatomic molecules.

The correspondence between the theoretical method and the basis set used for each atom determines to a large extent the quality of the calculations. While highly correlated *ab initio* methods are not very meaningful if small basis sets are used, and the same holds true in the reverse case, i.e. when huge basis sets are used with a poorly correlated method, as for instance HF. Special problems occur in systems with unusual bonding features, for instance when hydrogen-bonds or 3-center-2-electron bonds are to be described. In these cases it is absolutely necessary to provide sufficient amounts of diffuse functions and polarizations functions with the basis set in order to describe these bonds properly. On the other hand, as the number of two-electron integrals to be computed increases with increasing number of basis functions by N^4, the choice of the basis set is always a compromise between the desired quality of the calculations and the computing resources available.

In addition to the correspondence between the method and the basis set as such, it is utterly important that the basis set is well balanced with regard to all atoms involved because otherwise the basis set superposition error (BSSE) will increase dramatically.[29] The origin of the BSSE is the fact that excessive basis functions of one subunit may augment the basis functions of a neighboring atom in the molecule, which results in an artificial energy decrease of the augmented subunit.[30] BSSEs may be calculated according to the counterpoise method of Boys and Bernardi, which involves separate calculations of each subunit with the basis functions of another subunit.[31] However, a comparative study of BSSEs in transition-metal containing systems reveals that DFT is much less susceptible for the occurrence of BSSEs than conventional correlated *ab initio* methods.[32] This is in accord with the fact that the choice of the basis set is less crucial in DFT-calculations than for correlated *ab initio* methods.

Another problem which needs to be kept in mind is the problem of spin contamination, which is most dramatic for systems with a multiplicity other than one; but even singlets may suffer from spin contamination once they have diradicaloid character. For these species, unrestricted SCF calculations (UHF) are performed, where two complete sets of orbitals exist, one for the alpha electrons and one for the beta electrons. Usually these two sets of orbitals use the same set of basis functions but different molecular orbital coefficients. The advantage of unrestricted calculations is that they can be performed very efficiently. The disadvantage is that the wave function is no longer an eigenfunction of the total spin, $<S^2>$, thus some error, e.g. spin contamination, is introduced into the calculations. Spin contaminations result in wave functions which in addition to the desired spin state have some amounts of higher spin states mixed in. This occasionally results in slightly lowered computed total energies due to having more variational freedom; more often, the total energies are slightly raised since higher-energy states are being mixed-in. However, these changes are artifacts of incorrect wave functions. Since spin contamination is not a systematic error, the difference in energy between states will be adversely affected. A high spin contamination can affect the geometry and population analysis and significantly affect the spin density. As a check for the presence of spin contamination, most *ab initio* programs provide the expectation value of the total spin, $<S^2>$. If there is no spin contamination, this should equal $s(s+1)$ where s equals 1/2 times the number of unpaired electrons. The spin contamination is negligible if the value of $<S^2>$ differs from $s(s+1)$ by less than 10 % for non-metals and by less than 20 % for transition-metal involving species. Although this provides a quick test, it is always advisable to double check the results against experimental evidence or more rigorous calculations. Spin contamination is often seen in unrestricted Hartree-Fock (UHF) calculations but is somewhat less common in DFT calculations. Nevertheless, especially for iron-containing species these facts have to be kept in mind because of the low state splittings between various spin surfaces.

2.2 Fourier-Transform Ion Cyclotron Mass Spectrometry[33]

Some experiments in this work are performed in a Spectrospin-CMS-47X Fourier-transform ion-cyclotron resonance (FT-ICR) mass spectrometer. As the instrument has been described in detail previously,[34] only a short overview over the underlying principles and the important features of the instrument is given here. For more information on the technique as such, the reader is referred to a 1998 primer on FT-ICR mass spectrometry by Marshall et al.[35]

Basically, in a FT-ICR mass spectrometer the ions are trapped in the ICR cell which is located in a homogeneous magnetic field *B*. The motion of the ions is described by the cyclotron resonance condition, (Equation 2-13)

$$\omega_c = \frac{qB_0}{m}$$ Equation 2-13

in which the unperturbed ion cyclotron frequency is denoted as ω_c. Technically, the trapping works as follows: in the ICR-cell, three pairs of potential plates exist, the excitation plates and detection plates in the x- and y-directions of the cylinder (see Figure 2-1) and the trapping plates forming the bottom and top of the cylinder, perpendicular to the z-axis of the magnetic field. The trapping plates prevent the ions from leaving the ICR-cell. After excitation of the ions to phase-coherent motion by radio-frequency (rf)-broadband pulses from the excitation plates, the ions induce a time-dependent signal in the detection plates, which is a superposition of the signals of all ions in the cell. This signal, called time-domain, is converted into the frequency-domain by Fourier-transformation, thus displaying the m/z ratios of all ions. Excitation of ions by rf-broadband pulses has two more functions, i.e. (i) to accelerate ions to cyclotron radii larger than the radius of the ion trap and thus remove the ions effectively from the cell, and (ii) to increase the ions kinetic energy above the threshold of ion dissociation or ion-molecule reaction.

A schematic picture of the Spectrospin-CMS-47X Fourier-transform ion-cyclotron resonance mass spectrometer is shown in Figure 2-1. Not shown are the Bruker Aspect 3000 minicomputer, which controls the system, and the PC to which the data are transferred for further evaluation. The instrument consists of an external ion source, the ion transfer optics and the FT-ICR reaction cell inside a 7 Tesla magnet. Introduction of gases and volatile liquids as reactants and/or precursors for formation of ligated metal-species ML^+ is achieved using two leak valves and two pulsed valves. The source, transfer, and cell regions are differentially pumped by three turbomolecular pumps and several oil rotary pumps to maintain the vacuum. The background-pressure in the reaction cell is on the order of 1 – 4 x 10^{-9} mbar.

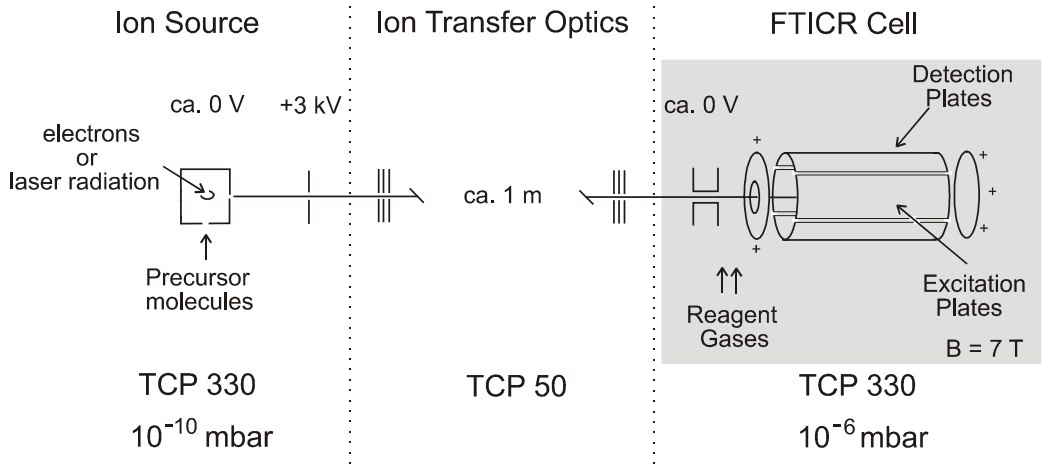

Figure 2-1: Schematic setup of the FT-ICR mass spectrometer.

The metal cations are generated from a metal target in the external ion source using a laser desorption/laser ionization technique. The ions are extracted from the external ion source and transferred into the analyzer cell which is located in the field of the magnet. This type of metal production may at least partially lead to formation of kinetically or electronically excited ions. Therefore, prior to any chemical reaction, the ions are collided with pulsed-in argon at pressures of 5 x 10^{-5} bar. Each ion undergoes about 200 collisions, thus achieving translational cooling to the temperature of the collision gas, e.g. 300 K. The following criteria allow to check whether efficient thermalization has been achieved:[36]

(i) The intensity of the reactant ion should strictly follow pseudo-first order kinetics.

(ii) Changing the thermalizing conditions, e.g. pulsing in argon at higher pressures, should not affect the measured branching ratio of the products.

(iii) In the absence of secondary reactions, the intensities of all observed products should increase with increasing reaction time.

As most targets do not consist of isotopically pure metals, after thermalization the most abundant metal isotope is isolated using FERETS, a computer controlled ion-ejection protocol which combines frequency sweeps and single frequency pulses to eject all undesired ions.[37] Metal-ligand complexes are then produced by leaking in appropriate reagents via pulsed valves. The metal-ligand complexes are mass-selected as described above and thermalized by collisions with argon prior to their ion-molecule reactions. In order to obtain satisfactory signal-to-noise ratios, 50 to 100 scans are accumulated. Generally, three types of experiments are performed with the FT-ICR instrument, i.e. (i) determination of pseudo first-order rate constants and branching ratios of product formation, (ii) bracketing experiments, and (iii) equilibrium measurements. A brief description of the different experiments is given next,

starting with the determination of rate constants and branching ratios. For these experiments, the reactants are leaked into the ICR-cell via the leak valves and are kept at steady pressures between 5 x 10^{-9} bar and 5 x 10^{-7} bar, depending on the reaction under investigation. The cell pressure is monitored by a calibrated ion gauge (Balzers IMG070). The product distribution is measured at several reaction times, and then the branching ratios and the rate constants are determined from the pseudo-first order decay of the reactant ion with increasing reaction time. Conversion to reaction efficiencies k/k_{coll} is achieved by comparison with the respective gas-kinetic collision rates (k_{coll}). Several models have been developed for the calculation of ion-molecule collision rates. Langevin applied the kinetic gas theory which describes the collision of ions with polarizable neutrals.[38] This theory was later further refined to the average dipole orientation (ADO) theory by Su and Bowers,[39] taking into account permanent dipole moments of the neutral reaction partners. Even more sophisticated is the so-called capture theory, provided by Su, which is used exclusively in this Thesis.[40] Branching ratios are reported with an estimated error of ± 10 %; absolute rate constants and reaction efficiencies have estimated errors of ± 30 % unless mentioned otherwise.

Bracketing experiments are used to estimate the bond-dissociation energy (D_0) of metal-ligand complexes $M(L)^+$.* The $M(L)^+$ ion is reacted with a ligand L' for which $D_0(M(L')^+)$ is known. If ligand-exchange ($M(L)^+ + L' \rightarrow M(L')^+ + L$) is indeed observed, an upper limit of $D_0(M(L)^+) < D_0(M(L')^+)$ may be calculated from the heats of reactions of the involved species. Lower limits may be obtained in a similar manner by reacting a $M(L'')^+$ species with the ligand under investigation.[41] The bracketing method is a valid and easily applicable method where no other methods are available. Nevertheless, sometimes the lack of suitable standard substrates ($M(L')^+$) with known D_0 leads to large error bars. Some refinement can be achieved by not only monitoring the occurrence or absence of ligand-exchange, but also considering the kinetics of ligand-exchange; errors of less than ± 2 kcal/mol in relative binding energies may be achieved.[42] In addition, the error of the reference used adds to the errors of the bracketing procedure.

* Strictly speaking, the FT-ICR monitors reactions occurring at 298 K, thus bracketing D_{298} instead of D_0. However, for most reactions studied in this Thesis, thermal corrections can solely be neglected.[19b] In critical cases, explicit reference to computational data for ΔH_0, ΔH_{298}, and ΔG_{298} has been made.

In some fortunate cases, however, equilibrium measurements[43] can be used as a much more precise method for the determination of relative D_0. If the heat of reaction ($\Delta_r H$) for a reaction is ± 5 kcal/mol and the reaction is not hindered by barriers in excess to the reaction thermochemistry, the reaction $M(L')^+ + L \rightleftarrows M(L)^+ + L'$ is reversible under FT-ICR conditions, thus allowing a thermochemical equilibrium to be established at an assumed temperature of 298 K.[36] $M(L)^+$ is trapped in mixtures of L and L' with different ratios of the two components. The exchange reactions are monitored at several reaction times and pressures. Equilibrium is assumed to be established when the ratio of $M(L')^+$ to $M(L)^+$ is time-independent.[44] The equilibrium constant K_{eq} is derived from the relative intensities (I_i) of the product ions and the relative pressures (p_i) of the neutral reactants (Equation 2-14).

$$K_{eq} = \frac{I_{M(L)^+} \times p_{L'}}{I_{M(L')^+} \times p_L}$$ Equation 2-14

The errors of the equilibrium constants depend on the experimental uncertainties as well as systematic errors; secondary reactions and competing processes in particular.[45] In some cases, rather large accuracies have been achieved in equilibrium measurements.[46] Note, that the considerable error in absolute pressure measurement[36] is not relevant here.

2.3 Guided-Ion Beam Mass Spectrometry

The guided-ion beam mass spectrometer shown in Figure 2-2 is used for some of the experiments and has been described in detail previously.[47,48] The instrument consists of five sections. In the first section, atomic metal ions are produced in a direct current discharge source connected to a flow tube. Inside the source, an iron cathode is held at 1.5 - 2.5 kV in a plasma consisting of about 90% helium and 10% argon. Ar^+ ions are produced in the discharge and accelerated towards the iron rod, thereby sputtering off neutral and ionic metal fragments. About 60 cm downstream from the discharge, metal-ligand complexes $M(L)^+$ are produced by adding the respective reaction gases to the flow. In the remaining 40 cm of the flow tube, the ions undergo $>10^4$ thermalizing collisions at a typical pressure of ~0.7 mbar. At the end of the flow tube, all ions are extracted, accelerated, and passed through a magnetic sector for reactant ion selection. The mass-selected ions are decelerated to the desired kinetic energies and focused into an rf-octopole device. The octopole is used to trap the reactant and product ions in the radial direction and therefore maintains good collection efficiency at low

kinetic energies. The octopole passes through a gas cell of known effective length (8.26 cm) filled with the neutral reactant or CID collision gas. The neutral is present in the reaction cell at relatively low steady pressures of 1 - 3 x 10^{-4} mbar to ensure single collision conditions. Unreacted ions and product ions drift from the reaction cell to the end of the octopole and are extracted into a quadrupole mass filter for mass analysis and subsequent detection by a secondary electron/scintillation detector.

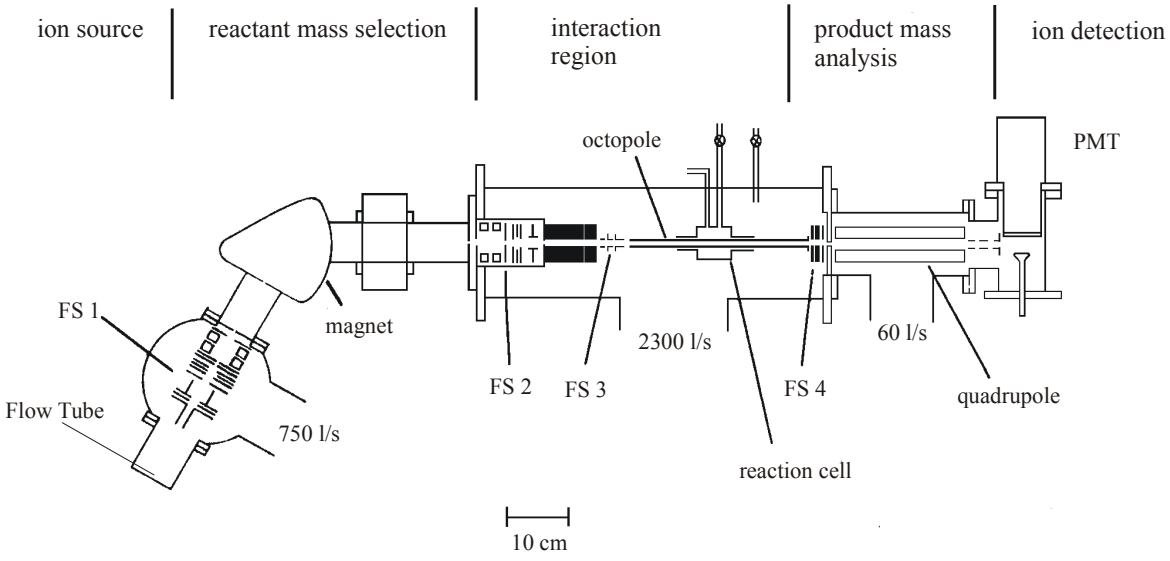

Figure 2-2: Experimental Setup of the GIB mass spectrometer.

Laboratory ion energies (E_{lab}) are converted into center-of-mass energies (E_{CM}) using $E_{CM} = E_{lab}\, M / (M + m)$ where M and m are the corresponding reactant neutral and ion masses. The absolute energy scale and the corresponding full width at half maximum (FWHM) of the ion beam kinetic energy distribution are determined as described in previous publications.[47] The beams have Gaussian kinetic energy distributions with an average FWHM of ca. 0.24 eV in the laboratory frame. The uncertainty of the absolute energy scale is ± 0.05 eV (lab). Details for the conversion of raw ion intensities into cross sections have been outlined previously.[47a] Absolute cross sections are estimated to be correct within ± 20 %.

Data analysis has been performed as follows. Cross sections are modeled using Equation 2-15,[47c,d]

$$\sigma(E) = \sigma_0 \Sigma\, g_i\, (E + E_i - E_0)^n / E \qquad \text{Equation 2-15}$$

where E denotes the relative translational energy, E_0 is the reaction threshold, σ_0 is an energy independent scaling factor, and n is a fitting parameter. The summation over ro-vibrational energy levels i with energies E_i and relative populations g_i explicitly includes the internal energies of polyatomic reactants. Relative populations g_i are obtained from a Maxwell-Boltzmann distribution of vibrational energy levels at 300 K, calculated using the Beyer-Swinehart algorithm.[48] The vibrational frequencies of the neutral reactants are taken from Ref. [49] and the vibrational frequencies of the metal-ligand complexes are obtained from calculations at the B3LYP/6-311+G* level of theory. After convolution of the model over the kinetic energy distributions of the reactants, the parameters σ_0, n, and E_0 are optimized to best reproduce the data using a least-squares criterion. Reported errors in E_0 comprise the range of values obtained for several data sets and the absolute uncertainty of the energy scale. Equation 2-15 inherently assumes that all of the internal energy is capable of coupling into the reaction coordinate, an assumption that has been shown to lead to accurate thermochemistry in numerous cases.[47c,47d,50-52]

However, some problems with the GIB-measurements should be mentioned, which arise from the low mass resolution of primary ion selection and product detection. If the parent ion beam and one possible product are only one or two masses apart, as for example in the FeS^+/H_2 system, where the parent ion FeS^+ is found only 2 amu below the product ion $FeSD^+$, because of mass overlap and the dominance of the parent ion beam, the shape of the $FeSD^+$ product cross section is only difficult to resolve and the noise level increases dramatically, especially in the threshold region at low interaction energies.

2.4 Sector-Field Mass Spectrometry

Some experiments in this Thesis are performed with a modified VG ZAB/HF/AMD 604 four-sector mass spectrometer of BEBE configuration (B stands for magnetic and E for electric sectors), shown in Figure 2-3. As the instrument has also been described in detail previously, it is again introduced only briefly.[53]

The instrument consists of an ion source, followed by a magnetic sector for primary mass selection. Between the two magnetic and two electric sectors, four field-free regions are arranged for the realization of collision experiments. The iron- and cobalt-complexes investigated in the present study are generated in a chemical ionization source (CI, repeller voltage ca. 0 V) by 100 eV electron bombardment of approximately 1:5 mixtures of $Fe(CO)_5$ or $Co(CO)_3(NO)$, respectively, with the substrate. For most experiments the ions are

accelerated to 8 keV kinetic energy and mass-selected by means of B(1)/E(1) at a resolution of m/Δm = 4000 - 5000 to provide separation of isobaric ions. Fragmentations occur in the field-free region preceding B(2) and are recorded by scanning B(2). The spectra are accumulated and on-line processed with the AMD-Intectra data system; 10 to 20 scans are averaged in order to improve signal-to-noise ratios. However, in some notorious cases it is indicated to use B(1) only for mass selection because of low parent or daughter ion intensities.[54] Fragmentations then occur in the collision cells preceding E(1) and are recorded by scanning this sector. Further, B(1) only mass-selection is used in the energy-resolved charge-reversal and charge-stripping experiments due to the superior energy resolution of E(1) vs. E(2). It needs to be kept in mind, however, that mass selection by B(1) only may give rise to artifact peaks and spectra have to be monitored very cautiously in that respect.[55] Several kinds of experiments can be performed with sector-MS and are briefly sketched below while a schematic summary is given in Table 2-1.

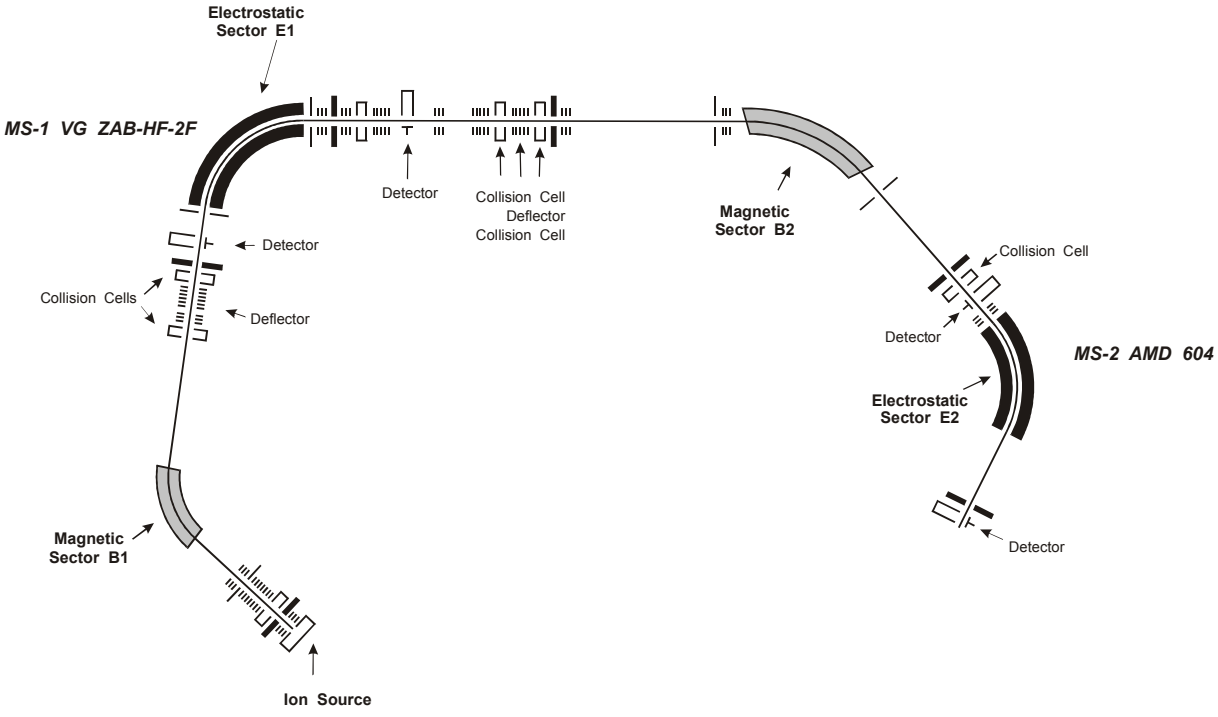

Figure 2-3: Experimental Setup of the four-sector mass spectrometer.

Metastable Ion (MI) Decay. Some of the ions generated in the ion source are rovibrationally excited and fragment within the μs timescale of the sector-MS experiment. This is a strictly unimolecular process; however, the metastable ions may rearrange before fragmentation, such that the fragmentation patterns of MI experiments contain valuable information about possible reaction intermediates.

Collisional Activation (CA). In these experiments, the ions are collided with helium in highly energetic collisions. Some of the translational energy of the collision is converted into internal energy of the ion, thus forming ro-vibrationally excited species. These species fragment almost immediately (within a ps time-frame), so that rearrangements are less likely and the results of CA experiments are often structure-indicative. Note, however, that MI processes are inherently always superimposed to the CA patterns.

Charge Reversal (CR).[56] Two types of CR experiments exist, in which either anions are converted to the corresponding cations by collision with an appropriate target gas ($^{-}CR^{+}$)[57] or vice versa, that charge inversion occurs from the cations to the anions ($^{+}CR^{-}$). Occurrence of only one collision with the target gas is assured by single-collision conditions (80 % transmission, T). Therefore, two collision events, i.e. two one-electron transfer reactions, are assumed to be negligible, and single, two-electron processes prevail.

Neutralization-Reionization (NR). In contrast to charge reversal described above, NR experiments involve intermediate formation of neutral species. Thus, this type of experiment allows to probe the existence and the reactivity of neutral species by mass-spectrometric means. In order to conduct NR experiments, two collision cells and an intermediate deflector are required. In the first collision cell, one-electron transfer is achieved by collision with an appropriate target gas to form the neutral species from the precursor ion. After leaving the collision cell, all remaining and/or formed ions are deflected and only the neutral species enter the second collision cell. Here, reionization is achieved by collisions with a second target gas. In principle, four types of NR experiments are feasible, i.e. $^{+}NR^{+}$, $^{+}NR^{-}$, $^{-}NR^{+}$, and $^{-}NR^{-}$; however, $^{-}NR^{-}$ experiments are not carried out in the present Thesis. The target gases for the different NR experiments are displayed in Table 2-1.

Charge Stripping (CS) and Charge Exchange (CE). In typical CS experiments,[58] monocation precursors are converted to dications in high-energy collisions with a quasi-stationary target gas. In the cases discussed in this Thesis, the energy of the projectiles is approximately 8000 eV and the target gas is molecular oxygen. In such a collision, the ionization is assumed to occur vertically; and the ionization energy (*IE*) of the monocation is provided by the energy of the projectile. This results in a shift of the dication signal on the kinetic energy scale, usually referred to as Q_{min} value.[59] To a first approximation, Q_{min} corresponds to the vertical ionization energy IE_v of the monocation. Experimental aspects of these measurements, e.g. calibration schemes and possible interferences, are discussed in more detail in the corresponding Chapters 3 and 4. The charge exchange is the reverse

reaction to charge stripping experiments, e.g. dications are converted by one-electron transfer to the corresponding monocations.

Table 2-1: Overview over different experiments conducted with sector-MS.

Experiment	reactant mass selection	collision gas (cell 1 / cell 2)
MI	B(1)/E(1)	none
CA	B(1)/E(1)	He, 80 % T
$^{-}CR^{+}$	B(1)/E(1)[a]	O_2, 80 % T
$^{+}CR^{-}$	B(1)	Xe, 60% T
$^{-}NR^{+60}$	B(1)/E(1)[a]	O_2/O_2, 80 % T / 80 % T
$^{+}NR^{-60}$	B(1)	Xe/Xe, 80% T / 80% T
$^{+}NR^{+}$	B(1)/E(1)	Xe/O_2, 80% T / 80% T
CS[61]	B(1)/E(1)[a]	O_2, 80% T
CE[62]	B(1)/E(1)	He/O_2, 80% T / 80 % T

[a] B(1) only for energy resolved measurements.

References

[1] P. v. R. Schleyer, N. L. Allinger, T. Clark, J. Gasteiger, P. A. Kollmann, H. F. Schafer III, P. R. Schreiner (Eds.) *The Encyclopedia of Computational Chemistry*, Wiley, Chichester, **1998**.

[2] (a) A. Szabo, N. S. Ostlund *Modern Quantum Chemistry*, Dover Publications Inc., New York, **1989**. (b) P. W. Atkins *Molecular Quantum Mechanics*, Oxford University Press, Oxford, **1993**. (c) F. Jensen *Introduction to Computational Chemistry*, Wiley, Chichester, **1999**.

[3] K. B. Lipkowitz, D. B. Boyd (Eds.), *Reviews in Computational Chemistry 1-7*, VCH, New York, **1990-1995**.

[4] For recent reviews on transition-metal theoretical chemistry, see: (a) M. B. Hall *Chem. Rev.* **2000**, *100*, 353. (b) M. Torrent, M. Solà, G. Frenking *Chem. Rev.* **2000**, *100*, 439. (c) G. Frenking, N. Fröhlich *Chem. Rev.* **2000**, *100*, 717.

[5] M. Born, R. J. Oppenheimer *Ann. Phys.* **1927**, *84*, 457.

[6] (a) D. R. Hartree *Prog. Camb. Phil. Soc.* **1928**, *24*, 89. (b) V. Fock *Z. Phys.* **1931**, *61*, 126.

[7] For detailed descriptions of DFT and its underlying formalisms, see (a) R. G. Parr, W. Yang *Density Functional Theory of Atoms and Molecules*, Oxford Univ. Press, Oxford, **1989**. (b) O. Gunnarson, R. G. Jones *Rev. Mod. Phys.* **1989**, *61*, 689. (c) T. Ziegler *Chem. Rev.* **1991**, *91*, 651. (d) T. Ziegler *Can. J. Chem.* **1995**, *73*, 743. (e) R. F. Nalewajski (Ed.), *Density Functional Theory I - IV* in Top. Curr. Chem. 180 - 183, Springer-Verlag, Berlin, **1996**.

[8] For DFT applications on transition-metal systems, see: (a) W. Koch, R. H. Hertwig *DFT-Applications to Transition Metal Problems* in Ref. 1. (b) W. Koch, M. C. Holthausen *A Chemists Guide to Density Functional Theory*, Wiley-VCH, Weinheim, **2000**.

[9] P. Hohenberg, W. Kohn *Phys. Rev. A* **1964**, *136*, 864.

[10] W. Kohn, L. Sham *Phys. Rev. A* **1965**, *140*, 1133.

[11] T. Ziegler *Pure Appl. Chem.* **1991**, *63*, 873.

[12] (a) A. D. Becke *Int. J. Quantum Chem.* **1983**, *23*, 1915. (b) A. D. Becke *J. Chem. Phys.* **1986**, *84*, 4524. (c) J. P. Perdew *Phys. Rev. B* **1986**, *33*, 8822. (c) A. D. Becke *Phys. Rev. A* **1988**, *38*, 3098. (d) C. Lee, W. Yang, R. G. Parr *Phys. Rev. B* **1988**, *37*, 785. (e) J. P. Perdew, Y. Wang *Phys. Rev. B* **1992**, *45*, 13244.

[13] (a) A. D. Becke *J. Chem. Phys.* **1993**, *98*, 1372. (b) A. D. Becke *J. Chem. Phys.* **1993**, *98*, 5684.

[14] P. J. Stephens, F. J. Devlin, C. F. Chabalowski, M. J. Frisch *J. Phys. Chem.* **1994**, *98*, 11623.

[15] (a) G. H. Loew, D. L. Harris *Chem. Rev.* **2000**, *100*, 407. (b) P. E. M. Siegbahn, M. R. A. Blomberg *Chem. Rev.* **2000**, *100*, 421.

[16] (a) S. Bärsch, I. Kretzschmar, D. Schröder, H. Schwarz, P. B. Armentrout *J. Phys. Chem.* **1999**, *103*, 5925. (b) S. Bärsch, D. Schröder, H. Schwarz *Chem. Eur. J.* in press. (c) S. Bärsch, D. Schröder, H. Schwarz *J. Phys. Chem.* in press.

[17] (a) K. Yoshizawa, Y. Shiota, T. Yamabe *Chem. Eur. J.* **1997**, *3*, 1160. (b) K. Yoshizawa, Y. Shiota, T. Yamabe *J. Am. Chem. Soc.* **1998**, *120*, 564. (c) K. Yoshizawa, Y. Shiota, T. Yamabe *Organometallics*, **1998**, *17*, 2825. (d) K. Yoshizawa, Y. Shiota, T. Yamabe *J. Chem. Phys.* **1999**, *111*, 538.

[18] (a) M. Sodupe, V. Branchadell, M. Rosi, C. W. Bauschlicher Jr. *J. Phys. Chem. A* **1997**, *101*, 7854. (b) A. Irigoras, J. E. Fowler, J. M. Ugalde *J. Am. Chem. Soc.* **1999**, *121*, 8549.

[19] (a) M. N. Glukhovtsev, R. D. Bach, C. J. Nagel *J. Phys. Chem. A* **1997**, *101*, 316. (b) C. B. Kellogg, K. K. Irikura *J. Phys. Chem. A* **1999**, *103*, 1150.

[20] C. Heinemann Ph.D. Thesis, TU Berlin D83, **1995**, and references cited therein.

[21] (a) M. C. Holthausen, C. Heinemann, H. H. Cornehl, W. Koch, H. Schwarz *J. Chem. Phys.* **1995**, *102*, 4931. (b) M. C. Holthausen, M. Mohr, W. Koch *Chem. Phys. Lett.* **1995**, *240*, 245.

[22] S. Bärsch, D. Schröder, H. Schwarz *Helv. Chim. Acta*, **2000**, *83*, 827.

[23] (a) O. Gunnarson, R. O. Jones *Phys. Rev. B* **1985**, *31*, 7588. (b) T. V. Russo, R. L. Martin, P. J. Hay *J. Chem. Phys.* **1994**, *101*, 7729. (c) C. W. Bauschlicher, Jr. *Chem. Phys.* **1996**, *211*, 163.

[24] J. Sugar, C. Corliss *J. Phys. Chem. Ref. Data* **1985**, *14*, Suppl. 2.

[25] *Gaussian 94* (Revision A.1), M. J. Frisch, G. W. Trucks, H. B. Schlegel, P. M. W. Gill, B. G. Johnson, M. A. Robb, J. R. Cheeseman, T. A. Keith, G. A. Petersson, J. A. Montgomery, K. Raghavachari, M. A. Al-Laham, V. G. Zakrzewski, J. V. Ortiz, J. B. Foresman, J. Cioslowski, B. B. Stefanov, A. Nanayakkara, M. Challacombe, C. Y. Peng, P. Y. Ayala, W. Chen, M. W. Wong, J. L. Andres, E. S. Replogle, R. Gomperts, R. L. Martin, D. J. Fox, J. S. Binkley, D. J. Defrees, J. Baker, J. P. Stewart, M. Head-Gordon, C. Gonzalez, J. A. Pople, Gaussian Inc., Pittsburgh **1995**.

[26] Molpro is an *ab initio* program package written by H.-J. Werner and P. J. Knowles, J. Almlöf, R. D. Amos, M. J. O. Deegan, S. T. Elbert, C. Hampel, W. Meyer, K. Peterson, R. Pitzer, A. J. Stone, P. R. Taylor, and R. Lindh.

[27] The ADF program package is a suite of programs employing DFT. ADF is available from: G. te Velde, E. J. Baerends Department of Theoretical Chemistry, Vrije Universiteit, Amsterdam, Netherlands. For information on ADF, see: (a) E. J. Baerends, D. E. Ellis Chem. Phys. 1973, 2, 71. (b) G. te Velde, E. J. Baerends *J. Comp. Phys.* **1992**, *99*, 84, and references cited therein.

[28] M. W. Schmidt, K. K. Baldridge, J. A. Boatz, S. T. Elbert, M. S. Gordon, J. H. Jensen, S. Koseki, N. Matsunaga, K. A. Nguyen, S. Su, T. L. Windus, M. Dupuis, J. A. Montgomery *J. Comp. Chem.* **1993**, *14*, 1347.

[29] (a) S. Simon, M. Duran, J. J. Dannenberg *Chem. Phys.* **1996**, *105*, 11024, and references cited therein. (b) S. Tsuzuki, T. Uchimaru, M. Mikami, K. Tanabe *J. Chem. Phys.* **1998**, *109*, 2169.

[30] E. R. Davidson, D. Feller *Chem. Rev.* **1986**, *86*, 681.

[31] S. F. Boys, F. Bernardi *Mol. Phys.* **1970**, *19*, 533.

[32] T. D. Dargel, R. H. Hertwig, W. Koch, H. Horn *J. Chem. Phys.* **1998**, *108*, 3876.

[33] (a) M. L. Gross, D. C. Rempel *Science* **1984**, *226*, 261. (b) A. G. Marshall *Acc. Chem. Res.* **1985**, *18*, 316. (c) M. V. Buchanan (Ed.) *Fourier Transform Mass Spectrometry: Evolution, Innovations, and Applications*, ACS Symposium Series 359, ACS, Washington DC, **1987**. (d) B. Asamoto *Analytical Applications of Fourier-Transform Mass Spectrometry*, VCH, Weinheim, **1991**. (e) N. M. M. Nibbering *Analyst* **1991**, *117*, 289.

[34] (a) K. Eller, H. Schwarz *Int. J. Mass Spectrom. Ion Processes* **1989**, *93*, 243. (b) K. Eller, W. Zummack, H. Schwarz *J. Am. Chem. Soc.* **1990**, *112*, 621.

[35] A. G. Marshall, C. L. Hendrickson, G. S. Jackson *Mass Spec. Rev.* **1998**, 17, 1.

[36] D. Schröder, H. Schwarz, D. E. Clemmer, Y.-M. Chen, P. B. Armentrout, V. I. Baranov, D. K. Böhme *Int. J. Mass Spectrom. Ion Processes* **1997**, *161*, 175.

[37] FERETS stands for front-end resolution enhancement with tailored sweeps: R. A. Forbes, F. H. Laukien, J. Wronka *Int. J. Mass Spectrom. Ion Processes* **1988**, *83*, 23.

[38] M. P. Langevin *Ann. Chim. Phys.* **1905**, *69*, 2243.

[39] (a) T. Su, M. T. Bowers *Int. J. Mass Spectrom. Ion Phys.* **1973**, *12*, 347. (b) T. Su, E. C. F. Su, M. T. Bowers *J. Chem. Phys.* **1978**, *69*, 2243.

[40] (a) T. Su, W. J. Chesnavich *J. Chem. Phys.* **1982**, *76*, 5183. (b) T. Su *J. Chem. Phys.* **1988**, *89*, 4102. (c) T. Su *J. Chem. Phys.* **1988**, *89*, 5355.

[41] For examples, see: (a) D. Schröder, J. Hrušák, I. C. Tornieporth-Oetting, T. M. Klapötke, H. Schwarz *Angew. Chemie* **1994**, *106*, 223; *Angew. Chem. Int. Ed. Engl* **1994**, *33*, 212. (b) I. Kretzschmar, D. Schröder, H. Schwarz, C. Rue, P. B. Armentrout *J. Phys. Chem. A* **1998**, *102*, 10060.

[42] G. Bouchoux, J. Y. Salpin, D. Leblanc *Int. J. Mass Spectrom. Ion Processes* **1996**, *153*, 37.

[43] For examples, see: (a) D. Schröder, J. Hrušák, R. H. Hertwig, W. Koch, P. Schwerdtfeger, H. Schwarz *Organometallics* **1995**, *14*, 312. (b) D. Schröder, H. Schwarz, J. Hrušák, P. Pyykkö *Inorg. Chem.* **1998**, *37*, 624.

[44] M. Dieterle, J. N. Harvey, D. Schröder, J. Schwarz, C. Heinemann, H. Schwarz *Chem. Phys. Lett.* **1997**, *277*, 399.

[45] The pressures have been corrected for relative sensitivity of the ion gauge towards different gases: (a) F. Nakao *Vakuum* **1975**, *25*, 431. (b) J. E. Bartmess, R. M. Georgiadis *Vacuum* **1983**, *33*, 149. (c) D. Schröder, Ph.D. Thesis, Technische Universität Berlin D83, **1992**.

[46] D. Schröder, R. Wesendrup, R. H. Hertwig, T. K. Dargel, H. Grauel, W. Koch, B. R. Bender, H. Schwarz *Organometallics*, in press.

[47] (a) K. M. Ervin, P. B. Armentrout *J. Chem. Phys.* **1985**, *83*, 166. (b) R. H. Schultz, P. B. Armentrout *Int. J. Mass Spectrom. Ion Processes* **1991**, *107*, 29. (c) R. H. Schultz, K. C. Crellin, P. B. Armentrout *J. Am. Chem. Soc.* **1991**, *113*, 8590. (d) P. B. Armentrout In *Advances in Gas Phase Ion Chemistry*, Vol. 1, N. G. Adams, L. M. Babcock (Eds.), JAI Press, Greenwich, **1992**, p. 83.

[48] T. Beyer, D. F. Swinehart *Comm. Assoc. Comput. Machines* **1973**, *16*, 379.

[49] G. Herzberg *Molecular Spectra and Molecular Structure*, reprint edition, Krieger, Malabar, Vol I, **1989**, and Vol. III, **1991**.

[50] L. S. Sunderlin, P. B. Armentrout *Int. J. Mass Spectrom. Ion Processes* **1989**, *94*, 149.

[51] (a) N. F. Dalleska, K. Honma, P. B. Armentrout *J. Am. Chem. Soc.* **1993**, *115*, 12125. (b) F. A. Khan, D. E. Clemmer, R. H. Schultz, P. B. Armentrout *J. Phys. Chem.* **1993**, *97*, 7978. (c) N. F. Dalleska, K. Honma, L. S. Sunderlin, P. B. Armentrout *J. Am. Chem. Soc.* **1994**, *116*, 3519.

[52] M. T. Rodgers, P. B. Armentrout *J. Phys. Chem. A* **1997**, *101*, 2614.

[53] (a) R. Srinivas, D. Sülzle, T. Weiske, H. Schwarz *Int. J. Mass Spectrom. Ion Processes* **1991**, *107*, 368. (b) R. Srinivas, D. Sülzle, W. Koch, C. H. DePuy, H. Schwarz *J. Am. Chem. Soc.* **1991**, *113*, 5970.

[54] J. N. Harvey, C. Heinemann, A. Fiedler, D. Schröder, H. Schwarz *Chem. Eur. J.* **1996**, *2*, 1230.

[55] D. Schröder, H. Schwarz *Int. J. Mass Spectrom. Ion Processes* **1995**, *146/147*, 183.

[56] M. M. Bursey *Mass Spectrom. Rev.* **1990**, *9*, 555.

[57] The charges of the parent ion and the product ion are indicated by superscripts. Thus, $^{-}CR^{+}$ denotes a charge reversal from the anion to the cation.

[58] D. Schröder, H. Schwarz *J. Phys. Chem. A* **1999**, *103*, 7385.

[59] K. Lammertsma, P. v. R. Schleyer, H. Schwarz *Angew. Chem. Int. Ed. Engl.* **1989**, *28*, 1321.

[60] N. Goldberg, H. Schwarz *Acc. Chem. Res.* **1994**, *27*, 347.

[61] T. Ast Adv. Mass Spectrom. A **1980**, 8, 555

[62] K. Vékey *Mass Spectrom. Rev.* **1995**, *14*, 195, and references cited therein.

3 Reactivity and Redox Chemistry of $FeO_mH_n^+$ (m = 1 - 2; n = 0 - 4)*

Transition-metal oxides and hydroxides are of fundamental relevance in numerous oxidation processes and their properties have been studied in great detail.[1,2] Their diversity and reactivity is responsible for their usefulness in several branches of chemistry, such as biochemistry, catalysis, and organic synthesis. Very prominent and technically useful examples are for instance iron oxides, which exist in high natural abundance and are used not only as iron ores, but also serve as catalysts in the synthesis of ammonia (together with aluminum oxide) and in dehydrogenation reactions (for instance styrene synthesis from ethylbenzene). Moreover, the reactive sites of some biological systems have been identified to consist of Fe–O units.[3] Nature for instance very efficiently catalyzes oxidation reactions using cytochrome P-450, and other powerful oxidation catalysts.[4,5] The reactive site of cytochrome P-450 is commonly believed to involve a high-valent iron-oxo species.

Due to these many occurrences and applications, there exists a high interest in understanding the reactivity and thermochemistry of iron-oxo species. The following chapter of this Thesis therefore presents (i) a reactivity study of the degenerate $^{16}O/^{18}O$ exchange in FeO^+ and $FeOH^+$ with $H_2{}^{18}O$, (ii) a combined reactivity and thermochemistry study of the related $Fe(H_2O_2)^{+/2+}$ complex, and (iii) a study of the thermochemistry of $FeO_mH_n^{2+}$ dications.[6]

The $^{16}O/^{18}O$ exchange reaction has been suggested as a probe for the involvement of reactive metal-oxo units in catalytic cycles.[7] The interest in $Fe(H_2O_2)^+$ stems from the role of iron salts in the activation of hydrogen peroxide in solution, i.e. Fenton chemistry.[8] Finally, the assessment of the redox-properties of $FeO_mH_n^{2+}$ dications is a contribution towards a more detailed understanding of processes occurring in the corrosion of iron in the aqueous phase.[9,10]

In this chapter, the B3LYP theoretical approach is combined with the standard all-electron 6-311+G* basis for oxygen and hydrogen,[11] and the Wachters-Hay all-electron basis for iron.[12]

* Parts of these results have been or will be published in (a) S.Bärsch, D. Schröder, H. Schwarz *Chem. Eur. J.* in press. (b) S. Bärsch, D. Schröder, H. Schwarz *Helv. Chim. Acta* **2000**, *83*, 827. (c) D. Schröder, S. Bärsch, H. Schwarz *J. Phys. Chem. A* in press.

3.1 A DFT-Study on the $^{16}O/^{18}O$-Exchange Reactions of the Prototype Iron-Oxygen Compounds FeO^+ and $FeOH^+$ with $H_2{}^{18}O$

Gas-phase chemistry as an option to obtain information about the electronic features of intermediates and the role of transients in the reactions of iron oxides and hydroxides in the absence of obscuring effects, e.g. aggregates, counter ions, solvents,[13] has been used extensively in the investigation of iron-oxo compounds. Previous studies of "bare" FeO^+, for instance, have been carried out in much detail and have provided valuable insight into the behavior of what is considered the "reactive species" in industrial and biochemical oxidation processes of hydrocarbons.[14] Among the many reported gas-phase reactions of FeO^+,[13,15] the degenerate $^{16}O/^{18}O$ exchange in the reaction with isotopically labeled water is especially interesting because occurrence of $^{16}O/^{18}O$ exchange has been suggested as a mechanistic probe for the intermediacy of reactive metal-oxo units in catalytic oxidations.[7] This chapter reports a detailed mechanistic investigation of this process in comparison to the related $^{16}O/^{18}O$ exchange in the reaction of $FeOH^+$ with $H_2{}^{18}O$.

Aside the occurrence of association reactions to afford $[Fe,O_2,H_2]^+$ and $[Fe,O_2,H_3]^+$, respectively, when trapping FeO^+ and $FeOH^+$ with water in the gas phase,[16,17] previous experimental studies[18,19] have also described the $^{16}O/^{18}O$ exchange of FeO^+ and $FeOH^+$ with $H_2{}^{18}O$. To resume the conclusions of these studies, $FeOH^+$ is found to undergo isotopic exchange three times faster than FeO^+. Two possible explanations for the different reaction rates have been suggested.[19] (i) In the reaction of FeO^+ with water, $^{16}O/^{18}O$ exchange requires two hydrogen shifts from one O-atom to the other, whereas only a single hydrogen migration is sufficient for $FeOH^+$. (ii) Based on computational studies of related iron(III) compounds, a quartet ground state is postulated for the iron dihydroxide cation $Fe(OH)_2^+$ as the key intermediate in the FeO^+/H_2O system, while the FeO^+ reactant has a $^6\Sigma^+$ ground state.[20] Hence, $^{16}O/^{18}O$ exchange in FeO^+ would require spin crossover between the sextet and quartet surfaces and vice versa, thus decreasing the reaction efficiency. Such kinetic restrictions due to spin constraints have been recently described in terms of a two-state reactivity concept.[21] In contrast, no spin inversions need to be involved in the $FeOH^+/H_2O$ system.

The work presented in this chapter aims at improving these tentative arguments towards a more elaborate understanding of the reactions of FeO^+ and $FeOH^+$ with water by means of a theoretical approach. In that respect, the different options of hydrogen migrations in the FeO^+/H_2O and $FeOH^+/H_2O$ systems are examined and particular attention is paid to the possible role of spin multiplicities of the relevant transition structures and intermediates.

3.1.1 Pathways, Structures, and Energetics

For each of the reactants, FeO^+ and $FeOH^+$, two pathways are conceivable for oxygen-atom exchange with water. The reactions may proceed via direct 1,3-hydrogen migration steps or via sequential 1,2-hydrogen migrations. As a third variant, combinations of 1,2- and 1,3-shifts may be possible in case of FeO^+, which are, however, not addressed explicitly. The 1,2-shift in the $FeO^+/H_2{}^{18}O$ system leads to formation of complex **2**, and a second 1,2-shift yields formation of the iron dihydroxide cation **3**; the latter is also the intermediate of the direct 1,3-migration (Figure 3-1).

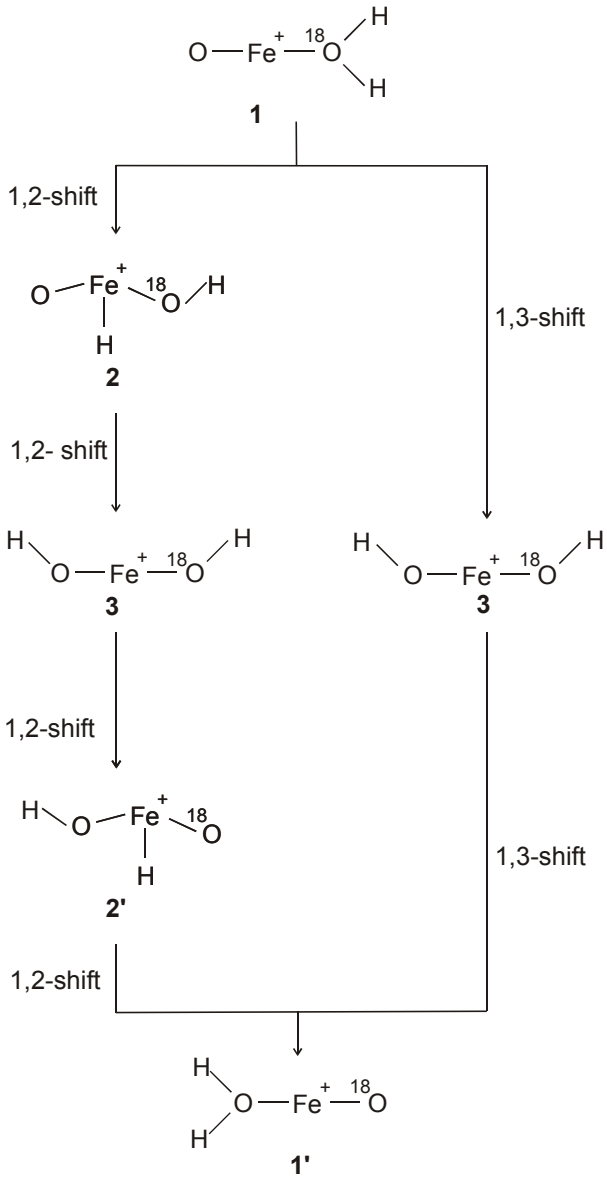

Figure 3-1: Schematic description of the two calculated reaction pathways of the $FeO^+/H_2{}^{18}O$ system.

The situation is slightly different in the $FeOH^+/H_2{}^{18}O$ system: here, the 1,3-shift mechanism does not involve any reaction intermediates while the consecutive 1,2-migrations proceed via the hydrido-dihydroxy intermediate **5** (Figure 3-2).

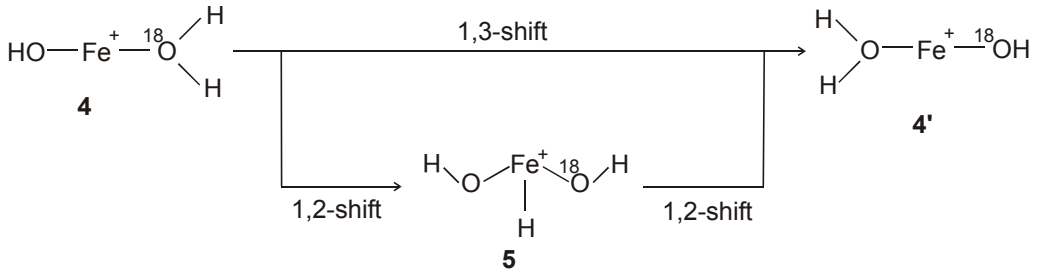

Figure 3-2: Schematic description of the two calculated reaction pathways of the $FeO^+/H_2{}^{18}O$ system.

In both cases, the respective low- and high-spin surfaces are considered, i.e. quartet/sextet for FeO^+/H_2O and triplet/quintet for $FeOH^+/H_2O$. For the sake of simplicity, and regarding the low symmetry of most species involved, the notation used throughout this chapter gives the spin multiplicities as superscripts preceding the formula while neglecting orbital symmetries, e. g. the sextet ground state FeO^+ ($^6\Sigma^+$) is referred to as $^6FeO^+$.

3.1.2 The System $FeO^+ + H_2O$

Reactants. In line with a number of previous theoretical studies using classical *ab initio* methods,[20,21a,22] pure DFT approaches,[23] and hybrid procedures,[22,24] the present computations predict a $^6\Sigma^+$ ground state for FeO^+ with an orbital occupation $1\sigma^2 2\sigma^2 1\pi^4 1\delta^2 2\pi^2 3\sigma^1$ in the valence space.[20,21] The bond length is computed as r_{FeO} = 1.64 Å, and the calculated bond dissociation energy of $D_0(Fe^+\text{-}O)$ = 78.2 kcal/mol agrees favorably with the experimental value of 80.0 kcal/mol.[25] However, this pleasing agreement is most likely due to a fortuitous error cancellation, as B3LYP and other density functionals show a bias of $3d^n$ over $3d^{n-1}4s^1$ configurations in the calculation of atoms and atomic ions, leading to an artificial preference for low spin $3d^n$ species. Thus, the B3LYP/6-311+G* level of theory predicts Fe^+ (^4F) to be 4.1 kcal/mol more stable than Fe^+ (^6D) (see Chapter 2).[26]

Using the B3LYP theoretical approach, the electronic state of $^4FeO^+$ cannot be assigned unambiguously and may either be $^4\Pi$ or $^4\Phi$. The occupation for these quasi-degenerate states according to NBO analysis is $1\sigma^2 2\sigma^2 1\pi^4 1\delta^3 2\pi^1 3\sigma^1$ in the valence space.[21] The calculated bond length of the quartet species (r_{FeO} = 1.70 Å) is large compared to previous *ab initio*

studies,[20-22] but matches the value of previous B3LYP calculations with different basis sets.[22-24] The long FeO bond in the quartet state should not be overrated as the potential-energy curve of $^4FeO^+$ is quite flat around the minimum, i.e. a geometry distortion by 0.01 Å translates to an energetic change of only about 0.2 kcal/mol.[20] More importantly, the calculated state splitting of 8.2 kcal/mol between $^6FeO^+$ and $^4FeO^+$ is significantly lower than calculated in previous studies employing the CCSD(T) and CASPT2 levels of theory, which yielded $^4FeO^+/^6FeO^+$ splittings in the order of 12 - 19 kcal/mol.[21,22] Nevertheless, the present result coincides with similar findings in recent B3LYP studies.[22-24]

An $^1A_1$ ground state is computed for the water molecule with r_{OH} = 0.96 Å well reproducing experimental data, while the HOH-angle α_{HOH} = 107.0° is slightly widened as compared to the tabulated geometry.[27] In the following, all energetics of the FeO^+/H_2O system refer to the $^6FeO^+ + {}^1H_2O$ asymptote, which is arbitrarily set to $E_{rel}(FeO^+ + H_2O)$ = 0.0 kcal/mol.

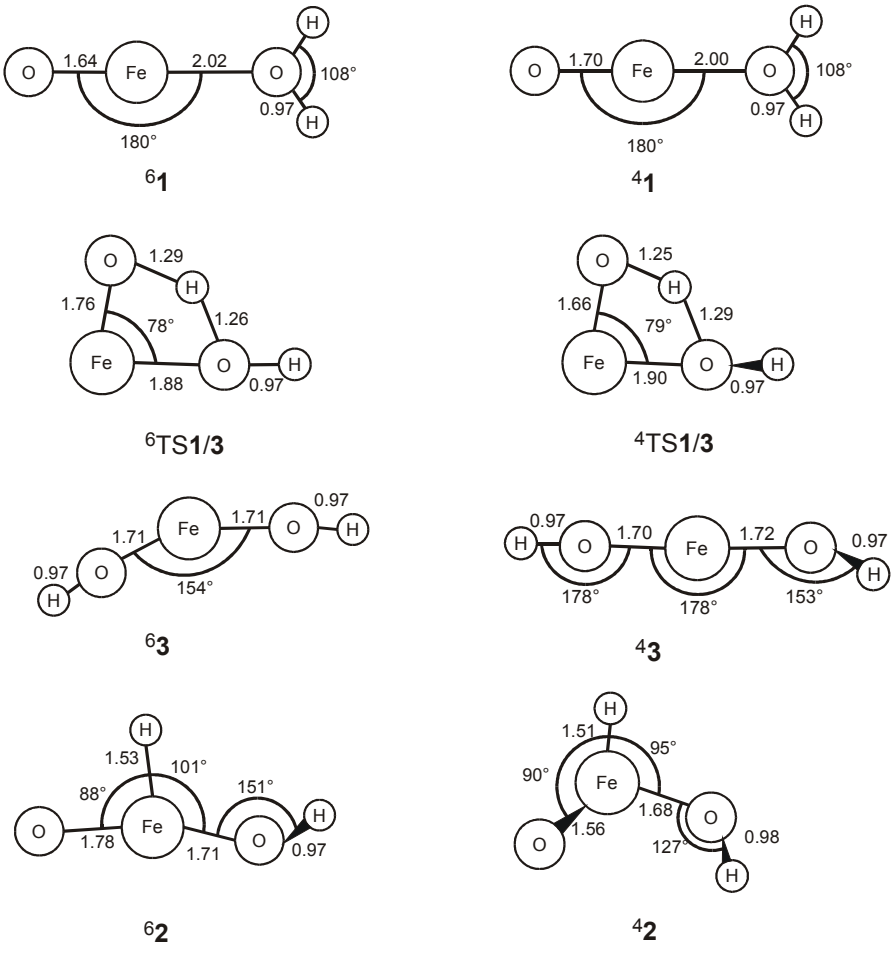

Chart 3-1: Stationary points of the $FeO^+ + H_2O$ PES. Bond lengths are in Å and angles in degree.

Encounter Complex. For the encounter complex **1**, $(H_2O)FeO^+$, a sextet ground state is located with the first excited quartet state 4.9 kcal/mol higher in energy. For both, ^{6}**1** and ^{4}**1**, the geometrical features of the separated FeO^+ and H_2O building blocks are mainly preserved. The bonds from the iron side of the FeO^+-moiety to the water ligands have comparable lengths of r_{FeO} = 2.02 Å and r_{FeO} = 2.00 Å for ^{6}**1** and ^{4}**1**, respectively (Chart 3-1). Given the similar geometries in conjunction with the flatness of the Fe-O potential in the bonding region of FeO^+ as described above, crossing between the sextet and the quartet surfaces is expected to be facile. Both encounter complexes are energetically located significantly below the entrance channel (E_{rel} = -53.1 and -48.2 kcal/mol for ^{6}**1** and ^{4}**1**, respectively). These well depths correspond to the binding energy of the water molecule to the FeO^+-unit and are rather strong compared to $D_0(Fe^+\text{-}OH_2)$ = 30.7 kcal/mol for naked iron;[25] an effect which will be evaluated in more detail later.

1,3-Mechanism. For reasons becoming obvious further below, the 1,3-route is discussed prior to the 1,2-variant. Along this mechanism, the reaction starting from **1** has to pass transition structure TS**1**/**3** to reach minimum **3**, $Fe(OH)_2^+$. The corresponding sextet and quartet states ^{6}TS**1**/**3** and ^{4}TS**1**/**3** are located at E_{rel} = -13.2 kcal/mol and E_{rel} = -8.4 kcal/mol, respectively. Three aspects are noteworthy in this context: (i) the sextet and quartet TS lie well below the $^6FeO^+ + {}^1H_2O$ entrance channel, (ii) the barriers for the 1,3-hydrogen migration are sizable (ca. 40 kcal/mol) with respect to the encounter complexes, and (iii) the sextet/quartet splitting has hardly changed going from **1** to **TS1/3**. As far as structural features are concerned, ^{6}TS**1**/**3** exhibits two different types of iron-oxygen bonds. The first one (r_{FeO} = 1.88 Å) shows a bond length between electrostatic bonding (as for instance r_{FeO} = 2.12 Å in $^6Fe(H_2O)^+$)[22b] and a formal Fe–O single bond (as for instance r_{FeO} = 1.71 Å in $^5FeOH^+$, see below). Compared to the iron-oxygen double bond in the iron-oxo unit of ^{6}**1** (r_{FeO} = 1.64 Å), the second Fe–O bond in ^{6}TS**1**/**3** is slightly elongated (r_{FeO} = 1.76 Å). While ^{4}TS**1**/**3** also shows one long Fe–O bond (1.90 Å), the second Fe–O bond (1.66 Å) is even shorter than that in the preceding minimum ^{4}**1**. However, except the differences in Fe–O bond lengths both transition structures are otherwise quite alike.

The imaginary frequencies of i1979 cm^{-1} (^{6}TS**1**/**3**) and i1939 cm^{-1} (^{4}TS**1**/**3**) correspond to migrations of a hydrogen atom from the water molecule to the oxo-ligand without intermediate formation of an Fe–H bond. Significant bending of the O–Fe–O units is required in the TS to allow migration of a hydrogen atom from one oxygen atom to the other without involving the metal center. Nevertheless, the minima connected to TS**1**/**3** show linear or at least almost linear arrangements. Therefore, prior to or simultaneously with the hydrogen

migrations in the TSs, the O–Fe–O units are required to bend and thereby decrease the O–Fe–O angle. Despite extensive searches for bent minimum structures of **1** and **3** in either spin state, only one such minimum, ^{6}**3**, was located at the applied level of theory. Additionally, even in ^{6}**3** the O–Fe–O angle is larger than in the corresponding transition structure. Instead, the IRC calculations connecting TS**1**/**3** with the corresponding minima show two features. The first one with steep slopes corresponds to the hydrogen migration from the water ligand to the oxo unit, and the second, more smooth curvature than comprises the widening of the O–Fe–O angle.

Following the reaction path after passing TS**1**/**3**, the dihydroxy-species **3** is reached. The sextet structure is predicted as the global minimum of the $[Fe,O_2,H_2]^+$ surface (E_{rel} = -66.4 kcal/mol for ^{6}**3** and -52.7 kcal/mol for ^{4}**3**). The geometrical features of the sextet show the expected structure, as both OH-moieties and their bonds to the iron cation are identical with α_{OFeO} = 154°. In contrast, the OH-groups are asymmetrically bound to iron in the quartet structure ^{4}**3**. While the Fe–O bond lengths are similar in ^{4}**3**, one Fe–O–H moiety is almost linear (178°) and the hydrogen atom of the second OH-group is distinctly distorted from the plane of the rest of the molecule (θ_{OFeOH} = 154°). Although dissimilar bonding in ^{4}**3** is conceivable, the computed geometry may also correspond to a spurious minimum due to symmetry breaking in the quasi-AB_2 type $Fe(OH)_2^+$ molecule. This issue, however, was not pursued any further because the symmetrical sextet ^{6}**3** is assigned as the electronic ground state of $Fe(OH)_2^+$ cation.

From **3**, oxygen-atom exchange can proceed via TS**1**/**3** again in the reverse direction to reach the product side (Figure 3-1: **1** → **3** → **1'**). Given the symmetry of ^{6}**3** and assuming a quasi-symmetric geometry of ^{4}**3**, both oxygen atoms are equilibrated in **3**. Overall, the computational prediction of TS**1**/**3**, lying 13.2 kcal/mol (^{6}TS**1**/**3**) and 8.4 kcal/mol (^{4}TS**1**/**3**) below the $^{6}FeO^+ + H_2O$ entrance channel can account for the $^{16}O/^{18}O$ exchange observed experimentally.[18,19]

1,2-Mechanism. The separated reactants as well as the encounter complexes are common to the 1,2- and 1,3-mechanisms (Figure 3-1, Chart 3-1). From the encounter complex, the reaction continues via a 1,2-hydrogen transfer to reach intermediate **2**, $(H)(OH)FeO^+$, where the metal center is surrounded by three ligands, i.e. H, O, and OH. The most prominent feature of **2** is the iron-hydrogen bond (r_{FeH} = 1.53 Å and 1.51 Å for ^{6}**2** and ^{4}**2**, respectively). The minima ^{6}**2** and ^{4}**2** are located at E_{rel} = 30.8 kcal/mol and E_{rel} = 13.2 kcal/mol. Because both structures are above the entrance channel as well as above any of the stationary points involved in the 1,3-pathways, explicit investigation of the TSs for the 1,2-routes deems

unnecessary. It is interesting to note, however, that the quartet state of the hydrido-species ^{4}**2** is 17.6 kcal/mol below ^{6}**2**. Hence, if O–H bond insertion to yield **2** would occur at elevated energies, it would involve spin crossover into the lower-lying quartet pathway. The computed high energy demand of **2** is in accord with the previous exclusion of the 1,2-mechanism based on the high oxidation states of the intermediates.[19] In fact, the bond lengths in either spin state of **2** indicate covalent bonding of iron to the ligands and thus support its assignment as a formal Fe(V) compound.

Finally, it needs to be noted that there exist other $[Fe,O_2,H_2]^+$ isomers, for instance, the cationic iron(I) complexes of hydrogen peroxide $Fe(H_2O_2)^+$ on the quartet and sextet surfaces. As these species are much higher in energy than **1** and **3** and even above the $FeO^+ + H_2O$ entrance channel,[6a-c,28] they cannot participate in the $^{16}O/^{18}O$ equilibration of the FeO^+/H_2O system under thermal conditions, but gain importance for the dications (Chapter 3.2).

3.1.3 The System $FeOH^+ + H_2O$

Reactants. An ^{5}A" ground state is found for $FeOH^+$ when calculated in C_s symmetry. While quintet ground states of $FeOH^+$ are also found in previous studies,[22b] the exact assignment of the ground state is more difficult for the close lying ^{5}A' and ^{5}A" states.[23] Probably due to cancellation of errors, the computed $D_0(Fe^+\text{-}OH)$ = 88.7 kcal/mol agrees quite well with the experimental value of 87.4 kcal/mol. The putative $HFeO^+$ isomers are situated much above the $^5FeOH^+$ cation,[22b] and are therefore excluded from further consideration. Similarly, the lowest-lying triplet state $FeOH^+$ (^{3}A') is 38.8 kcal/mol higher in energy than $^5FeOH^+$. It is therefore reasonable to assume that the triplet surface will have only little influence on the minimum energy path of oxygen-atom exchange; consequently, the role of low-spin state species along the reaction coordinate will be kept short. The structures of quintet and triplet $FeOH^+$ are very much alike, being bent with similar bond lengths. As the water molecule was already mentioned above, it remains to note that the following energetics are given with respect to the $^5FeOH^+ + {}^1H_2O$ asymptote, i.e. $E_{rel}(FeOH^+ + H_2O)$ = 0.0 kcal/mol.

Encounter complex. The encounter complex **4** consists of a $FeOH^+$ cation complexed by an intact H_2O ligand on both spin surfaces (Chart 3-2). The Fe–O–H units are almost linearized compared to free $FeOH^+$, and the hydroxy- and the water ligands reside on exactly opposite sides of the metal center (α_{OFeO} = 180°). Although both spin states result in geometrically similar structures, the state splitting (E_{rel} = -53.9 kcal/mol and -11.6 kcal/mol for ^{5}**4** and ^{3}**4**, respectively) is even slightly larger than for the $FeOH^+$ reactant.

Similar to the interaction between water and FeO^+ in **1**, the computed ligand-binding energy $D_0(HOFe^+\text{-}OH_2)$ = 53.9 kcal/mol is large compared to that of the bare metal, i.e. $D_0(Fe^+\text{-}OH_2)$ = 30.7 kcal/mol.[25]

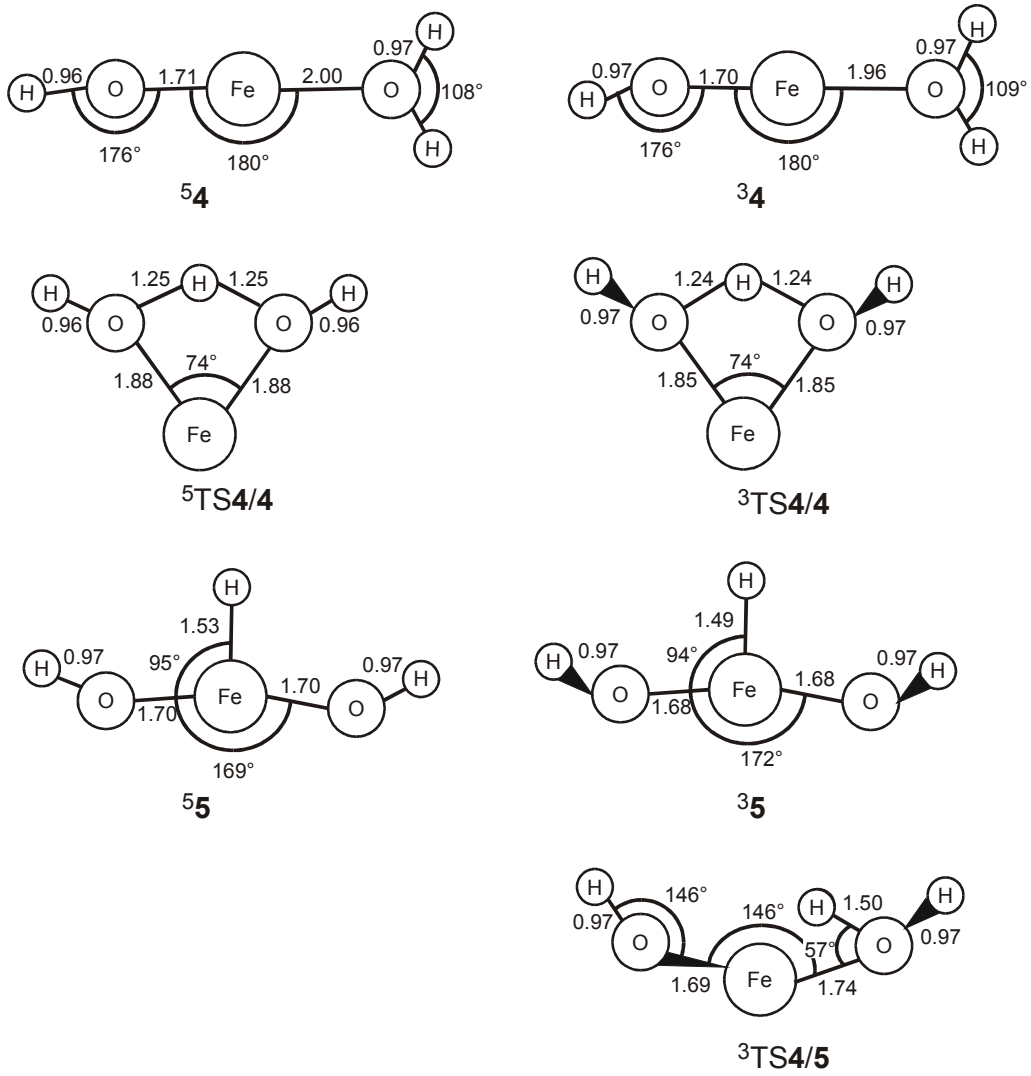

Chart 3-2: Stationary points of the $FeOH^+ + H_2{}^{18}O$ PES. Bond lengths are given in Å and angles in degree.

1,3-Mechanism. In contrast to the FeO^+/H_2O system, 1,3-hydrogen transfer is degenerate for **4** and results in immediate $^{16}O/^{18}O$ exchange in the $FeOH^+/H_2O$ system without involving a second step (Chart 3-2, Figure 3-2). On the quintet surface, the corresponding ^{5}TS**4**/**4** is located at E_{rel} = -17.3 kcal/mol; thus well below the energy demand of the isolated reactants $FeOH^+$ and H_2O (E_{rel} = 0.0 kcal/mol). The TSs in the two spin states are structurally very much alike as are the imaginary frequencies (i1695 cm^{-1} and i1601 cm^{-1} for ^{5}TS**4**/**4** and ^{3}TS**4**/**4**, respectively). Not surprisingly, the Fe–O bonds, the O–H distances of the migrating hydrogen atom, and the two "stationary" O–H bonds are exactly equivalent in the transition

structures. In analogy to TS**1**/**3** of the FeO^+/H_2O system, the O–Fe–O units in TS**4**/**4** are bent, while these are almost linear in the corresponding minima ^{5}**4** and ^{3}**4**. However, extensive computational search gives no indications for the existence of bent minima of **4** in either spin state.

1,2-Mechanism. In contrast to the 1,3-mechanism, the 1,2-route comprises two steps and a reaction intermediate which exhibits an iron-hydrogen bond, i.e. $(H)Fe(OH)_2^+$, **5**. This reaction intermediate is found at E_{rel} = 11.2 kcal/mol (^{5}**5**) and E_{rel} = 23.3 kcal/mol (^{3}**5**) on the respective spin surfaces. Although both structures of **5** almost have C_{2v} symmetry, the calculations proceeded only after reducing the symmetry to C_1. The hydrogen atoms are slightly bent out of plane in the optimized structures (1 - 2°), and seemingly equivalent bond lengths of the hydroxy bonds differ up to 0.04 Å. In analogy to the FeO^+/H_2O system, the location of **5** above the $^5FeOH^+ + {}^1H_2O$ entrance channel and above the stationary points associated with the 1,3-mechanism, lead to exclusion of the 1,2-route in the oxygen-atom exchange of the $FeOH^+/H_2O$ system under thermal conditions. Note that ^{3}TS**4**/**5** (E_{rel} = 35.3 kcal/mol) which was located at an early stage of this investigation is only slightly bent to form a O–Fe–O angle of 146° with an imaginary mode of i1140 cm^{-1} due to 1,2-hydrogen migration.

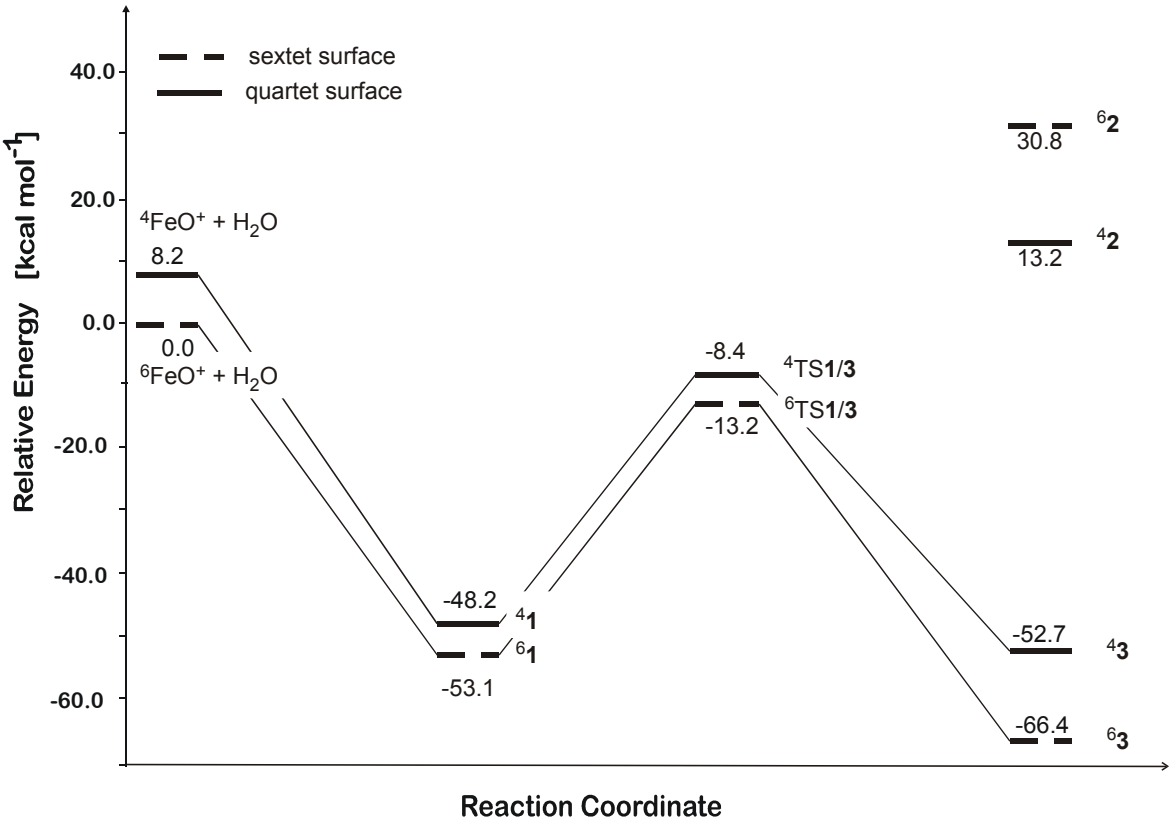

Figure 3-3: B3LYP/6-311+G* surface of the FeO^+/H_2O system.

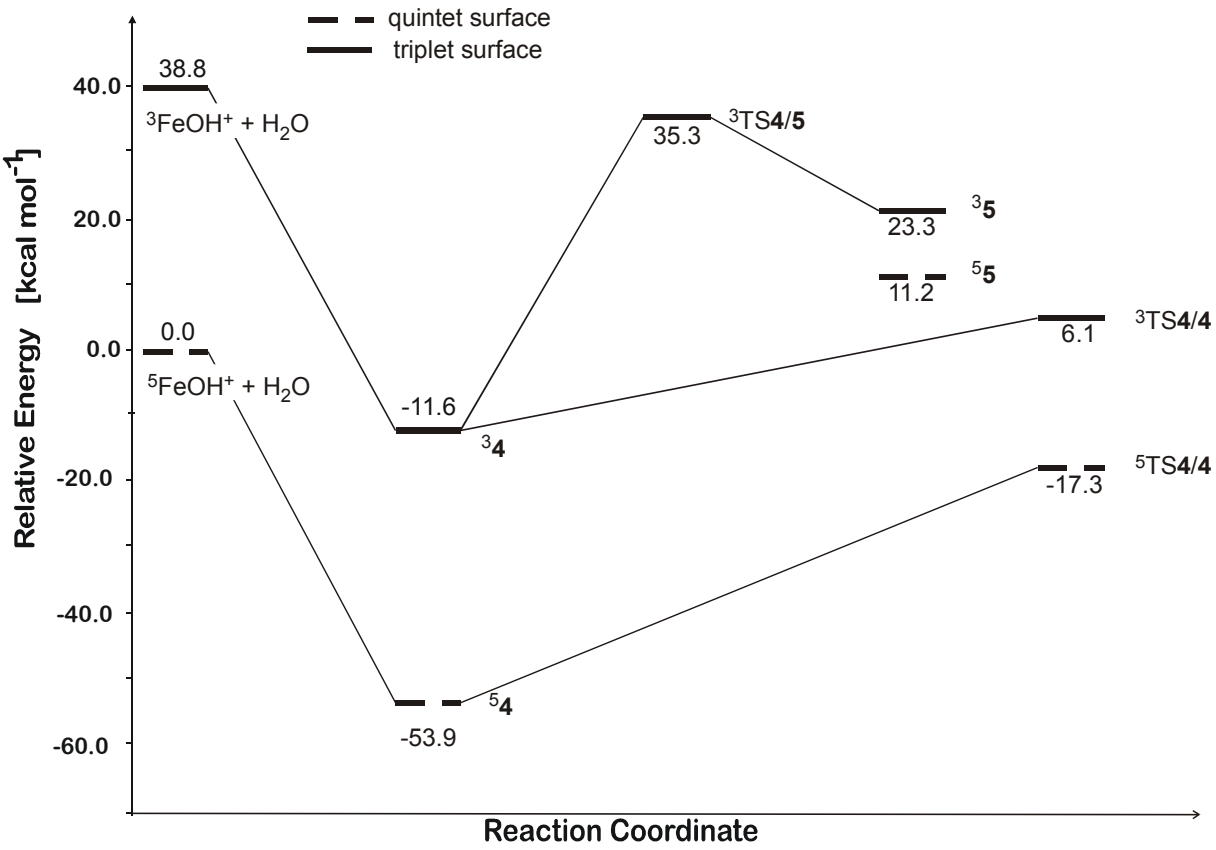

Figure 3-4: B3LYP/6-311+G* surface of the $FeOH^+/H_2O$ system.

3.1.4 Comparison of FeO^+ and $FeOH^+$

The computed potential-energy surfaces of both reactions are depicted in Figures 3–3 and 3–4. Some general features are outlined first, followed by a comparison of the 1,2- versus 1,3-mechanisms and a discussion of the role of spin states in the isotopic exchange of the oxygen-atoms in FeO^+ and $FeOH^+$ with $H_2{}^{18}O$.

In the description of the encounter complexes $(H_2O)FeO^+$ (**1**) and $(H_2O)FeOH^+$ (**4**), substantially increased binding energies of water to FeO^+ and $FeOH^+$ are noticed, compared to the bare metal, i.e. $D_0(OFe^+\text{-}OH_2)$ = 53.1 kcal/mol and $D_0(HOFe^+\text{-}OH_2)$ = 53.9 kcal/mol versus $D_0(Fe^+\text{-}OH_2)$ = 30.6 kcal/mol.[25] While some enhancement of water binding upon ligation of iron cation has been reported in other cases, e.g. $D_0(HFe^+\text{-}OH_2)$ = 32.7 kcal/mol,[29] and $D_0((H_2O)Fe^+\text{-}OH_2)$ = 39.2 kcal/mol,[25] the present increases of the binding energies by ca. 80% indicate rather strong ligand effects. While no experimental thermochemistry is available for **1** and **4**, the observed difference of more than three orders of magnitude in the rates of termolecular association of bare Fe^+ and FeO^+ with water[16] supports the computational prediction of a substantially larger binding energy in the case of FeO^+. These effects can be

explained in terms of increased ion-dipole interactions between the metal center and the water molecule in $(H_2O)FeO^+$ and $(H_2O)FeOH^+$ due to the presence of the electron-withdrawing oxygen- or hydroxyl-ligands which increase the net positive charge on the metal. This conjecture is qualitatively consistent with the computed partial charges of the water ligands; according to Mulliken population analysis, the charges increase from 0.12 in $^6Fe(OH_2)^+$ to 0.22 in $^6(H_2O)FeO^+$ and 0.19 in $^5(H_2O)FeOH^+$.

Despite the stabilizing effect of the water ligand, **1** is not the global minimum of the $[Fe,O_2,H_2]^+$ system. Instead, hydrogen migration leads to the iron dihydroxide cation **3** which is 13.3 kcal/mol more stable than **1** on the lowest-lying sextet surface. This result has considerable implications for the conceptual understanding of oxidation catalysis. Metal-oxo units are often considered as essential reactive units in various bond-activation processes, not only in gas-phase oxidations,[13] but also in other reactions induced by ionic metal fragments, e.g. the oligomerization of butadiene induced by ligated lanthanide cations.[30] In contrast, the corresponding dihydroxides, although bearing the same formal oxidation state, are often much less reactive.[30,31] Formation of $Fe(OH)_2^+$ has further been identified as the limiting sink to the turnover number in the catalytic gas-phase oxidation of ethane.[32] Asides the role of kinetic aspects, the consideration of thermochemical patterns derived from this work and additional literature data[25] supports the non-negligible influence of water on the oxidizing strengths of the formal iron(III) compounds FeO^+ and $(H_2O)FeO^+$. For example, one-electron reduction to formal iron(II) according to Equation 3-1 is much more exothermic for the metal-oxo species FeO^+ and $(H_2O)FeO^+$ compared to the dihydroxide $Fe(OH)_2^+$.

$FeO^+ + H^\bullet$	$\rightarrow FeOH^+$	$\Delta_r H$ = -109.3 kcal/mol	Equation 3-1a
$(H_2O)FeO^+ + H^\bullet$	$\rightarrow (H_2O)FeOH^+$	$\Delta_r H$ = -110.1 kcal/mol	Equation 3-1b
$Fe(OH)_2^+ + H^\bullet$	$\rightarrow (H_2O)FeOH^+$	$\Delta_r H$ = -96.8 kcal/mol	Equation 3-1c
FeO^+	$\rightarrow Fe^+ + O$	$\Delta_r H$ = 80.0 kcal/mol	Equation 3-2a
$(H_2O)FeO^+$	$\rightarrow (H_2O)Fe^+ + O$	$\Delta_r H$ = 102.4 kcal/mol	Equation 3-2b
$Fe(OH)_2^+$	$\rightarrow (H_2O)Fe^+ + O$	$\Delta_r H$ = 115.7 kcal/mol	Equation 3-2c

Further, the Fe–O bond in FeO^+ (Equation 3-2a) is significantly weaker than in $(H_2O)FeO^+$ (Equation 3-2b); liberation of an oxygen atom from the dihydroxide is even more energy demanding (Equation 3-2c). Given $\Delta_r H$ = -88.6 kcal/mol for the oxygenation of methane according to $CH_4 + O \rightarrow CH_3OH$, the bare FeO^+ cation is thus capable of transferring an O-

atom to methane, while $(H_2O)FeO^+$ and $Fe(OH)_2^+$ are not. Likewise, hydroxylation of the weaker tertiary C–H bond in *i*-butane ($\Delta_r H$ = -102 kcal/mol) is exothermic for FeO^+, thermoneutral for $(H_2O)FeO^+$, and considerably endothermic for $Fe(OH)_2^+$. Consequently, hydration of metal-oxo species can result in the formation of less, or even unreactive metal dihydroxides. In other words, the catalytic activity of metal-oxo units is likely to be reduced in the presence of water. Translation of this microscopic behavior to a macroscopic scale is, however, not straightforward, because the addition of water to the reactant stream can also have positive effects on the performance of catalysts, e.g. the removal of catalyst poisons as well as surface soot.[33]

As far as the mechanistic course of oxygen-atom exchange is concerned, the clear energetic preference for the 1,3-route is beyond any doubt in both systems. Specifically, the associated transition structures TS**1**/**3** and TS**4**/**4** are well below the entrance channels, thereby accounting for the experimentally observed $^{16}O/^{18}O$ exchange under thermal conditions.[18,19] In contrast, the occurrence of the 1,2-mechanism is excluded from further considerations for both systems because already the reaction intermediates **2** and **5** lie above the respective entrance channels. This result validates the previous speculation that the 1,2-mechanisms are unlikely to occur in terms of unfavorable high oxidation states of the putative intermediates.[19]

In both systems, the reactions can be envisioned to proceed on the respective high-spin surfaces exclusively. While this result was expected for the $FeOH^+/H_2O$ couple, precisely the opposite was suggested in the FeO^+/H_2O system in which a quartet ground state for the iron-dihydroxy intermediate was assumed. In fact, the statement "if the lessons learned from the FeO^+/H_2 and FeO^+/CH_4 systems ... are taken into account, $Fe(OH)_2^+$ can be deduced to have a quartet ground state"[19] is not confirmed as the ground state of $Fe(OH)_2^+$ corresponds to a sextet. The previous argument was based on the quartet ground states predicted for the various insertion intermediates of iron, e.g. $HFeOH^+$,[21,22b,23] CH_3FeOH^+,[24] $C_6H_5FeOH^+$,[34] and $CH_3FeCH_3^+$;[35] however, a recent study of Ugalde and coworkers suggests that $^6HFeOH^+$ is slightly lower in energy than $^4HFeOH^+$.[22b] In marked contrast to these perfect pairing situations, the $FeCl_2^+$ cation is predicted to have a sextet ground state.[36] Quite obviously, the electronegativity of the substituents plays a role in the determination of the electronic ground states, in that more electronegative ligands can better accommodate high-spin situations by localization of electrons on the ligands. Further, the O–Fe–O angle of 154° in sextet $Fe(OH)_2^+$ disfavors efficient overlap of the π-type molecular orbitals, thus also facilitating a high-spin situation. The $Fe(OH)_2^+$ cation is somewhat in between these examples, but more similar to

the $FeCl_2^+$ case. Thus, the B3LYP assignment of a sextet ground state to **3** appears quite plausible. In contrast to the previous suggestion,[19] oxygen-atom exchange in the FeO^+/H_2O can therefore proceed on a single spin surface, and there is no need to involve two-state reactivity.[21]

After having mapped out the relevant parts of the potential-energy surfaces, the key question still remains to be answered, i.e. why the $^{16}O/^{18}O$ exchange is faster for $FeOH^+/H_2{}^{18}O$ than for $FeO^+/H_2{}^{18}O$. At first, it is essential to note that the computed barriers for the rate-determining 1,3-hydrogen migrations are both well below, but yet relatively close to the respective entrance channel. This computational result is in accord with the experimental finding that $^{16}O/^{18}O$ exchange does not occur with collision frequency in either system. Secondly, the computed barrier is ca. 4 kcal/mol lower for $FeOH^+/H_2O$ compared to FeO^+/H_2O. Such an energy difference of the transition structures may well be responsible for the 3 : 1 ratio of the rate constants observed experimentally, as in an Arrhenius-type formalism already small differences in barrier heights lead to large differences in the apparent rate constants. Thirdly, even if the barriers were of the same height relative to the entrance channel in both systems, isotopic exchange in FeO^+/H_2O is statistically disfavored over that in $FeOH^+/H_2O$, as both reactions do not have unit efficiency.

To further illustrate this argument, let us briefly refer to a "Gedankenexperiment". To this end, the same schematic potential-energy profiles for the oxygen exchange in FeO^+/H_2O and $FeOH^+/H_2O$ are considered, i.e. the barriers have similar locations with respect to the entrance channels and the same kinetic restrictions apply. The only difference is that O-atom exchange in $FeOH^+$ is completed after a single hydrogen migration, whereas FeO^+ requires two steps. In the diluted gas phase, formation of the encounter complexes occurs at the gas kinetic collision rate k_c. If the intermediate barriers are low, the forward reaction k_f is fast relative to redissociation into the reactants k_d (Figure 3-5a). For degenerate isotopic exchange, the backward reaction rate k_b is of course equal to k_f. Accordingly, for $k_f >> k_d$ complete isotope equilibration occurs at the collision rate. If, however, the intermediate barriers are closer to the entrance channels - which is the case in both systems studied here - dissociation of the encounter complexes competes with the isotopic exchange, thereby reducing the reaction efficiency. In the extreme case of $k_f << k_d$, isotopic exchange in FeO^+ is only half as efficient as for $FeOH^+$, because the kinetic restriction imposed by the barrier applies twice in the FeO^+/H_2O system.

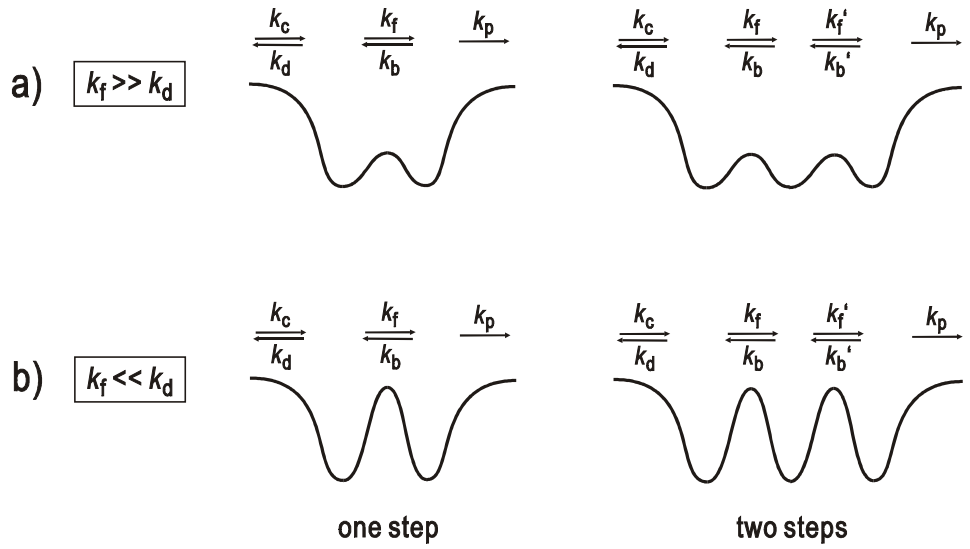

Figure 3-5: Hypothetical energy profiles for degenerate ion/molecule reactions involving two and three intermediates: (a) negligible barrier and thus $k_f >> k_d$, (b) high barrier and thus $k_f << k_d$.

Finally, let us briefly consider the previous use of bond additivity schemes in the discussion of the different mechanistic scenarios.[19] For the isomers **1** and **3**, bond additivity predicts a difference of 47 kcal/mol in favor of the dihydroxide **3**,[37] while theory predicts a difference of only 13 kcal/mol. Consideration of the extra stabilization of the oxo cation by the water ligand as predicted by theory, i.e. $D_0(OFe^+\text{-}OH_2)$ - $D_0(Fe^+\text{-}OH_2)$ = 22.5 kcal/mol, diminishes the difference between **1** and **3** to ca. 25 kcal/mol, but the deviation from the computed value remains significant. It is obvious that the discrepancy is due to the neglection of the effect of the formal valence state on the Fe–OH bonds, i.e. the assumption $D_0(HOFe^+\text{-}OH) \approx D_0(Fe^+\text{-}OH)$ = 87.4 kcal/mol is not justified.[25] Instead, increasing valency of the iron obviously reduces the ability to form further covalent bonds. Thus, the B3LYP calculations predict $D_0(Fe^+\text{-}OH)$ = 88.7 kcal/mol in good agreement with experiment, but only $D_0(HOFe^+\text{-}OH)$ = 67.4 kcal/mol for the second bond of iron cation to a hydroxy ligand. Similarly, the exclusion of the 1,2-mechanism based upon assuming simple bond additivity suggests that hydrogen migration from the water ligand in **1** to the metal to form **2** is endothermic by only ca. 12 kcal/mol,[39] while the B3LYP calculations predict a stability difference of as much as 66 kcal/mol in favor of **1**. Quite obviously, the assumption of bond additivity fails completely for high-valent iron compounds. Thus, while the qualitative implications of the additivity scheme may be applicable as far as the relative ordering of the isomers is concerned, the quantitative considerations are almost meaningless. This result questions - but by no means refutes - the use of additivity schemes when no other information is available, as changes in the formal oxidation states must be taken into account.

3.1.5 Summary

Theoretical analysis of the degenerate $^{16}O/^{18}O$ exchange reactions of FeO^+ and $FeOH^+$ with $H_2{}^{18}O$ confirms previous speculations about the mechanism of these fundamental reactions. Specifically, both reactions proceed via 1,3-hydrogen shifts from one oxygen atom to the other, thereby circumventing high-valent intermediates having Fe–H bonds. The more rapic reaction of $FeOH^+$ compared to FeO^+ is attributed to the joint action of two facts: (i) the requirement of a two-step reaction in FeO^+/H_2O versus a one-step reaction in $FeOH^+/H_2O$ and (ii) the energetically slightly more demanding transition structure involved in the FeO^+/H_2O system. However, the previous suggestion[19] that spin constraints may cause the different rate constants is disproved by the theoretical study, as the isotopic exchange can occur on the high-spin surface for both systems without any need to involve spin crossovers.

From a conceptual point of view, it is interesting to note that the role of the water in the passivation of the iron-oxo unit in FeO^+ has two facets. At first, the mere coordination complex exhibits a pronounced binding to the water ligand, thereby enhancing the Fe–O bond strength and in turn reducing the ability of the oxo unit to act as an oxidizing agent. Second, O–H bond activation of water by the metal-oxo unit leads to a metal dihydroxide having a significantly reduced oxidizing strength as compared to the metal oxide.

3.2 The Interactions of 'Bare' Fe^+ and Fe^{2+} with Hydrogen Peroxide

In the previous section it was mentioned shortly that another isomer of $[Fe,O_2,H_2]^+$ exists, i.e. the iron cation complexed by hydrogen peroxide. This species is particularly interesting as its reactions constitute a gas-phase analog to Fenton chemistry,[8] which is a prominent solution-phase example, where the simultaneous presence of reducing and oxidizing agents provides access to a rich redox chemistry. Specifically, the treatment of iron(II) salts with hydrogen peroxide gives rise to the production of hydroxyl radicals (Equation 3-3) which can initiate a broad variety of oxidation and degradation reactions via hydrogen atom abstractions (Equation 3-4), addition to unsaturated systems etc.[40] In the presence of reducing agents,[41] $Fe(II)_{aq}$ can be regenerated (Equation 3-5), thus closing a catalytic cycle in which H_2O_2 serves to produce alkyl radicals (Equation 3-6).

$Fe(II)_{aq} + H_2O_2 \rightarrow Fe(III)_{aq} + OH^- + OH^{\bullet}$ Equation 3-3

$R–H + OH^{\bullet} \rightarrow R^{\bullet} + H_2O$ Equation 3-4

$Fe(III)_{aq} + e \rightarrow Fe(II)_{aq}$ Equation 3-5

$R–H + H_2O_2 + e \rightarrow R^{\bullet} + H_2O + OH^-$ Equation 3-6

As a gas-phase analog of solution-phase Fenton chemistry, the interaction of hydrogen peroxide with the mono- and dications of bare iron in the gas phase is investigated next. Upon oxidation by H_2O_2, the iron(I) and iron(II) species Fe^+ and Fe^{2+} may give rise to formation of iron(II) - iron(IV) compounds according to Equations 3–7 - 3–10. The one-electron oxidations of the metal concomitant with homolytic cleavage of the O–O bond in Equations 3–7 and 3–9 constitute analogs of the Fenton chemistry, while the reactions in Equation 3–8 and 3–10 comprise oxygen-atom transfer from the peroxide to the metal, thereby affecting formal two-electron oxidations of the metal.

$Fe^+ + H_2O_2 \rightarrow FeOH^+ + OH^{\bullet}$ Equation 3-7

$\rightarrow FeO^+ + H_2O$ Equation 3-8

$Fe^{2+} + H_2O_2 \rightarrow FeOH^{2+} + OH^{\bullet}$ Equation 3-9

$\rightarrow FeO^{2+} + H_2O$ Equation 3-10

Previous gas-phase experiments have demonstrated that complexation of peroxides ROOR' by transition-metal ions is followed by facile insertion of the metal into the peroxidic O–O bond and subsequent fragmentations.[42,43] In case of Fe^+, formation of the insertion species $RO–Fe^+–OR'$ corresponds to a transition from formal iron(I) to iron(III); here, RO and R'O are considered as one electron acceptors, i.e. $[R'O^-\cdots Fe^{3+}\cdots OR^-]$. When hydrogen peroxide (R = R' = H) is reacted with bare Fe^+, Equations 3-7 and 3-8 compete with each other to afford $FeOH^+$ and FeO^+ in a ca. 4 : 1 ratio.[42b] Similarly, collisional activation of $Fe(H_2O_2)^+$ gives rise to $FeOH^+$ and FeO^+ fragments with a preference for the former.[42a] However, the nature of the interaction between the metal and the peroxide, the structures of possible reaction intermediates involved, and the details of the competition between bond homolysis and O-atom transfer remained unknown.

3.2.1 Structures and Energetics

Theory offers a complementary way to experiments in order to examine the $[Fe,O_2,H_2]^{+/2+}$ potential-energy surfaces.[6a,28b] On the monocation PES, the ground state encounter complex of $Fe(H_2O_2)^+$ is found on the quartet surface, with the corresponding sextet state 12.2 kcal/mol above. The geometries of ^{4}**6** and ^{6}**6** are quite similar and featured by characteristic lengths of the O–O bonds of $r_{OO} \approx 1.45$ Å in ^{4}**6** and ^{6}**6**; the major structural difference concerns r_{FeO} which is somewhat larger in the high-spin species (Chart 3-3). In these complexes, the geometry of H_2O_2 is hardly perturbed as compared to the free ligand, and both electromers can be described by predominating electrostatic interactions of the Fe^+ cation with the dipolar neutral. Because B3LYP tends to overestimate metal-ligand binding,[22b] a ligand-exchange reaction (Equation 3-11) is considered in order to estimate the binding energy $D_0(Fe^+\text{-}H_2O_2)$, using the experimental value $D_0(Fe^+\text{-}H_2O) = 30.7 \pm 1.2$ kcal/mol[25] as an anchor point.[44]

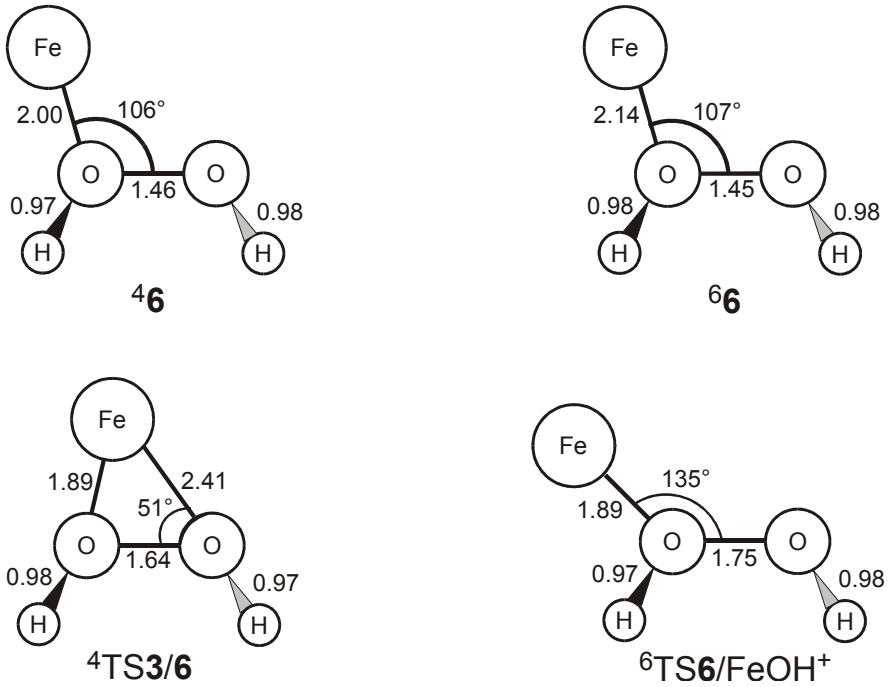

Chart 3-3: Structures of the monocationic $Fe(H_2O_2)^+$ PES. Bond lengths are given in Å and angles in degree. Note, that only the structures are displayed which have not been described in Chapter 3.1.2.

$$Fe(H_2O)^+ + H_2O_2 \rightarrow Fe(H_2O_2)^+ + H_2O \qquad \text{Equation 3-11}$$

B3LYP/6-311+G* predicts a reaction enthalpy of $\Delta_r H_0$(Equation 3-11) = 4.6 kcal/mol for the quartet species.[45] Hence, water is more strongly bound to Fe^+ than hydrogen peroxide, and $D_0(Fe^+\text{-}H_2O_2) = 26 \pm 3$ kcal/mol is assigned.[46] Weaker bonding of H_2O_2 than H_2O to Fe^+

correlates with the difference in proton affinities of these two bases, i.e. $PA(H_2O_2)$ = 161.1 kcal/mol versus $PA(H_2O)$ = 165.0 kcal/mol.[47,48] Much more interesting than the binding energy is the stability of **6** with respect to insertion of the metal into the peroxidic O–O bond of the ligand.

Table 3-1: Experimental and calculated reaction enthalpies ($\Delta_r H$ at 0 K in kcal/mol) and the resulting deviations ΔE related to the monocationic $[Fe,O_2,H_2]^+$ system.[a]

Reaction	$\Delta_r H_{exp}$	$\Delta_r H_{calc}$[b]	ΔE[c]
$^6Fe^+ \rightarrow {}^4Fe^+$	5.8[d]	-4.2	10.0
$^6Fe^+ + H_2O_2 \rightarrow {}^6FeO^+ + H_2O$	-47.0	-46.7	-0.3
$^6Fe^+ + H_2O_2 \rightarrow {}^5FeOH^+ + {}^2OH$	-37.7	-45.1	7.4
$^6FeO^+ \rightarrow {}^6Fe^+ + {}^3O$	80.0	78.2	1.8
$^6FeO^+ \rightarrow {}^4FeO^+$	12.5[e]	8.0	4.5
$^5FeOH^+ \rightarrow {}^6Fe^+ + {}^2OH$	87.4	88.7	-1.3
$^6Fe(H_2O)^+ \rightarrow {}^6Fe^+ + H_2O$	30.7	37.2	-6.5
$^4Fe(H_2O)^+ \rightarrow {}^4Fe^+ + H_2O$	33.7[f]	41.8	-8.1
$^6FeO^+ + {}^4Fe(H_2O)^+ \rightarrow 2\ {}^5FeOH^+$	-50.1	-41.1	-9.0
$^6FeO^+ + {}^6Fe(H_2O)^+ \rightarrow 2\ {}^5FeOH^+$	-47.4	-49.9	2.5
$^5FeOH^+ + {}^2OH \rightarrow {}^6FeO^+ + H_2O$	-9.3	-1.6	-7.7
$^6Fe(H_2O)^+ + {}^2OH \rightarrow {}^5FeOH^+ + H_2O$	-56.7	-51.5	-5.2
		average[g]	± 5.3

[a] Unless mentioned otherwise, experimental reaction enthalpies in Table 3-1 are derived from refs. 25 and 52 and show errors less than ± 3 kcal/mol. [b] The calculated reaction enthalpies $\Delta_r H_{calc}$ refer to this work at the B3LYP /6-311+G* level of theory. [c] ΔE is defined as $\Delta E = \Delta_r H_{exp} - \Delta_r H_{calc}$. [d] Atomic splitting of Fe^+ taken from: Ref. 26. [e] $^6FeO^+/{}^4FeO^+$ splitting [CCSD(T)/TZVP+G(3df2p)]; ref. 22b. [f] $^6Fe(H_2O)^+/{}^4Fe(H_2O)^+$ splitting [CCSD(T)/TZVP+G(3df2p)]; ref. 22b. [g] Mean of absolute deviations.

Before addressing this issue, let us briefly discuss some relevant exit channels in order to evaluate the performance of the theoretical approach as far as energetics are concerned. Inspection of the data compiled in Table 3-1 reveals that the computational approach reproduces the experimental values reasonably well. Although calculations of bare transition-metal atoms are associated with considerable errors,[22b,49] the set of data reported in Table 3-1 justifies to adopt the ± 6 kcal/mol error margins previously suggested for B3LYP studies of

iron containing compounds.[35c,36a,50] Nevertheless, a note of caution is indicated concerning the quality of the DFT calculations. Recent calculations by Ugalde and coworkers[22b] on the reactions of transition-metal cations with water show strong discrepancies between DFT and high-level *ab initio* results for some species. Therefore, single point calculations at a higher level of theory may be indicated in the present study as well.

Table 3-2: Total energies (including ZPVE, in Hartree), relative energies (including ZPVE, in kcal/mol) and $<S^2>$ eigenvalues of the monocationic $[Fe,O_2,H_2]^+$ system.

Species	total energy (+ ZPVE)	relative energy (+ ZPVE)	$<S^2>$
$^4FeO^+ + H_2O$	-1414.9807	8.0	4.48
$^6FeO^+ + H_2O$	-1414.9935	0.0	8.77
$^4\mathbf{1}^+$	-1414.9849	5.4	3.80
$^6\mathbf{1}^+$	-1414.9655	17.6	8.75
$^4\mathbf{2}^+$	-1415.0775	-52.7	4.02
$^6\mathbf{2}^+$	-1415.0982	-65.7	8.76
$^4\mathbf{3}^+$	-1415.0664	-45.8	4.47
$^6\mathbf{3}^+$	-1415.0742	-50.6	8.77
$^4TS\mathbf{2}^+/\mathbf{3}^+$	-1415.0076	-8.9	3.94
$^6TS\mathbf{2}^+/\mathbf{3}^+$	-1415.0164	-14.4	8.76
$^4TS\mathbf{1}^+/\mathbf{2}^+$	-1414.9786	9.3	3.98
$^6TS\mathbf{1}^+/FeOH^+$	-1414.9532	25.3	8.80

In this Thesis, however, the B3LYP results are not refined by a more elaborate approach but rather viewed in a more qualitative sense for two reasons: (i) comparison between known literature thermochemistry and the present calculations leads to good agreement with an error of ± 6 kcal/mol, and (ii) high-level *ab initio* calculations are only useful if a very large basis set with many diffuse functions is used in order to correctly describe the O–O bond in hydrogen peroxide. This type of calculation would require computational efforts which by far exceed the current possibilities with respect to computing time. For instance, in a trial single-point calculation at the CCSD(T) level of theory with a valence triple-zeta atomic natural orbital (ANO) basis set according to Roos et al.[51] on the B3LYP/6-311+G* optimized structure of $Fe(H_2O_2)^+$ a single SCF-cycle occupied 400 Mw memory and took 4 hours to be finished. Scaling this up to approximately 60 SCF-cycles until SCF-convergence is achieved,

this would result in approximately 340 hours of computing time blocking most of the currently available resources for a single-point calculation of only one species.

Total and relative energies of all species considered in this chapter as well as the corresponding $<S^2>$ eigenvalues are summarized in Table 3-2. Evaluation of the $<S^2>$ values shows no relevant spin contamination for the high-spin species and only a small degree of spin-contamination (max. 15 % for $^4FeO^+$) in the low-spin species.

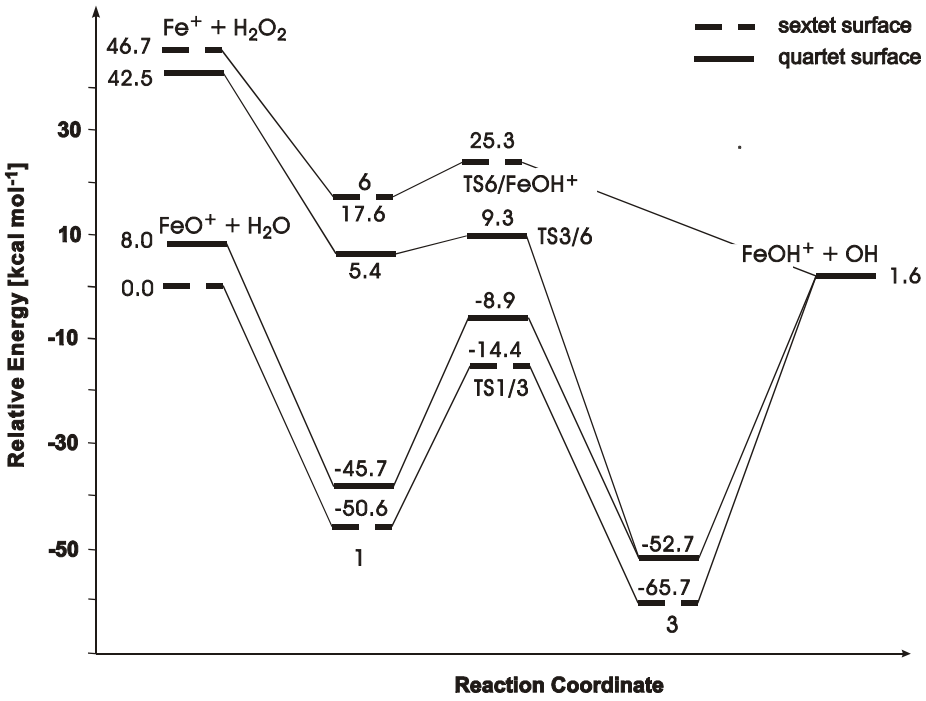

Figure 3-6: Schematic potential-energy surface of $[Fe,O_2,H_2]^+$ calculated at the B3LYP/6-311+G* level of theory (solid line: sextet; dotted line: quartet); energies in kcal/mol including zero-point vibrational energies.

The encounter complexes ^{4}**6** and ^{6}**6** are located way above the global minimum of the monocation surface, which corresponds to the iron dihydroxide cation $Fe(OH)_2^+$ in its sextet ground state, the quartet ^{4}**3** is 13 kcal/mol higher in energy.[6,52,53] Note that these structures have been presented in Chapter 3.1.2 and are therefore not shown again. Further, even the dissociation channels to afford $FeO^+ + H_2O$ and $FeOH^+ + OH^\bullet$ are lower in energy than **6**. Given the weakness of the peroxidic O–O bond, insertion of the metal is expected to proceed easily. Indeed, the associated quartet transition structure ^{4}TS**3/6** (*i633* cm^{-1}) to afford formation of ^{4}**3** lies only 3.9 kcal/mol above ^{4}**1**$^+$. Similarly, the sextet TS associated with O–O bond cleavage is only 7.7 kcal/mol above minimum ^{6}**6**. However, the high-spin TS is not associated with insertion of iron into the peroxidic bond, but instead leads to bond homolysis to afford $FeOH^+$ concomitant with liberation of $OH^\bullet$ radical according to Equation 3-7. Hence,

this structure is denoted as ^{6}TS**6/FeOH**$^+$ (*i653* cm^{-1}); despite extensive search, a saddle point corresponding to ^{6}TS**3/6** could not be found. Given the shape of both spin surfaces, interaction of bare Fe^+ with H_2O_2 is likely to produce $Fe(H_2O_2)^+$ only as a transient which then rapidly rearranges to $Fe(OH)_2^+$ along the quartet PES or decomposes to $FeOH^+ + OH^\bullet$ on the sextet PES (Figure 3-6).

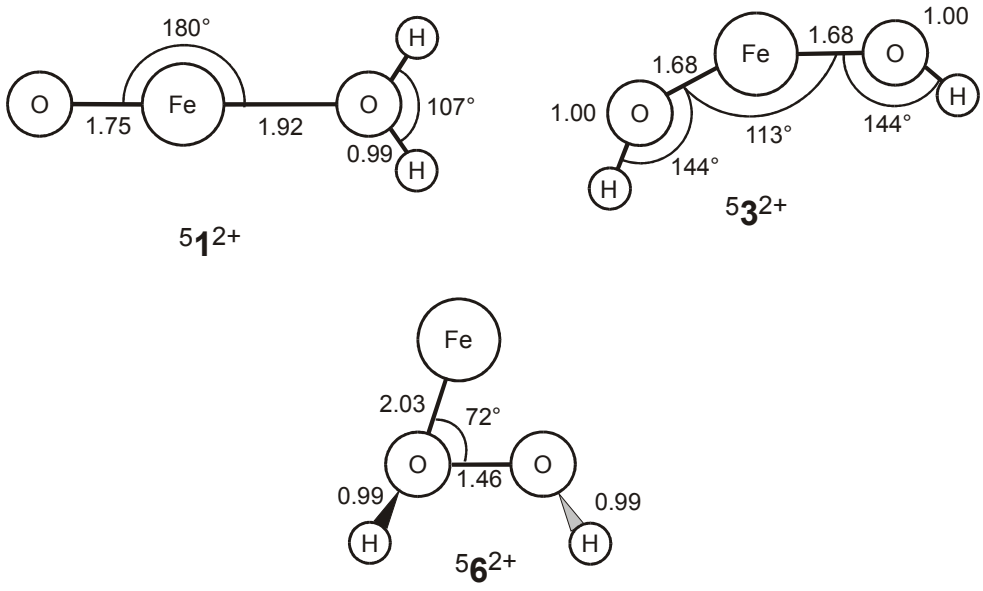

Chart 3-4: Structures of the dication species. Bond lengths are given in Å and angles in degree.

Interestingly, the branching between these options is a matter of spin multiplicity in that only the low-spin species can access the insertion intermediate **3**, while the high-spin surface solely leads to bond homolysis and thus dissociation into $FeOH^+$ and hydroxyl radical (Equation 3-7).[21] Irrespective of the spin state in which the dihydroxide **3** is formed from $Fe^+ + H_2O_2$, it is generated with a large amount of excess energy (> 95 kcal/mol) which is sufficient for fragmentation into $FeOH^+ + OH^\bullet$ (Equation 3-7) as well as rearrangement of **3** via TS**1/3** to the hydrated iron oxide cation **1** and subsequent fragmentation into $FeO^+ + H_2O$ (Equation 3-8). Given the excess energy and the considerable height of the barrier associated with TS**1/3**, direct dissociation of **3** is expected to be preferred, thereby accounting for the experimentally observed preference for the $FeOH^+$ product,[42] even though the generation of FeO^+ according to Equation 3-8 is more exothermic. Resuming Figure 3-6 in terms of redox behavior, hydrogen peroxide can easily oxidize iron(I) to the iron(II) compound $FeOH^+$ as well as to the iron(III) species FeO^+.

Interestingly, the sequence of relative stabilities of the possible isomers is completely reversed on the dication surface (for the structures, see Chart 3-4); only quintet species are

considered here.[6b] Hydrogen peroxide coordinated to the bare iron dication, i.e. $\mathbf{6}^{2+}$, is the most stable dicationic species of the $[Fe,O_2,H_2]^{2+}$ surface, while the isomers $\mathbf{3}^{2+}$ and $\mathbf{1}^{2+}$ are by about 10 kcal/mol higher in energy (Figure 3-7).

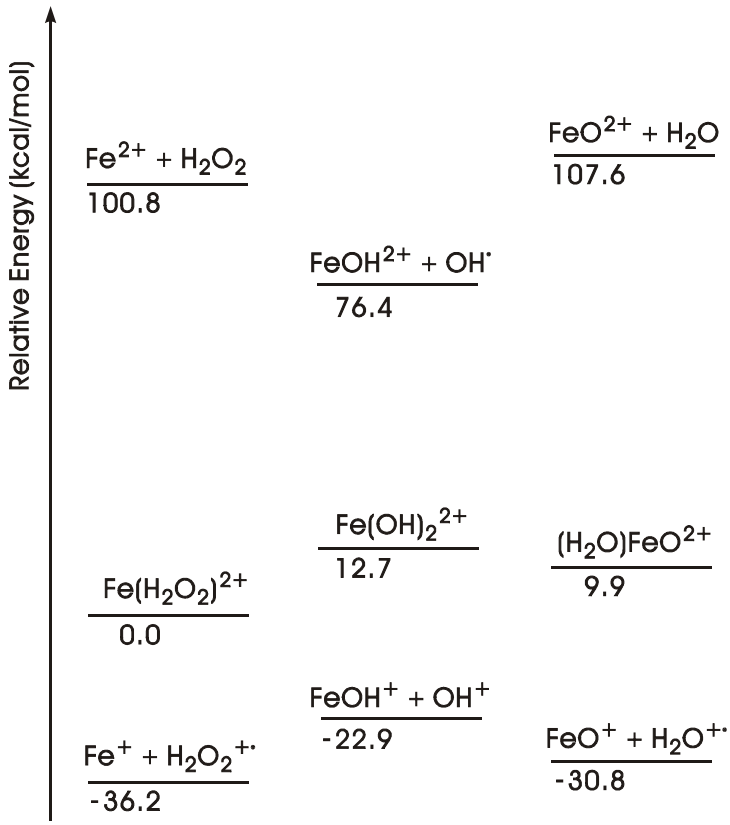

Figure 3-7: Thermochemistry of $[Fe,O_2,H_2]^{2+}$ calculated at the B3LYP/6-311+G* level of theory; energies in kcal/mol.

Preference for $\mathbf{6}^{2+}$ clearly demonstrates the avoidance of high oxidation states required in the formal iron(IV) compounds $\mathbf{3}^{2+}$ and $\mathbf{1}^{2+}$. While differences or even reversals in isomer stabilities of mono- and dications are not at all uncommon,[54,55] comparison of Figures 3–6 and 3–7 reveals enormous stability differences between the mono- and dication surfaces for $[Fe,O_2,H_2]^{+/2+}$. With respect to the lowest-lying electronic states, $Fe(OH)_2^+$ monocation is 71.1 kcal/mol more stable than $Fe(H_2O_2)^+$, whereas $Fe(H_2O_2)^{2+}$ is preferred by 12.7 kcal/mol compared to $Fe(OH)_2^{2+}$ for the dications. A rationale for this change in relative stabilities by more than 80 kcal/mol is provided by consideration of the formal valence of iron. Thus, $\mathbf{6}^{2+}$ and **3** share the common Fe(II)/Fe(III) oxidation states, whereas structures **6** and $\mathbf{3}^{2+}$ correspond to less favorable Fe(I) and Fe(IV) compounds, respectively.[56] Notwithstanding the favorable energetics of $Fe(H_2O_2)^{2+}$, all molecular $[Fe,O_2,H_2]^{2+}$ dications are metastable with respect to the charge-separation asymptotes of the corresponding monocationic fragments, i.e.

$Fe^+ + H_2O_2^{+\bullet}$, $FeO^+ + H_2O^{+\bullet}$, and $FeOH^+ + OH^+$ (Figure 3-7). Nevertheless, the long-lived $[Fe,O_2,H_2]^{2+}$ dications can exist in the gas phase[6b] because charge separation of dications is hindered by a barrier due to Coulomb repulsion of the monocation fragments.[55]

Returning to the redox reactions in Equations 3−7 - 3−10, the B3LYP results clearly predict both the oxidations of Fe^+ to formal Fe(II) in Equation 3-7 and Fe(III) in Equation 3-8 as considerably exothermic; i.e. $\Delta_r H$(Equation 3-7) = -45.1 kcal/mol and $\Delta_r H$(Equation 3-8) = -46.7 kcal/mol. Similarly, oxidation to Fe(III) is exothermic for the Fe^{2+} dication, $\Delta_r H$(Equation 3-9) = -24.4 kcal/mol, whereas the generation of a formal Fe(IV)compound in Equation 3-10 is endothermic, i.e. $\Delta_r H$(Equation 3-10) = 6.8 kcal/mol. Although these results refer to isolated species in the gas phase, the trends match quite well the Fenton chemistry of iron salts with hydrogen peroxide in solution, i.e. $Fe(II)_{aq}$ reacts with H_2O_2 under liberation of $HO^\bullet$ radicals concomitant with formation of $Fe(III)_{aq}$, rather than yielding high-valent metal-oxo species. The remarkable features of Fenton chemistry can thus be traced back to the particular role of formal oxidation states which are accessible in the $Fe(II)/H_2O_2$ couple and represent intrinsic properties of the system irrespective of the possible role of oxidants, solvents, substrates etc.

3.3 $FeO_mH_n^{2+}$ Dications (m = 1, 2; n ≤ 4)

After having mapped out the reactivity of some iron-oxo species in the previous two chapters, the last part of Chapter 3 considers the thermochemistry of these ions as well as their corresponding dications. The interest in these species stems from the chemistry of corrosion processes, i.e. the chemistry of iron in humid or aqueous media, clouds etc., which is of fundamental relevance in material sciences. Besides the understanding of underlying mechanisms at a molecular level, the foundation for the understanding of corrosion processes is the existence of a database of the thermochemistry of the involved species. The gas-phase approach presented in this Thesis has contributed to both, the understanding of reaction mechanisms as well as the assignment of thermochemical data.[6,19,57,58] In this chapter the evaluation of the thermochemistry of iron oxides and hydroxides is presented.

The generation of $FeO_mH_n^{2+}$ dications (m = 1, 2; n ≤ 4) by means of charge-stripping (CS) mass spectrometry[55,59] as well as experimental and theoretical results concerning the *IE*s of the corresponding monocations are presented. Specifically, CS experiments with Fe^+, FeO^+, $FeOH^+$, $Fe(H_2O)^+$, $[Fe,O_2,H_2]^+$, $(H_2O)FeOH^+$, and $Fe(H_2O)_2^+$ monocations in conjunction with calculations conducted at the B3LYP/6-311+G* level of theory are reported. Combination of

the experimental and theoretical data allows the assessment of the vertical and adiabatic ionization energies of the iron compounds under study. Further, Born-Haber cycles are used to correlate the dication energetics with the corresponding redox-properties of the mononuclear iron compounds.[36b,58]

3.3.1 General Considerations

Although the general experimental setup has been described in Chapter 2, special problems in the generation and measurement of $FeO_mH_n^{2+}$ species require additional informations on the experimental and theoretical approaches. In the CS experiments, ionization to dications can be assumed to occur vertically, and the ionization energy of the monocation $IE(M(L)^+)$ is provided by the kinetic energy of the projectile. This results in a shift of the dication signal on the kinetic energy scale, usually referred to as Q_{min} value.[54] To a first approximation, Q_{min} corresponds to the vertical ionization energy of of the monocation, $IE_v(M(L)^+)$ and is determined from the difference between the high-energy onsets of the mono- and the dication peaks in charge-stripping experiments. Conversion of vertical ionization energies (IE_v) to adiabatic values IE_a is obtained by complementary *ab initio* studies. For calibration of the kinetic energy scale, charge stripping of the molecular ion of toluene is applied, $C_7H_8^+ \rightarrow C_7H_8^{2+}$ with $Q_{min}(C_7H_8^+) = 15.7$ eV,[36b,54,55,59] using both additive and multiplicative calibration schemes[54] as discussed further below. For the errors involved it is important to note that the determination of Q_{min} values relies on four separate energy-resolved measurements, i.e. the mono- and dication signals of interest and the mono- and dications of toluene ion serving as a reference.

The aim of the computational part of this study is the assessment of the differences between the vertical and adiabatic ionization energies of the species rather than providing a set of *ab initio* thermochemical data for $[Fe,O_m,H_n]^{+/2+}$. Therefore, the calculations follow the scheme outlined next. First, the monocationic species are fully optimized on the respective low- and high-spin surfaces, where the choice of electronic states to be considered is guided by literature studies of these and related systems as described below. Then, vertical ionization energies are determined for each low-lying spin state by calculating the dication energies at the respective monocations' geometries. Finally, the lowest-lying states of the dications are geometry-optimized in order to determine the differences between adiabatic and vertical ionization energies. Even though all geometry-optimized species are characterized as minima by means of frequency calculations, zero-point vibrational energies are generally not included

in the data given below, because this appears inappropriate in the comparison of vertical and adiabatic properties.

3.3.2 Charge Stripping of $FeO_mH_n^{2+}$ (m = 1, 2; n = 1 – 4)

The $FeO_mH_n^+$ cations of interest in this study are generated by chemical ionization (CI) of mixtures of $Fe(CO)_5$, N_2O, and H_2O. In the CI plasma, a manifold of reactions occur after (dissociative) ionization of $Fe(CO)_5$, either directly or, more likely, via charge transfer with ionized N_2O and/or H_2O as major components of the CI mixtures used. Starting from bare Fe^+, the FeO^+ cation can be formed with N_2O according to Equation 3-12.[60] The iron hydroxide $FeOH^+$ may arise from either Equation 3-13a and/or 3–13b which are both endothermic,[25,44,61] but nevertheless occur in the CI plasma to some extent. The iron-water complex $Fe(H_2O)^+$ is most likely generated via ligand exchange according to Equation 3-14.[62] The $FeO_2H_n^+$ cations can then be regarded as association products of these primary ions (Equations 3–15 - 3–17).[16,46,63] In addition, efficient formation of $[Fe,O_2,H_2]^+$ has been reported in the reaction of $Fe(H_2O)^+$ with N_2O.[32]

$Fe^+ + N_2O$	$\rightarrow$	$FeO^+ + N_2$	Equation 3-12
$Fe^+ + H_2O$	$\rightarrow$	$FeOH^+ + H$	Equation 3-13a
$FeO^+ + H_2O$	$\rightarrow$	$FeOH^+ + OH$	Equation 3-13b
$Fe(CO)^+ + H_2O$	$\rightarrow$	$Fe(H_2O)^+ + CO$	Equation 3-14
$FeO^+ + H_2O$	$\rightarrow$	$[Fe,O_2,H_2]^+$	Equation 3-15
$FeOH^+ + H_2O$	$\rightarrow$	$(H_2O)FeOH^+$	Equation 3-16
$Fe(H_2O)^+ + H_2O$	$\rightarrow$	$Fe(H_2O)_2^+$	Equation 3-17

In this contribution, almost exclusively the Q_{min} values determined for the monocations generated in the CI plasma are addressed, paying particular attention on several experimental aspects. As an illustration of the experimental data, Table 3-3 shows the Q_{min} values obtained in several independent experiments and the resulting averages. While there exist two different calibration schemes in charge-stripping measurements,[54] the multiplicative correction method is used throughout in this section; comparison to the additive calibration scheme is made in the discussion.

Table 3-3: Measured Q_{min} values (in eV) for charge stripping of mass-selected $FeO_mH_n^+$ monocations to the corresponding dications determined in several independent experiments 1 - 8 and the derived averages.

Precursor	1	2	3	4	5	6	7	8	Mean
Fe^+	15.40	15.19	15.73	15.23					15.39 ± 0.25
FeO^+	18.56	18.95	18.83	18.77	18.24	18.26	18.64	18.76	18.63 ± 0.26
$FeOH^+$	17.11	17.06	17.39	16.92	17.67	17.23	17.54	17.47	17.30 ± 0.26
$Fe(H_2O)^+$	14.08	14.45	14.75	14.78	14.54	14.37	14.07	14.23	14.41 ± 0.28
$[Fe,O_2,H_2]^+$	13.98	14.06	13.55	12.36	14.10	13.65	15.05	14.70	13.93 ± 0.81
$(H_2O)FeOH^+$	15.38	16.08	15.74	16.37	15.64				15.84 ± 0.39
$Fe(H_2O)_2^+$	12.25	12.86	12.35	12.81	12.87				12.63 ± 0.30

$Fe^{+/2+}$. Mass selection of Fe^+ cations generated under CI conditions and subsequent energy-resolved charge stripping provides $Q_{min}(Fe^+)$ = 15.39 ± 0.25 eV (Table 3-3). The measured value is clearly outside the error margins of the spectroscopic reference $IE(Fe^+)$ = 16.1879 ± 0.0012 eV.[26] In contrast, previous charge-stripping experiments of McCullough-Catalano and Lebrilla[64] gave $Q_{min}(Fe^+)$ = 16.3 ± 0.4 eV. Underestimation of $Q_{min}(Fe^+)$ in the sector-MS experiments indicates the presence of excited states in the beam of mass selected Fe^+ monocations.[55] This is in fact quite conceivable as dissociative ionization of $Fe(CO)_5$ is known to generate significant amounts of electronically excited Fe^+ cations.[65] The observed shift between the measured $Q_{min}(Fe^+)$ = 15.39 ± 0.25 eV and $IE(Fe^+)$ = 16.1879 ± 0.0012 eV is mostly consistent with contribution of excited Fe^+ (^4D) to the precursor beam which lies 0.98 eV above the Fe^+ (^6D) ground state. Reproduction of the spectroscopic value by McCullough-Catalano and Lebrilla[64] can be attributed to their use of fast atom bombardment (FAB) as ionization method which is known to be a softer ionization technique than electron ionization and often leads to the formation of atomic ions in their ground states.[66] Interestingly, also Fe^+ generated by dissociative electron ionization of ferrocene has been reported to reproduce the spectroscopic $IE(Fe^+)$ within experimental error.[67]

The presence of electronically excited states in the monocation beams could also affect the Q_{min} data of the molecular species addressed. Rovibronic excitation of the monocation precursors is a less severe problem because it is likely to be mapped onto the dication surface upon vertical ionization, and - to a first approximation - the differential shapes of the mono- and dication surfaces are accounted for in the correction from vertical to adiabatic ionization energies using theoretical data. Electronic excitations of the monocations, however, have dramatic effects because ionization of excited monocations is energetically easier than that of

the ground states by the amount of the state splitting (provided that the dication ground-state is accessible from both monocation states). In this respect, it is particularly important that the cross section of charge stripping drastically decreases with increasing ionization energy.[68] As a consequence, even minor contributions of electronically excited monocations in the precursor beam can result in substantially underestimated Q_{min} values,[69] for which Fe^+ generated by CI of $Fe(CO)_5/N_2O/H_2O$ is an example. Notwithstanding, there is no indication for the presence of excited states for the $FeO_mH_n^+$ cations examined here, and it is therefore assumed that these undergo efficient thermalization in the CI plasma. In contrast, it is precisely the bare metal cation that is likely to experience less thermalization in the plasma compared to $FeO_mH_n^+$ species under study because Fe^+ is formed as a primary product of the dissociative ionization of $Fe(CO)_5$ which is known to yield excited cations. While quenching to the ground state might occur in the CI plasma, Fe^+ is also consumed in reactions with the CI components (e.g. Equations 3-12 and 3-13a). In contrast, the generation of the $FeO_mH_n^+$ ions requires the occurrence of ion/molecule reactions in the source, thereby these ions are more likely to undergo thermalizing collisions. As a consequence, contributions of excited states are more likely for Fe^+ than for the $FeO_mH_n^+$ species extracted from the CI source.

$FeO^{+/2+}$. Mass-selected FeO^+ cation yields $Q_{min}(FeO^+)$ = 18.63 ± 0.26 eV which is consistent with a previous figure of $Q_{min}(FeO^+)$ = 18.3 ± 0.3 eV.[58] While it is possible that slightly different populations of FeO^+ monocation states are sampled in these experiments, both values are comparable within experimental error. In the present context, let us prefer the higher value determined in the same set of experiments as for the other $FeO_mH_n^+$ ions. The Q_{min} value of FeO^+ is not affected by changing the $Fe(CO)_5/N_2O$ ratios, the overall pressure, addition of methane etc., while notable deviations to lower Q_{min} values occur upon admixture of high partial pressures of water to the CI plasma. These can be attributed to an interference of $^{56}FeO^+$ by isobaric $^{54}Fe(H_2O)^+$ (both 72 amu); the latter ion has a much smaller ionization energy than FeO^+ (see below). Contribution of $^{54}Fe(H_2O)^+$ is also obvious from the significant $^{54}Fe^+$ signals observed in the CA spectrum of the 72 amu ions generated at higher water pressures.

$FeOH^{+/2+}$. The experiments yield $Q_{min}(FeOH^+)$ = 17.30 ± 0.26 eV which is consistent with the (additive) value of 17.0 ± 0.4 eV determined by McCullough-Catalano and Lebrilla.[64] Notable deviations to higher Q_{min} values are found if partial pressures of water are too low, i.e. hardly any $^{56}FeOH^+$ is formed, while Equation 3-12 can still yield isobaric $^{57}FeO^+$ (both 73 amu). Further confidence to the measured figure is given by the fact that no changes in

Q_{min} are observed upon CI of a $Fe(CO)_5/N_2O/CH_4$ mixture which is known to serve as an efficient source for $FeOH^+$ cation.[13b,16]

$Fe(H_2O)^{+/2+}$. The Q_{min} measurements of this ion are nicely reproducable independent of ionization conditions and lead to $Q_{min}(Fe(H_2O)^+)$ = 14.41 ± 0.28 eV. The low magnitude of this value provides a clue for the robustness against variations of the experimental conditions because conceivable isobaric interferences, e.g. $Fe^{18}O^+$ and $^{57}FeOH^+$, have much larger IEs (see above). The CI plasma cannot warrant to sample equilibrated species only, but nevertheless participation of isomeric species such as the insertion intermediates $HFeOH^+$ can be excluded. This is because irrespective of spin-state considerations, several *ab initio* studies predict this isomer to be considerably less stable than $Fe(H_2O)^+$ while the barrier for hydrogen migration is low.[20,22,23]

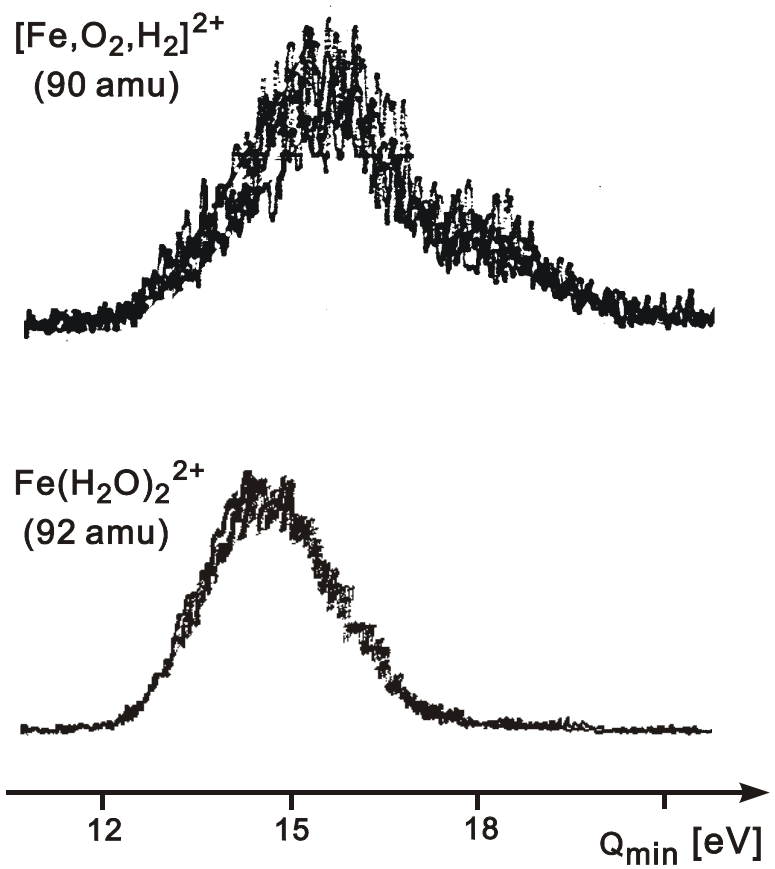

Figure 3-8: Upper trace: Energy resolved CS signal of B(1)-selected $[^{56}Fe,O_2,H_2]^+$ ions interfered by isobaric $^{54}Fe(H_2O)_2^+$ (both 90 amu). Lower trace: Energy resolved CS signal of B(1)-selected $^{56}Fe(H_2O)_2^+$ (92 amu) recorded in the same series of experiments under identical conditions. The Q_{min} scale given is approximate.

$[Fe,O_2,H_2]^{+/2+}$. The composition of this ion leaves some ambiguity as far as the ion's connectivity is concerned. Considering the mode of ion generation in the $Fe(CO)_5/N_2O/H_2O$

plasma, at least iron dihydroxide $Fe(OH)_2^+$ and hydrated iron oxide $(H_2O)FeO^+$ appear conceivable.[6,19] The Q_{min} value of 13.93 ± 0.81 determined for mass selected $[Fe,O_2,H_2]^+$ shows a notably increased spread with the extremes ranging from 12.36 eV to 15.05 eV. One may attribute this spread to variations in the contributions of the different isomers, having different Q_{min} values, to the monocation precursor beam. However, notable $^{54}Fe^+$ fragments are observed in the CA mass spectra of the monocations particularly in those experiments which gave the lowest Q_{min} values, thus indicating isobaric interference of $[^{56}Fe,O_2,H_2]^+$ by $^{54}Fe(H_2O)_2^+$ (both 90 amu), of which the latter has a rather small Q_{min} value (see below). In fact, the charge-stripping peak obtained at increased energy-resolution (Figure 3-8, upper trace) is composed of at least two features as becomes obvious from the comparison with the peak obtained for genuine $^{56}Fe(H_2O)_2^+$ (lower trace in Figure 3-8). Attempts to deconvolute the composite peak indicate that at least three different processes contribute to the charge stripping peak of the ions at 90 amu. Therefore, this topic is postponed to the discussion section after having also considered the computational results for the $[Fe,O_2,H_2]^{+/2+}$ mono- and dications.

$(H_2O)FeOH^{+/2+}$. Although formed in only moderate amounts upon CI of $Fe(CO)_5/N_2O/H_2O$ mixtures, this ion appears to lack isobaric interferences by iron-containing cations, and $Q_{min}((H_2O)FeOH^+)$ = 15.84 ± 0.39 is obtained. In this particular case, however, the proximity of the Q_{min} value to that of isobaric $C_7H_7^+$ ($Q_{min}(C_7H_7^+)$ = 15.7 eV),[70] formed from the toluene calibrant, could imply some overlap because mass selection is done with B(1) only. This conjecture can be excluded for several reasons: (i) No typical fragments of $C_7H_7^+$, e.g. $C_5H_5^+$, are observed in the CA spectrum of mass selected $(H_2O)FeOH^+$. (ii) Interference of $(H_2O)FeOH^+$ (90.949 amu) by $C_7H_7^+$ (91.042 amu) would mean that the latter has a lower kinetic energy. Specifically, if the kinetic energy of $(H_2O)FeOH^+$ is adjusted to the typical value of 7993 eV, transmission of the heavier $C_7H_7^+$ species through B(1) occurs at a kinetic energy of only 7985 eV. Hence, even if some $C_7H_7^+$ contributes to the B(1)-selected beam, it would not affect the high-energy onset of the dication signal. (iii) Relative Q_{min} values determined in the absence of the toluene calibrant are consistent with those determined for the other $FeO_mH_n^+$ ions under study. Hence, the measured Q_{min} value is assigned to $(H_2O)FeOH^+$, and the similarity to $Q_{min}(C_7H_7^+)$ is considered as a mere coincidence.

$Fe(H_2O)_2^{+/2+}$. Similar to the $Fe(H_2O)^+$ cation, the bisligated $Fe(H_2O)_2^+$ complex yields nicely reproducable results, independent of the ionization conditions, and $Q_{min}(Fe(H_2O)_2^+)$ = 12.63 ± 0.30 is obtained. Even though interference by $C_7H_8^+$ stemming from the calibrant (both 92 amu) is conceivable, it cannot affect the result considering the arguments raised

above for $(H_2O)FeOH^+$ and the fact that the Q_{min} value of the toluene reference ion (15.7 eV) is much too large to affect the high-energy threshold of the charge-stripping peak to any notable extent. Further, the energy-resolved charge-stripping signal of $Fe(H_2O)_2^+$ has no indications of an overlapping component (lower trace in Figure 3-8).

3.3.3 Computational Determination of Adiabatic *IE*s

The differences of vertical and adiabatic ionization energies of the mono- to the dications are of particular relevance for the conversion of the experimental Q_{min} values to thermochemical data. In this respect, the B3LYP approach offers a good compromise between the accuracy of the description and the computational costs.[71-73] A summary of the computational results is given in Table 3-4 where the computed total energies and ionization energies from the mono- to the dications are tabulated. Due to the mere size of second ionization energies, the previously used unit of kcal/mol is switched to eV while discussing the dication energetics (1 eV = 23.06 kcal/mol).

$Fe^{+/2+}$. Many computational approaches using density functional theory tend to prefer low- versus high-spin states due to overestimation of correlation energy. In fact, B3LYP/6-311+G* predicts the low-spin state Fe^+ (^{4}F) as 0.18 eV more stable than Fe^+ (^{6}D), while the latter is the ground state of iron cation with a splitting of 0.25 eV to the Fe^+ (^{4}F) quartet state.[26] Overall, this means that the B3LYP approach is in error by about 0.4 eV for the bare atom. Errors of similar size have been found in several other B3LYP studies of iron compounds, and often an uncertainty of ± 0.5 eV is assigned to this approach.[36,50,56,71,74]

As far as ionization to dications is concerned, the effect on the monocation coincides with a slight destabilization of the Fe^{2+} (^{5}D) dication for the very same reason, leading to an overestimation of *IE*(Fe^+, calc.) = 16.52 eV in comparison to the spectroscopic value of *IE*(Fe^+) = 16.19 eV.[26] For the transition Fe^+ (^{4}F) → Fe^{2+} (^{5}D), the erroneous ground-state assignment with B3LYP leads to *IE*(Fe^+ (^{4}F), calc.) = 16.70 eV compared to the experimental *IE* of only 16.01 eV for Fe^+ (^{4}F). These deviations between spectroscopic data of the atom and the theoretical values may serve as a guide for the assessment of the absolute accuracy of the computational predictions. Nevertheless, note that the computational errors of the molecular ions are expected to be somewhat smaller as the effect of the overestimation of the low-spin species is most pronounced for atomic ions.

Table 3-4: Total energies (E_{SCF}, in Hartree), ionization energies of the $FeO_mH_n^+$ monocations (*IE*, in eV), and offsets between vertical and adiabatic transitions ($\Delta IE_{v/a}$, in eV) calculated at the B3LYP/6-311+G* level of theory for $FeO_mH_n^{+/2+}$ mono- and dications.

	charge	type[a]	spin	E_{SCF}[b]	*IE*	$\Delta IE_{v/a}$
Fe	+2		5	-1262.7492	16.52	
	+1		6	-1263.3563		
	+2		5	-1262.7492	16.70	
	+1		4	-1263.3630		
FeO	+2	sp(6)	5	-1337.8771	18.93	0.18
	+2	opt	5	-1337.8837	18.75	
	+1	opt	6	-1338.5727		
	+1	opt	4	-1338.5597		
FeOH	+2	sp(5)	4	-1338.6075	17.63	0.35
	+2	opt	4	-1338.6204	17.28	
	+2	sp(5)	6	-1338.6224	17.23	0.33
	+2	opt	6	-1338.6344	16.90	
	+1	opt	5	-1339.2554		
	+1	opt	3	-1339.1936		
$Fe(H_2O)$	+2	sp(4)	5	-1339.3527	14.25	0.02
	+2	opt	5	-1339.3532	14.23	
	+1	opt	4	-1339.8763		
	+2	sp(6)	5	-1339.3458	14.04	0.20
	+2	opt	5	-1339.3532	13.84	
	+1	opt	6	-1339.8617		
$Fe(OH)_2$	+2	sp(6)	5	-1414.4656	17.87	0.35
	+2	opt	5	-1414.4787	17.52	
	+1	opt	6	-1415.1223		
	+1	opt	4	-1415.1005		
$(H_2O)FeO$	+2	sp(6)	5	-1414.4757	17.02	0.20
	+2	opt	5	-1414.4831	16.82	
	+2	sp(6)	3	-1414.4673		
	+1	opt	6	-1415.1012		
	+1	opt	4	-1415.0934		

Table 3-4 continued: Total energies (E_{SCF}, in Hartree), ionization energies of the $FeO_mH_n^+$ monocations (*IE*, in eV), and offsets between vertical and adiabatic transitions ($\Delta IE_{v/a}$, in eV) calculated at the B3LYP/6-311+G* level of theory for $FeO_mH_n^{+/2+}$ mono- and dications.

	charge	type[a]	spin	E_{SCF}[b]	*IE*	$\Delta IE_{v/a}$
$Fe(H_2O_2)$	+2	sp(4)	5	-1414.4843	14.39	0.38
	+2	opt	5	-1414.4990	13.99	
	+1	opt	4	-1415.0132		
	+2	sp(6)	5	-1414.4779	14.03	0.57
	+2	opt	5	-1414.4990	13.46	
	+1	opt	6	-1414.9936		
$(H_2O)FeOH$	+2	sp(5)	4	-1415.1945	16.07	0.27
	+2	opt	4	-1415.2047	15.80	
	+1	opt	5	-1415.7852		
	+1	opt	3	-1415.7178		
$Fe(H_2O)_2$	+2	sp(4)	5	-1415.9280	12.46	0.04
	+2	opt	5	-1415.9295	12.42	
	+1	opt	4	-1416.3860		
	+1	opt	6	-1416.3354		

[a] sp: single-point calculation of the dication at the geometry of the monocation, the spin state is indicated in brackets, opt: fully geometry optimized dication of given multiplicity. [b] 1 Hartree = 27.2116 eV.

$FeO^{+/2+}$. While the accurate theoretical description of bare Fe^+ is already difficult, the FeO^+ cation belongs to the most challenging problems among small 3d-metal compounds. The Fe–O bond in FeO^+ is highly polarized and has significant multi-reference character. Notwithstanding, all computational studies made so far agree upon a $^6\Sigma^+$ ground state of FeO^+ even though the calculated state splittings diverge;[20,22-24] recent experimental data further support the sextet ground state.[75] For the dication, the quintet FeO^{2+} ($^5\Delta$) predicted by Yoshizawa et al. is considered.[24] The B3LYP calculations predict $IE_v(FeO^+)$ = 18.93 eV and $IE_a(FeO^+)$ = 18.75 eV, respectively. The offset between vertical and adiabatic ionization energies, $\Delta IE_{v/a}$ = 0.18 eV, can be attributed to the different bond lengths, i.e. $r_{Fe\text{-}O}$ = 1.64 Å in the mono- and 1.83 in the dication (Chart 3-5). However, the difference is much smaller than $\Delta IE_{v/a}$ = 0.6 ± 0.1 eV estimated in a previous study based on the analogy to the related $FeS^{+/2+}$ system.[58]

($^4\Pi$,$^4\Phi$) ($^6\Sigma^+$) ($^5\Delta$)

Chart 3-5: Structures and electronic states of FeO^+ and FeO^{2+} according to the B3LYP/6-311+G* calculations. Bond lengths in Å.

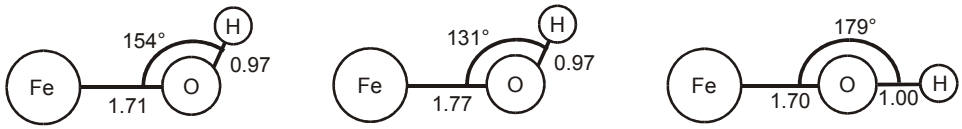

(^{5}A") (^{3}A') (^{6}A')

Chart 3-6: Structures and electronic states of $FeOH^+$ and $FeOH^{2+}$ according to the B3LYP/6-311+G* calculations. Bond lengths are given in Å and angles in degree.

$FeOH^{+/2+}$. Previous computational studies have predicted a quintet ground state for iron hydroxide cation.[23,74] According to the present set of calculations, triplet $FeOH^+$ is 1.68 eV higher in energy and therefore not considered any further. Ionization of the quintet to the dication surface results in $IE_v(FeOH^+)$ = 17.23 eV as well as $IE_a(FeOH^+)$ = 16.90 eV and thus $\Delta IE_{v/a}$ = 0.33 eV. Interestingly, the major source for the offset is the bond angle which changes from α_{FeOH} = 154° in $FeOH^+$ to a practically linear arrangement in the sextet ground state of the dication, whereas r_{FeO} remains virtually unchanged. In a simple bonding scheme, the linear arrangement of $FeOH^{2+}$ can be understood as protonation of FeO^+ ($^6\Sigma^+$) at an oxygen-centered σ-type orbital. As with the isoelectronic FeO^+, a low-lying quartet state exists for $FeOH^{2+}$. Consistent with the bonding mnemonic of the sextet, the quartet state of $FeOH^{2+}$ is bent (Chart 3-6, r_{FeO} = 1.92 Å, r_{OH} = 1.00 Å, α_{FeOH} = 160°). Elongation of r_{FeO} in the dication gives rise to $\Delta IE_{v/a}$ = 0.35 eV for the transition $FeOH^+$ (^{5}A') → $FeOH^{2+}$ (^{4}A'). Whether or not the B3LYP assignment of the quartet/sextet splitting is correct, the similar $\Delta IE_{v/a}$ values predicted for both states permit a straightforward adjustment of the experimental Q_{min} value to from IE_v to IE_a.

$Fe(H_2O)^{+/2+}$. As with bare Fe^+, density functional methods encounter a spin problem also in the case of the $Fe(H_2O)^+$ complex. The prediction of the computations in this Thesis is a $^4A_2$ ground state[22a,23] while high-level *ab initio* methods clearly prefer a sextet state ($^6A_1$).[22b,76] Similarly, the B3LYP results show an overestimated stability of the quartet species. For the

$Fe(H_2O)^{2+}$ dication, a quintet ground state is predicted by B3LYP. For the transition $^6Fe(H_2O)^+ \rightarrow {}^5Fe(H_2O)^{2+}$, $IE_v(Fe(H_2O)^+)$ = 14.04 eV, and $IE_a(Fe(H_2O)^+)$ = 13.84 eV is obtained. This results in $\Delta IE_{v/a}$ = 0.20 eV, while $IE_v(Fe(H_2O)^+)$ = 14.25 eV, $IE_a(Fe(H_2O)^+)$ = 14.23 eV, and $\Delta IE_{v/a}$ = 0.02 eV are obtained for $^4Fe(H_2O)^+ \rightarrow {}^5Fe(H_2O)^{2+}$. The different offsets between vertical and adiabatic transitions for the low- and high spin species are consistent with the associated changes in geometry. The geometries of $^4Fe(H_2O)^+$ and $^5Fe(H_2O)^{2+}$ are close to each other, thus resulting in a negligible $\Delta IE_{v/a}$, whereas r_{FeO} is significantly larger in the high-spin monocation $^6Fe(H_2O)^+$ than in the corresponding dication. The failure to reproduce the correct monocation ground state and the ambiguity associated with respect to the $\Delta IE_{v/a}$ value to be applied to the experimental Q_{min} slightly adds to the uncertainty in the evaluation of the thermochemistry of $Fe(H_2O)^{2+}$ dication, as is further discussed below.

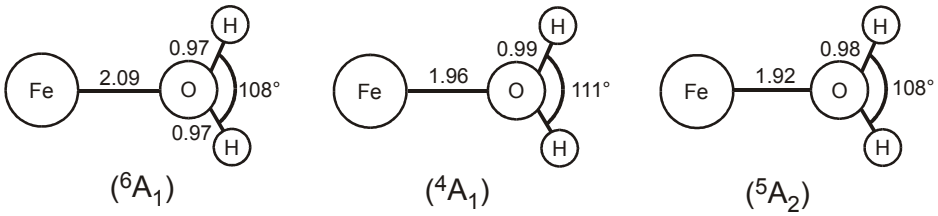

Chart 3-7: Structures and electronic states of FeH_2O^+ and FeH_2O^{2+} according to the B3LYP/6-311+G* calculations. Bond lengths are given in Å and angles in degree.

$[Fe,O_2,H_2]^{+/2+}$. For this elemental composition, at least three different structural isomers need to be considered:[6] the iron dihydroxides $Fe(OH)_2^{+/2+}$, the water complexes of ionized iron oxide $(H_2O)FeO^{+/2+}$, and the iron complexes of hydrogen peroxide $Fe(H_2O_2)^{+/2+}$. As all of these species have been described in detail in Chapters 3.1 and 3.2, only some additional information is given in this context. For the singly-charged ions, B3LYP predicts $Fe(OH)_2^+$ as global minimum with $(H_2O)FeO^+$ and $Fe(H_2O_2)^+$ being 0.57 eV and 2.96 eV less stable. In marked contrast, $Fe(H_2O_2)^{2+}$ is predicted to form the global minimum of the dication surface, whereas $(H_2O)FeO^{2+}$ is 0.43 eV and $Fe(OH)_2^{2+}$ even 0.55 eV higher in energy (Chapter 3.2). The variation in mono- and dication stabilities of the different isomers give a set of ionization energies which range from 13.46 eV for the adiabatic transition $^6Fe(H_2O_2)^+ \rightarrow {}^5Fe(H_2O_2)^{2+}$ to 17.86 eV for the vertical ionization $^6Fe(OH)_2^+ \rightarrow {}^5Fe(OH)_2^{2+}$. Attributing these computational values to the different features observed experimentally is further complicated by the isobaric interferences apparent in the charge-stripping studies (see above); this aspects will be further evaluated below.

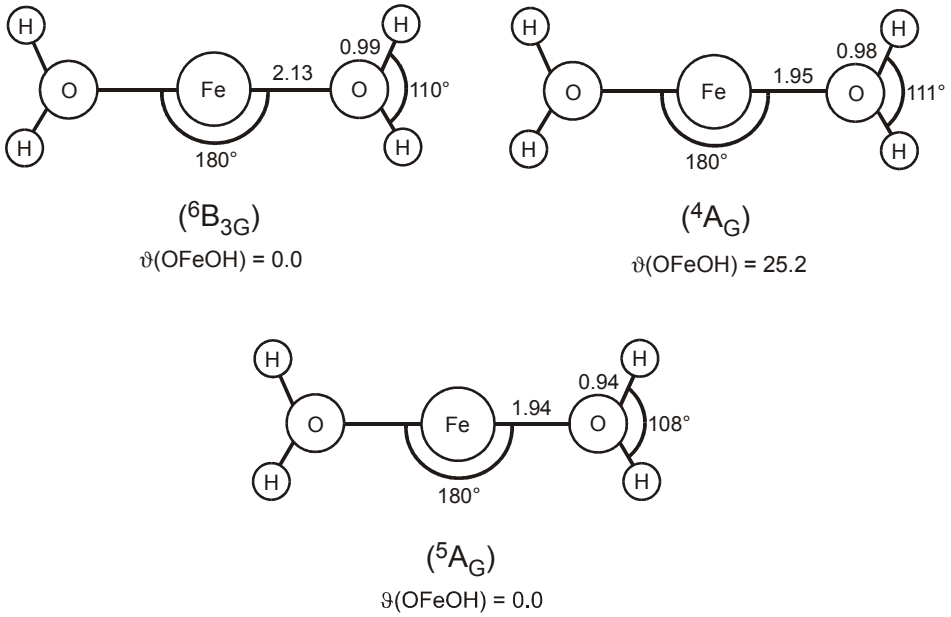

Chart 3-8: Structures and electronic states of $Fe(H_2O)_2^{+/2+}$ according to the B3LYP/6-311+G* calculations. Bond lengths are given in Å and angles in degree.

$Fe(H_2O)OH^{+/2+}$. The $Fe(H_2O)OH^+$ monocation is also described in detail in Chapter 3.1, for the evaluation of the mono- and dication structures see Chart 3-2, and Chart 3-4, respectively.[6a] In analogy to the results for the unsolvated $FeOH^+$ cation described above, $Fe(H_2O)OH^+$ is calculated with a quintet ground-state; the corresponding triplet is much higher in energy (1.83 eV) and therefore not considered any further. Given the small size of the quartet/sextet splitting in $FeOH^{2+}$, the presence of an additional water ligand leads us to assume a quartet ground state for the $Fe(H_2O)OH^{2+}$ dication, for which the calculations predict $IE_v(Fe(H_2O)OH^+)$ = 16.07 eV and $IE_a(Fe(H_2O)OH^+)$ = 15.80 eV. The energy offset $\Delta IE_{v/a}$ = 0.27 eV is close to that found for the unsolvated $FeOH^{2+}$ dication (0.33 eV). However, unlike the negligible perturbation of the Fe-O bond length upon ionization of $FeOH^+$, the transition $^5Fe(H_2O)OH^+ \rightarrow {}^4Fe(H_2O)OH^{2+}$ is associated with a shortening of r_{FeO} to the water ligand (from 2.00 to 1.92 Å) and a lengthening of r_{FeO} to the hydroxy group (from 1.71 to 1.88 Å). By analogy to the geometry differences in the transition $^6Fe(H_2O)^+ \rightarrow {}^5Fe(H_2O)^{2+}$, these effects can tentatively be attributed to the removal of a 4s-type electron in a non-bonding σ-orbital upon ionization of $^5Fe(H_2O)OH^+$ to the dication, thereby increasing the ion/dipole interaction with water, while simultaneously weakening the Fe–OH bond.

$Fe(H_2O)_2^{+/2+}$. According to previous *ab initio* studies, the bisligated monocation $Fe(H_2O)_2^+$ has a $^4B_{1g}$ ground state.[76] Hence, the ligand field generated by two water molecules favors a

low-spin state in the case of $Fe(H_2O)_2^+$, unlike the sextet ground state of $Fe(H_2O)^+$. For the dication, a quintet ground state is predicted with $IE_v(Fe(H_2O)_2^+)$ = 12.46 eV and $IE_a(Fe(H_2O)_2^+)$ = 12.42 eV. The geometries of the mono- and dications are very similar (see Chart 3-8), and $\Delta IE_{v/a}$ amounts to only 0.04 eV.

3.3.4 Monocation Thermochemistry

The measured Q_{min} values and the calculated ionization energies are summarized in Table 3-5. Overall, the agreement between theory and experiment allows to evaluate the different calibration schemes applied in charge-stripping experiments. Large deviations between experiment and theory occur for bare Fe^+ and $[Fe,O_2,H_2]^+$, and in both cases shortcomings of the experimental data are obvious. The former case has been discussed above, and the difference between the measured Q_{min} and $IE(Fe^+)$ can be attributed to contribution of electronically excited Fe^+ to the monocation beam. The $[Fe,O_2,H_2]^+$ system, however, is rather subtle and deserves discussion in a separate section.

Calibration schemes. The overall agreement observed between experiment and theory allows to evaluate the two different calibrations schemes used in charge-stripping experiments. Calibration is required to account for errors in the measurement of the absolute ions' kinetic energies in the keV regime and differences in the focussing conditions of mono- and dications in the instrument. As $Q_{min}(C_7H_8^+)$ = 15.7 eV for the transition of toluene molecular ion $C_7H_8^+ \rightarrow C_7H_8^{2+}$ is a well defined reference, it serves as an absolute anchor point for calibrating the kinetic energy scale. The kinetic energies of toluene mono- and dication, $E_{kin}(C_7H_8^+)$ and $E_{kin}(C_7H_8^{2+})$, are measured and used to correct those found for the mono- and dication of interest, $E_{kin}(M(L)^+)$ and $E_{kin}(M(L)^{2+})$. Note that the apparent energy of a dication is $E_{kin}(M(L)^{2+})/2$ because transmission through an electric sector is proportional to the mass-to-charge ratio. In the literature, two different calibration schemes are established.[54] The additivity method assumes that the abberation of the mono- and dications' kinetic energies is a constant resulting in $Q_{min}(add) = E_{kin}(M(L)^+) - E_{kin}(M(L)^{2+}) + \delta$, where δ = 15.7 eV - $[E_{kin}(C_7H_8^+) - E_{kin}(C_7H_8^{2+})]$. The multiplicative scheme assumes a proportional scaling, $Q_{min}(mult) = [E_{kin}(M(L)^+) - E_{kin}(M(L)^{2+})] \bullet \delta$, with δ = 15.7 eV / $[(E_{kin}(C_7H_8^+) - E_{kin}(C_7H_8^{2+})]$. By definition, both methods coincide at the Q_{min} value of the reference, here, $Q_{min}(C_7H_8^+)$ = 15.7 eV.

Table 3-5: Measured Q_{min} values for charge stripping of mass-selected $FeO_mH_n^+$ monocations to the corresponding dications using either the multiplicative (mult) or additive (add) correction schemes. Further, the calculated (calc) vertical and adiabatic *IE*s are given, and other determinations are included for comparison; all data in eV.

	Q_{min}(mult)[a]	Q_{min}(add)	IE_v(calc)	IE_a(calc)	other values
Fe^+	15.39 ± 0.29	15.42 ± 0.26	16.52[b]	16.52[b]	16.19[c], 16.3 ± 0.4[d], 16.6 ± 0.5[e]
FeO^+	18.63 ± 0.30	18.10 ± 0.25	18.93	18.75	18.3 ± 0.3[f]
$FeOH^+$	17.30 ± 0.30	17.03 ± 0.23	17.23	16.90	17.0 ± 0.4[d]
$Fe(H_2O)^+$	14.41 ± 0.31	14.65 ± 0.30	14.04[g]	13.84[g]	
$[Fe,O_2,H_2]^+$	13.93 ± 0.82	14.27 ± 0.63	see text		
$(H_2O)FeOH^+$	15.84 ± 0.41	15.81 ± 0.34	15.80	16.07	
$Fe(H_2O)_2^+$	12.63 ± 0.33	13.23 ± 0.25	12.42	12.46	

[a] The errors are slightly larger than those given in Table 3-1 because they also include the error of ± 0.14 eV obtained in repetitive measurements of the toluene calibrant against itself. [b] For the transition Fe^+ (^6D) → Fe^{2+} (^5D), see text. [c] Spectroscopic value for $IE(Fe^+)$, ref. 26. [d] Previous Q_{min} value using the additive calibration scheme and a different ionization technique, ref. 64. [e] Previous Q_{min} value with ferrocene as precursor, ref. 66. [f] Previous Q_{min} value using CI of $Fe(CO)_5/N_2O$ and the multiplicative calibration scheme, ref. 58. [g] For the transition $Fe(H_2O)^+$ ($^6B_2$) → $Fe(H_2O)^{2+}$ ($^5A_2$), see text.

Inspection of Table 3-5 reveals generally better agreement between IE_v(calc) and Q_{min}(mult) compared to IE_v(calc) and Q_{min}(add). Except for Fe^+ and $[Fe,O_2,H_2]^+$, a maximum deviation of 0.37 eV is found between IE_v(calc) and Q_{min}(mult) of $Fe(H_2O)^+$, while errors up to 0.8 eV occur between IE_v(calc) and Q_{min}(add) of FeO^+, $Fe(H_2O)^+$, and $Fe(H_2O)_2^+$. Even more instructive is a plot of the differences between the computed IE_v(calc) and the measured Q_{min} data as a function of IE_v(calc). While the data based on the multiplicative scheme spread around zero, as expected for statistical deviations, the data derived from the additivity scheme show a clear trend to overestimate low and underestimate high IE_v (Figure 3-9). Of course, this analysis relies on the absolute B3LYP results, but the trend of the latter values would only become physically meaningful, if B3LYP would precisely show the opposite behavior, i.e. a systematic underestimation of low- and overestimation of high IE_v. As there is no indication to support this assumption,[77] the conclusion is that at least in the present system the multiplicative correction method is more appropriate.

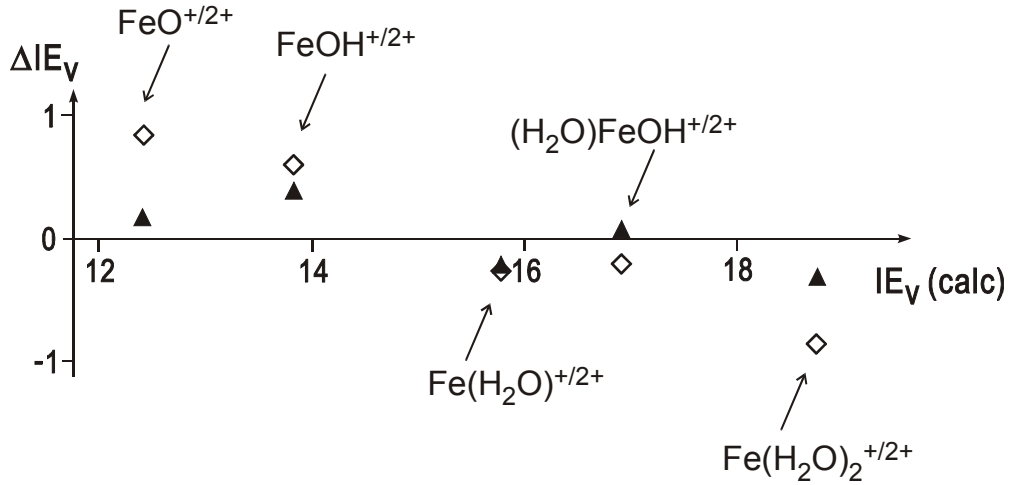

Figure 3-9: Deviations $\Delta IE_{mult} = Q_{min}$(mult) - IE_v(calc) (▲) and $\Delta IE_{add} = Q_{min}$(add) - IE_v(calc) (◇) as functions of IE_v(calc) for FeO^+, $FeOH^+$, $Fe(H_2O)^+$, $(H_2O)FeOH^+$, and $Fe(H_2O)_2^+$; all data in eV.

$[Fe,O_2,H_2]^{+/2+}$. Due to the existence of several isomers and the occurrence of isobaric interferences in the experimental studies, the $[Fe,O_2,H_2]^{+/2+}$ system is far from being trivial. Figure 3-10 gives a schematic survey of the $[Fe,O_2,H_2]^{+/2+}$ isomers of interest here. For each of the monocation isomers (and for each spin state as well), B3LYP predicts different IE_v and IE_a. If CI of $Fe(CO)_5/N_2O/H_2O$ is assumed to lead to generation of ground state $Fe(OH)_2^+$ as the most stable monocationic species, Q_{min} = 17.87 eV is expected from the computed IE_v. However, the precursor mixture used in CI also implies the generation of $(H_2O)FeO^+$ via the association reaction Equation 3-15. For this isomers, the calculations predict a somewhat lower Q_{min} value of only 17.02 eV. Although it appears unlikely, small amounts of $Fe(H_2O_2)^+$ might be generated in the ion source and contribute to the Q_{min} measurements because ionization energies of only about 14 eV are predicted for the different spin states. While this situation is already quite complex, also a non-negligible interference of $[Fe,O_2,H_2]^+$ by $^{54}Fe(H_2O)_2^+$ is apparent in the experimental study.

Qualitatively, the low-energy component of the charge-stripping peak shown in the upper trace of Figure 3-8 can be attributed to $^{54}Fe(H_2O)_2^+$, giving rise to the onset of the CS peak at about 12 eV. The high-energy component leading to the high-energy tail between 17 and 20 eV is due to $Fe(OH)_2^+$. The central component, also giving rise to the peak maximum at ca. 16 eV, is of unknown origin. Using the dication signal of $Fe(H_2O)_2^+$ (lower trace of Figure 3-8) as a reference, the shape of the dication signal in the upper trace can indeed be modeled assuming three different components. However, several assumptions are required in this procedure; in particular, it is obvious that also more than three components can contribute. In view of the ambiguities associated with such a deconvolution of overlapping features,

quantitative analysis of the experimental data does not seem appropriate. Anyhow, it is apparent that the Q_{min} values given in tables 3–3 and 3–5 do not reflect meaningful quantities for any of these species because non-composite charge-stripping signals are assumed in the threshold analysis. Thus, for the time being only the computational predictions are available in the subsequent analysis of the $[Fe,O_2,H_2]^{2+}$ dications.

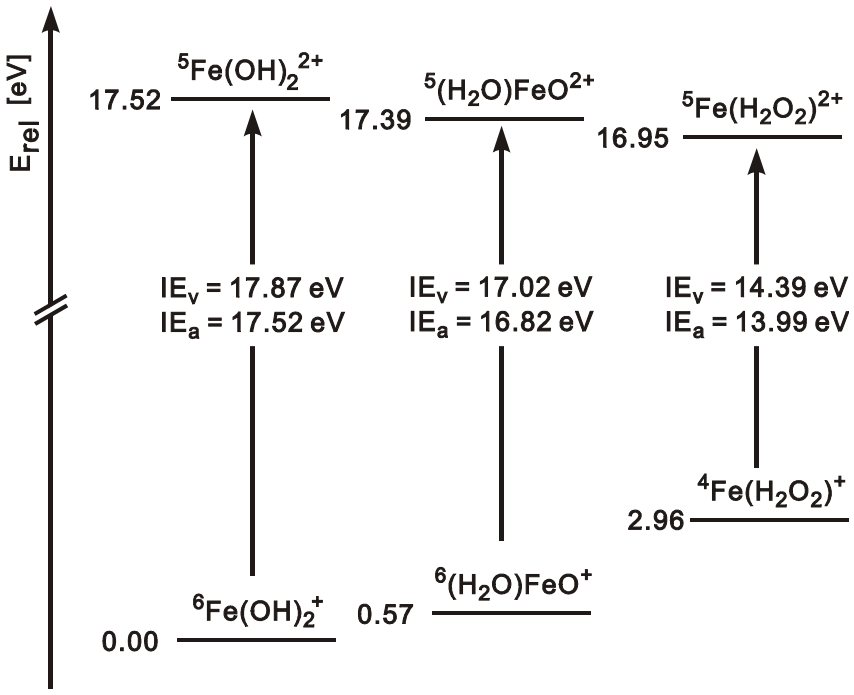

Figure 3-10: Energetics (in eV) of singly and doubly charged $[Fe,O_2,H_2]^{+/2+}$ ions computed at the B3LYP/6-311+G* level of theory; spin states are indicated as superscripts.

Best estimates. In this section, the experimental and theoretical data are critically reviewed in order to determine best estimates for the ionization energies of the $FeO_mH_n^+$ cations as a basis for the further evaluation of the thermochemistry of the $FeO_mH_n^{2+}$ dications. This procedure includes an evaluation of errors and limitation of the data to the significant digits. As far as the conversion of Q_{min} values to IE_a is concerned, an error of ± 0.1 eV is added to the experimental data in order to account for uncertainties in $\Delta IE_{v/a}$ and effects of vibrational progression in the transition from mono- to dications.[64] Based on the evaluation of the two calibration schemes, the multiplicative Q_{min} values are used throughout.

In the case of bare Fe^+, the spectroscopic value $IE(Fe^+)$ = 16.1879 ± 0.0012 eV is adopted.[26] Next, $IE_a(FeO^+)$ = 18.3 ± 0.4 eV and $IE(FeOH^+)$ = 17.0 ± 0.4 eV are derived from the different sets of experimental data given in Table 3-3 in conjunction with the calculated $\Delta IE_{v/a}$. For $Fe(H_2O)^+$, the conversion of Q_{min} to IE_a is more problematic (Figure 3-11). B3LYP

predicts a wrong order of states for the monocations together with different $\Delta IE_{v/a}$ for both. Hence, depending on the choice of the reference state different corrections need to be applied. For example, if it is assumed that only the sextet ground state of $Fe(H_2O)^+$ is formed upon CI, the measured Q_{min} = 14.41 ± 0.31 eV would yield IE_a = 14.21 eV. Instead, $\Delta IE_{v/a}$ is negligible for the quartet monocation, suggesting IE_a = 14.38 eV for $^4Fe(H_2O)^+$; the latter value changes to IE_a = 14.26 eV if referring to the $^6Fe(H_2O)^+$ ground state predicted in CCSD(T) calculations.[22b] Due to these ambiguities, the error margin of the correction are increased by ± 0.1 eV and a best estimate of $IE_a(Fe(H_2O)^+)$ = 14.3 ± 0.5 eV is derived. As mentioned above, only computational data are available for $[Fe,O_2,H_2]^+$, which predict $IE_a(Fe(OH)_2^+)$ = 17.5 ± 0.5 eV and $IE_a((H_2O)FeO^+)$ = 16.8 ± 0.5 eV; the error estimate is derived from the accuracy of the other predictions. Using similar considerations as for FeO^+ and $FeOH^+$, $IE((H_2O)FeOH^+)$ = 15.6 ± 0.5 eV and $IE(Fe(H_2O)_2^+)$ = 12.6 ± 0.4 eV are obtained for the two remaining species. With respect to the multiplicative calibration schemes, the absolute dication energetics predicted by B3LYP are consistent within the ± 0.5 eV error estimate associated with this level of theory; not unexpectedly, the bare metal atom shows the largest deviation.[22a,74]

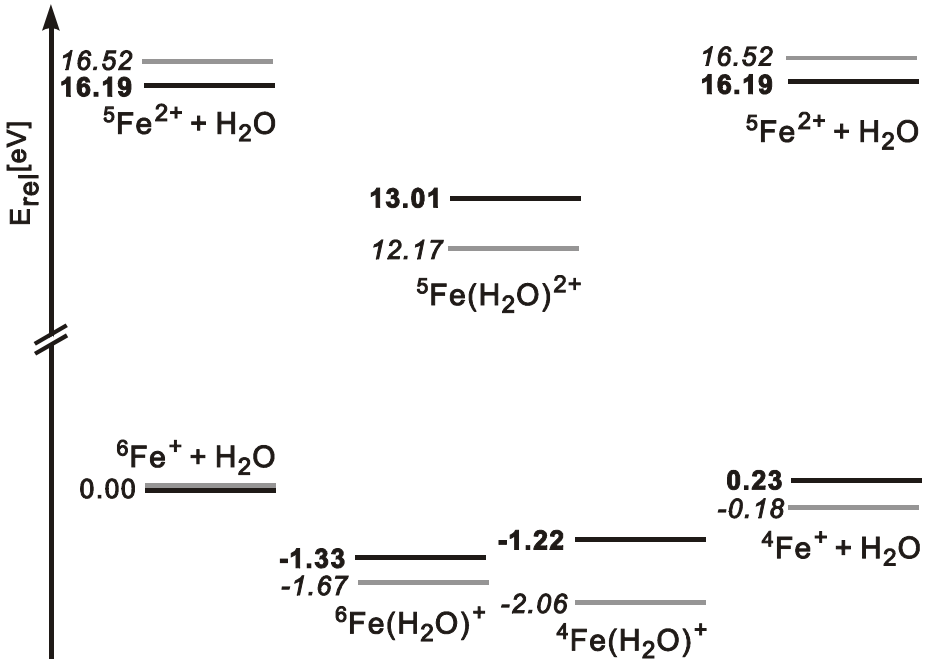

Figure 3-11: Energetics (in eV) of singly and doubly charged $Fe(H_2O)^{+/2+}$ computed at the B3LYP/6-311+G* level of theory (grey lines, italic figures) and the 'best estimates' based on literature data (black lines, bold figures); spin states are indicated as superscripts.

Table 3-6: Best estimates of $IE_a(FeO_mH_n^+)$, derived heats of formation (Δ_fH_{0K}), and low-lying charge separation limits (ΔE_{sep} with monocation fragments indicated) of the corresponding $FeO_mH_n^{2+}$ dications, as well as proton affinities (PA)[a] of the related monocations $FeO_mH_{(n-1)}^+$; all data in eV.[b]

	$IE_a(M^+)$[c]	Δ_fH_{0K} (M^{2+})	ΔE_{sep}	PA
Fe	16.19	28.4		
FeO	18.3 ± 0.4	29.6	- 1.2 ($Fe^+ + O^+$)	
FeOH	17.0 ± 0.4	25.8	- 4.5 ($Fe^+ + OH^+$)	1.4
$Fe(H_2O)$	14.3 ± 0.5	22.7	- 0.4 ($Fe^+ + H_2O$)	2.0
$Fe(OH)_2$	17.5 ± 0.5	23.4	- 1.2 ($FeOH^+ + OH^+$)	1.1
$(H_2O)FeO$	16.8 ± 0.5	23.3	- 1.8 ($FeO^+ + H_2O^+$)	1.2[d]
$(H_2O)FeOH$	15.6 ± 0.5	19.6	- 0.7 ($FeOH^+ + H_2O^+$)	2.2[e]
			- 2.1 ($FeO^+ + H_3O^+$)	1.7[f]
$Fe(H_2O)_2$	12.6 ± 0.4	16.8	+ 1.7 ($Fe(H_2O)^+ + H_2O^+$)	3.0
			- 1.8 ($FeOH^+ + H_3O^+$)	

[a] Not defined for Fe^+ and FeO^+. [b] For the derived values, the errors are equal or even exceed those of the IE_a data, but are omitted for the sake of clarity. [c] Best estimates, see text. [d] Using Δ_fH_{0K} ($OFeOH^+$) = 8.6 ± 0.5 eV. [e] Referring to $Fe(OH)_2^+$. [f] Referring to $(H_2O)FeO^+$.

3.3.5 Dication Thermochemistry

Based upon the best estimates derived above and complementary literature data of the neutral and cationic species, the heats of formation (Δ_fH_{0K}) of the dications are displayed in Table 3-6. Subsequently, the entire thermochemistry of the dications under study can be evaluated using Born-Haber cycles.[58,56,64]

A property of particular relevance for dications is their thermochemical stability in the gas phase, i.e. the energetic location of the dication minima relative to possible charge separation asymptotes yielding two singly charged fragments ("Coulomb explosion"). If the dication is lower in energy than the lowest-lying charge-separation fragment ($\Delta E_{sep} > 0$), the dication is termed thermochemically stable in the gas phase.[55] If $\Delta E_{sep} < 0$, the dications are metastable with respect to charge separation, provided dissociation is hindered by barriers.[36b,54,55,59] Except $Fe(H_2O)_2^{2+}$, however, charge-separations via direct Fe–O cleavages to the corresponding monocationic fragments are exothermic for all $FeO_mH_n^{2+}$ dications under study. Even though $IE_a(Fe(H_2O)^+)$ is almost 2 eV lower than $IE(Fe^+)$, charge separation to

afford $Fe^+ + H_2O^+$ is still slightly exothermic. In contrast, for the bisligated $Fe(H_2O)_2^{2+}$ complex direct Fe–O cleavage to the charge-separated products $Fe(H_2O)^+ + H_2O^+$ is indeed endothermic by 1.7 eV, but facile proton migration from one to the other water ligand[78] provides access to the $FeOH^+ + H_3O^+$ asymptote which is still 1.8 eV lower in energy than the dication minimum. Thus, none of the $FeO_mH_n^{2+}$ dications studied here is thermochemically stable.

$$(H_2O)FeOH^+ + NeH^+ \rightarrow Fe(H_2O)_2^{2+} + Ne \qquad \text{Equation 3-18}$$

The last process considered, i.e. the charge separation $Fe(H_2O)_2^{2+} \rightarrow FeOH^+ + H_3O^+$, leads us directly to a second peculiar question in the chemistry of dications, i.e. the proton affinities (*PA*s) of the corresponding monocations. In conjunction with complementary thermochemical data, the heats of formation given in Table 3-1 can be used to evaluate these figures. For example, the comparison of Δ_fH_{0K} ($FeOH^{2+}$) = 25.8 eV with Δ_fH_{0K} (FeO^+) = 11.3 eV and Δ_fH_{0K} (H^+) = 15.9 eV implies a proton affinity of 1.4 eV for the FeO^+ monocation. Thus, diatomic FeO^+ monocation has a positive proton affinity. Similary, $FeOH^+$, $OFeOH^+$, $Fe(OH)_2^+$, $(H_2O)FeO^+$, and $(H_2O)FeOH^+$ bear positive *PA*s. While most of these monocation *PA*s are small compared to that of typical neutral molecules, the considerable $PA((H_2O)FeOH^+)$ = 3.0 eV suggests that cation/cation reactions are conceivable in which proton transfer from a monocation to another one yields a dication concomitant with a neutral species. For example, the hypothetical protonation of $(H_2O)FeOH^+$ by the protonated rare gas NeH^+ according to Equation 3-18 is exothermic by 1.0 eV.

Of course, protonation of a cation is hindered by a considerable barrier due to Coulomb repulsion of the monocationic reactants. Despite its exothermicity, the process described in Equation 3-18 is therefore not expected to occur at room temperature. However, the occurrence of cation/cation reactions - even at elevated energies - offers an interesting perspective for gas-phase ion chemistry and physics.[55]

Let us now turn to some properties of the various $FeO_mH_n^{+/2+}$ species as functions of formal valence state and of ligation. The first systematic charge-stripping studies of ligated transition-metal ions are due to Lebrilla and coworkers.[79,80] However, these investigations are mostly focussed on the variation of the metal while keeping the ligand fixed. Instead, the results on the dication energetics for a single metal, i.e. selected $FeO_mH_n^{2+}$ dications, permit a more detailed analysis of the effect of ligation on dication energetics of iron compounds. In

particular, the influence of the formal valence on the bond strengths as well as the role of water as a solvating ligand is addressed.

Table 3-7: Fe-O bond strengths in $FeO_mH_n^{+/2+}$ mono- and dications (in eV) and formal valencies[a] of the iron atom.

Fe–O		D_0	Fe–OH		D_0	Fe–OH_2		D_0
$(H_2O)Fe^+$–O	III_{solv}	4.5[b]	$(H_2O)Fe^+$–OH	II_{solv}	4.8[b]	$(H_2O)Fe^+$–OH_2	I_{solv}	1.7[c]
Fe^+–O	III	3.5[c]	Fe^+–OH	II	3.8[c]	Fe^+–OH_2	I	1.3[c]
$(H_2O)Fe^{2+}$–O	IV_{solv}	2.0	$(H_2O)Fe^{2+}$–OH	III_{solv}	3.5	$(H_2O)Fe^{2+}$–OH_2	II_{solv}	3.4
Fe^{2+}–O	IV	1.4	$HOFe^+$–OH	III	3.3	$HOFe^+$–OH_2	II	2.3[b]
			Fe^{2+}–OH	III	3.0	Fe^{2+}–OH_2	II	3.2
			$HOFe^{2+}$–OH	IV	2.8	OFe^+–OH_2	III	2.3[b]
						$HOFe^{2+}$–OH_2	III	3.7
						OFe^{2+}–OH_2	IV	3.8

[a] The formal oxidation states of iron are given in roman numbers; see text for definition. [b] This work. [c] Taken from ref. 25.

Table 3-7 displays the Fe–O bond dissociation energies (D_0) of the $FeO_mH_n^{+/2+}$ mono- and dications under study together with the formal valencies of iron given in roman numbers. Here, the oxo- and hydroxy ligands are considered as strict two- and one-electron acceptors, i.e. O^{2-} and HO^-, respectively, and the positive charges are counted as extra valencies. While H_2O ligands do not affect the oxidation state, the presence of these solvating ligands is indicated by a subscript. For example, FeO^+ mono- and $FeOH^{2+}$ dication are formal Fe(III) compounds, $(H_2O)FeO^+$ is $Fe(III_{solv})$ etc. According to this formalism, both $D_0(Fe^{+/2+}\text{-O})$ and $D_0(Fe^{+/2+}\text{-OH})$ show clear trends towards decreasing dissociation energies with increasing valence of iron. These observations are consistent with the redox-chemistry of iron in solution where Fe(II) and Fe(III) are favored over all other oxidation states. Further, solvation of the metal by a water ligand is found to significantly increase the respective $Fe^{+/2+}$–O and $Fe^{+/2+}$–OH bonds strengths which is consistent with a stabilization of the polar, covalent bonds to the oxo- and hydroxy ligands in the presence of an additional ligand. Instead, $D_0(Fe^{+/2+}\text{-}OH_2)$ does not correlate with the formal oxidation state, but rather increases with net charge. This is consistent with the description of the binding to the water ligand as a primarily electrostatic interaction. Differential stabilization of the dications by the water ligands, i.e.

ΔIE_{solv} = $IE_a(M^+)$ - $IE_a(M(H_2O)^+)$, amount to 1.9 eV for $Fe^+/Fe(H_2O)^+$, 1.5 eV for $FeO^+/Fe(H_2O)O^+$, 1.4 eV for $FeOH^+/Fe(H_2O)OH^+$, and 1.7 eV for $Fe(H_2O)^+/Fe(H_2O)_2^+$. These values are quite similar (average ΔIE_{solv} = 1.6 ± 0.3 eV) and close to the mere ion-dipole interaction of 1.5 eV for water and a positive charge at a distance of ca. 1.9 Å. Hence, the differential stabilization of the hydrated iron dications can by and large be attributed to electrostatic forces.

3.3.6 Summary

Charge-stripping mass spectromety in conjunction with theoretical studies can be used to assess the energetics of $FeO_mH_n^{2+}$ dications. Given the error limits of the different approaches, the agreement between experiment and theory is reasonably good. In fact, the theoretical predictions assist to trace the origin of the discrepancies due to interferences of excited electronic states or isobaric ions. Further, the present results indicate that the multiplicative calibration scheme is more appropriate for correction of the charge-stripping data.

Evaluation of the dication energetics via Born-Haber cycles allows to analyze some of the dication thermochemical properties. None of the $FeO_mH_n^+$ dications studied is thermochemically stable as in all cases lower lying charge-separation asymptotes exist. With respect to bond strengths in the mono- and dications, the $Fe^{+/2+}$–O and $Fe^{+/2+}$–OH bonds show clear dependencies of the formal valence of iron and decrease with increasing oxidation state, whereas the interaction with water is dominated by the net charge and is primarily electrostatic. After all, these data allow to asses the ion thermochemistry of iron oxides and hydroxides in the gas phase, which might be of relevance in modeling the role of these iron compounds in the atmospheric chemistry and in corrosion phenomena.

3.4 Conclusions

In seemingly simple systems as FeO^+/H_2O and $FeOH^+/H_2O$ the reaction mechanisms turn out to be everything but simple. For instance, for the degenerate oxygen-exchange in FeO^+ and $FeOH^+$ with labeled water, speculations concerning the reaction mechanism from previous experimental data are shown to be invalid. Instead of involving two-state reactivity in order to explain the lower reactivity of FeO^+/H_2O versus $FeOH^+/H_2O$, kinetic effects are

proven to be responsible for the experimentally observed behavior, i.e. the energetically more demanding TS in FeO^+/H_2O and the requirement of a two-step reaction vs. only one step in $FeOH^+/H_2O$. In addition, the FeO^+/H_2O system has several conceivable reaction intermediates, i.e. $FeO(H_2O)^+$, $Fe(OH)_2^+$, and $Fe(H_2O_2)^+$. The $Fe(OH)_2^+$ is the most stable species, however, on the dication surface a reversed stability is observed with the high-energy isomer of the monocation surface ($Fe(H_2O_2)^+$) being the most stable dicationic isomer. This dramatic change is attributed to the formal oxidation states of iron in the different complexes, e.g. the formal iron(II) and iron(III) complexes $Fe(OH)_2^+$, $FeO(H_2O)^+$ and $Fe(H_2O_2)^{2+}$ are more stable than the corresponding formal iron(I) and iron(IV) compounds, thus allowing future predictions of the stability of complexes based on their formal oxidation states. The measured adiabatic and vertical ionization energies provide access to the redox-properties of the above and more $FeO_mH_n^{+/2+}$ species, which allow for a quantitative rather than qualitative understanding of their reactions. All the these data together provide valuable insight into the fundamental problem of redox-chemistry.

As far as the calculations are concerned, B3LYP has once more proven its applicability towards this type of problem. The calculated results are in good agreement with literature thermochemistry, as far as literature data are known. Moreover, B3LYP even shows predictive power when disproving the earlier suggestions for the reaction mechanism of the degenerate oxygen-exchange in FeO^+ with labeled water. This result is very promising from the chemical point of view. As transition-metal systems are a real challenge also for highly-correlated *ab initio* methods, application of the B3LYP method maybe a compromise leading to reasonably accurate results while keeping the need of computing time and power reasonably low.

References

[1] (a) V. E. Heinrich, P. A. Cox In: *The Surface Science of Metal Oxides*, Cambridge University Press, Oxford, **1994**. (b) C. R. N. Rao, B. Raveau *Transition Metal Oxides*, 2nd ed., Wiley-VCH, New York, **1998**.

[2] (a) R. H. Holm *Chem. Rev.* **1987**, *87*, 1401. (b) A. E. Shilov, G. B. Shulpin *Chem. Rev.* **1997**, *97*, 2879.

[3] W. Kaim, B. Schwederski *Bioanorganische Chemie*, Teubner, Stuttgart, **1991**.

[4] (a) P. R. Ortiz de Montellano (Ed.) *Cytochrome P-450; Structure, Mechanism, and Biochemistry*, Plenum-Press, New York, **1995**. (b) W.-D. Woggon, *Top. Curr. Chem.*, Springer-Verlag, Berlin, **1996**. (c) M. Sono, M. P. Roach, E. D. Coulter, J. H. Dawson *Chem. Rev.* **1996**, *96*, 2841.

[5] (a) B. Meunier *Chem. Rev.* **1992**, *92*, 1411. (b) A. Sorokin, B. Meunier *Chem. Eur. J.* **1996**, *2*, 1308. (c) A. E. Shilov, G. B. Shul'pin *Chem. Rev.* **1997**, *97*, 2879.

[6] (a) S.Bärsch, D. Schröder, H. Schwarz *Chem. Eur. J.* in press. (b) S. Bärsch, D. Schröder, H. Schwarz *Helv. Chim. Acta* **2000**, *83*, 827. (c) D. Schröder, S. Bärsch, H. Schwarz *J. Phys. Chem. A* in press.

[7] (a) K. A. Lee, W Nam *J. Am. Chem. Soc.* **1997**, *119*, 1916. (b) J. Bernadou, B. Meunier *Chem. Comm.* **1998**, 2167.

[8] For leading references, see: (a) C. Walling C. *Acc. Chem. Res.* **1998**, *31*, 155. (b) P. A. MacFaul, D. D. M. Wayner, K. U. Ingold *Acc. Chem. Res.* **1998**, *31*, 159. (c) S. Goldstein, D. Meyerstein *Acc. Chem. Res.* **1999**, *32*, 547.

[9] F. Jacobsen, J. Holcman, K. Sehested *Int. J. Chem. Kinet.* **1998**, *30*, 215.

[10] R. Dressler In *Chemistry in Extreme Environments*, C. Y. Ng, R. Dressler, Eds., Phys. Chem. Ser., Singapore, in preparation.

[11] A. D. McLean, G. S. Chandler *J. Chem. Phys.* **1980**, *72*, 5639.

[12] (a) A. H. J. Wachters *J. Chem. Phys.* **1972**, *52*, 1033. (b) P. J. Hay *J. Chem. Phys.* **1977**, *66*, 4377. (c) K. Raghavachari, G. W. Trucks *J. Chem. Phys.* **1989**, *91*, 1062.

[13] (a) D. Schröder, H. Schwarz *Angew. Chem.* **1995**, *107*, 2123, Angew. Chem Int. Ed. Engl. **1995**, *34*, 1973. (b) D. Schröder, H. Schwarz In: *Metal-Oxo and Metal-Peroxo Species in Catalytic Oxidations*, B. Meunier (Ed.), Springer, Berlin, in press.

[14] (a) D. Schröder, H. Schwarz *Angew. Chem.* **1990**, *102*, 1468, *Angew. Chem. Int. Ed. Engl.* **1990**, *29*, 1433. (b) D. Schröder, A. Fiedler, J. Hrušák, H. Schwarz *J. Am. Chem. Soc.* **1992**, *114*, 1215. (c) D. Schröder, H. Schwarz, D. E. Clemmer, Y. Chen, P. B. Armentrout, V. I. Baranov, D. K. Böhme *Int. J. Mass Spectrom. Ion Processes* **1997**, *161*, 175.

[15] L. Capron, H. Mestdagh, C. Rolando *Coord. Chem. Rev.* **1998**, *178/180*, 269.

[16] V. Baranov, G. Jahavery, A. C. Hopkinson, D. K. Böhme *J. Am. Chem. Soc.* **1995**, *117*, 12801.

[17] P. Pradel, L. Poisson, J. P. Visticot, H. Mestdagh, C. Rolando *J. Chem. Soc. Faraday Trans.* **1997**, *93*, 1607.

[18] O. Blum, D. Stöckigt, D. Schröder, H. Schwarz *Angew. Chem.* **1992**, *104*, 637; *Angew. Chem. Int. Ed. Engl.* **1992**, *31*, 603.

[19] M. Brönstrup, D. Schröder, H. Schwarz *Chem. Eur. J.* **1999**, *4*, 1176.

[20] A. Fiedler, J. Hrušak, W. Koch, H. Schwarz *Chem. Phys. Lett.* **1993**, *211*, 242.

[21] (a) A. Fiedler, D. Schröder, S. Shaik, H. Schwarz *J. Am. Chem. Soc.* **1994**, *116*, 10734. (b) S. Shaik, D. Danovich, A. Fiedler, D. Schröder, H. Schwarz *Helv. Chim. Acta* **1995**, *78*, 1393. (c) S. Shaik, M. Filatov, D. Schröder, H. Schwarz *Chem. Eur. J.* **1998**, *4*, 193. (d) D. Plattner A. *Angew. Chem. Int. Ed.* **1999**, *38,* 86. (d) D. Schröder, H. Schwarz, S. Shaik *Acc. Chem. Res.* **2000**, *33*, 139.

[22] (a) M. Sodupe, V. Branchadell, M. Rosi, C. W. Bauschlicher Jr. *J. Phys. Chem. A* **1997**, *101*, 7854. (b) A. Irigoras, J. E. Fowler, J. M. Ugalde *J. Am. Chem. Soc.* **1999**, *121*, 8549.

[23] M. Filatov, S. Shaik *J. Phys. Chem. A* **1998**, *102*, 3835.

[24] (a) K. Yoshizawa, Y. Shiota, T. Yamabe *Chem. Eur. J.* **1997**, *3*, 1160. (b) K. Yoshizawa, Y. Shiota, T. Yamabe *J. Am. Chem. Soc.* **1998**, *120*, 564. (c) K. Yoshizawa, Y. Shiota, T. Yamabe *Organometallics*, **1998**, *17*, 2825. (d) K. Yoshizawa, Y. Shiota, T. Yamabe *J. Chem. Phys.* **1999**, *111*, 538.

[25] P. B. Armentrout, B. L. Kickel In: *Organometallic Ion Chemistry*, B. S. Freiser (Ed.), Kluwer, Dordrecht, **1996**, p. 1.

[26] J. Sugar, C. Corliss *J. Phys. Chem. Ref. Data* **1985**, *14*, Suppl. 2.

[27] R. C. Weast CRC *Handbook of Chemistry and Physics*, 2nd ed., CRC Press Inc., Boca Raton, Florida **1990**.

[28] D. Schröder, C. A. Schalley, H. Schwarz In: *Peroxide Chemistry*, W. Adam (Ed.), Wiley-VCH, Weinheim, in press.

[29] B. L. Tjelta, P. B. Armentrout *J. Am. Chem. Soc.* **1996**, *118*, 9652.

[30] H. H. Cornehl, R. Wesendrup, J. N. Harvey, H. Schwarz *J. Chem. Soc. Perkin Trans. 2* **1997**, 2283.

[31] (a) C. J. Cassady, B. S. Freiser *J. Am. Chem. Soc.* **1985**, *107*, 1566. (b) D. Schröder, R. Wesendrup, C. A. Schalley, W. Zummack, H. Schwarz *Helv. Chim. Acta* **1996**, *79*, 123.

[32] D. Schröder, H. Schwarz *Angew. Chem.* **1990**, *102*, 1466; *Angew. Chem. Int. Ed. Engl.* **1990**, *29*, 1431.

[33] For a discussion of this phenomenon, see: M. Diefenbach, M. Brönstrup, M. Aschi, D. Schröder, H. Schwarz *J. Am. Chem. Soc.* **1999**, *121*, 10614, and references cited therein.

[34] K. Yoshizawa, Y. Shiota, T. Yamabe *J. Am. Chem. Soc.* **1999**, *121*, 147.

[35] (a) M. Rosi, C. W. Bauschlicher Jr., S. R. Langhoff, H. Partridge *J. Phys. Chem.* **1990**, *94*, 8656. (b) M. C. Holthausen, A. Fiedler, W. Koch, H. Schwarz *Angew. Chem.* **1995**, *107*, 2430, *Angew. Chem. Int. Ed. Engl.* **1995**, *34*, 2282. (c) M. C. Holthausen, A. Fiedler, W. Koch, H. Schwarz, *J. Phys. Chem.* **1996**, *100*, 6236.

[36] (a) R. D. Bach, D. S. Shobe, H. B. Schlegel, C. J. Nagel, *J. Phys. Chem.* **1996**, *100*, 8770. (b) D. Schröder, S. Bärsch, H. Schwarz, *Int. J. Mass Spectrom.* **1999**, *192*, 125.

[37] This estimation works as follows (thermochemical data are taken from refs. 25 and 38):
Δ_fH_0(**1**) ≈ $\Delta_fH_0(Fe^+)$ + Δ_fH_0(O) + $\Delta_fH_0(H_2O)$ - $D_0(Fe^+\text{-O})$ - $D_0(Fe^+\text{-}OH_2)$ and
Δ_fH_0(**3**) ≈ $\Delta_fH_0(Fe^+)$ + 2 Δ_fH_0(OH) - 2 $D_0(Fe^+\text{-OH})$, thus
Δ_fH_0(**1**) - Δ_fH_0(**3**) = Δ_fH_0(O) + $\Delta_fH_0(H_2O)$ - 2 Δ_fH_0(OH) - $D_0(Fe^+\text{-O})$ - $D_0(Fe^+\text{-}OH_2)$ + 2 $D_0(Fe^+\text{-OH})$.
With Δ_fH_0(O) + $\Delta_fH_0(H_2O)$ - 2 Δ_fH_0(OH) = - 16.78 ± 0.07 kcal/mol, $D_0(Fe^+\text{-H})$ = 80.0 ± 1.4 kcal/mol, $D_0(Fe^+\text{-}OH_2^+)$ = 30.6 ± 1.2 kcal/mol, and $D_0(Fe^+\text{-OH})$ = 87.4 ± 3.4 kcal/mol, **1** is estimated to be 47.4 ± 3.9 kcal/mol less stable than **3**.

[38] J. Berkowitz, G. B. Ellison, D. Gutman *J. Chem. Phys.* **1994**, *98*, 2744.

[39] This estimation works as follows (thermochemistry taken from refs. 25 and 38):
Δ_fH_0(**1**) ≈ $\Delta_fH_0(FeO^+)$ + $\Delta_fH_0(H_2O)$ - $D_0(Fe^+\text{-}OH_2)$ and
Δ_fH_0(**2**) ≈ $\Delta_fH_0(FeO^+)$ + Δ_fH_0(OH) + Δ_fH_0(H) - $D_0(Fe^+\text{-OH})$ - $D_0(Fe^+\text{-H})$, thus
Δ_fH_0(**1**) - Δ_fH_0(**2**) = - D_0(H-OH) - $D_0(Fe^+\text{-}OH_2)$ + $D_0(Fe^+\text{-OH})$ + $D_0(Fe^+\text{-H})$.
With D_0(H-OH) = 118.1 ± 0.05 kcal/mol, $D_0(Fe^+\text{-}OH_2^+)$ = 30.6 ± 1.2 kcal/mol, $D_0(Fe^+\text{-OH})$ = 87.4 ± 3.4 kcal/mol, and $D_0(Fe^+\text{-H})$ = 48.9 ± 1.4 kcal/mol, **1** is estimated to be 12.4 ± 3.9 kcal/mol more stable than **2**.

[40] For a recent case study, see: G. Ghigo, G. Tonachini *J. Am. Chem. Soc.* **1999**, *121*, 8366.

[41] Similarly, the counterintuitive presence of oxidizers and reducing agents is required in several selective oxidations using O_2 as terminal oxidant; for examples, see: (a) T. Mukaiyama In: *The Activation of Dioxygen and Homogeneous Catalytic Oxidation*, D. H. R. Barton, A. E. Martell, D. T. Sawyer (Eds.), Plenum, New York, **1993**, p. 133. (b) D. H. R. Barton, *Tetrahedron* **1998**, *54*, 5805.

[42] For H_2O_2 and hydroperoxides, see: (a) C. A. Schalley, R. Wesendrup, D. Schröder, H. Schwarz, *Organometallics* **1996**, *15*, 678. (b) Ref. 28a.

[43] For dialkylperoxides, see: (a) C. A. Schalley, R. Wesendrup, D. Schröder, T. Weiske, H. Schwarz, *J. Am. Chem. Soc.* **1995**, *117*, 7711. (b) R. Wesendrup, C. A. Schalley, D. Schröder, H. Schwarz, *Chem. Eur. J.* **1995**, *1*, 608. (c) C. A. Schalley, R. Wesendrup, D. Schröder, K. Schroeter, H. Schwarz, *J. Am. Chem. Soc.* **1995**, *117*, 12235.

[44] Auxiliary thermochemical data taken from: (a) S. G. Lias, J. E. Bartmess, J. F. Liebman, J. L. Holmes, R. D. Levin, W. G. Mallard, *Gas Phase Ion and Neutral Thermochemistry, J. Phys. Chem. Ref. Data, Suppl. 1* **1988,** *17*. (b) Ref. 38.

[45] B3LYP fails in predicting the correct sextet ground state for $Fe(H_2O)^+$ (see ref. 22b); the CCSD(T) state splitting of the $^6A_1$ and $^4B_2$ states (2.6 kcal/mol) is therefore included in the estimation of the error range.

[46] Calculated binding energies relative to bare $^4Fe^+$, $^6Fe^+$, and $^5Fe^{2+}$, respectively: $D_0(Fe^+\text{-}H_2O_2)$ = 37.1 kcal/mol for $^4\mathbf{1}^+$ and 29.1 kcal/mol for $^6\mathbf{1}^+$, $D_0(Fe^+\text{-}H_2O)$ = 41.8 kcal/mol for the quartet and 37.2 kcal/mol for the sextet, $D_e(Fe^{2+}\text{-}H_2O_2)$ = 100.8 kcal/mol for $^5\mathbf{1}^{2+}$, and $D_e(Fe^{2+}\text{-}H_2O)$ = 100.5 kcal/mol for the quintet.

[47] E. P. L. Hunter, S. G. Lias, *J. Phys. Chem. Ref. Data* **1998**, *27*, 413.

[48] Correlations between metal-ligand binding energies and the ligands' PAs are quite frequently reported in gas-phase chemistry of metal-ions; for examples, see: (a) J. S. Uppal, R. H. Staley, *J. Am. Chem. Soc.* **1982**, *104*, 1238. (b) R. W. Jones, R. H. Staley, *J. Am. Chem. Soc.* **1982**, *104*, 2296. (c) L. Operti, E. C. Tews, B. S. Freiser, *J. Am. Chem. Soc.* **1988**, *110*, 5847. (d) M. S. El-Shall, K. E. Schriver, R. L. Whetten, M. Meot-Ner, *J. Phys. Chem.* **1989**, *93*, 7969. For a deviation from this trend, see: (e) D. Schröder, J. Hrušák, R. H. Hertwig, W. Koch, P. Schwerdtfeger, H. Schwarz, *Organometallics* **1995**, 14, 312..

[49] C. W. Bauschlicher, *Chem. Phys.* **1996**, *211*, 163.

[50] C. B. Kellogg, K. K. Irikura, *J. Phys. Chem. A* **1999**, *103*, 1150.

[51] (a) P.O. Widmark, P.A. Malmqvist, B. Roos *Theor. Chim. Acta* **1990**, *77*, 291 (b) P.O. Widmark, B. J. Persson, B. Roos *Theor. Chim. Acta* **1991**, *79*, 419. (c) R. Pou-Amerigo, M. Merchan, I. Nebot-Gil, P.O. Widmark, B. Roos *Theor. Chim. Acta* **1995**, *92*, 149.

[52] For experimental studies of $[Fe,O_2,H_2]^+$, see: (a) Ref. 14a. (b) Ref. 16. (c) Ref. 19. (d) Ref. 28b. (e) Ref. 31a. (f) Ref. 31b.

[53] Similarly, high-spin ground states were predicted for the metal dihydroxide monocations $Co(OH)_2^+$ and $Ni(OH)_2^+$, see: A. Ricca, C. W. Bauschlicher, *J. Phys. Chem. A* **1997**, *101*, 8949.

[54] K. Lammertsma, P. v. R. Schleyer, H. Schwarz, *Angew. Chem.* **1989**, *101*, 1313; *Angew. Chem. Int. Ed. Engl.* **1989**, *28*, 1321.

[55] D. Schröder, H. Schwarz, *J. Phys. Chem. A* **1999**, *103*, 7385.

[56] A similar reversal of stabilities occurs for the $FeCl_2^+/Fe(Cl_2)^+$ and $FeCl_2^{2+}/Fe(Cl_2)^{2+}$ couples, see Chapter 4.

[57] D. Schröder, A. Fiedler, J. Schwarz, H. Schwarz *Inorg. Chem*. **1994**, *33*, 5094.

[58] J. N. Harvey, C. Heinemann, A. Fiedler, D. Schröder, H. Schwarz *Chem. Eur. J.* **1996**, *2*, 1230.

[59] K. Vekéy *Mass Spectrom. Rev.* **1995**, *14*, 195.

[60] M. M. Kappes, R. H. Staley *J. Am. Chem. Soc.* **1981**, *103*, 1286.

[61] Unless mentioned otherwise, auxiliary thermochemical data are taken from ref. 38 and 44 (for non-metal species) and ref. 25 (for gaseous iron compounds).

[62] M. S. Foster, J. L. Beauchamp *J. Am. Chem. Soc.* **1975**, *97*, 4808.

[63] N. F. Dalleska, K. Honma, L. S. Sunderlin, P. B. Armentrout *J. Am. Chem. Soc.* **1994**, *116*, 3519.

[64] S. McCullough-Catalano, C. B. Lebrilla *J. Am. Chem. Soc.* **1993**, *115*, 1441.

[65] P. R. Kemper, M. T. Bowers *J. Phys. Chem.* **1991**, *95*, 5134, and references cited therein.

[66] M. Rabrenovic, T. Ast, J. H. Beynon *Int. J. Mass Spectrom Ion Processes* **1984**, *61*, 31.

[67] C. J. Porter, C. J. Proctor, T. Ast, J. H. Beynon *Int. J. Mass Spectrom Ion Phys.* **1982**, *41*, 265.

[68] M. Guilhaus, R. G. Kingston, A. G. Brenton, J. H. Beynon *Int. J. Mass Spectrom. Ion Processes* **1985**, *63*, 101.

[69] C. Heinemann, D. Schröder, H. Schwarz *J. Phys. Chem.* **1995**, *99*, 16195, and references cited therein.

[70] R. G. Cooks, T. Ast, J. H. Beynon *Int. J. Mass Spectrom Ion Phys.* **1973**, *11*, 490.

[71] M. C. Holthausen, C. Heinemann, H. H. Cornehl, W. Koch, H. Schwarz *J. Chem. Phys.* **1995**, *102*, 4931.

[72] M. C. Holthausen, M. Mohr, W. Koch *Chem. Phys. Lett.* **1995**, *240*, 245.

[73] M. R. A. Blomberg, P. E. M. Siegbahn, M. Svensson *J. Chem. Phys.* **1996**, *104*, 9546.

[74] M. N. Glukhovtsev, R. D. Bach, C. J. Nagel *J. Phys. Chem. A* **1997**, *101*, 316.

[75] J. Husband, F. Aguirre, P. Ferguson, R. Metz *J. Chem. Phys.* **1999**, *111*, 1433.

[76] M. Rosi, C. W. Bauschlicher Jr. *J. Chem. Phys.* **1990**, *92*, 1876.

[77] Although no systematic studies have been performed so far, B3LYP calculations have provided reasonably accurate results for various types of dications. For recent examples, see: (a) J. Hrušák, Z. Herman, S. Iwata *Int. J. Mass Spectrom.* **1999**, *192*, 165. (b) S. Petrie, L. Radom *Int. J. Mass Spectrom.* **1999**, *192*, 173.

[78] For related examples of proton migration in hydrated metal ions and further references on this topic, see: M. Beyer, E. R. Williams, V. E. Bondybey, *J. Am. Chem. Soc.* **1999**, *121*, 1565.

[79] S. M. McCullough, A. D. Jones, C. B. Lebrilla *Int. J. Mass Spectrom. Ion Processes* **1991**, *107*, 545.

[80] P. Dai, S. McCullough-Catalano, M. Boulton, A. D. Jones, C. B. Lebrilla *Int. J. Mass Spectrom. Ion Processes* **1995**, *144*, 67.

4 Redox Properties of Charged and Neutral Iron Chlorides $FeCl_m^n$ (m = 1 - 3; n = -1, 0, +1, and +2)*

Iron chlorides are important in geochemical processes, ore refinery, and corrosion processes. In particular, ferrous chloride $FeCl_3$ is a valuable single-electron oxidant used in several synthetic procedures as well as numerous applied processes, for instance in the etching of copper in the manufacturing of electronic devices. The gas-phase properties of ferric and ferrous chloride have been studied quite extensively by experimental and theoretical methods.[1] Recently, some comprehensive studies of the thermochemistry of iron chlorides have been published,[2] and a survey of the present knowledge on the $FeCl_m^n$ system (m = 1 - 3; n = -1, 0, +1) is given in Table 4-1. For the sake of consistency, all values are taken from a recent theoretical study[2b] at the QCISD level of theory, which agrees favorably well with experimental literature data.

Table 4-1: Adiabatic electron affinities (EA_a, eV), adiabatic ionization energies (IE_a, eV) of $FeCl_m$ (m = 1 - 3), and the respective bond dissociation energies (eV) D_0(Fe-Cl^-), D_0(Fe-Cl), and D_0(Fe^+-Cl).

	EA_a	IE_a	D_0(Fe-Cl^-)	D_0(Fe-Cl)	D_0(Fe^+-Cl)
FeCl	1.54	7.89	1.58	3.55	3.45
$FeCl_2$	0.99	10.10	2.23	4.74	2.52
$FeCl_3$	3.90		2.97	2.55	

In this chapter, a study of the redox properties of iron chlorides in the gas phase is reported by examining electron transfer occurring in high-energy collisions using tandem mass-spectrometry. It comprises a variety of experiments, e.g. CA, CR, NR, CS, and CE. Energy demands of the associated vertical electron-transfer processes are extracted from energy-resolved measurements. In order to compare the experimental data with the literature thermochemistry of iron chlorides, theoretical methods employing the B3LYP hybrid functional are used to estimate the relevant differences between the adiabatic and vertical electron-transfer processes involved.

* Published in part in: D. Schröder, S. Bärsch, H. Schwarz *Int. J. Mass Spectrom.* **1999**, *192*, 125.

4.1 General Considerations

While the sector-MS instrument has been described in detail in Chapter 2, some specific problems of the energy-resolved measurements need to be pointed out. $FeCl_m^-$ anions (m = 2 - 4) and $FeCl_m^+$ cations (m = 1 - 3) are produced by either chemical ionization (CI) of a ca. 1 : 10 mixture of $Fe(CO)_5$ and molecular chlorine or by electron ionization (EI) of gaseous $FeCl_3$. The $FeCl_m^{2+}$ dications instead (m = 1, 2) are generated by EI of $FeCl_3$ at electron energies exceeding 30 eV.

Due to natural isotope abundances, the mass spectra of $^{56}Fe^{35}Cl_m^n$ species (m = 1 - 4; n = -1, +1, +2) always contain some $^{54}Fe^{37}Cl^{35}Cl_{(m-1)}^n$ as shown by signals due to $^{54}Fe^+$, $^{37}Cl^-$, etc. Other isobaric interferences as well as $Fe_2Cl_{2m}^{2+}$ are negligible, and all $FeCl_m^n$ species (m = 1 - 4; n = -1, +1, +2) under study show the expected isotope patterns.

All species generated in the ion source are characterized by CA; in addition, the $FeCl_m^-$ anions (m = 3, 4) are examined by $^-CR^{+3}$ and $^-NR^{+4}$ experiments. Quantitative comparison of the $^-CR^+$ and $^-NR^+$ spectra in terms of the recently developed NIDD scheme (NIDD = neutral and ion decomposition difference)[5,6] provides information about the behavior of the transient neutral iron chlorides formed in these experiments. In this scheme, subtraction of the intensities measured in the $^-CR^+$ mass spectrum from those intensities observed in the $^-NR^+$ experiment results in a difference spectrum which permits to trace back the contributions of the neutral transient species. Further, $^+CR^-$, $^+NR^-$, $^+NR^{+5}$, and CS[7] spectra of the $FeCl_m^+$ cations (m = 1 - 3) are recorded. The $FeCl_m^{2+}$ dications (m = 1, 2) produced in the ion source are also examined by CE[8] from the dications to the corresponding monocations as well as CS to possibly afford trications.[9,10]

Because of the superior energy resolution of E(1), the energy-resolved experiments are performed with B(1)-only mass-selected ions.[11] In order to quantitatively analyze the energy demands of the electron-transfer processes involved, the parent and recovery ions in charge-reversal and charge-stripping experiments are scanned at energy resolutions E/ΔE of ca. 5000 in conjunction with appropriate calibration schemes. In the net balance, $^-CR^+$, $^+CR^-$, and CS are all endothermic processes, and the energies required are provided by the translational energies of the keV projectiles, thereby giving rise to a decrease of the ions' kinetic energies. To a first approximation,[11,12] these energy balances can be described as follows.

(i) In $^-CR^+$, the energy difference ΔE_{-CR^+} corresponds to the removal of two electrons from a polyatomic anion A^-, i.e. the vertical transition $A^- \rightarrow A^+$. It is obvious that $\Delta E_{-CR^+} \geq EA_a(A) + IE_a(A)$, i.e the sum of the adiabatic electron affinity (EA_a) and the adiabatic ionization

energy (IE_a), because the cation formed upon vertical two-electron oxidation of the anion is generally not formed at the equilibrium geometry of A^-.

(ii) The corresponding energy balance ΔE_{+CR-} is composed of the energy gain upon addition of two electrons to a cation A^+ and the energy loss by removal of two electrons from the target, here xenon.[12-14] There are two conceivable scenarios for the removal of the two electrons in the $^+CR^-$ process. The first situation is a stepwise electron transfer, i.e. $A^+ + 2\ T \rightarrow A^- + 2\ T^+$, where the necessary excess energy is provided by the kinetic energy of the projectile. Thus, the minimum value of ΔE_{+CR-} corresponds to $2 \bullet IE(Xe) = 24.26$ eV minus the energy gained in the vertical transition $A^+ \rightarrow A^-$. Due to the geometry differences of the associated vertical transitions, the term (24.26 eV - ΔE_{+CR-}) would therefore be expected to be equal or smaller than the sum of EA_a and IE_a. The second scenario corresponds to a direct transfer of two electrons in a single collision, i.e. $A^+ + T \rightarrow A^- + T^{2+}$.[14,15] However, this process would appear at much lower kinetic energies than the high-energy onset of the recovery signal due to sequential electron transfer, because $2 \bullet IE(T) << IE(T) + IE(T^+)$; here, $2 \bullet IE(T) = 24.26$ eV compared to the energy demand of 33.43 eV for double ionization of xenon.

(iii) The kinetic energy deficit of dications formed in CS, usually referred to as Q_{min} value,[16] roughly corresponds to the vertical ionization energy of the monocation $IE_v(A^+)$. All these energy deficits can be determined from the high-energy onsets of the precursor ion and the corresponding recovery ion beams, provided appropriate calibration schemes are employed. Significant differences may exist between the energy deficits for a single two-electron transfer in one collision cell, i.e. ΔE_{CR}, versus double single-electron transfer in two consecutive collision cells with intermediate selection of the neutral species, i.e. ΔE_{NR}.[14,17] However, for the iron chlorides examined the high-energy onsets of the recovery ions in the energy-resolved CR and NR spectra are identical within the experimental error (± 0.3 eV) in the direct comparison of the measurements. Therefore, only the more sensitive CR experiments are taken into account.

The following electron-transfer processes are used in the calibration of the respective energy scales: (i) charge inversion of halide ions $X^- \rightarrow X^+$ (X = F, Cl, Br, I) and $O_2^- \rightarrow O_2^+$ for $^-CR^+$,[11,14,17] (ii) charge inversion of the halogen cations $X^+ \rightarrow X^-$ for (X = Cl, Br, I) as well as $O_2^+ \rightarrow O_2^-$ for $^+CR^-$,[12-14,17] and (iii) charge-stripping of the molecular ion of toluene, $C_7H_8^+ \rightarrow C_7H_8^{2+}$, with $Q_{min}(C_7H_8^+) = 15.7$ eV.[8,16] Note that the calibration schemes for CR used several references, while the energy scale of CS relies on $Q_{min}(C_7H_8^+)$ as a single anchor.

As far as the computational approach is concerned, some additional comments need to be made. The thermochemistry of $FeCl_m^n$ (m = 1 - 3; n = -1, 0, +1 except for $FeCl_3^+$) has recently been treated comprehensively by Bach et al.,[2b] who applied a range of theoretical levels including density functional methods.[2c,2d] Therefore, the primary aim of the theoretical investigation is the assessment of the differences between the vertical electron transfers sampled in the mass-spectrometric experiments and the corresponding adiabatic processes, rather than providing a more complete set of accurate ab initio thermochemical data of the iron chlorides. The B3LYP functional with the 6-311+G* basis set for chlorine and the Wachters-Hay all electron basis for Fe^+ is applied.[18] This level of theory is expected to provide reasonable descriptions of $FeCl_m^n$ (m = 1 - 3; n = -1, 0, +1) within about ± 0.5 eV uncertainty. Moreover, the accuracy of relative energies within the potential-energy surface of a given species is much better, and therefore, this level of theory is deemed to be adequate for converting the experimentally measured vertical energy deficits to the corresponding adiabatic processes.

In general, the geometries and states reported by Bach et al.[2b] are used as starting points in the calculations, followed by full geometry optimizations and frequency calculations. Note, however, that one cannot exclude other states of the species studied (either in symmetry or in multiplicity)[2c] which are lower in energy[19] because the minimum search is restricted solely to the input structures of Bach et al.[2b] The use of B3LYP for the estimation of the differences between vertical and adiabatic electron transfers appears nevertheless appropriate, given the reasonable assumption that the potential-energy surfaces of these states are similar. The correction scheme for vertical versus adiabatic transitions is the following. The adiabatic properties given below refer to 0 K values, i.e. they include the zero-point vibrational energies (ZPVEs). The differences between vertical and adiabatic electron transfer are derived by calculating the energy of a certain species, e.g. $FeCl^-$, using the geometry obtained in the optimization of the same species having a different charge, e.g. $FeCl^+$ or FeCl. Thus, as an example, the energy difference of an $FeCl^-$ anion having the bond length of the geometry-optimized $FeCl^+$ cation (r_{FeCl} = 2.07 Å) and of the $FeCl^-$ minimum (r_{FeCl} = 2.30 Å) represents the energy difference between the vertical and adiabatic charge inversions $FeCl^+ \rightarrow FeCl^-$. This methodology implies a two-electron transfer in a single step for the transitions $FeCl_m^+ \rightarrow FeCl_m^-$ and $FeCl_m^- \rightarrow FeCl_m^+$ (m = 1 - 3). The vertical/adiabatic energy difference for a two-step, single-electron transfer scenario, e.g. $FeCl^+ \rightarrow FeCl \rightarrow FeCl^-$ is examined as well. However, due to the small geometry changes between the different charge states involved, the same results are obtained within the error of the method for both mechanistic schemes.

Therefore, only the values for the above mentioned one-step, two-electron transfer are tabulated below. In the calculation of these energy differences, the ZPVEs are not included.

Table 4-2: Ion intensities in the CA, CR, and NR mass spectra of B(1)/E(1) mass-selected $FeCl_m^{-/+}$ ions (m = 1 - 4).

	Spectrum	$FeCl_3$	$FeCl_2$	FeCl	Cl_2	Fe	Cl	other species
$FeCl_3^-$	CA		100				10	
	$^-CR^+$	4	100	45	2	15	5	
	$^-NR^+$	6	40	100	1	35	8	
	$^-NIDD^+$ [a]	1	-38	26	0	10	1	
$FeCl_4^-$ [b]	CA	100	1				1	
	$^-CR^+$	60	90	100	4	15	8	
	$^-NR^+$	12	65	100	3	45	12	
	$^-NIDD^+$ [a]	-17	-5	6	0	14	2	
$FeCl^+$	CA					100	1	$FeCl^{2+}$ (1)
	CS					100	2	$FeCl^{2+}$ (4)
	$^+NR^+$			100		40	3	
$FeCl_2^+$	CA			100		3		
	CS			100		4	<1	$FeCl_2^{2+}$ (<1)
	$^+NR^+$		95	100	1	25	3	
$FeCl_3^+$	CA		100	20		1		
	CS		100	15	<1	3	<1	$FeCl_3^{2+}$ (<1)
	$^+NR^+$	25	90	100	12	30	4	
$FeCl_4^+$ [c]	CA	100	30	10				

[a] $^-NIDD^+$ spectrum derived from the data of the $^-CR^+$ and $^-NR^+$ spectra given in the preceding lines. By definition, the sum of the NIDD intensities is zero; for details, see ref. 5,6. [b] Even at maximum sensitivity, no recovery signal due to $FeCl_4^+$ was observed. [c] The intensity of $FeCl_4^+$ was too low for CS and $^+NR^+$ experiments.

4.2 Dissociation Pattern and Calculated Thermochemistry of $FeCl_m^n$ (m = 1 – 4, n = -1 – 2)

The experimental data given in this section refer to $FeCl_m^n$ ions (m = 1 - 4; n = -1, +1, +2) generated by electron ionization (EI) of gaseous $FeCl_3$, and if not mentioned otherwise, the

results obtained with chemical ionization (CI) of $Fe(CO)_5/Cl_2$ are identical within experimental error. This section is organized such that we first describe the experimental and theoretical results for the neutral and singly charged species, followed by the data for $FeCl_m^{2+}$ dications (m = 1 - 3). A comprehensive discussion of the experimental and theoretical results is given in Chapter 4.3.

4.2.1 Dissociation Behavior of $FeCl_m^n$ Ions (m = 1 - 4; n = -1, +1)

As a consequence of the limited size of the system, none of the $FeCl_m^n$ species underwent structure-specific unimolecular reactions. Thus, the corresponding metastable ion (MI) mass spectra are identical to the collisional activation (CA) mass spectra, except much lower fragment ion intensities. In fact, rather than being due to metastable ions, the minor fragmentations observed in these experiments may possibly arise from collision-induced dissociation with residual background gases present in the mass spectrometer.[20]

Table 4-2 summarizes the ion intensities observed in the CA, CR, and NR mass spectra. The intensities are given relative to the base peak = 100% and contributions of ^{54}Fe and ^{37}Cl isotopes are neglected. The CA spectra of the $FeCl_m^-$ anions (m = 3, 4) show simple fragmentation patterns in which losses of atomic chlorine prevail. In the CA spectrum of $FeCl_3^-$, the $FeCl_2^-$ fragment dominates over the Cl^- fragment although $EA(FeCl_2)$ = 0.99 eV (Table 4-1) is lower than $EA(Cl)$ = 3.62 eV.[21] This may be attributed to the mass discrimination in detecting Cl^- (35 amu) versus $FeCl_2^-$ (126 amu)[22] as well as the difference between the vertical and the adiabatic neutralization of $FeCl_2^-$ (see below). In turn, despite a moderate parent ion intensity of $FeCl_2^-$, no significant CA mass spectrum is obtained, thus suggesting that electron detachment prevails. This conclusion is in accord with $EA(FeCl_2)$ = 0.99 eV being much lower than the energy demands of the conceivably competing bond cleavages to afford FeCl + Cl^- (2.23 eV) and $FeCl^-$ + Cl (4.31 eV). Also, none of the CA spectra of $FeCl_m^-$ displays a significant signal due to the formation of Cl_2^- molecular anion, although this species may be formed in keV collisions.[5]

Sequential losses of atomic chlorine also prevail in the CA spectra of the $FeCl_m^+$ cations (m = 1 - 4). Asides some dication signals due to charge stripping, the cation CA spectra confirm the purity of the mass-selected ion beams in that no fragments other than expected for $FeCl_m^+$ (m = 1 - 4) are observed.

Some information with respect to the fragmentation of the neutral iron chlorides $FeCl_m$ (m = 3, 4) is obtained from quantitative analysis of the $^{-}CR^{+}$ and $^{-}NR^{+}$ spectra in terms of the recently introduced NIDD scheme.[5,6] The $^{-}CR^{+}$ and $^{-}NR^{+}$ spectra of $FeCl_3^{-}$ and $FeCl_4^{-}$ are dominated by intense signals due to $FeCl_m^{+}$ with m = 1, 2 for $FeCl_3^{-}$ and m = 1 - 3 for $FeCl_4^{-}$. The extensive degree of degradation in the spectra may be regarded as an indication for expulsions of molecular chlorine, rather than sequential losses of chlorine atoms. For example, the positive signal for $FeCl^{+}$ in the $^{-}NIDD^{+}$ spectrum of $FeCl_3^{-}$ suggests the fragmentation of the neutral species according to $FeCl_3 \rightarrow FeCl + Cl_2$. Occurrence of this reaction would, however, require that the complementary signal of Cl_2^{+} formed upon reionization of neutral Cl_2 would increase in the $^{-}NR^{+}$ relative to the $^{-}CR^{+}$ spectrum, and thus appear on the positive scale of the $^{-}NIDD^{+}$ spectrum of $FeCl_3^{-}$.[5] Experimentally, the Cl_2^{+} intensities are low, and the signal belongs to the negative scales of the $^{-}NIDD^{+}$ spectra of $FeCl_3^{-}$ and $FeCl_4^{-}$. Instead, the positive $^{-}NIDD^{+}$ signals for Cl^{+} are consistent with sequential Fe-Cl bond cleavages. The more extensive fragmentation in NR than in CR can be traced back to the fact that the former requires two high-energy collisions by definition, while the charge reversal of anions may well occur in a single collision.[5,14] In comparison, fragmentations are less pronounced in the $^{+}NR^{+}$ spectra of the $FeCl_m^{+}$ cations (m = 1 - 3), for which sizable recovery signals are observed. These differences are consistent with the smaller changes in geometry in the $^{+}NR^{+}$ sequence, i.e. $FeCl_m^{+} \rightarrow FeCl_m \rightarrow FeCl_m^{+}$, compared to charge inversion, i.e. $FeCl_m^{-} \rightarrow FeCl_m^{+}$.

In essence, the fragmentation patterns of $FeCl_m^{n}$ species confirm the intuitive conjecture that sequential reduction of the metal chlorides is more facile than loss of molecular chlorine. Some circumstantial evidence will be discussed further below, which does indeed suggest that formation of Cl_2^{+} is probably due to fragmentations of excited cation states.

Except for $FeCl_4^{-}$, all $FeCl_m^{n}$ species exhibit recovery signals in charge-reversal as well as neutralization-reionization experiments. Specifically, $FeCl_m^{-}$ (m = 2, 3) and $FeCl_m^{+}$ (m = 1 - 3) yield reionized parent ions in $^{-}CR^{+}$, $^{-}NR^{+}$, $^{+}CR^{-}$, $^{+}NR^{-}$, and $^{+}NR^{+}$ experiments, respectively. Further, the $FeCl_m^{+}$ (m = 1 - 3) monocations give rise to the corresponding dication signals in charge stripping experiments (see below). These results are in accord with the expected, reasonably strong covalent bonds between iron and chlorine.[1c,2b,2c]

The mere presence of the recovery signals allows to probe the redox properties of the iron chlorides in the gas phase by means of energy-resolved CR spectra of the recovery ions in which the associated energy differences (ΔE_{CR}) can be determined from the high-energy

onsets of the recovery ions.[11-14,17] These experiments are quite sensitive because instead of full mass spectra, only a narrow region in the vicinity of the recovery signal is monitored. Compared to other spectroscopic techniques, however, the precision of the measured energies is poor, mostly because of the limited energy resolution of our mass spectrometer.[23] Experimentally, the following differences were determined: $\Delta E_{-CR^+}(FeCl_2^-) = 11.9 \pm 0.8$ eV, $\Delta E_{-CR^+}(FeCl_3^-) = 19.8 \pm 1.1$ eV, $\Delta E_{+CR^-}(FeCl^+) = 14.7 \pm 1.0$ eV, $\Delta E_{+CR^-}(FeCl_2^+) = 12.9 \pm 0.8$ eV, and $\Delta E_{+CR^-}(FeCl_3^+) = 10.1 \pm 0.9$ eV; $FeCl_4^-$ did not yield a detectable recovery signal in $^-CR^+$. The relevance of these data with respect to the associated vertical electron transfers involved is discussed further below.

Table 4-3: Computed structures of $FeCl_m^{+/0/-}$. Bond lengths are given in Å and bond angles in degree.

species	symmetry/ computed state	r_{FeCl}	α_{ClFeCl}
$FeCl^+$	$C_{\infty v}$, $^6A_1$	2.07	
FeCl	$C_{\infty v}$, 6Δ	2.21	
$FeCl^-$	$C_{\infty v}$, 5Δ	2.30	
$FeCl_2^+$	C_{2v}, $^6A_1$	2.08	140
$FeCl_2$	$D_{\infty h}$, $^5\Delta$	2.15	180
$FeCl_2^-$	C_{2v}, $^5A'$	2.32	110
$FeCl_3^+$	D_{3h}, $^5A'$	2.08	120
$FeCl_3$	D_{3h}, $^6A'$	2.15	120
$FeCl_3^-$	D_{3h}, $^5A'$	2.26	120

4.2.2 B3LYP Calculated Thermochemistry of $FeCl_m^n$ (m = 1 - 3, n = -1, 0, +1)

Table 4-3 shows the calculated geometries for the neutrals as well as the singly charged ions. In comparison with the data evaluated by Bach et al.[2b] (Table 4-1), our B3LYP/6-311+G* approach generally performs quite well for the iron chlorides (Table 4-4). Similar conclusions were drawn by Bauschlicher[2c] and Glukhovtsev et al.[2d] in their recent computational studies of iron halides. In fact, the reasonable accuracy of the empirical B3LYP hybrid functional in conjunction with moderate computational costs is a major factor for the extensive application of this method.

Table 4-4: Computed adiabatic electron affinities (EA_a, eV), ionization energies (IE_a, eV) of $FeCl_m^n$ (m = 1 - 3; n = -1, 0, +1), and the respective bond dissociation energies (eV) D_0(Fe-Cl^-), D_0(Fe-Cl), and D_0(Fe^+-Cl) of the iron chlorides as predicted by B3LYP/6-311+G* calculations. In addition, some calculated properties of the atomic fragments along with experimental values (in brackets)[b] are given.

	EA	*IE*	D_0(Fe-Cl^-)	D_0(Fe-Cl)	D_0(Fe^+-Cl)
FeCl	1.91	7.91	1.63	3.45	3.46
$FeCl_2$	1.09	10.29	1.94	4.58	2.19
$FeCl_3$	4.31	10.93	2.68	2.09	1.44
Fe		7.99 (7.89)			
Fe^+		16.51 (16.18)			
Cl	3.72 (3.62)	13.08 (12.97)			
Cl_2		11.59 (11.48)[b]			

[a] Taken from ref. 21. [b] B3LYP significantly underestimates D_0(Cl-Cl), predicting a value of only 46.9 kcal/mol compared to the experimental value (57.2 kcal/mol[21]).

Table 4-5: Calculated B3LYP/6-311+G* energies (in eV) for $FeCl_m^n$ species (m = 1 - 3; n = -1, 0, +1) having the optimized geometries of the anionic, neutral, and cationic minima, respectively.[a,b,c]

species	geometry	FeCl	$FeCl_2$	$FeCl_3$
cation	cation	*7.90*	*10.29*	*10.93*
	neutral	8.05	10.40	11.16
	anion	8.26	11.10	11.57
neutral	cation	0.13	0.31	0.30
	neutral	*0.00*	*0.00*	*0.00*
	anion	0.05	0.91	0.23
anion	cation	-1.64	-0.27	-3.50
	neutral	-1.87	0.20	-3.75
	anion	*-1.90*	*-1.08*	*-4.30*

[a] All energies are given relative to the corresponding neutral iron chloride. [b] The adiabatic properties (IE_a and $-EA_a$) are given in italics. [c] Zero-point energies are not included.

Upon closer inspection, the deviations of the B3LYP energetics from the data given in Table 4-1 increase with the formal oxidation state of iron, i.e. the bond energies for anionic, neutral, and cationic FeCl are reproduced reasonably well with B3LYP, whereas the Fe-Cl bond strengths in cationic $FeCl_2^+$ as well as neutral $FeCl_3$ are underestimated by 0.33 and 0.46

eV, respectively. While this inaccuracy seems acceptable, some evidence discussed further below indicates that the B3LYP approach may exhibit some systematic errors as to the absolute energetics of electron transfer, which also involves a change of the formal oxidation state. Notwithstanding, we are confident that B3LYP treats the species of interest reasonably well in the vicinity of the respective minima. For example, B3LYP has been shown to provide accurate geometries for several neutral and charged iron compounds.[2b-2d,19] Thus, the B3LYP/6-311+G* level of theory is assumed to yield good predictions for the differences between vertical and adiabatic electron transfer for the systems of interest (Table 4-5), even though the absolute values may be less reliable.

Not unexpected for transition metal halides, the geometries of $FeCl_m^n$ (m = 1 - 3; n = -1, +1) change smoothly upon sequential oxidation or reduction. The Fe-Cl bond lengths slightly decrease from the anionic to the cationic species, and most changes are not all that dramatic. For example, the computed stabilities of $FeCl^-$ relative to FeCl are -1.90 eV for the optimized anion (r_{FeCl} = 2.30 Å), -1.87 eV for the anion having the bond length of neutral FeCl (r_{FeCl} = 2.21 Å), and -1.64 eV for the anion having the bond length of $FeCl^+$ (r_{FeCl} = 2.07 Å). Similarly, the vertical ionizations of the neutral and anion structures to $FeCl^+$ and $FeCl_3^+$ cations result in energy differences of no more than 0.6 eV compared to the adiabatic processes. The largest differences between vertical and adiabatic transitions are found for iron dichloride. This effect can be attributed to the fact that neutral $FeCl_2$ is linear, whereas $FeCl_2^-$ and $FeCl_2^+$ have bent structures.[2b,24] For the geometry-optimized structure of $FeCl_2^-$ (r_{FeCl} = 2.32 Å, α = 110°), B3LYP/6-311+G* predicts an adiabatic $EA_a(FeCl_2)$ of 1.08 eV which compares reasonably well with $EA_a(FeCl_2)$ = 0.99 eV.[2b] However, the vertical electron affinity of $FeCl_2$ having the structure obtained in the geometry optimization of the cationic species (r_{FeCl} = 2.08 Å, α = 140°) is only 0.27 eV. The vertical electron affinity of the linear, neutral $FeCl_2$ molecule (r_{FeCl} = 2.15 Å, α = 180°) is even predicted to be negative, $EA_v(FeCl_2)$ = -0.20 eV. In this particular case, bending seems therefore to be more important for the stability of $FeCl_2^-$ anion than the differences in r_{FeCl}.

4.2.3 $FeCl_m^{2+}$ (m = 1 - 3) Dications

The first systematic charge-stripping studies of transition-metal halides are due to Lebrilla and coworkers.[25] In the present system, the $FeCl_m^+$ monocations (m = 1- 3) are oxidized to the corresponding dications upon charge-stripping (CS) with molecular oxygen in keV collisions.

Relative to the base peaks of the CS spectra (Table 4-2), the intensities of the charge-stripping signals are 4 % for $FeCl^{2+}$, 0.2 % for $FeCl_2^{2+}$, and only 0.05 % for $FeCl_3^{2+}$. Thus, the intensities of the $FeCl_m^{2+}$ dication signals relative to the singly charged fragments decrease with increasing m. This trend can be regarded as a consequence of the increasing manifold of low-lying fragmentation channels for $FeCl_2^+$ and $FeCl_3^+$ compared to diatomic $FeCl^+$ in conjunction with the corresponding dication stabilities. Energy-resolved charge-stripping experiments yield $Q_{min}(FeCl^+)$ = 15.9 ± 0.4 eV, $Q_{min}(FeCl_2^+)$ = 17.6 ± 0.7 eV, and $Q_{min}(FeCl_3^+)$ = 16.0 ± 0.4 eV. Within the experimental uncertainty, EI of gaseous $FeCl_3$ and CI of $Fe(CO)_5/Cl_2$ yield identical Q_{min} values for $FeCl^+$ and $FeCl_3^+$.

Charge stripping of $FeCl_2^+$, however, deserves some more detailed discussion. First, the experimental error of $Q_{min}(FeCl_2^+)$ is significantly larger than those of $Q_{min}(FeCl^+)$ and $Q_{min}(FeCl_3^+)$, although the ions are examined under essentially identical conditions. Second, while EI of gaseous $FeCl_3$ yields $Q_{min}(FeCl_2^+)$ = 17.6 ± 0.7 eV, a drastic decrease to $Q_{min}(FeCl_2^+)$ = 15.2 ± 0.5 eV occurs when the monocation precursors are generated by CI of $Fe(CO)_5/Cl_2$. Both findings suggest contributions of isomeric structures and/or excited states present in the $FeCl_2^+$ precursor ion beam; this aspect is discussed in more detail further below.

$FeCl_m^{2+}$ dications (m = 1 - 3) can also be generated directly by EI of gaseous $FeCl_3$. The intensities of $FeCl^{2+}$ and $FeCl_2^{2+}$ are sufficient to probe the dications in charge-exchange (CE) experiments using helium as a collision gas. The CE spectrum of $FeCl^{2+}$ (Figure 4-1a) displays signals due to the monocations of $FeCl^+$, Fe^+, and Cl^+ as well as the Fe^{2+} dication due to homolytic bond cleavage of the dication. The Fe^+ and Cl^+ signals are composite, showing characteristic features due to Coulomb explosion of $FeCl^{2+}$ into $Fe^+ + Cl^+$. Thus, the central components of the peaks are due to charge exchange followed by fragmentation of the $FeCl^+$ monocation, while the high- and low-mass components can be assigned to dished-topped peaks arising from charge separation of the $FeCl^{2+}$ dication. Similarly, the CE spectrum of $FeCl_2^{2+}$ (Figure 4-1b) shows composite peaks which can be attributed to charge exchange as well as the charge separations into $FeCl^+ + Cl^+$ and $Fe^+ + Cl_2^+$, respectively. In addition, some charge-exchange to afford $FeCl_2^+$ monocation is observed as well as are homolytic bond cleavages of the dication resulting in formation of $FeCl^{2+}$ and Fe^{2+}. In the corresponding CE spectra with oxygen as collision gas (not shown), formation of monocations due to charge exchange prevails. The differences in CE with oxygen and helium as the collision gases can be explained by considering that $IE(O_2)$ = 12.07 eV[21] is much lower than $IE(FeCl_m^+) \approx$ 15-18 eV, such that despite a Coulombic barrier, electron transfer from the target to the dication is

favorable for oxygen, whereas charge exchange is quite endothermic with helium (*IE*(He) = 24.48 eV)[21] as a collision partner.

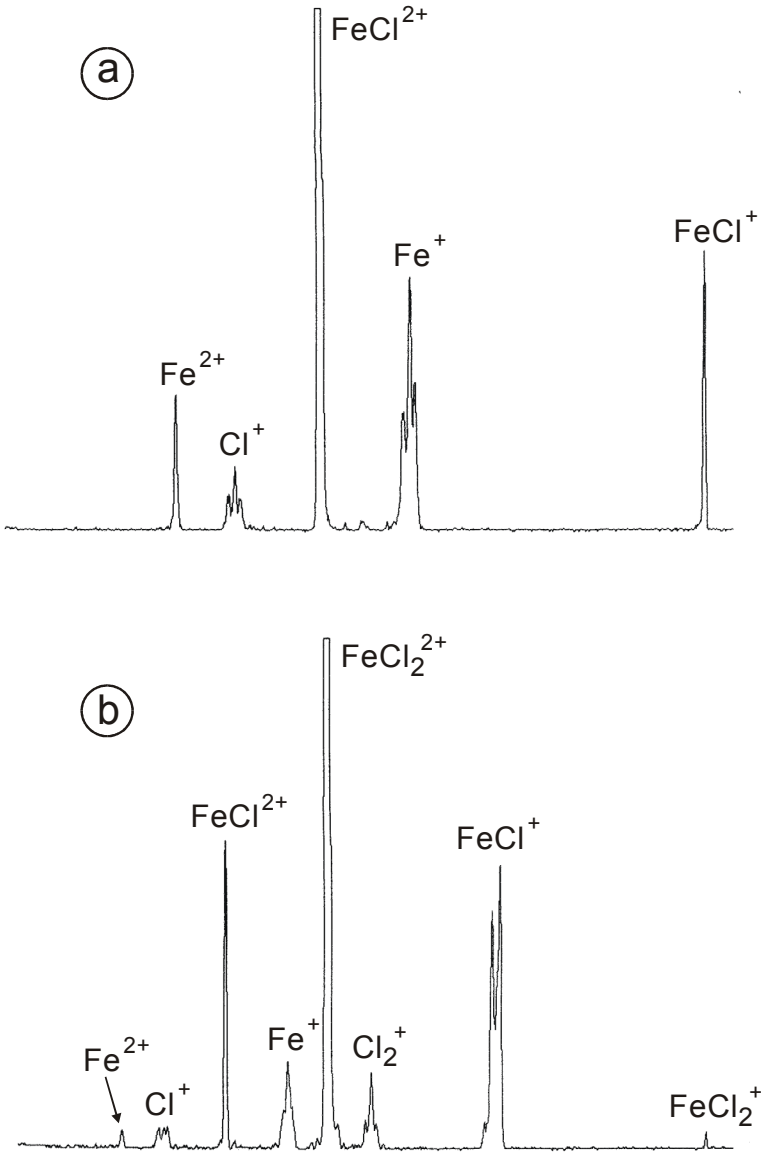

Figure 4-1: (a) CE-spectrum of B(1)/E(1) mass-selected $FeCl^{2+}$ dication (helium, 80 % T). The $FeCl^{2+}$ precursor is off-scale; the gain factor is 500. The Fe^+ and Cl^+ signals show typical peak shapes due to overlap of charge-exchange and Coulomb explosion. (b) CE-spectrum of B(1)/E(1) mass-selected $FeCl_2^{2+}$ dication (helium, 60 % T). The $FeCl_2^{2+}$ precursor is off-scale; the gain factor is 300. The $FeCl^+$, Cl_2^+, Fe^+, and Cl^+ signals show typical peak shapes due to overlap of charge-exchange and Coulomb explosion.

The B3LYP/6-311+G* calculations predict very minor geometry changes going from the $FeCl_m^+$ mono- to the $FeCl_m^{2+}$ dications (m = 1 - 3), i.e. r_{FeCl} = 2.07 Å in $FeCl^+$ ($^5\Delta$) versus 2.08 Å in $FeCl^{2+}$ ($^6\Sigma$), r_{FeCl} = 2.08 Å in $FeCl_2^+$ ($^6A_1$) versus 2.09 Å in $FeCl_2^{2+}$ ($^5B_2$), r_{FeCl} = 2.08 Å in $FeCl_3^+$ ($^5A'$) versus 2.09 Å in $FeCl_3^{2+}$ ($^6A''$). Therefore, the vertical and adiabatic ionization

energies of the monocations are considered more or less identical and the measured Q_{min} values are regarded as good approximations for the adiabatic *IE*s of the iron halide cations. Compared to the results for the singly charged and neutral iron chlorides, the agreement between the experimental and calculated energetics is poor for $FeCl^{2+}$ and $FeCl_3^{2+}$. Thus, the computed *IE*s are more than 1 eV larger than the measured Q_{min} values for these ions, while the data agree reasonably well for $FeCl_2^{2+}$ (see Table 4-6), a feature which will be discussed in more detail further below. The Q_{min} error bars in Table 4-6 include one standard deviation of several independent measurements using charge stripping of ionized toluene as a reference and the differences between vertical and adiabatic *IE*s are neglected, because the geometries of mono- and dications match each other within < 0.02 Å.

Table 4-6: Measured Q_{min} values (eV) and computed ionization energies (*IE*, eV) of $FeCl_m^+$ monocations (m = 1 - 3).

	Q_{min}	*IE*
$FeCl^+$	15.9 ± 0.4	17.19
$FeCl_2^+$	17.6 ± 0.7[a]	17.42
	15.2 ± 0.5[b]	13.72[c]
$FeCl_3^+$	16.0 ± 0.4	17.04

[a] EI of $FeCl_3$. [b] CI of $Fe(CO)_5/Cl_2$. [c] Here, the computed value refers to the adiabatic transition $Fe(Cl_2)^+ \rightarrow Fe(Cl_2)^{2+}$; the respective vertical ionization of $Fe(Cl_2)^+$ is expected to be higher in energy.

Another interesting aspect concerns the $FeCl_2^{2+}$ dication. In addition to the bent iron dichloride dication $FeCl_2^{2+}$ ($^5B_2$) with r_{FeCl} = 2.09 Å and α = 99°, the B3LYP calculations predict the existence of a second minimum with r_{FeCl} = 2.40 Å, α = 51°, and a r_{ClCl} distance of only 2.09 Å. This isomer is best described as molecular chlorine complexed to Fe^{2+} dication, i.e. $Fe(Cl_2)^{2+}$ ($^5A_1$). Moreover, the B3LYP calculations predict $Fe(Cl_2)^{2+}$ ($^5A_1$) to be 0.58 eV lower in energy than $FeCl_2^{2+}$ ($^5B_2$). Accordingly, we also searched for an isomeric species for the monocation and were able to locate a $Fe(Cl_2)^+$ ($^6A_1$) species with r_{FeCl} = 2.82 Å and r_{ClCl} = 2.06 Å on the sextet surface which is calculated to be 3.1 eV higher in energy than the $FeCl_2^+$ ($^6A_1$) ground state. Thus, the adiabatic *IE* of this isomer is predicted as *IE*($Fe(Cl_2)^+$) = 13.7 eV. Considering the significant difference in r_{FeCl} between $Fe(Cl_2)^+$ and $Fe(Cl_2)^{2+}$, the experimentally measured Q_{min} value of 15.2 ± 0.5 eV is in qualitative agreement with the theoretical findings.

Finally, the ion-source spectra are examined for the possible formation of long-lived $FeCl_m^{3+}$ trications (m = 1 - 3)[9,10] as well as $FeCl_m^{2-}$ dianions (m = 3, 4).[26] However, in none of these studies any indications are given for the formation of these multiply charged ions.

4.3 Redox Properties of $FeCl_m^n$ (m = 1 - 3, n = -1, 0, +1, +2)

The experimentally determined redox properties of the iron chlorides agree reasonably well with the literature thermochemistry (Table 4-1), if the differences between vertical and adiabatic electron transfer are taken into account.

The experimental value $\Delta E_{-CR^+}(FeCl_2^-)$ = 11.9 ± 0.8 eV is somewhat larger than the sum of the adiabatic EA_a and IE_a of $FeCl_2$ (11.1 eV). Nevertheless, the difference agrees nicely with the calculated energy difference of 0.81 eV between ground state $FeCl_2^+$ and the cation having the geometry of the anionic species (r_{FeCl} = 2.32 Å, α = 110°). In contrast, the experimental $\Delta E_{-CR^+}(FeCl_3^-)$ = 19.8 ± 1.1 eV is far beyond the sum of EA_a and IE_a (ca. 14.8 eV), suggesting that charge inversion of $FeCl_3^-$ leads to the formation of $FeCl_3^+$ in a high-lying electronically excited state. Apparently, generation of long-lived, ground state $FeCl_3^+$ is disfavored by the energy disposal in the keV collision in conjunction with the low Cl_2Fe^+-Cl bond strength (1.44 eV, Table 4-4).

For analyzing the charge inversion of cations, the net energy balances have to be considered, i.e. ΔE_{+CR-} = 2 • IE(Xe) - $RE_v(FeCl_m^+)$ - $EA_v(FeCl_m)$, where RE_v is the vertical recombination energy of the cation and EA_v is the vertical electron affinity of the neutral. Note, that the more likely mechanism, e.g. stepwise single-electron transfer, is assumed in the above equation. With IE(Xe) = 12.13 eV,[21] the measured set of data $\Delta E_{+CR-}(FeCl^+)$ = 14.7 ± 1.0 eV, $\Delta E_{+CR-}(FeCl_2^+)$ = 12.9 ± 0.8 eV, and $\Delta E_{+CR-}(FeCl_3^+)$ = 10.1 ± 0.9 eV translates into $RE_v(FeCl^+)$ + EA_v(FeCl) = 9.6 ± 1.0 eV, $RE_v(FeCl_2^+)$ + $EA_v(FeCl_2)$ = 11.4 ± 0.8 eV, and $RE_v(FeCl_3^+)$ + $EA_v(FeCl_3)$ = 14.2 ± 0.9 eV. These sums agree reasonably well with literature data. For the process $FeCl^+ \rightarrow FeCl^-$ the sum of IE_a and EA_a amounts to 9.43 eV (Table 4-1), and the energy difference due to vertical charge inversion of the cation is only 0.26 eV (Table 4-5).

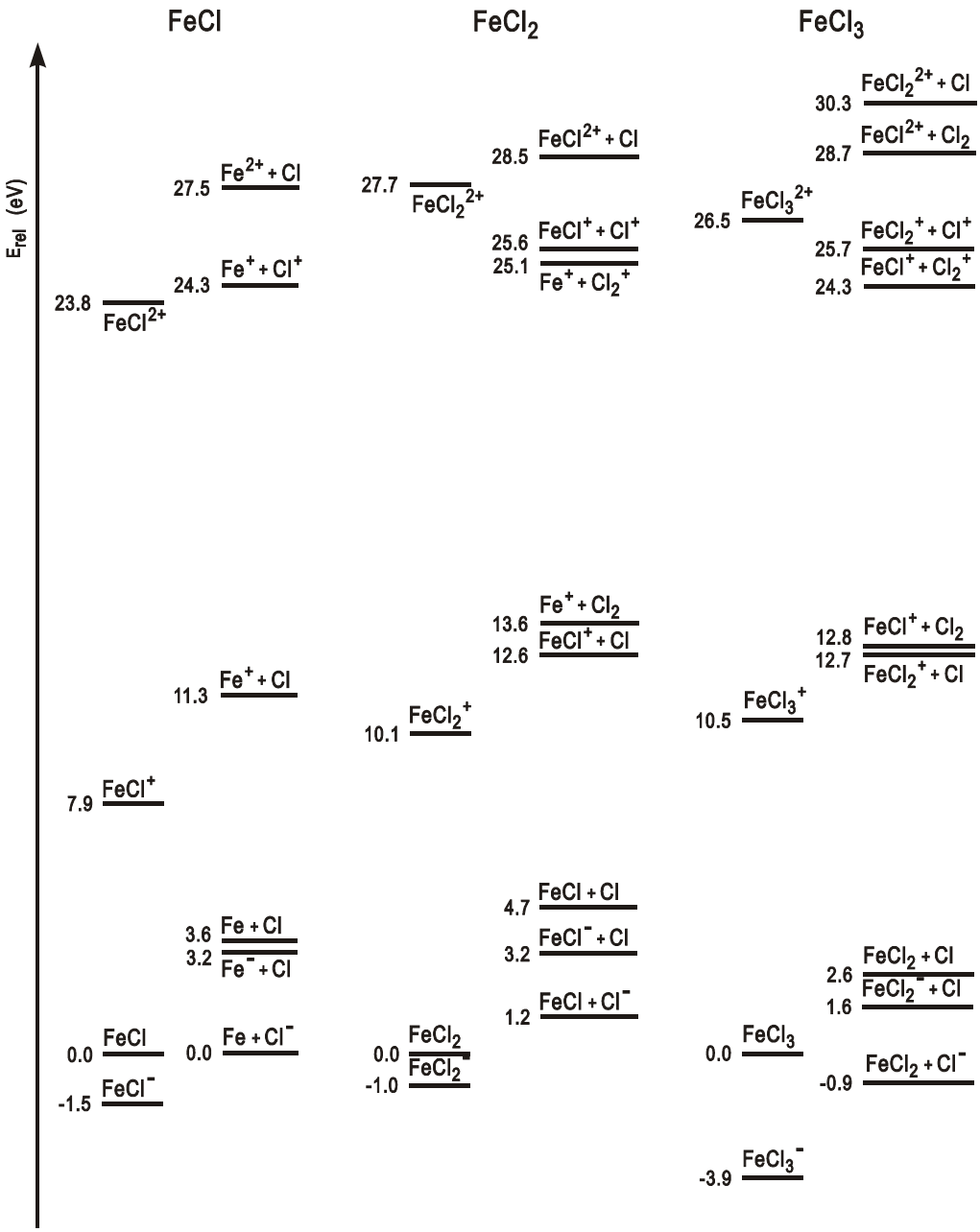

Figure 4-2: Redox properties and thermochemical stabilities (in eV) of $FeCl_m^n$ (m = 1 -3; n = -1, 0, +1, +2) species and relevant fragmentation channels relative to the respective neutral iron chlorides as obtained from experiments.

For $FeCl_2$, the experimental figure is also consistent with $IE_a + EA_a = 11.1$ eV, although a somewhat lower value would have been expected if only the vertical transition $FeCl_2^+ \rightarrow FeCl_2^-$ occurs. Finally, the experimental value for $FeCl_3^+$ agrees with $IE_a + EA_a = 14.8$ eV, and the additional energy demand of 0.80 eV associated with the vertical transition $FeCl_3^+ \rightarrow FeCl_3^-$. The differences between vertical and adiabatic electron transfer appear to be less important in the charge inversion of cations.[17] This finding is indeed plausible because the high-energy onsets of the $^+CR^-$ signals on the kinetic energy scale are due to the occurrence of

sequential electron transfer from the target to the projectile in two separate collisions rather than double electron transfer in a single collision event[5,12] provided that the transient neutral species have lifetimes in (or beyond) the microsecond regime.[14] This analysis of the redox properties (Figure 4-2) used one particular value which is not given in ref. 2b, i.e. the ionization energy of $FeCl_3$. For the time being, we rely on $IE(FeCl_3)$ = 10.93 eV as predicted by the B3LYP/6-311+G* calculations, although this value is likely to be slightly too large (see below).

Using thermochemical cycles with known properties of the fragments, the Q_{min} values allow to assess the dication stabilities with respect to the corresponding dissociation asymptotes.[25c] According to the measured $Q_{min}(FeCl^+)$ = 15.9 ± 0.4 eV, $FeCl^{2+}$ adds to the series of thermochemically stable, diatomic dications, of which most belong to the metal halide series.[9,10,27] Thus, $D(Fe^{2+}\text{-}Cl)$ = 3.7 ± 0.5 eV is significant and Coulomb explosion to $Fe^+ + Cl^+$ is calculated to be endothermic by 0.5 ± 0.5 eV (Figure 4-3). Considering that charge separation is hindered by a Coulombic barrier, whereas simple bond homolysis to afford Fe^{2+} can be assumed to have no barrier in excess of endothermicity, the sizable amount of the Fe^{2+} fragment in CE spectrum of $FeCl^{2+}$ (Figure 4-1a) finds a rationale. These results imply that the Fe-Cl bond strength is slightly larger in the dication than in the monocation. This conclusion is qualitatively consistent with the removal of a formally non-bonding electron in the transition $FeCl^+$ ($^5\Delta$) → $FeCl^{2+}$ ($^6\Sigma$).

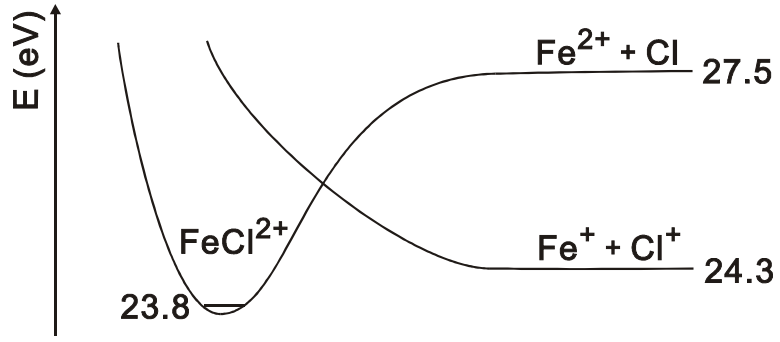

Figure 4-3: Schematic potential-energy curves for $FeCl^{2+}$ dication. The energies (in eV) are derived from the experimental data and are given relative to neutral FeCl.

The $FeCl_2^{2+}$ and $FeCl_3^{2+}$ dications are predicted to be metastable with respect to Coulomb explosion (Figure 4-2). Interestingly, the CE spectrum of $FeCl_2^{2+}$ (Figure 4-1b) does not only show charge separation into $FeCl^+ + Cl^+$ but also peaks due to $Fe^+ + Cl_2^+$. Thus, the dication surface allows for formation of the dichloride $FeCl_2^{2+}$ species as well as the $Fe(Cl_2)^{2+}$ isomer in which molecular chlorine is complexed to Fe^{2+}. In fact, the B3LYP calculations predict that

$Fe(Cl_2)^{2+}$ is more stable than $FeCl_2^{2+}$. This energetic situation of the dications as well as the associated fragmentation channels are shown in Figure 4-4.

The existence of two structural isomers of the dication also explains the significant dependence of the Q_{min} values from mode of ion generation. While EI of gaseous $FeCl_3$ is assumed to yield $FeCl_2^+$ cation exclusively, CI of $Fe(CO)_5/Cl_2$ may also lead to the formation of the isomeric $Fe(Cl_2)^+$ monocation via ligand-exchange, e.g. $Fe(CO)^+ + Cl_2 \rightarrow Fe(Cl_2)^+ + CO$. Even if this isomer is formed in only very small quantities, its propensity to undergo charge-stripping is much larger, because the energy required for ionization to the dication is significantly lower than for the iron dichloride. Thus, the B3LYP calculations predict $IE_a(Fe(Cl_2)^+) = 13.7$ eV and $IE_a(FeCl_2^+) = 17.4$ eV. Note that the stabilities of $Fe(Cl_2)^{+/2+}$ relative to $FeCl_2^{+/2+}$ may be underestimated by theory, because bonding of molecular chlorine is not properly described with B3LYP/6-311+G* (see footnote c to Table 4-4).

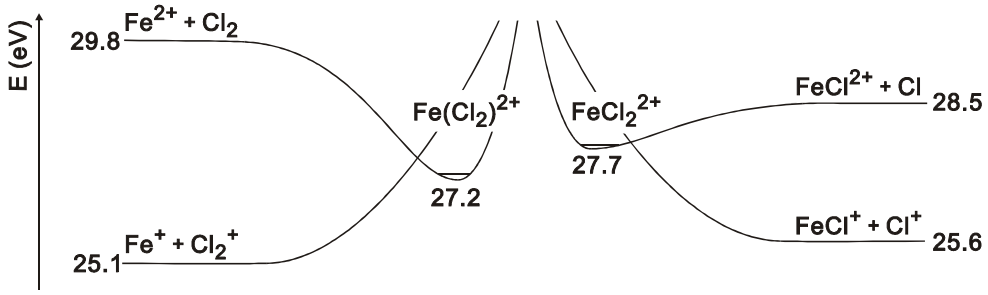

Figure 4-4: Schematic potential-energy curves (energies in eV) for the $Fe(Cl_2)^{2+}$ and $FeCl_2^{2+}$ dications. The area in which the curves intersect is arbitrarily chosen and actually unknown. The energies (in eV) are derived from the experimental data and are given relative to neutral $FeCl_2$; an exception is $Fe(Cl_2)^{2+}$ which was located according to the calculated stability difference between $Fe(Cl_2)^{2+}$ and $FeCl_2^{2+}$.

Finally, the significant deviation between the experimental and theoretical data for $FeCl^{2+}$ and $FeCl_3^{2+}$ should be discussed (Table 4-6). The measured Q_{min} values are more than 1 eV lower than the calculated figures. In fact, the calculations predict that $FeCl^{2+}$ dication is not thermochemically stable as implied by $Q_{min}(FeCl^+)$, but metastable with respect to the Coulomb explosion into Fe^+ and Cl^+. As noted above, Franck-Condon effects cannot account for these discrepancies, because the geometries of the mono- and dications are reasonably close to each other. Moreover, even if there were significant differences between the vertical and adiabatic ionization energies, these would result in Q_{min} values which are larger than the adiabatic *IE*s, while the opposite trend is observed. The deviation between theory and experiment is clearly beyond the previously reported uncertainty of the B3LYP approach in

calculating thermochemical properties of iron compounds [2b-d] and calls for more detailed consideration.

As far as the experiments are concerned, Q_{min} values lower than IE_a can only occur if a considerable fraction of the precursor monocations is electronically excited; and electronic excitation is indeed conceivable in ion generation using conventional ion sources. Nevertheless, the observation that the Q_{min} values of $FeCl^+$ and $FeCl_3^+$ are identical within experimental error under EI and CI conditions disfavors this option.[28] Note, however, that a secure thermalization of the precursor ions cannot be assumed in our experiments, and other approaches are required for a more definitive elaboration.

Notwithstanding these objections, some trends in the computational results indicate that the B3LYP approach may systematically underestimate dication stabilities in the present system. To illustrate this criticism, let us consider Tables 4–1 and 4–4 in some more detail. As stated above, on average B3LYP seems to perform quite well compared to the data given in Table 4-1, however, the deviations are not statistically spread, but deviate systematically. As previously outlined by Bauschlicher,[2c] this behavior can be attributed to the imperfect treatment of electron correlation with B3LYP resulting in a systematic overestimation of stabilities with increasing number of electrons in a given system. This pitfall results in an artificial stabilization of low oxidation states, and the trend is indeed clearly shown by comparison of the data given in Tables 4–1 and 4–4. The computed *EA*s are up to 0.4 eV larger with B3LYP, i.e. the anions are too stable. On the other hand, B3LYP slightly overestimates the IEs, i.e. the cations' stabilities are too low. The same conclusion can be drawn from the comparison of the data for the atomic fragments in the lower part of Table 4-4. With B3LYP/6-311+G*, the *EA* of chlorine is overestimated by 0.1 eV as compared to the experimental figure, and along this trend the ionization energies of Fe, Cl, and Cl_2 are about 0.1 eV too large. Accordingly, it is also not surprising that $IE(Fe^+)$ is overestimated by 0.33 eV with B3LYP, and that the computed energy demand for the double ionization $Fe \rightarrow Fe^{2+}$ is 0.42 eV above experiment. The present data base is much too limited to assess the generality of this trend; however, the good results obtained with the same combined experimental and computational approach on iron-oxo and iron-hydroxy compounds in Chapter 3 lead to the speculation, that the insufficient description of the chlorine atom and the iron-chlorine bonds is responsible for the for the problems encountered in this chapter. It needs to be noted in that respect, that B3LYP and related density functional methods show indeed some deficiencies in predicting *IE*s and *EA*s for main group elements.[29]

Finally, let us briefly address the formation of Cl_2^+ as a prominent fragment (> 10 %) in the $^+NR^+$ spectrum of $FeCl_3^+$ (Table 4-2) and the CE spectrum of $FeCl_2^{2+}$ (Figure 4-1b). In both cases, we believe that this particular fragment is due to reactions of electronically excited monocation states formed in the electron-transfer processes involved. Let us begin with analyzing the situation for $FeCl_3^+$. If the Cl_2^+ fragment in the $^+NR^+$ spectrum of $FeCl_3^+$ were due to collisional activation of $FeCl_3^+$ ground state after reionization, the same fragment would be expected upon collisional activation of $FeCl_3^+$. In the corresponding CA and CS spectra of $FeCl_3^+$, however, the Cl_2^+ signals are negligible. Further, as described above formation of molecular chlorine by dissociation of neutral $FeCl_3$ is disfavored by the analysis of the $^-NIDD^+$ spectrum of $FeCl_3^-$. Generation of electronically excited $FeCl_3^+$ is supported by the large value of ΔE_{-CR^+} = 19.8 ± 1.1 eV determined for charge inversion of $FeCl_3^-$, which is by about 5 eV above the energy demand of the corresponding adiabatic transition $FeCl_3^- \rightarrow FeCl_3^+$. An even more direct hint for the formation of excited monocation states giving rise to the Cl_2^+ fragment is the pronounced central component of the Cl_2^+ signal in the CE spectrum of $FeCl_2^{2+}$ (Figure 4-1b). Because this component of the peak is not broadened due to Coulomb explosion, it must originate from a monocation species. The latter is unlikely to correspond to $FeCl_2^+$ ground state, because otherwise the Cl_2^+ fragment is expected to appear in the CA and CS spectra of $FeCl_2^+$ as well, which is not the case. Moreover, the similar magnitudes of the central components of the Fe^+ and Cl_2^+ signals in Figure 4-1b conflict with thermochemistry, which implies a large preference for formation of Fe^+ instead of Cl_2^+, i.e. IE(Fe) = 7.89 eV versus $IE(Cl_2)$ = 11.48 eV. Similar arguments apply if the ground state of the $Fe(Cl_2)^+$ isomer is considered. Therefore, we remain with the suggestion that an electronically excited monocation is inter alia formed upon charge exchange of $FeCl_2^{2+}$ dication with helium.

4.4 Conclusions

Electron transfer from or to iron chlorides can be probed using tandem mass spectrometry, thereby revealing the stabilities and possible dissociation processes ranging from the monoanions to the dications. In addition, energy-resolved experiments allow for an evaluation of gas-phase thermochemistry, although the precision is limited. Energy-resolved charge-stripping is demonstrated to be one of few fundamental methods to determine dication energetics;[8] particular significance is achieved if the differences between vertical and adiabatic ionization are taken into account. For $FeCl_2^n$ (n = +1, +2), charge stripping even

provides firm evidence for the existence of isomeric $Fe(Cl_2)^n$ species, at both the mono- and dication surfaces.

Nevertheless, there remain some uncertainties with respect to the conversion of measured Q_{min} values into adiabatic ionization energies. In particular, ion production in a conventional ion source cannot safely exclude the formation of electronically excited monocations, which would lead to Q_{min} values lower than the adiabatic ionization energies of the monocations. On the other hand, the B3LYP approach shows problems in properly describing Cl-Cl and Fe-Cl bonds, such that sizable discrepancies between the theoretically predicted and experimentally measured ionization energies of $FeCl_m^+$ occur and further experimental and theoretical efforts are indicated. Considering the volatility of $FeCl_3$ as well as the minor geometry differences between the mono- and dications, photoionization studies of $FeCl_3$ could be particularly helpful and could possibly provide additional anchor points for the accurate calibration of the energy scales employed in charge-stripping experiments.

References

[1] (a) M. Tanimoto, S. Saito, T. Okabayashi *Chem. Phys. Lett.* **1985**, *242*, 153. (b) M. L. Mandich, M. L. Steigerwald, W. D. Reents Jr. *J. Am. Chem. Soc.* **1986**, *108*, 6197. (c) A. E. Alvarado-Swaisgood, J. F. Harrison *J. Phys. Chem.* **1988**, *92*, 5896. (d) E. R. Fisher, R. H. Schultz, P. B. Armentrout *J. Phys. Chem.* **1989**, *93*, 7382. (e) R. Bakthiar, J. J. Drader, D. B. Jacobson *Org. Mass Spectrom.* **1993**, *28*, 797. (f) D. Schröder, J. Hrušák, H. Schwarz *Ber. Bunsenges. Phys. Chem.* **1993**, *97*, 1085.

[2] (a) D. L. Hildenbrand *J. Chem. Phys.* **1995**, *103*, 2634. (b) R. D. Bach, D. S. Shobe, H. B. Schlegel, C. J. Nagel *J. Phys. Chem.* **1996**, *100*, 8770. (c) C. W. Bauschlicher *Chem. Phys.* **1996**, *211*, 163. (d) M. N. Glukhovtsev, R. D. Bach, C. J. Nagel *J. Phys. Chem. A* **1997**, *101*, 316. (e) S. G. Wang, W. H. E. Schwarz *J. Chem. Phys.* **1998**, *109*, 7252.

[3] M. M. Bursey *Mass Spectrom. Rev.* **1990**, *9*, 555.

[4] N. Goldberg, H. Schwarz *Acc. Chem. Res.* **1994**, *27*, 347.

[5] C. A. Schalley, G. Hornung, D. Schröder, H. Schwarz *Int. J. Mass Spectrom.* **1998**, *172/173*, 181.

[6] C. A. Schalley, G. Hornung, D. Schröder, H. Schwarz *Chem. Soc. Rev.* **1998**, *27*, 91.

[7] T. Ast *Adv. Mass Spectrom. A* **1980**, *8*, 555.

[8] K. Vékey *Mass Spectrom. Rev.* **1995**, *14*, 195, and references cited therein.

[9] D. Schröder, J.N. Harvey, H. Schwarz *J. Phys. Chem. A* **1998**, *21*, 3639.

[10] D. Schröder, M. Diefenbach, T. M. Klapötke, H. Schwarz *Angew. Chem. Int. Ed. Engl.* **1999**, *38*, 137.

[11] J. N. Harvey, C. Heinemann, A. Fiedler, D. Schröder, H. Schwarz *Chem. Eur. J.* **1996**, *2*, 1230.

[12] D. Schröder, J. N. Harvey, M. Aschi, H. Schwarz *J. Chem. Phys.* **1998**, *108*, 8446.

[13] D. Schröder, C. A. Schalley, N. Goldberg, J. Hrušák, H. Schwarz *Chem. Eur. J.* **1996**, *2*, 1235.

[14] D. Schröder, C. Heinemann, H. Schwarz, J. N. Harvey, S. Dua, S. J. Blanskby, J. H. Bowie *Chem. Eur. J.* **1998**, *4*, 2550.

[15] N. Jeffreys, I. W. Griffiths, D. E. Parry, F. M. Harris *Int. J. Mass Spectrom. Ion Processes* **1997**, *164*, 133, and references cited therein.

[16] K. Lammertsma, P. v. R. Schleyer, H. Schwarz *Angew. Chem. Int. Ed. Engl.* **1989**, *28*, 1321.

[17] J. N. Harvey, D. Schröder, H. Schwarz *Bull. Soc. Chim. Belg.* **1997**, *106*, 447.

[18] (a) A. J. H. Wachters *J. Chem. Phys.* **1972**, *52*, 1033. (b) P. J. Hay *J. Chem. Phys.* **1977**, *66*, 4377. (c) K. Raghavachari, G. W. Trucks *J. Chem. Phys.* **1989**, *91*, 1062.

[19] O. Hübner, V. Termath, A. Berning, J. Sauer *Chem. Phys. Lett.* **1998**, *294*, 37.

[20] D. Schröder, H. Schwarz Int. J. Mass Spectrom. Ion Processes **1995**, 146/147, 183.

[21] S. G. Lias, J. E. Bartmess, J. F. Liebman, J. L. Holmes, R. D. Levin, W. G. Mallard Gas Phase Ion and Neutral Thermochemistry, *J. Phys. Chem. Ref. Data* **1988**, *17*, Suppl. 1.

[22] B. A. Rumpf, C. E. Allison, P. J. Derrick *Org. Mass. Spectrom.* **1986**, *21*, 295.

[23] For an instrument with much higher resolution, see: A. G. Brenton, C. M. Lock *Rapid Commun. Mass Spectrom.* **1997**, *11*, 1155.

[24] M. Hargittai, N. Y. Subbotina, M. Kolonits, A. G. Gershikov *J. Chem. Phys.* **1991**, *94*, 7278.

[25] (a) S. M. McCullough, A. D. Jones, C. B. Lebrilla *Int. J. Mass Spectrom. Ion Processes* 1991, 107, 545. (b) S. McCullough-Catalano, C. B. Lebrilla *J. Am. Chem. Soc.* **1993**, *115*, 1441. (c) P. Dai, S. McCullough-Catalano, M. Boulton, A. D. Jones, C. B. Lebrilla *Int. J. Mass Spectrom. Ion Processes* **1995**, *144*, 67.

[26] A. I. Boldyrev, M. Gutowski, J. Simons *Acc. Chem. Res.* **1996**, *29*, 497.

[27] M. Kolbuszewski, J. S. Wright, R. J. Buenker *J. Chem. Phys.* **1995**, *102*, 7519

[28] C. Heinemann, D. Schröder, H. Schwarz *J. Phys. Chem.* **1995**, *99*, 16195, and references cited therein.

[29] L. A. Curtiss, P. C. Redfern, K. Raghavachari, J. A. Pople *J. Chem. Phys.* **1998**, *109*, 42, and references cited therein.

5 The Reactivity of FeS^+ Cations Towards Dihydrogen and Methane*

The unique properties of iron sulfides are exploited in metallurgy, industrial catalysis, and biology. In addition, oxidic and sulfidic iron ore is the major source for the industrial production of iron. In catalysis, transition-metal sulfides in general are at the focus of research because they show similar turn-over rates as their oxygen analogs, but are much less sensitive to poisoning. Some applications include hydrogenation-catalysts, as well as catalysts for the hydrodesulfurization and hydrodenitrogenation of mineral oils.[1] Last but not least, in biology both homonuclear and heteronuclear iron-sulfide cores are found as reactive sites in many enzymes, including hydrogenases, sulfite reductases, and nitrogenases.[2-5] Therefore, the importance of iron-sulfides can hardly be overrated; accordingly, extensive research is carried out on these systems.

This chapter aims at contributing towards a better understanding of the H–H and C–H bond activation by iron sulfide. A more detailed understanding of the fundamental processes involved in these activations may shine some light on the chemistry and the role of electronic structures in more complex systems.[6] Despite the relevance of transition-metal sulfides, relatively few gas-phase studies have been carried out on these systems, although the research activity increases rapidly.[7-10] The FeS^+ cation investigated in this chapter can be regarded as the smallest possible model system to mimic larger iron-clusters; understanding its reactivity is therefore of extended interest. In the following, the reactions of FeS^+ with molecular hydrogen and with methane are presented.

5.1 Computational Details

The computational part of this section is carried out using the B3LYP approach and the 6-311+G* basis set as implemented in the Gaussian94 program package.[11] This basis consists of the 6-311G basis for first-row atoms[12] and the Wachters-Hay all electron basis set for iron, using the scaling factors of Raghavachari and Trucks.[13] A set of single polarization functions is requested by the *-notation and the +-notation adds diffuse functions to the basis set.[14]

* Part of this chapter has already been published: S. Bärsch, I. Kretzschmar, D. Schröder, H. Schwarz, P. B. Armentrout *J. Chem. Phys. A* **1999**, *103*, 5925.

The species of interest are calculated in several conceivable spin multiplicities. Note in that respect, that for the sake of simplicity the notation used throughout this chapter gives the spin multiplicities as superscripts preceding the formula while neglecting orbital symmetries, e.g. the sextet ground state of FeS^+ ($^6\Sigma^+$) is referred to as $^6FeS^+$.

5.2 The Reaction of FeS^+ with Molecular Hydrogen[15]

The prototype reaction of FeS^+ with molecular hydrogen is the simplest model for the chemical behavior of iron sulfide in σ-bond activation processes. Here, a study is reported on the FeS^+/H_2-system using two advanced mass-spectrometric methods, i.e., the guided-ion beam (GIB) technique as well as Fourier-transform ion-cyclotron resonance (FT-ICR), combined with a computational study using density functional theory (DFT).

5.2.1 GIB Experiments

In the GIB experiments, deuterium is used instead of molecular hydrogen to reduce the mass overlap which occurs due to the limited mass resolution of the quadrupole analyzer. In contrast, the FT-ICR studies as well as the theoretical treatment refer to the protio variants. Owing to the use of deuterium instead of hydrogen the GIB reaction thresholds differ slightly as compared to the unlabeled system. For comparison with the protio system, the calculated zero-point energies of the labeled and unlabeled species are considered, and both, the thresholds for the FeS^+/D_2- and the ZPVE corrected thresholds for the FeS^+/H_2-system are given in Scheme 5-1. The reaction of FeS^+ with D_2 yields Fe^+, FeD^+, and $FeSD^+$ as ionic products according to Equations 5–1 - 5–3 (Scheme 5-1). The product distribution resembles that detected in the reaction of FeO^+ with molecular hydrogen (H_2, HD, and D_2) where the corresponding products Fe^+, FeH^+ (FeD^+), and $FeOH^+$ ($FeOD^+$) are observed.[26a] The thermochemistry indicated in the equations is calculated using the 0 K heats of formation and bond dissociation energies from the literature and refers to the formation of the species in their ground states.[16,18,21] The thermochemistry given in parentheses refers to the FeS^+/H_2-system, needed further below for comparison with FT-ICR data and theoretical results.

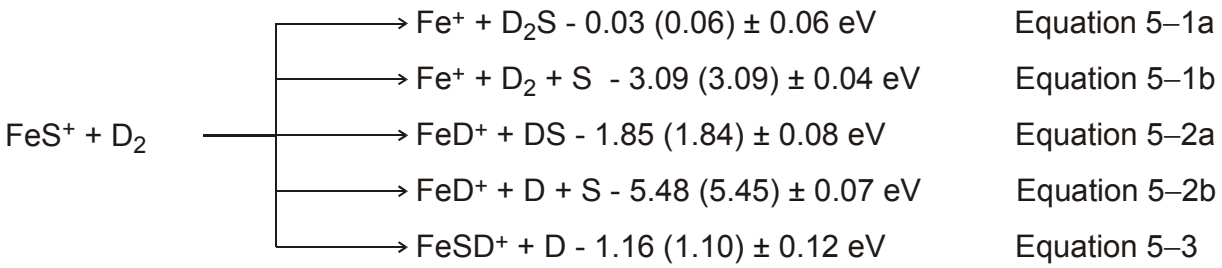

Scheme 5-1: Products observed in the reaction $FeS^+ + D_2$.

The cross sections for all three ionic products are depicted in Figure 5-1. The least endothermic process observed is formation of Fe^+, Equation 5–1. The Fe^+ cross section rises from an apparent threshold of about 0.6 eV, increases more slowly between 1.3 and 1.8 eV but again more rapidly above 1.8 eV. Then, the Fe^+ cross section peaks at about 2.8 eV and rises again above 3.5 eV. Analysis of the threshold region yields E_0 = 0.64 ± 0.11 eV (Table 5-1), i.e. ca. 0.6 eV above the thermochemical threshold of Equation 5–1a. This result implies that the measured threshold of the Fe^+ channel reflects a kinetic barrier rather than the thermochemical threshold; this aspect will be evaluated in more detail below. The change in slope at about 1.5 eV coincides with the appearance of the $FeSD^+$ product channel, pointing to a competition between both channels. The slight increase of $\sigma(Fe^+)$ above 3.5 eV can be assigned to simple collision-induced dissociation (CID) of FeS^+, Equation 5–1b.

Table 5-1: Summary of parameters for the fits of the cross sections according to Equation 2-15. The E_0 values are the average of several threshold fits with uncertainties of one standard deviation.

reaction	E_0, eV	σ_0	n
$FeS^+ + D_2 \rightarrow Fe^+ + D_2S$	0.64 ± 0.11	0.91 ± 0.30	1.29 ± 0.28
$FeS^+ + D_2 \rightarrow FeD^+ + DS$	1.82 ± 0.35	0.42 ± 0.20	1.16 ± 0.51
$FeS^+ + D_2 \rightarrow FeSD^+ + D$	1.52 ± 0.14	3.86 ± 0.35	1.19 ± 0.13

Formation of FeD^+ is the least efficient reaction channel. Its formation according to Equation 5–2b can be ruled out immediately due to its high thermodynamic threshold, which is beyond the range of energies studied. Thus, the experimental threshold is assigned to Equation 5–2a, along with formation of a SH-radical as the corresponding neutral. Analysis of the FeD^+ cross section according to the procedure outlined in Chapter 2 yields E_0 = 1.82 ± 0.35 eV (Table 5-1). This agrees well with the threshold of 1.85 ± 0.08 eV calculated from literature thermochemistry.[17] The threshold difference between the protio- and deutero

systems is small as the contributions from H_2 and D_2 versus FeH^+ + HS and FeD^+ + DS cancel each other to a large extent**.** Taking calculated ZPVEs into account, the threshold of the protio variant is given as E_0 = 1.82 ± 0.35 eV.

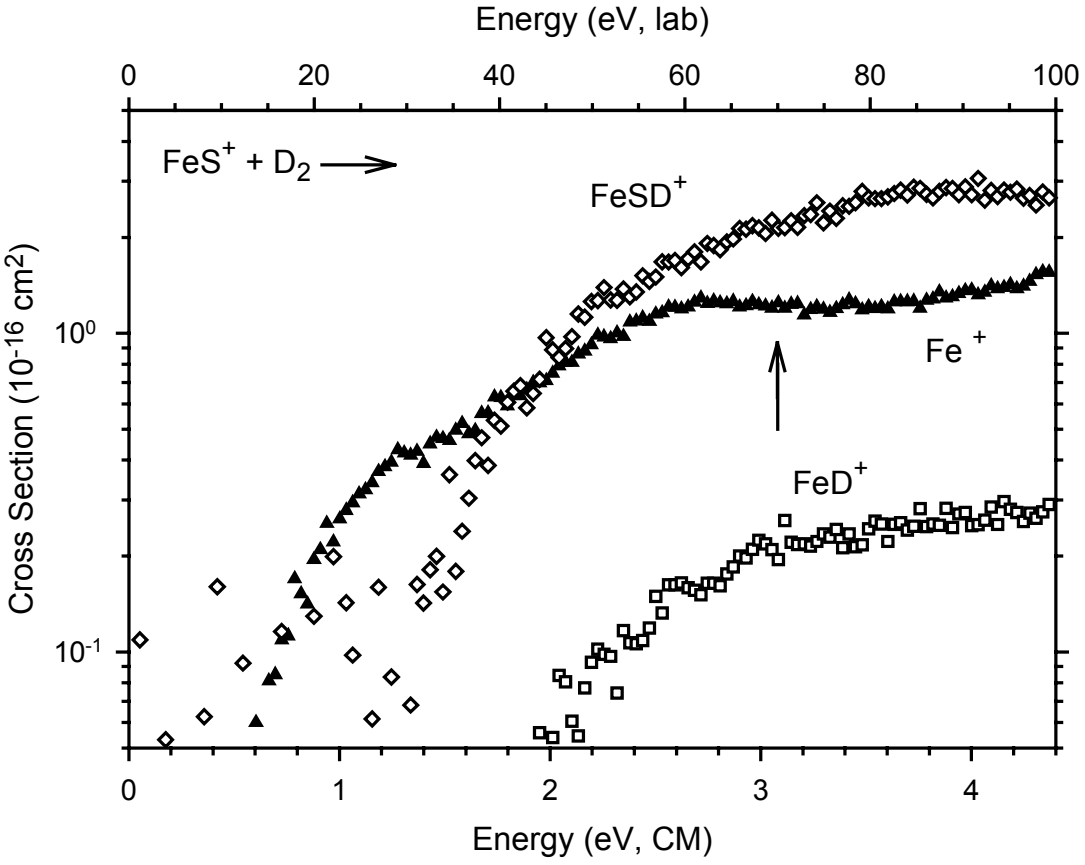

Figure 5-1: Product cross sections for the reaction of FeS^+ and D_2 to form Fe^+ (▲), FeD^+ (□), and $FeSD^+$ (◊) as a function of kinetic energy in the center-of-mass (lower axis) and laboratory (upper axis) frames. The arrow marks the Fe^+-S bond energy at 3.09 ± 0.04 eV.

The $FeSD^+$ channel rises from an apparent threshold of about 1.4 eV and peaks at about 4.0 eV. The formation of $FeSD^+$ is the most efficient channel observed above 2 eV. However, mass overlap with the close-lying parent-ion beam (FeS^+) causes a low signal/noise ratio in the data, especially at low interaction energies. Therefore, a minor, less endothermic contribution to the $FeSD^+$ channel with a cross section < 10^{-17} cm^2 cannot be excluded at low interaction energies. Analysis of the apparent threshold region yields E_0 = 1.52 ± 0.14 eV (Table 5-1) which translates into D_0(Fe^+-SD) = 57.6 ± 3.4 kcal/mol and D_0(Fe^+-SH) = 56.9 ± 3.4 kcal/mol for the protio variant, respectively.

5.2.2 FT-ICR Experiments

Some quite general thermochemical considerations indicate doubt in the assignment of the above presented GIB results as thermodynamic thresholds and the corresponding values for $D_0(Fe^+\text{-SD})$ and $D_0(Fe^+\text{-SH})$. For example, an Fe^+-SH bond energy of 56.9 ± 3.4 kcal/mol would be significantly smaller than $D_0(Fe^+\text{-S})$ = 71.3 ± 0.9 kcal/mol.[18] Exactly the opposite trend is observed for the $FeO^+/FeOH^+$ couple,[19] where the bond strength of Fe^+–OH exceeds that of Fe^+–O by 7.4 kcal/mol. Further, the NH and NH_2 fragments, isoelectronic with O and OH, respectively, also show an increase in going from Fe^+–NH (69.0 ± 2.0 kcal/mol)[20] to Fe^+–NH_2 (73.9 ± 2.3 kcal/mol).[19] However, a slight decrease from $D_0(Fe^+\text{-S})$ to $D_0(Fe^+\text{-SH})$ may occur, considering the general differences between second- and third-row elements. For example, the differences[21] between the first and second bond strengths in the element hydrides (EH_n), i.e. $D_0(H_{n-1}E\text{-H})$ and $D_0(H_{n-2}E^{\bullet}\text{-H})$, amount to 16.8 kcal/mol for E = O (n = 2) and 10.9 kcal/mol for E = N (n = 3), compared to only 6.8 kcal/mol for E = S (n = 2). Overall, however, a decrease from $D_0(Fe^+\text{-S})$ = 71.3 ± 0.9 kcal/mol to $D_0(Fe^+\text{-SH})$ = 56.9 ± 3.4 kcal/mol is unexpected and thus indicates an anomalous trend for the iron/sulfur bonding. Therefore, the bond-dissociation energy $D_0(Fe^+\text{-SH})$ is evaluated by applying the bracketing technique and performing equilibrium measurements in the FT-ICR instrument.

Ligand exchange is one obvious way to obtain upper and lower bounds for the Fe^+–SH bond strength. To this end, the ligand-exchange reactions $FeX^+ + H_2S \rightarrow FeSH^+ + XH$ (X = OH, Cl, and Br; Equations 5–4 - 5–6 in Scheme 5-2) are investigated by FT-ICR mass spectrometry.

$FeOH^+ + H_2S$	$\rightarrow$	$FeSH^+ + H_2O$	Equation 5-4
$FeCl^+ + H_2S$	$\rightarrow$	$FeSH^+ + HCl$	Equation 5-5
$FeBr^+ + H_2S$	$\rightarrow$	$FeSH^+ + HBr$	Equation 5-6

Scheme 5-2: Bracketing reactions under investigation in the FT-ICR to establish the $FeSH^+$ thermochemistry.

Equation 5-4 occurs with a moderate efficiency (k/k_{capt} = 0.3),[22] while the use of chlorine as a ligand according to Equation 5-5, causes the reaction efficiency to drop by an order of magnitude (k/k_{capt} = 0.03). The exchange of the bromine ligand for SH as suggested in Equation 5-6 is not observed within the experimental accuracy (k/k_{capt} < 0.0005). Given the bond dissociation energies of Fe^+–OH, Fe^+–Cl, and Fe^+–Br of 87.5 ± 2.9, 79.6 ± 2.5, and 76.1

± 5.0 kcal/mol, [17,19,23-25] a bracket of 59.5 ± 3.0 kcal/mol ≤ $D_0(Fe^+\text{-SH})$ ≤ 79.4 ± 5.0 kcal/mol is provided by Equations 5–4 and 5–6. Because of fortunate circumstances, $D_0(Fe^+\text{-SH})$ can be further refined by consideration of Equation 5-5. The low reaction rate of Equation 5-5 may be rationalized in two ways: (i) either the reaction is slightly endothermic, or (ii) a significant but surmountable barrier is involved. This ambiguity can be resolved by conducting FT-ICR equilibrium measurements. In order to establish an equilibrium, $FeSH^+$ is trapped in ca. 1:2 and 1:1 mixtures of H_2S and HCl at different total pressures in the range of 5×10^{-9} to 2×10^{-8} mbar.

The analysis of these experiments yields an equilibrium constant K_{eq} = 0.6 ± 0.2 and thus $\Delta_r G_{298}$ = 0.3 ± 0.2 kcal/mol. $\Delta_r G_{298}$ is converted into $\Delta_r H_{298}$ = 0.7 ± 0.2 kcal/mol using $\Delta_r S_{298}$ = 1.5 cal/mol K derived from the calculated entropies of the involved species. Further, $\Delta_r H_{298}$ is transformed to 0 K thermochemistry by use of the calculated enthalpy corrections, which leads to $\Delta_r H_0$ = 1.3 ± 0.2 kcal/mol. Consequently, $D_0(Fe^+\text{-SH})$ = 66.0 ± 2.6 kcal/mol and $\Delta_f H_0(FeSH^+)$ = 248.3 ± 3.2 kcal/mol are derived.

Combined with literature thermochemistry, $D_0(Fe^+\text{-SH})$ leads to $\Delta_r H_0$ = 26.7 ± 2.8 kcal/mol for Equation 5–3, which is in obvious disagreement with E_0 = 1.49 ± 0.14 eV (34.4 ± 3.2 kcal/mol) as derived from GIB measurements with H/D correction. There are several ways to rationalize this discrepancy. One possibility is that different products are formed in the two experimental approaches, i.e., either $FeSH^+$ vs. $HFeS^+$ isomers and/or different electronic states. However, if the same product is formed in the same state in both experiments, the only reasonable explanation would be the presence of a significant barrier in the reaction described by Equation 5–3.

5.2.3 The PES of the FeS^+/H_2-System

Clarification of the origin of the discrepancies between the FT-ICR and GIB results for $D_0(Fe^+\text{-SH})$ can be achieved by consulting the calculated potential-energy surface for the FeS^+/H_2-system. Note, that in analogy to the related FeO^+/H_2 system,[25,26] tunneling phenomena are neglected in the present system.

Two conceivable mechanisms are considered after formation of the encounter complex $(H_2)FeS^+$, **1** (Scheme 5-3).[26b,27] (i) Concerted 1,1-addition of dihydrogen to the sulfur atom to form the $Fe(SH_2)^+$ product complex, **3**. (ii) 1,2-Addition across the Fe-S bond leading initially to the insertion intermediate $HFeSH^+$, **2**, which subsequently proceeds to $Fe(SH_2)^+$ via

hydrogen migration (**2** → TS**2**/**3** → **3**). In the following, structures, symmetries, and electronic states of all stationary points are presented and subsequently, both mechanistic schemes are discussed in detail. The error of the calculations is estimated to be ± 6.0 kcal/mol.[28]

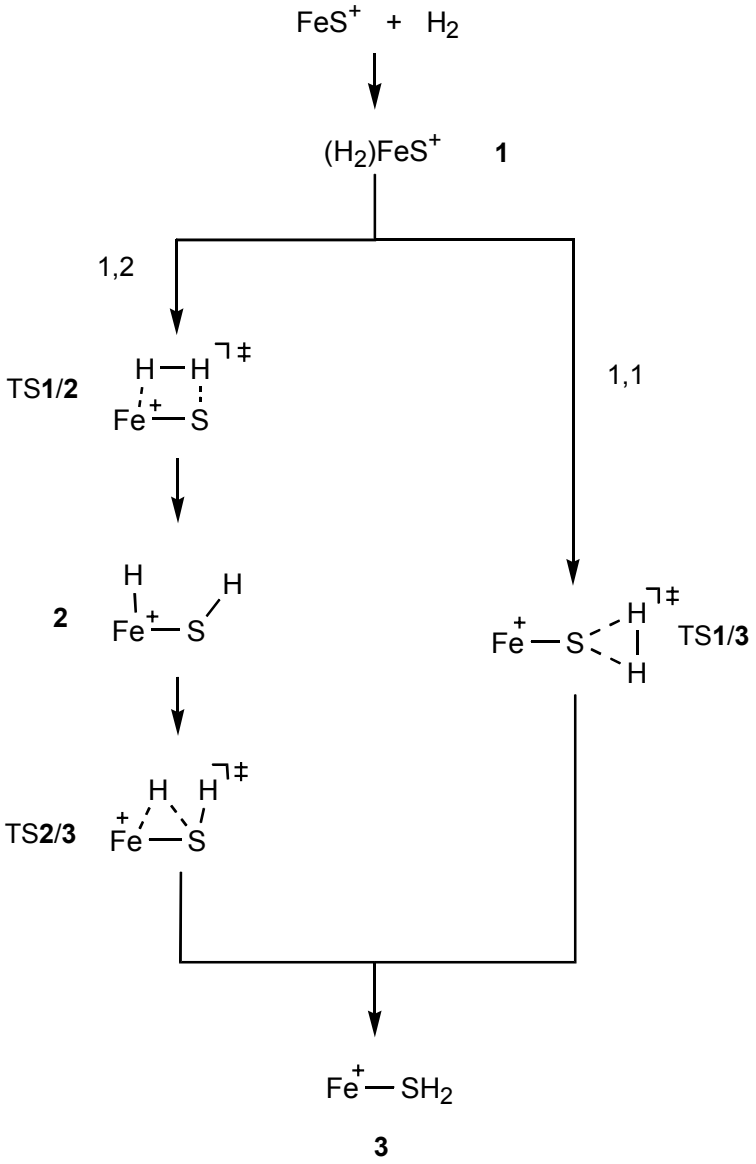

Scheme 5-3: Conceivable reaction mechanisms for the reaction of FeS^+ with molecular hydrogen.

Reactants. In agreement with earlier results,[9f,29] FeS^+ shows a $^6\Sigma^+$ ground-state with a $^4\Pi$ state 5.5 kcal/mol higher in energy. The $^6\Sigma^+$ state is represented by a $1\sigma^2 2\sigma^2 1\pi^4 1\delta^2 2\pi^2 3\sigma^1$ occupation of the valence orbitals in a one-configuration picture.[26c,30] B3LYP/6-311+G* predicts the r_{FeS} bond lengths as 2.06 Å ($^6FeS^+$) and 2.11 Å ($^4FeS^+$), respectively. H_2 has a $^1\Sigma_g^+$ ground state with a bond length (r_{HH}) of 0.74 Å. In the following, all calculated

energetics will be given with respect to the $^6FeS^+ + {}^1H_2$ asymptote (E_{rel} = 0.0 kcal/mol), if not stated otherwise.

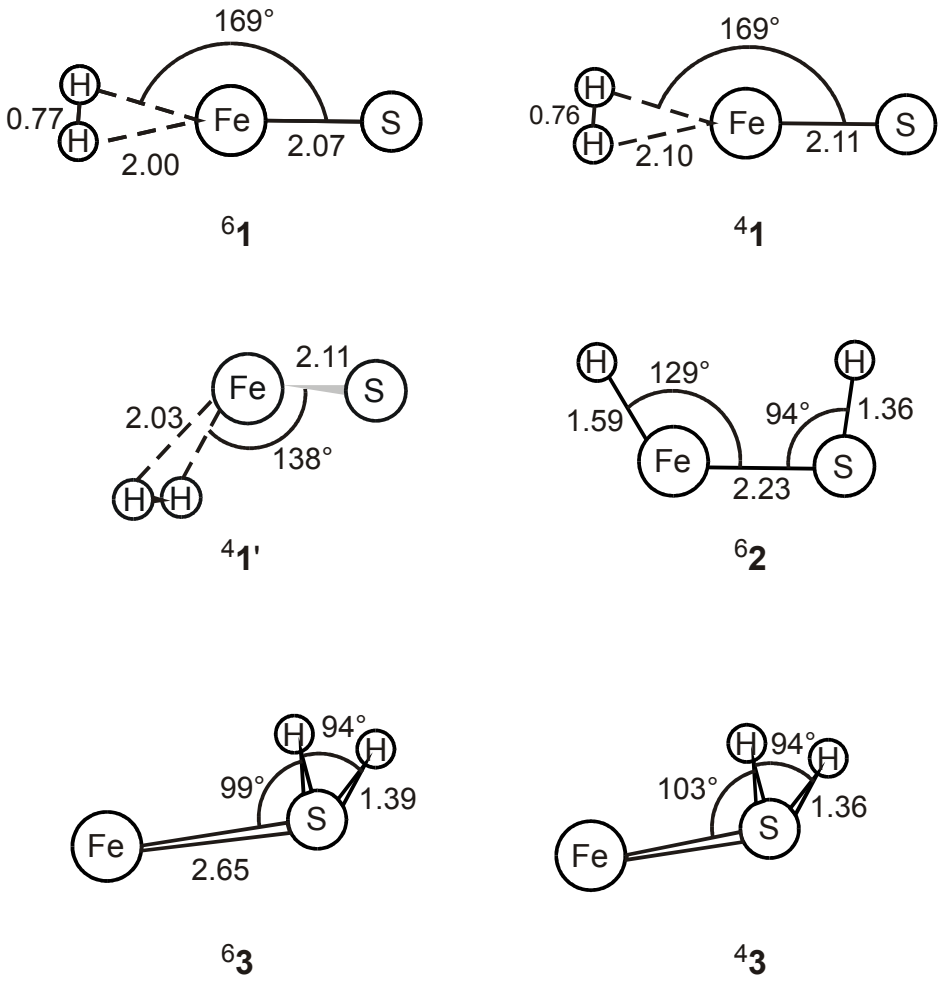

Chart 5-1: Minima found along the $FeS^+ + H_2$ reaction coordinate. Bond lengths are given in Å and angles in degree.

Minima. Three sets of minima are located for the FeS^+/H_2-system starting from $FeS^+ + H_2$. The first minimum (Chart 5-1) is the encounter complex **1** with a $^6A_1$ ground-state, ^{6}**1**. It shows a planar C_{2v} geometry where the intact H_2 molecule (r_{HH} = 0.77 Å) approaches the iron atom side-on along the extended FeS-axis. This coordination seems reasonable as most of the charge in the FeS^+ cation is localized at the iron center (q_{Fe}: +0.64) and the bonding in the encounter complex is determined by ion/induced-dipole interactions. Accordingly, ^{6}**1** is only 8.9 kcal/mol below the entrance channel. The analogous quartet minimum ^{4}**1** is not perfectly planar, but exhibits a ^{4}A' state in C_s-symmetry. It is located 5.5 kcal/mol above the corresponding sextet ground-state ^{6}**1**. A second bent structure ^{4}**1'** in a ^{4}A" state shows the H_2 again approaching the iron atom side-on but from below the FeS^+ axis, thereby forming two

HFeS angles of 138°. This structure lies only 0.3 kcal/mol above ^{4}**1**. Note, that the small energy separation of ^{4}**1** and ^{4}**1'** prevents a definitive assignment of the quartet minimum and implies that the quartet surface is quite flat with respect to the rotation of the H_2 unit around the iron atom.

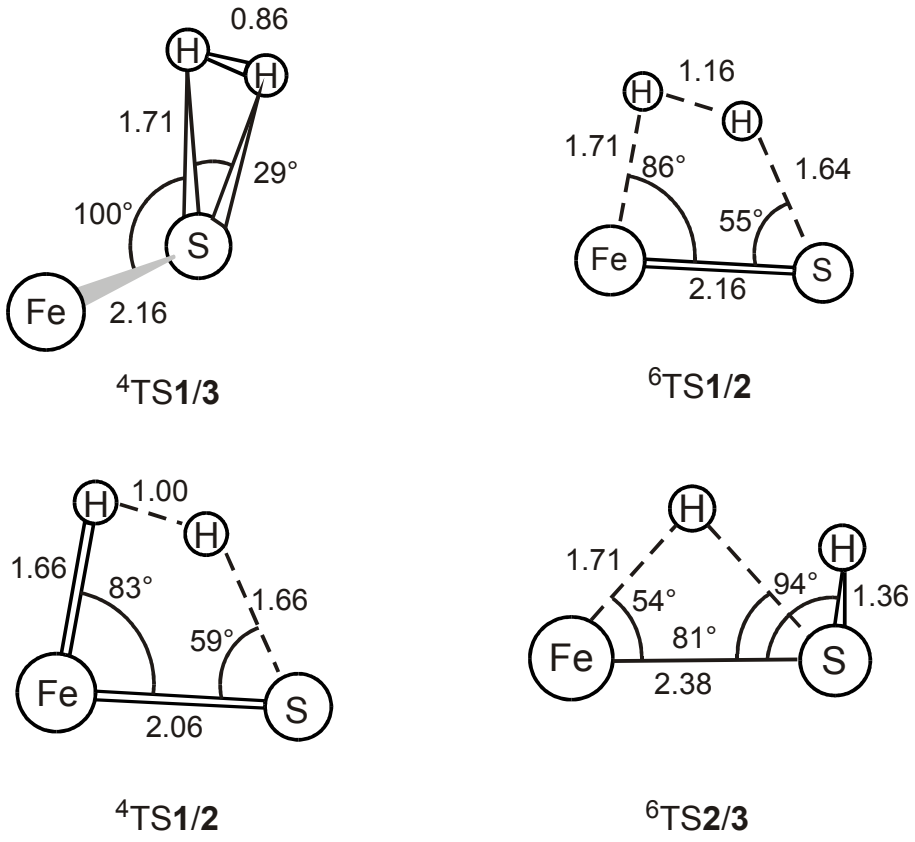

Chart 5-2: Transition states found along the $FeS^+ + H_2$ reaction coordinate. Bond lengths are given in Å and angles in degree.

The next minimum on the sextet surface is the 1,2-addition product, ^{6}**2**, calculated in a ^{6}A' state. It has a planar structure with a considerably elongated FeS-bond as compared to ^{6}**1** and free FeS^+ (2.23 vs 2.07 Å and 2.06 Å, respectively). The rationale for the bond lengthening is the formation of the two bonds to hydrogen which causes a reduction of the Fe-S bond order. No comparable minimum structure is found on the quartet surface (see below). The third type of minima are the C_s-symmetric $Fe(SH_2)^+$ complexes ^{4}**3** and ^{6}**3** in their respective ^{4}A" and ^{6}A" spin states. The geometries of the H_2S moieties in these two complexes are similar to each other and resemble that of free H_2S (1.35 Å, 93°). The Fe-S bond length is of particular interest, in that the quartet state has a much closer contact than the sextet (2.34 vs 2.65 Å). In addition, a planar $Fe(SH_2)^+$ complex with C_{2v}-symmetry in a $^6B_2$ state, ^{6}**3'**, (not shown) is located 8.9 kcal/mol above ^{6}**3**. While one might intuitively expect the

H_2S dipole to be aligned with the positive charge on Fe^+, the existence of similar bent minima has previously been reported for $M(H_2O)^+$ and $M(H_2S)^+$ complexes and is traced back to the balance between electrostatic and covalent bonding in the bent structures.[31,32]

Transition structures. The 1,1-addition mechanism proceeds via a single transition structure, denoted as TS**1**/**3** (Chart 5-2), en route to the formation of the $Fe(SH_2)^+$ complex **3**. Conceptually, the 1,1-route in the FeS^+/H_2 system corresponds to the 'oxene-pathway' proposed in the chemistry of transition-meal oxenoids.[33] Thus, interconversion of **1** into **3** requires reorientation of the complexed hydrogen molecule from the iron to sulfur prior to passage via TS**1**/**3**. The IRC calculations confirm that no additional minima are involved in the sequence **1** → TS**1**/**3** → **3**. The transition structure located on the quartet surface at E_{rel} = 18.6 kcal/mol has C_s-symmetry (^{4}A") and is characterized by a somewhat elongated H–H bond (0.86 vs 0.77 Å) concomitant with two S–H bonds that are longer than those found in free H_2S (1.71 vs 1.35 Å). The imaginary frequency (i1256 cm^{-1}) of ^{4}TS**1**/**3** corresponds to the movement of the two hydrogen atoms towards the sulfur atom under elongation of the H–H bond. Location of an equivalent ^{6}TS**1**/**3** is not further pursued, because vertical excitation to the sextet surface at the optimized geometry of ^{4}TS**1**/**3** led to a splitting of 74.1 kcal/mol. This huge energy demand leads to exclusion of the 1,1-route on the sextet surface from further consideration. Note, that the assumption of similar geometries for sextet and quartet species is justified by comparison to the geometric parameters of other stationary points (Charts 5–1 and 5–2).

The 1,2-addition mechanism involves two consecutive steps. The reaction commences with an addition of H_2 across the FeS^+ unit**,** **1** → **2,** followed by a 1,2-hydrogen shift from iron to sulfur**,** **2** → **3**. The transition structure ^{6}TS**1**/**2** for the 1,2-addition (E_{rel} = 17.6 kcal/mol) comprises a planar, four-membered ring in which the H–H bond (1.16 Å) is already much longer than that of an intact H_2 molecule (0.74 Å) and the Fe–H bond is close to that of ^{6}**2** (1.71 vs. 1.59 Å), while the S–H interaction is still weak (1.64 vs. 1.36 Å). The imaginary frequency (i1603 cm^{-1}) is assigned to the stretch of the H_2 moiety with simultaneous movement of the H atoms towards iron and sulfur. The corresponding quartet species ^{4}TS**1**/**2** with an (^{4}A") state and E_{rel} = 12.8 kcal/mol shows a structure close to ^{6}TS**1**/**2**, but with shorter H–H, Fe–H, and Fe–S bond lengths; the largest difference of 0.16 Å is found for the H–H distance. In the quartet TS, the imaginary frequency can be attributed to the same motion as for the sextet, although the frequency itself is about 30% lower (i1096 cm^{-1}). Qualitatively,

the Fe–S and H–H bonds are more reactant like in the quartet TS than in the sextet, and hence the TS is earlier than on the sextet surface.

The subsequent 1,2-hydrogen shift from iron to sulfur to form $Fe(SH_2)^+$ can occur via the C_1-symmetrical ^{6}TS**2**/**3** with E_{rel} = 17.4 kcal/mol. In ^{6}TS**2**/**3**, the Fe–H bond is lengthened and the hydrogen atom is located approximately above the middle of the Fe–S bond (Chart 5-2). The imaginary frequency (i1107 cm^{-1}) can be assigned to the motion of the hydrogen atom from iron to sulfur. In accord with the 1,2-hydrogen shift**,** a lengthening of the Fe–S bond by 0.15 Å is observed between ^{6}**2** and ^{6}TS**2**/**3**. Attempts to locate a similar TS on the quartet surface failed (see below).

Products. Experimentally, Fe^+, FeD^+, and $FeSD^+$ are observed as ionic products in the reaction of FeS^+ with D_2, Equation 5–1 – Equation 5–3, Scheme 5-1. After considering H and D variants, the thresholds of these reactions for the corresponding protio species are 15.8 ± 2.5 kcal/mol, 42.0 ± 8.1 kcal/mol, and 34.4 ± 3.2 kcal/mol (Table 5-1), respectively, as compared to the thermochemical reaction enthalpies of 0.7 ± 1.3 kcal/mol, 42.7 ± 1.8 kcal/mol, and 26.7 ± 2.8 kcal/mol. At the B3LYP/6-311+G* level of theory, the ground state of Fe^+ is predicted to be Fe^+ (^{4}F), being 5.0 kcal/mol more stable than the ^{6}D state. A reversed order is found experimentally with the Fe^+ (^{6}D) ground state located 5.8 kcal/mol below the ^{4}F state.[34] This phenomenon is already described in Chapter 2 and is attributed to a bias toward $3d^n$ configurations over $3d^{n-1}4s^1$ configurations almost inherent to the description of atomic transition-metal ions with DFT methods.[35] Therefore, the calculation of the bare Fe^+ ion is associated with a larger error than the other parts of the PES. To account for this in the PES, the experimental state splitting between the ^{6}D and ^{4}F states is used; however, the energies of all other species are not adjusted.[36]

For $[Fe,S,H]^+$, two different connectivities, $SFeH^+$ and $FeSH^+$, are conceivable. The formation of ground-state $^5FeSH^+$ in its ^{5}A' state is calculated to be endothermic by 25.2 kcal/mol. This value is in excellent agreement with $\Delta_r H_0$ = 26.7 ± 2.8 kcal/mol calculated for the protiated version of Equation 5–3 using D_0(Fe^+-SH) from the FT-ICR experiments. $^5FeSH^+$ has C_s-symmetry with an FeSH angle of 94°, r_{FeS} = 2.17 Å, and r_{SH} = 1.36 Å. Another bent quintet structure in an ^{5}A" state is located 18.0 kcal/mol above the $^5FeSH^+$ ground state, with an FeSH angle of 110°. Excitations to the lowest triplet (^{3}A') and septet (^{7}A') states require 17.9 kcal/mol and 43.8 kcal/mol, respectively. The lowest electronic state of the second structural isomer, $SFeH^+$ (^{3}A'), is calculated to lie 45.7 kcal/mol higher in energy than the ground-state of $^5FeSH^+$ and is therefore excluded from further consideration.

Formation of the third reaction product, FeH^+, is calculated to be endothermic by 36.5 kcal/mol, in agreement with the literature thermochemistry of 42.7 kcal/mol calculated for the protiated version of Equation 5–2. The ground state of FeH^+ is a quintet ($^5\Delta$),[37] while the lowest triplet state ($^3\Pi$)[38] lies 32 kcal/mol higher in energy at the B3LYP/6-311+G* level.

When the calculated stationary points are combined, the potential-energy surface depicted in Figure 5-2 is obtained. Energies for the product channels are adopted from the literature data. In the following section, the 1,1- and 1,2-addition mechanisms will be discussed with respect to the quartet and sextet surfaces.

5.2.4 Comparison of Experimental and Theoretical Data

Starting from the ground state entrance channel, $^6FeS^+ + {}^1H_2$, and the encounter complexes (**1**, Chart 5-1), the reaction can proceed by at least two different pathways.[39]

1,1-Addition. The occurrence of 1,1-addition entirely on the sextet surface is excluded from further considerations due to the high barrier associated with TS**1**/**3** (see above). Instead, the system may cross from the sextet to the quartet surface at the putative crossing point C_1 located between ^{6}**1** and ^{4}TS**1**/**3**. The relevance of such crossings in oxidations and the requirements for "violation" of the spin-conservation principle have been discussed in detail previously.[26a,27,30,40] As verified by IRC calculations, the system proceeds from ^{4}TS**1**/**3** to the global minimum ^{4}**3**. The $^5FeSH^+ + H$ and $^4Fe^+ + H_2S$ product channels can be accessed from ^{4}**3** without further structural rearrangements, while the formation of $^6Fe^+ + H_2S$ requires a second surface crossing back to the sextet surface at C_3. In summary, the $FeS^+ + H_2$ reaction can progress via a 1,1-addition on the quartet surface, but this involves a surface crossing and a barrier. Considering the estimated uncertainty of ± 6 kcal/mol in the calculations, the predicted barrier height (E_{rel} = 18.6 kcal/mol) is somewhat higher but still within the error margin of the experimental threshold of 15.8 ± 2.5 kcal/mol for the formation of Fe^+.

Note, that the predicted barrier is far below the thermochemical threshold for formation of $FeSH^+$. Further, the 1,1-addition mechanism does not explain the apparent barrier in the $FeSH^+$ channel, and formation of FeH^+ cannot be directly accessed via the 1,1-route, which implies that the 1,2-pathway must contribute to the observed reactivity.

1,2-Addition. The respective sextet and quartet surface are discussed separately for the 1,2-addition sequence because the two surfaces differ dramatically. On the sextet surface, the 1,2-addition proceeds from the encounter complex **1** via ^{6}TS**1**/**2** to minimum ^{6}**2** as revealed by IRC calculations. The insertion intermediate ^{6}**2** has three options for further reaction. It can

either (i) decompose to the reactants, (ii) undergo a second hydrogen shift via ^{6}TS**2**/**3**, or (iii) directly dissociate into the FeH^+ + HS and $FeSH^+$ + H fragments. Once the required energy is available, dissociations are expected to be favored and should lead to the formations of FeH^+ and $FeSH^+$ at their thermodynamic thresholds. Note, that this is again in disagreement with the experimentally observed barrier for $FeSH^+$ formation. Processes (i) and (ii) have similar barriers with ^{6}TS**2**/**3** being a little lower shifting the reaction towards ^{6}**3**. As soon as ^{6}**3** is reached, formation of ground-state $FeSH^+$ and Fe^+ is conceivable without further structural rearrangement. Both barriers for formation of Fe^+ on the sextet surface (17.9 and 17.4 kcal/mol) are somewhat higher than the experimentally observed threshold (15.8 ± 2.5 kcal/mol) but still within experimental error.

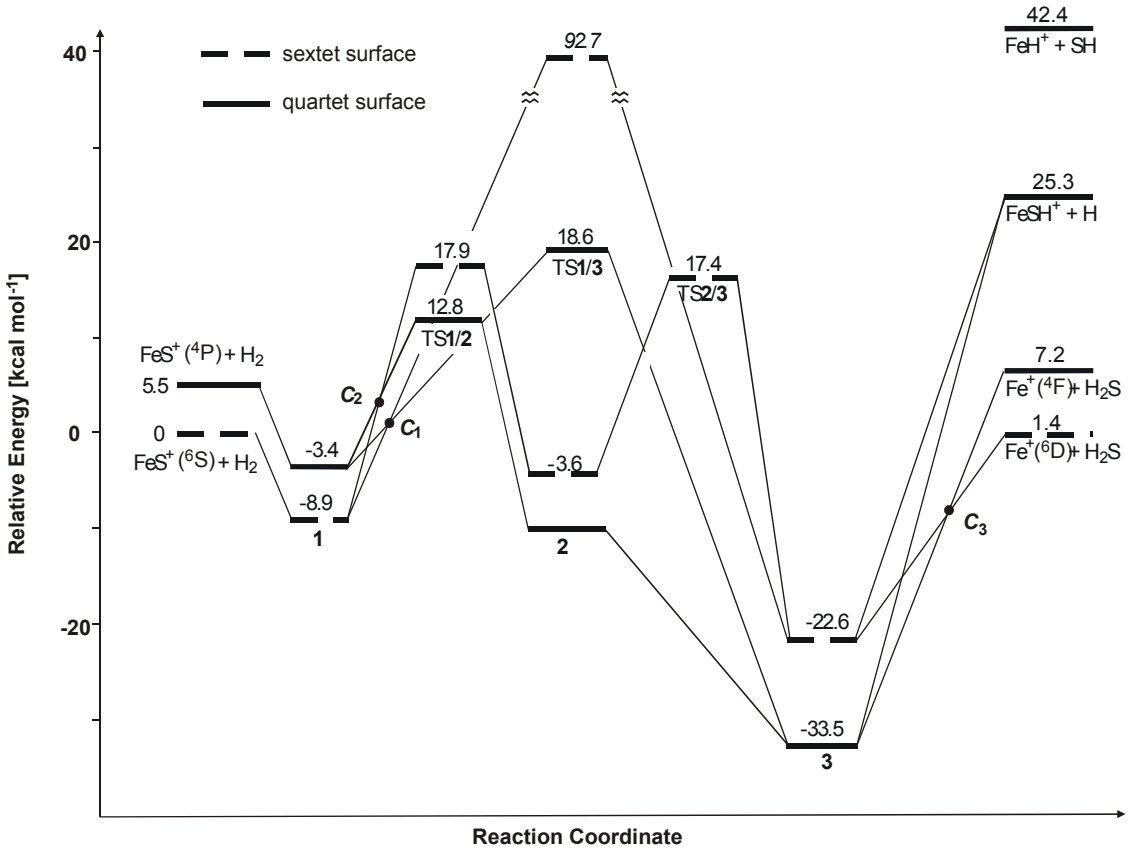

Figure 5-2: Potential-energy surface of the reaction $FeS^+ + H_2$. Energies (in kcal/mol) are given relative to the FeS^+ ($^6\Sigma^+$) + H_2 ($^1\Sigma^+$) entrance channel and include ZPVE corrections.

On the quartet surface, the 1,2-addition very much resembles the situation found for the sextets at structures **1**, **3**, and TS**1**/**2**. However, the quartet and sextet surfaces differ entirely in the region between TS**1**/**2** and **3**. While the inserted structure ^{6}**2** and the related transition structure ^{6}TS**2**/**3** exist as stationary points on the sextet surface, neither of the corresponding

quartet species can be located. Instead, tedious IRC-calculations starting from ^{4}TS**1**/**2** lead to the picture shown in Figure 5-3.

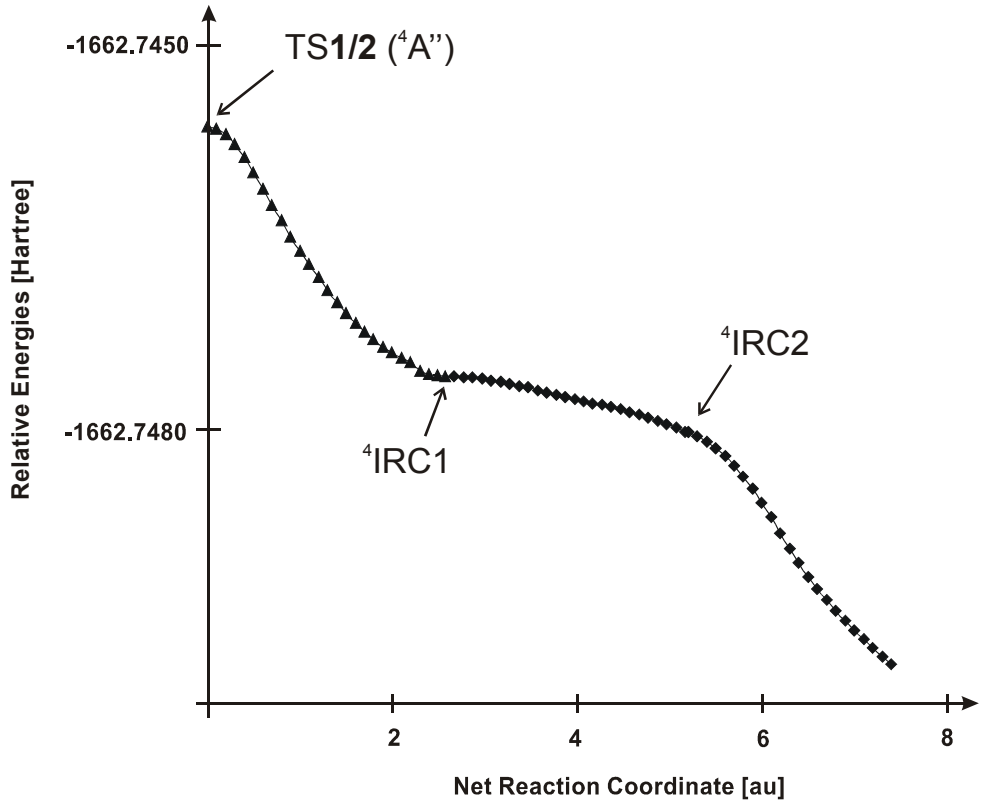

Figure 5-3: IRC calculation from ^{4}TS**1**/**2** to $Fe(SH_2)^+$, ^{4}**3**.

In Figure 5-3, energies are given in Hartree without ZPVE correction. Following the imaginary modes of ^{4}TS**1**/**2**, the H–H distance elongates while the Fe–H and S–H bonds shorten. Simultaneously, the HSFe and SFeH angles increase until a stationary point ^{4}IRC1 is reached which is located by IRC calculations using the "normal" convergence criteria (Chart 5-3).[41] The structure of the planar ^{4}IRC1 is comparable to that of ^{6}**2** but cannot be assigned to the quartet insertion intermediate, as a frequency calculation on this structure yields a sizable imaginary frequency (i357.6 cm^{-1}). The latter corresponds to an out-of-the-plane rotation of the two hydrogen atoms viz. a rotation around the Fe–S bond. Structure ^{4}IRC1, at which the B3LYP IRC-calculation terminates using the "normal" convergence criteria, can therefore not be regarded as a stationary point, but rather as a spurious minimum. In fact, when the IRC calculation is restarted at the geometry of ^{4}IRC1 while applying "tight" convergence criteria,[41] the system further proceeds to lower energies, though the potential is much flatter. The associated structural change is best described as an increase of the dihedral HFeSH angle

concomitant with a slight elongation of the Fe-S bond. At a dihedral angle of about 80°, the mode for the out-of-plane rotation has almost deceased (sketched as structure ^{4}IRC2 in Chart 5-3) and a new mode corresponding to the 1,2-hydrogen shift from Fe towards S begins to contribute to the reaction coordinate. Following the new mode the energy decreases more rapidly, and the IRC calculation terminates at a structure close to that of minimum ^{4}**3**.

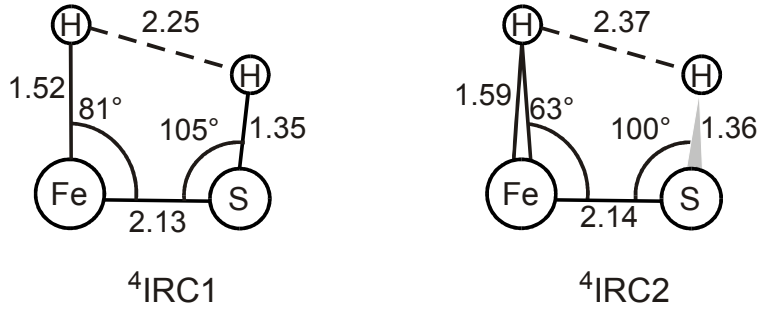

Chart 5-3: Structures of ^{4}IRC1 and ^{4}IRC2. Bond lengths are given in Å and angles in degree.

A similar phenomenon was found by Tilson and Harrison,[42] who reported calculations on the reaction of cationic scandium sulfide with dihydrogen, where the inserted structure also does not correspond to a true minimum, but rather to a saddle point from which the energy further decreases by rotation of the hydrogen atoms out of the plane of the molecule. It may be possible to further resolve the shape of the "plateau" between ^{4}IRC1 and ^{4}IRC2 by use of different methods and basis sets. This is deemed unnecessary**,** however, as any barrier associated with this TS would still be very small, leading to similar conclusions and arguments as presented below. The IRC-calculation depicted in Figure 5-3 reveals that the region between ^{4}IRC1 and ^{4}IRC2 is rather flat (within 5 kcal/mol). Thus for the reaction under study, which is performed at thermal conditions (298 K), any minima in this region may be neglected, and the putative insertion structure ^{4}IRC1 should be treated as a contributing dimension to the density of states of excited ^{4}**3**. Overall, this implies that once the FeS^+/H_2 couple has enough energy to overcome the barrier associated with ^{4}TS**1**/**2** (E_{rel} = 12.8 kcal/mol), it continues through ^{4}IRC1 and ^{4}IRC2 to the product complex ^{4}**3**. Note, that ^{4}TS**1**/**2** has the lowest energy demand of all TSs considered for the FeS^+/H_2-system and falls within the error margins of the experimentally observed threshold for $Fe^+ + H_2S$ formation. From ^{4}**3**, the $^4Fe^+$ and $^5FeSH^+$ channels can be accessed directly, while formation of ground-state $^6Fe^+$ requires a surface crossing from the quartet back to the sextet surface at C_3. Compared to the sextet surface, the FeH^+ channel is less likely to be accessed from the quartet surface due to the absence of a distinct minimum for structure ^{4}**2**.

In summarizing the mechanistic details, the following picture emerges: (i) formation of ground-state $^6Fe^+$ is most likely to proceed via the 1,2-addition mechanism with two surface crossings at C_2 and C_3 leading to a prediction of an activation barrier having E_{rel} = 12.8 ± 6.0 kcal/mol, which is in reasonable agreement with the threshold E_0 = 15.8 ± 2.5 kcal/mol measured for reaction 5−1a. Note, however, that formation of excited $^4Fe^+$ is also feasible, as it does not require a second spin crossing at C_3 and is energetically accessible at all energies above the measured activation barrier. (ii) None of the calculated barriers gives a reasonable explanation for the formation of $FeSH^+$ with an apparent threshold of E_0 = 34.4 ± 3.2 kcal/mol. This is particularly surprising because the process described in Equation 5−3 can be viewed as a simple hydrogen atom abstraction from H_2 by the FeS^+ unit, a reaction that is not expected to show a very large barrier in excess of reaction endothermicity. Thus, a more profound consideration of the entire PES is indicated.

Direct access of the $FeSH^+$ + H exit channel is conceivable from ^{6}**2**, ^{4}**3**, and ^{6}**3**. Starting from **3**, however, thermochemistry predicts the formation of $FeSH^+$ to be 24.0 ± 3.1 kcal/mol energetically disfavored compared to the $Fe^+ + H_2S$ channel which is also accessible from **3**. This fact is likely to result in a strong competition between the two channels, with the $FeSH^+$ channel being disfavored. Such competition could cause a delayed threshold for the $FeSH^+$ channel. However, ^{6}**2** should allow efficient formation of $FeSH^+$ because no competition with the Fe^+ channel is expected. This is because hydrogen migration to form ^{6}**3** is associated with the significant barrier ^{6}TS**2**/**3**, which renders the Fe^+ channel only 7.9 kcal/mol energetically more favorable than formation of $FeSH^+$, in contrast to the situation on the quartet surface. Nevertheless, there are two reasons why ^{6}**2** has only a low probability to be formed. First, the predicted energetic position of ^{6}TS**1**/**2** at E_{rel} = 17.9 kcal/mol does not allow for formation of ^{6}**2** below this energy. Second, if an efficient crossing between the sextet and quartet surfaces is assumed at C_2, most of the sextet species will flip spin and cross to the quartet surface. The experimental results suggest that the efficiency of the crossing at C_2 should be sufficient to allow for reasonably intense formation of Fe^+ as soon as the interaction energy exceeds the barrier of ^{4}TS**1**/**2**. The probability for the reactant complex to traverse ^{6}TS**1**/**2** at the calculated energy of E_{rel} = 17.9 kcal/mol is strongly reduced because of the lower energy demand of ^{4}TS**1**/**2** for which the calculations predict E_{rel} = 12.8 kcal/mol. Hence, only a small percentage of reactant collisions will reach intermediate ^{6}**2** at low interaction energies while at higher interaction energies the crossing probability decreases, as the motion of the reactants speeds up. Thus, more particles traverse ^{6}TS**1**/**2** and access ^{6}**2**, where they primarily continue to form

$FeSH^+$. Here again, a delayed threshold is expected for the formation of $FeSH^+$ due to the competition between ^{4}TS**1**/**2** and ^{6}TS**1**/**2**.

To summarize, the late threshold for the formation of $FeSH^+$, i.e. 34.4 ± 3.2 kcal/mol in the H/D corrected GIB experiment as compared to the literature value of 26.7 ± 2.8 kcal/mol, is attributed to the joint action of two related phenomena: (i) The non-existence of the insertion structure on the quartet surface prompts the reaction to continue to form ^{4}**3**. Here, competition between the $Fe^+ + H_2S$ and $FeSH^+ + H$ exit channels discriminates against the latter channel by 26.0 kcal/mol which results in a delayed formation of $FeSH^+$. (ii) The competition between ^{4}TS**1**/**2** and ^{6}TS**1**/**2** hinders the access to ^{6}**2** and therefore delays the formation of $FeSH^+$ on the sextet surface. Finally, it is conceivable that loss of atomic hydrogen from the intermediates **1** - **3** (either quartet or sextet) is hindered by a potential-energy barrier in excess of reaction endothermicity, in contradiction to the assumptions made above. Such a scenario would provide an alternative explanation for the delayed appearance of the $FeSH^+$ channel. For the time being, this aspect cannot be treated comprehensively; however, recent theoretical studies of the related FeO^+/H_2-system[27,43] gave no indications for the presence of such kind of barriers associated with hydrogen-atom loss.

5.2.5 Summary

In the seemingly simple reaction of FeS^+ with dihydrogen, only the high-energy channel leading to FeH^+ appears to proceed at thermochemical threshold, while hydrodesulfurization to yield Fe^+ is affected by barriers and the explanation of the threshold for formation of $FeSH^+$ also requires consideration of the competing Fe^+ channel. The differences between experimental and calculated data are resolved by an inspection of the potential-energy surface, thereby explaining the product branching as a consequence of competing processes. In addition, $D_0(Fe^+\text{-SH})$ = 66.0 ± 2.6 kcal/mol is derived from FT-ICR equilibrium measurements and is used to establish the thermochemistry of $FeSH^+$ formation from FeS^+ and H_2, $\Delta_r H_0$ = 26.7 ± 2.8 kcal/mol.

These results are in line with a two-step 1,2-addition mechanism which involves a change of spin multiplicity from the sextet surface of the reactants to the quartet surface for the intermediates. Specifically, the formation of the $FeD^+ + SD$ product channel shows good agreement between literature thermochemistry (1.85 ± 0.08 eV) and GIB experiments (1.82 ± 0.35 eV). The threshold for $Fe^+ + D_2S$ formation in the GIB of 0.64 ± 0.11 eV (14.8 ± 2.5 kcal/mol) can be rationalized by the predicted barriers on both sextet and quartet surfaces (see

Figure 5-2). In contrast, the delayed threshold of $FeSD^+$ formation in the GIB experiment cannot be explained by involving the minima and barriers alone, but rather requires consideration of the competition between both the low-lying fragmentation channels and the spin crossing to the quartet surface versus adiabatic reaction on the sextet surface.

5.3 FeS^+-Mediated Conversion of Methane to Methanethiol

This chapter continues with the investigation of the reaction of FeS^+ with methane, thus extending the work described in the previous chapter on the FeS^+/H_2-system. While H_2 is the most simple substrate to be investigated in terms of structure, as there is only one homolytic bond to be broken in the course of the reaction, this seemingly straightforward system turns out to be quite complex with regard to the mechanistic details of product formation and does already require advanced theoretical work in order to explain the experimentally observed behavior. While methane is structurally only slightly more complex than H_2, methane activation by transition metals is a field of active research due to (i) the large resources of easily accessible methane in the earths crust, making it an economically interesting raw material for the production of more valuable substrates, and (ii) the low reactivity of methane, which constitutes a challenge for chemists.[44] Not surprisingly, the development of efficient catalysts for the activation of methane is represented as one of the ten most important challenges in catalyst development.[45] Thus, reactions of 'bare' transition metals as well as ligated transition-metal species with methane have been investigated quite extensively.[46,47,48] In the following section, a combined GIB and computational study on FeS^+/CH_4 is presented.

5.3.1 GIB-Measurements of the FeS^+/CH_4-System

Before presenting the results on the FeS^+/CH_4-couple obtained in this Thesis, a short discussion of earlier results related to this system is indicated. Following that, the experimental investigation of the deuterated variant of this system as studied in the guided-ion beam (GIB) mass spectrometer will be presented.

In earlier mass spectrometric experiments, no reaction of FeS^+ with methane was observed under thermal conditions.[9b] Instead, the reverse reaction of Fe^+ and methanethiol leads to formations of $FeSCH_2^+$ and FeS^+ ions (branching ratios of 59:41).[9b,49] Formation of FeS^+ corresponds to the reverse reaction of that investigated in the current study, i.e. $FeS^+ + CH_4$;

while loss of H_2 most likely proceeds via dehydrogenation of intermediate $Fe(CH_3SH)^+$, and is therefore not likely to be observed for the FeS^+/CH_4 couple examined here.

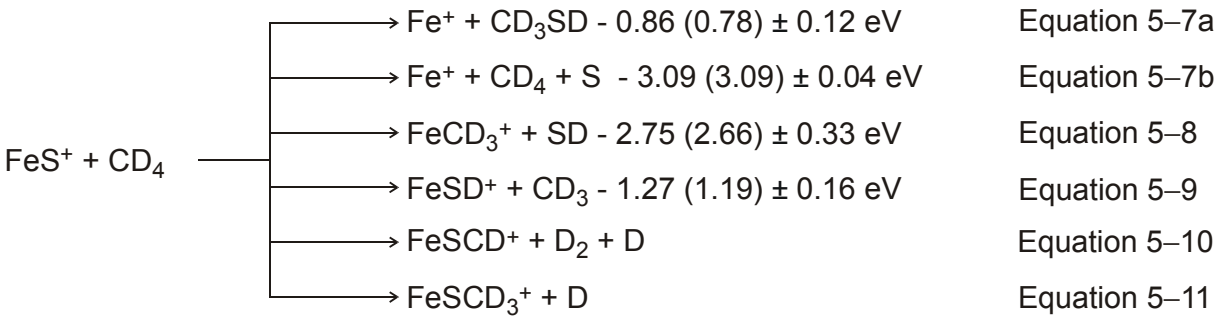

Scheme 5-4: Products observed in the reaction $FeS^+ + CH_4$.

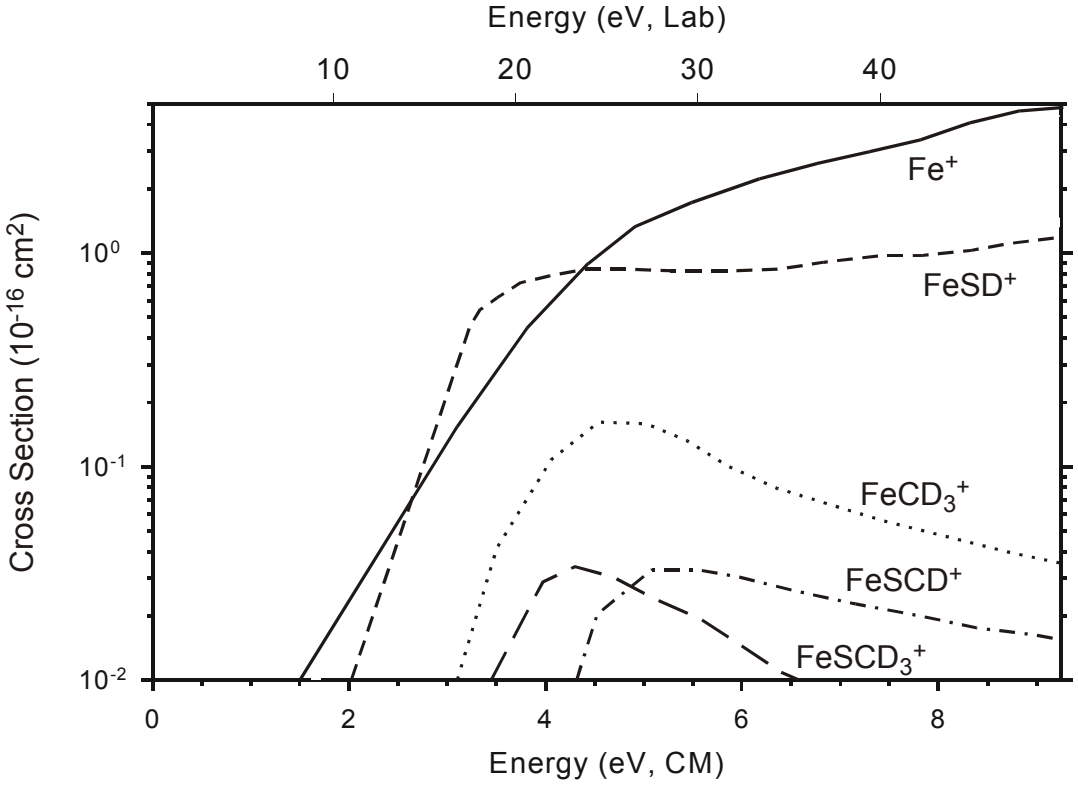

Figure 5-4: Reproduction of the product distributions obtained in the reaction of FeS^+ with CD_4 in the GIB instrument. Note, that for the sake of simplicity these are not the real data points but graphic representations. Fe^+ (——), $FeSD^+$ (- - -), $FeCD_3^+$ (· · ·), $FeSCD_3^+$ (— —), and $FeSCD^+$ (- · - ·)

Experimental Results. The use of fully deuterated methane in the GIB experiments is necessary to reduce the mass overlap of products due to the limited mass resolution of the quadrupole analyzer in the GIB instrument. This results in slightly different thresholds

compared to the computationally investigated, unlabeled system. For comparison with the protio-system, calculated zero-point energies of the labeled and unlabeled species are used to correct the experimental thresholds. Both, the uncorrected and the corrected thresholds for the protio- and the deutero-system are given below. In analogy to the chapter on the FeS^+/H_2-system, kinetic isotope effects as well as tunneling phenomena are neglected. The reaction of FeS^+ with CD_4 in the GIB yields five ionic products, i.e. Fe^+, $FeSD^+$, $FeCD_3^+$, $FeSCD_3^+$, and $FeSCD^+$, according to Equation 5–7 - Equation 5–11 (Scheme 5-4). The product distribution is similar to that observed for the oxygen-analog reaction of FeO^+ with methane as investigated by different experimental techniques.[26a,26d,26f,46a,50] The thermochemical data given in Equation 5–7 - Equation 5–9 are calculated using literature values for the 0 K heats of formation and bond dissociation energies and refer to the species in their electronic ground states. The values in parentheses correspond to the thermochemistry of the analogous protio-system for comparison with theoretical data.

Figure 5-4 gives an overview of the product distribution as a function of relative kinetic energy of the reactant ions. This picture yields qualitative information only, but regarding the fact that the intensities are depicted on a logarithmic scale, the products Fe^+ and $FeSD^+$ by far dominate the reaction. Compared to the work on FeS^+/H_2 couple described above, the present system is slightly more rich in possible product channels, however, with regard to the number of conceivable intermediates involved it is an order of magnitude more complex. In the experimental section, therefore only the formation of the two most abundant products, Fe^+ and $FeSD^+$, is discussed. The experimental cross sections of these two products are depicted in Figure 5-5 and are further evaluated below. The cross sections of the remaining products $FeCD_3^+$, $FeSCD_3^+$, and $FeSCD^+$ are small ($\sigma_{max} \leq 0.1$ Å^2), and the data are scattered. While refraining from a rigorous quantitative analysis, qualitatively the $FeSCD^+$ channel rises where the $FeSCD_3^+$ product starts decreasing rapidly. It may therefore be assumed that $FeSCD^+$ evolves as a consecutive fragment of $FeSCD_3^+$. Further information about the minor product channels can be obtained by combining experimental and theoretical work (see below).

Let us now elucidate the two major product channels, starting with the formation of Fe^+ in Equation 5–7a and Equation 5–7b (see Figure 5-5). As a result of the fitting procedure, the Fe^+ cross section can only be modeled with a bimodal behavior. The first process dominates up to about 2.8 eV, and at elevated energies a faster rising, second process takes over. Analysis of the threshold region yields $E_0 = 0.65 \pm 0.11$ eV (Table 5-2). Note, that this result is in line with literature thermochemistry for the formation of Fe^+ and CD_3SD as the neutral counterpart, Equation 5–7a. The threshold of the second feature in the cross section is

analyzed to be E_0 = 3.39 ± 0.3 eV, in which the considerably increased error is due to uncertainties in the subtraction of the mathematical fit for the first feature. Nevertheless, the threshold is consistent with the tabulated bond dissociation energy for FeS^+ (D_0 = 3.09 ± 0.04 eV), thus implying that this onset is due to a simple collision-induced dissociation (CID) of FeS^+ according to Equation 5–7b.[51]

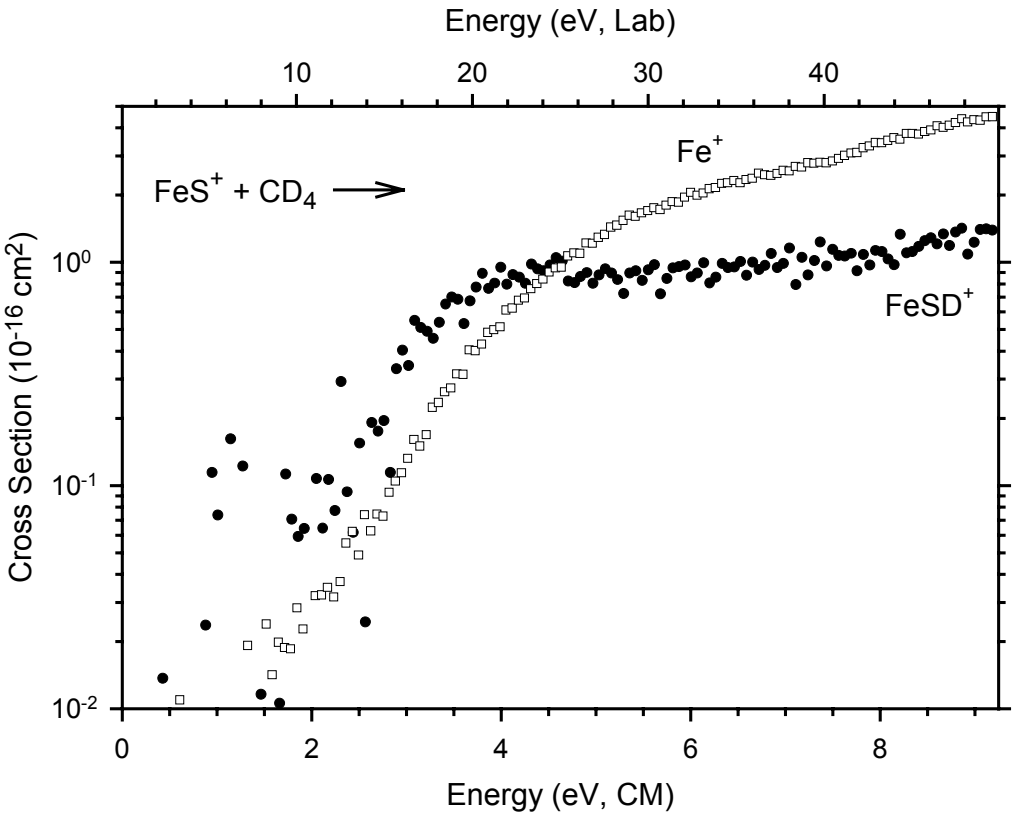

Figure 5-5: Product cross sections for the reaction of FeS^+ with CD_4 to form Fe^+ (□) and $FeSD^+$ (●) as a function of kinetic energy in the center-of-mass (lower axis) and laboratory frames (upper axis).

While the $FeSD^+$ product is less abundant than Fe^+ at elevated energies (cross section σ_{max} ≈ 1.5 Å^2 for $FeSD^+$ compared to σ_{max} ≈ 5 Å^2 for Fe^+), it dominates over the Fe^+ channel at energies below E_{CM} = 4 eV. Unfortunately, the data of the $FeSD^+$ channel strongly scatter in the threshold region. The reason for the high noise level in the $FeSD^+$ channel is the proximity in mass to the abundant parent-ion beam of FeS^+. As the $FeSD^+$ thermochemistry is known from the investigation reported in Chapter 5.2, a rigorous quantitative analysis of the $FeSD^+$ channel does not seem necessary under the experimental conditions. Instead, in a more qualitative sense, the $FeSD^+$ channel rises from an apparent threshold of 2 eV, way above the

threshold expected from literature thermochemistry (1.27 eV); this feature will be discussed in more detail in the discussion section.

Table 5-2: Summary of Parameters in Eq. 1 Used for the Fits of the Cross Sections.

Reaction	E_0, eV	σ_0	n
$FeS^+ + CD_4 \rightarrow Fe^+ + CD_3SD$[a]	0.65 ± 0.11	0.01	3.76
$FeS^+ + CD_4 \rightarrow Fe^+ + S + CD_4$[a]	3.39 ± 0.35	1.70	1.28
$FeS^+ + CD_4 \rightarrow FeSD^+ + CD_3$[b]	1.27	0.12	1.97
$FeS^+ + CD_4 \rightarrow FeSD^+ + CD_3$[c]	3.10	2.39	0.36

[a] The E_0 values are the average of several threshold fits with uncertainties of one standard deviation. [b] Data fit of the assumed first feature of the $FeSD^+$ data channel with a fixed E_0 = 1.27 eV, calculated from literature thermochemistry. [c] Threshold fit of the second feature of the $FeSD^+$ data channel after subtraction of the first feature.

5.3.2 The PES of the FeS^+/CH_4-System

After the presentation of the experimental results, a theoretical investigation of the FeS^+/CH_4-system is indicated due to the many questions that remain open. In particular, the pathway of product formation as well as possible structures of the $FeSCD^+$ product observed in the GIB need to be clarified. In the following, the different routes for the activation of CH_4 by FeS^+ are investigated. The theoretical investigations include two conceivable reaction mechanisms which differ by the orientation of Fe and S relative to the C–H bond being activated (Figure 5-6).

Both mechanisms start with formation of the encounter complex **4**, followed by insertion of FeS^+ into one C–H bond to afford the reaction intermediates $CH_3–Fe–SH^+$ (**5**), or $H–Fe–SCH_3^+$, (**7**). From both intermediates, the reaction may continue toward formation of $Fe(CH_3SH)^+$ (**6**); note that direct dissociation of the insertion intermediates **5** and **7** also is feasible (Figure 5-6). In addition to the several mechanistic pathways, at least two reaction pathways on two spin-surfaces need to be considered in an investigation of the FeS^+/CH_4-PES for two reasons: (i) the calculated energy difference of the low-lying sextet and quartet states of FeS^+ is only 5.0 kcal/mol.[9f] (ii) The analogous oxygen system FeO^+/CH_4, involves both, the sextet and quartet PES.[48] In the next section the structures of the stationary points are presented briefly.

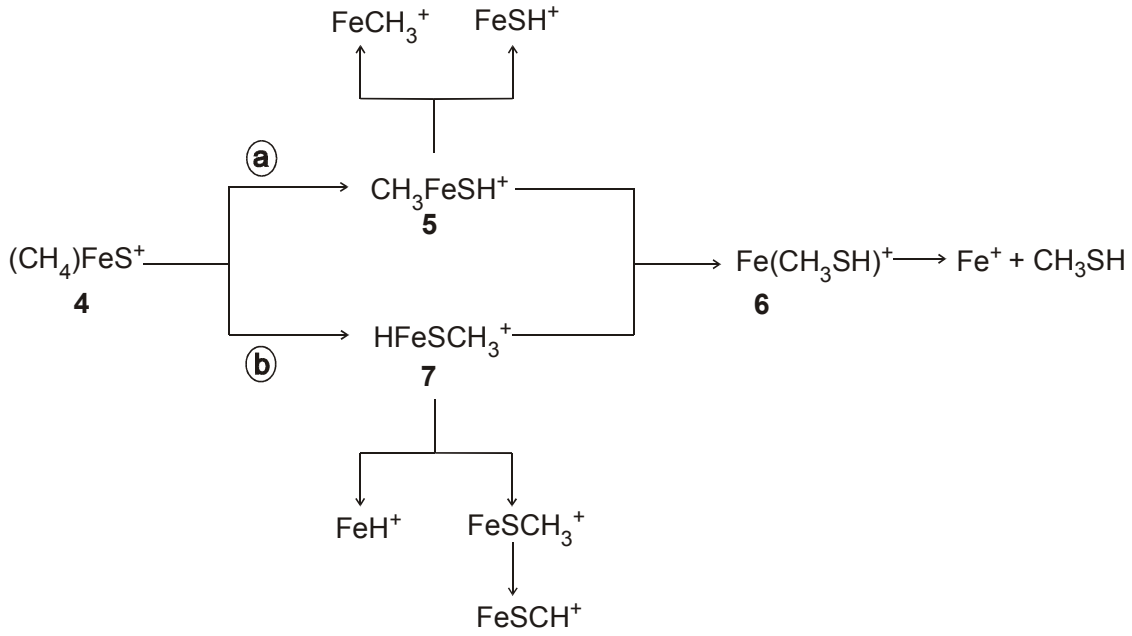

Figure 5-6: Schematic description of the two calculated reaction pathways ⓐ and ⓑ of the FeS^+/CH_4-system. Note, that only the minima are displayed; transition structures that connect the minima are left out for the sake of simplicity and are discussed in the text.

Reactants. The FeS^+-reactant has already been described earlier in the reaction of FeS^+ with H_2. Therefore, the information given here is limited to the methane molecule, which shows the expected tetrahedral symmetry and exhibits an $^1A_1$ ground state. In the following, all calculated energies will be given with respect to the $^6FeS^+ + CH_4$ asymptote (E_{rel} = 0.0 kcal/mol), if not stated otherwise.

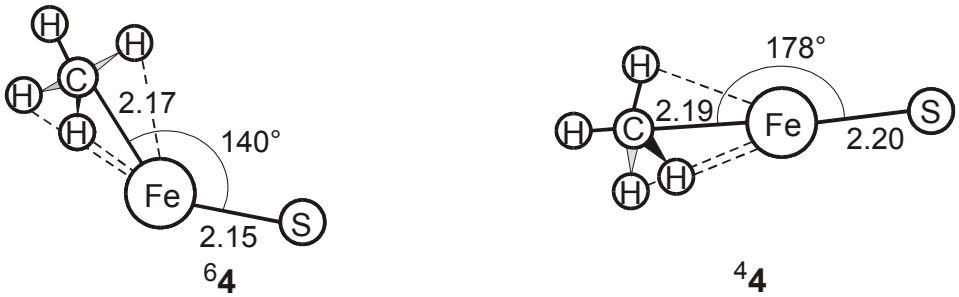

Chart 5-4: Encounter complexes of the FeS^+/CH_4-system (**4**) obtained using the B3LYP/6-311+G* approach. Bond lengths are given in Å and angles in degree.

Encounter Complex. Starting from the reactants, the first minimum along both reaction pathways is the encounter complex **4**. Although different isomers can be thought of for **4**, i.e., the methane molecule may interact with either end of the FeS^+ unit and for each of these

options several geometric conformations are feasible, only the η^3-iron-bound structures ^{4}**4** and ^{6}**4** are identified as minima along the PES for both spin states, see Chart 5-4. Even though there may still exist sulfur-bound methane complexes, it is reasonable to assume that iron-bound structures such as **4** are energetically most favorable. The latter is rationalized in an ion-induced dipole picture because the iron-end of the FeS-unit carries the larger positive charge (q_{Fe} = 0.64) and thus interacts more strongly with the methane molecule. The ground state (^{6}**4**) is found on the sextet surface at E_{rel} = - 16.3 kcal/mol, with its quartet analog (^{4}**4**) located only 1.5 kcal/mol above at E_{rel} = -14.8 kcal/mol. This close energy splitting renders the assignment of the ground state somewhat ambiguous. In ^{6}**4**, the CH_4 moiety is bound to iron at a distance r_{FeC} = 2.17 Å, such that an S–Fe–C angle of 139.5° is formed. The quartet complex, ^{4}**4**, shows a quasi-linear arrangement of FeS^+ and the methane molecule (α_{SFeC} = 179°), with the CH_4 unit attached to the iron atom at a distance of r_{FeC} = 2.19 Å. The iron-carbon bond lengths correspond to purely electrostatic bonding, as is expected for a closed-shell ligand such as methane. Notably a rotation of the methane unit around Fe^+ is easy, i.e., a movement of CH_4 by 20° toward the sulfur atom results in a change in energy of only 0.8 kcal/mol. Given the energetic and geometric similarities of ^{4}**4** and ^{6}**4**, in conjunction with the flatness of the potential in this region, facile crossing between the sextet and the quartet surfaces is expected.

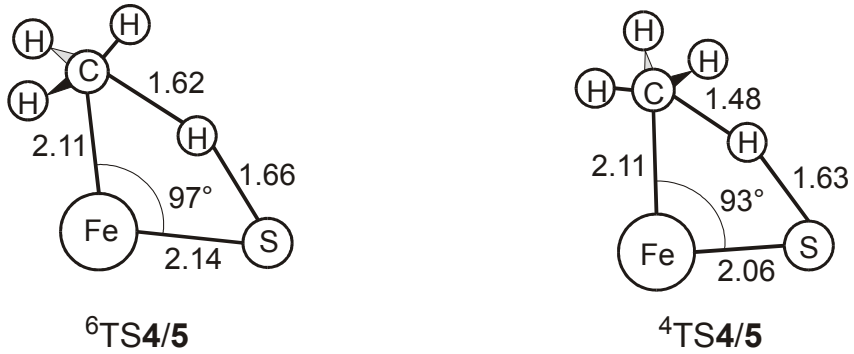

^{6}TS**4/5** ^{4}TS**4/5**

Chart 5-5: TS**4**/**5** of the FeS^+/CH_4-system obtained using the B3LYP/6-311+G* approach. Bond lengths are given in Å and angles in degree.

Reaction along the CH_3–Fe–SH^+ intermediate. (Figure 5-6, path ⓐ) The encounter complex **4** and the insertion structure **5**, CH_3–Fe–SH^+, are connected by TS**4**/**5** (Chart 5-5). The sextet and quartet TSs (^{6}TS**4**/**5** and ^{4}TS**4**/**5**) are localized at E_{rel} = 19.5 and 13.5 kcal/mol, respectively. Structurally both TSs are quite similar, having planar, four-membered rings. The imaginary frequencies (^{6}TS**4**/**5**: ν = i1575cm^{-1} and ^{4}TS**4**/**5**: ν = i1382 cm^{-1}) correspond to the

hydrogen migrations from the carbon to the sulfur atom. In the sextet TS, the Fe-S bond and the C-H distance of the migrating hydrogen atom are notably longer than in the quartet TS (^{6}TS**4**/**5**: r_{FeS} = 2.14 Å and r_{CH} = 1.62 Å; ^{4}TS**4**/**5** vs. r_{FeS} = 2.06 Å and r_{CH} = 1.48 Å), suggesting stronger bonds and a more perfect-pairing-like situation in the quartet TS, thus explaining its lower energy demand. Passing TS**4**/**5**, the reaction reaches the insertion species CH_3–Fe–SH^+ (**5**). The quartet ground state ^{4}**5** is located at E_{rel} = -13.6 kcal/mol, with the sextet ^{6}**5** at E_{rel} = -8.0 kcal/mol.

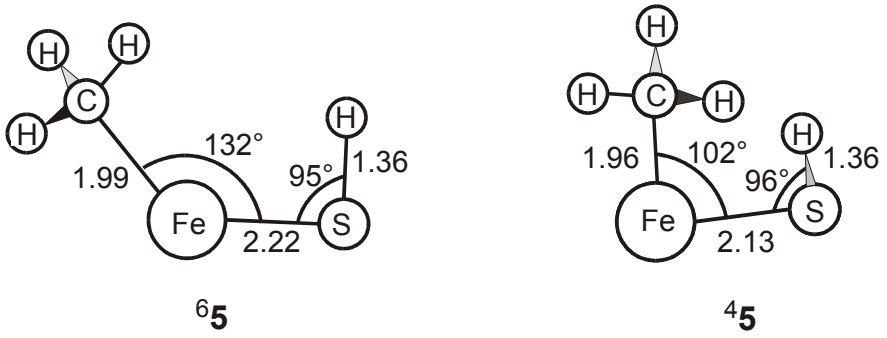

^{6}**5** ^{4}**5**

Chart 5-6: CH_3–Fe–SH^+ inserted structure (**5**) of the FeS^+/CH_4-system obtained using the B3LYP/6-311+G* approach. Bond lengths are given in Å and angles in degree.

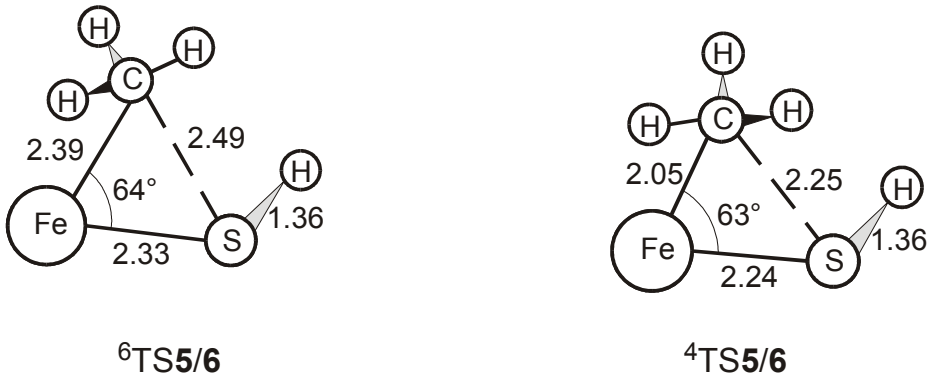

^{6}TS**5**/**6** ^{4}TS**5**/**6**

Chart 5-7: TS**5**/**6** of the FeS^+/CH_4-system obtained using the B3LYP/6-311+G* approach. Bond lengths are given in Å and angles in degree.

The quartet structure is distinctly non-planar, showing a dihedral angle of θ_{CFeSH} = -85.8°, whereas the corresponding sextet obeys planarity in this respect (Chart 5-6). From **5**, the reaction continues via TS**5**/**6** to the thiomethanol complex **6** as the global minimum of the FeS^+/CH_4 surface. The TSs depicted in Chart 5-7 are located at E_{rel} = -0.6 kcal/mol and E_{rel} = 27.5 kcal/mol on the quartet and sextet PESs, respectively. Although energetically well separated, the TSs show quite similar planar, three-membered ring structures (Chart 5-7). The

imaginary frequencies of i386 cm^{-1} and i525 cm^{-1} for ^{6}TS**5**/**6** and ^{4}TS**4**/**6**, respectively, correspond to the methyl migrations from the iron atom towards sulfur.

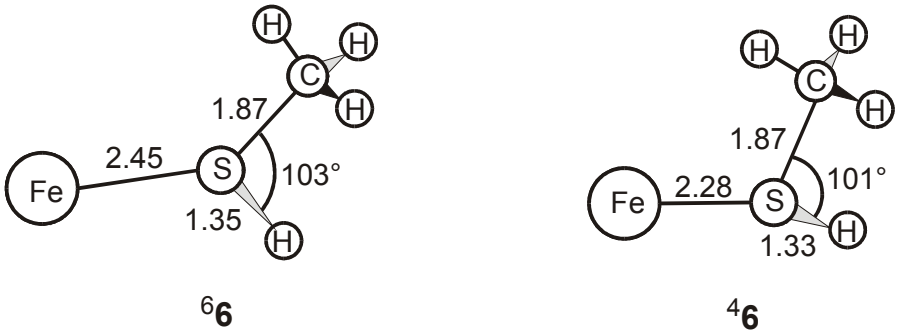

Chart 5-8: Product complexes of the FeS^+/CH_4-system obtained using the B3LYP/6-311+G* approach. Bond lengths are given in Å and angles in degree.

The product complex $Fe(CH_3SH)^+$ is located at E_{rel} = -24.2 and -8.5 kcal/mol for ^{4}**6** and ^{6}**6**, respectively. The geometries of the CH_3SH moieties are very similar in both complexes, while the Fe-S bond lengths differ in the two spin states, as expected upon the change from a merely electrostatic interaction in the sextet (r_{FeS} = 2.45 Å) to a coordinative bond in the quartet state (r_{FeS} = 2.28 Å), see Chart 5-8. The change in bond order can also explain the higher stability of ^{4}**6** over ^{6}**6**. The product complexes as well as the inserted structures may dissociate to give rise to several products which are described further below.

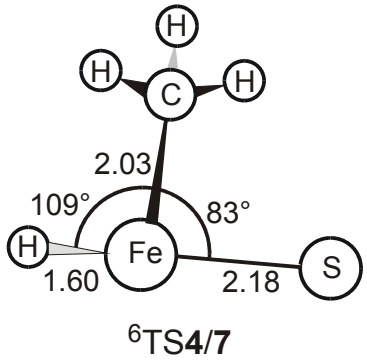

Chart 5-9: TS**4**/**7** of the FeS^+/CH_4-system obtained using the B3LYP/6-311+G* approach. Bond lengths are given in Å and angles in degree.

Reaction along the H-Fe-SCH_3^+ intermediate. (Figure 5-6, path ⓑ) The reaction proceeds from encounter complex **4** via TS**4**/**7** to give the insertion intermediate **7**. To reach the TS, two types of motion have to occur, (i) methyl-migration to the sulfur, and (ii) hydrogen-migration to the iron; thus the structure of TS**4**/**7** is difficult to guess. The sextet TS (E_{rel} =

44.8 kcal/mol) exhibits a structure, where iron is almost inserted into a C-H bond of the methane molecule with bond lengths r_{FeC} = 2.03 Å and r_{FeH} = 1.60 Å. The imaginary frequency of i212cm^{-1} corresponds to the motion of the methyl group from iron to sulfur in conjunction with a rotation of the methyl group around the iron-carbon bond. The quartet TS, however, could not be located despite extensive search. Nevertheless, a single-point calculation on the geometry of the sextet TS locates ^{4}TS**4**/**7** at E_{rel} = 64.8 kcal/mol as a very first approximation. The frequency calculation reveals two imaginary frequencies for this structure on the quartet PES (i359 and i153 cm^{-1}). The smaller corresponds to the motion and rotation of the methyl group in analogy to the sextet counterpart, while the larger corresponds to a an increase of the H–Fe–S–C dihedral angle. The energy and structure of an optimized ^{4}TS**4**/**7** will most likely change somewhat, but the TS is expected to be energetically located far above both, the entrance channel and TS**4**/**5**. Therefore, this pathway is unlikely to occur and is further on neglected in the overall interpretation of the data.

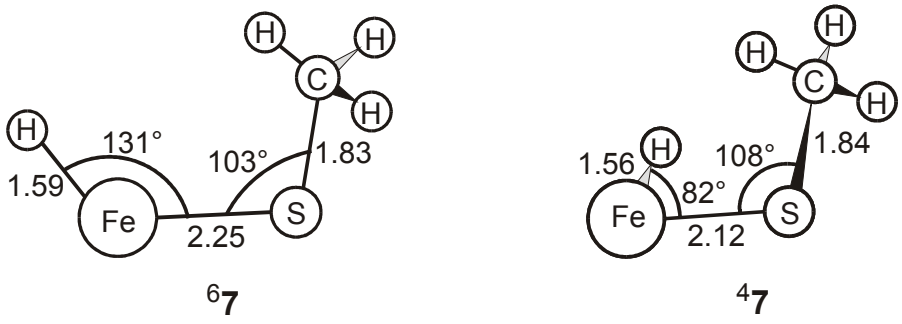

^{6}**7** ^{4}**7**

Chart 5-10: Insertion intermediate H**–**Fe**–**SCH_3^+ (**7**) of the FeS^+/CH_4-system obtained using the B3LYP/6-311+G* approach. Bond lengths are given in Å and angles in degree.

The quartet and sextet states of the insertion intermediate **7**, H–Fe–SCH_3^+, are located at E_{rel} = 0.3 and 2.0 kcal/mol, respectively. While ^{4}**7** is non-planar with a dihedral angle of θ_{HFeSC} = 75.2°, the sextet structure ^{6}**7** shows a planar arrangement of the HFeSC-substructure (θ_{HFeSC} = 0°), see Chart 5-10. Again, crossing between the sextet and quartet surfaces is assumed to be facile, given the similar geometries and energies. From **4**, the reaction can continue via TS**6**/**7** toward the product complex **6** which has been described above.

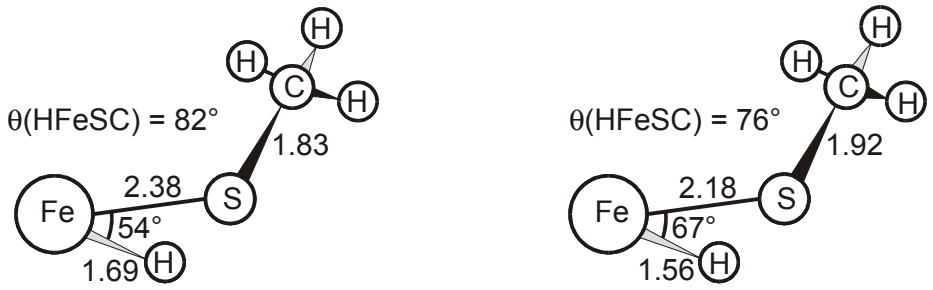

^{6}TS**6**/**7** ^{6}TS**6**/**7**

Chart 5-11: TS**6**/**7** of the FeS^+/CH_4-system obtained using the B3LYP/6-311+G* approach. Bond lengths are given in Å and angles in degree.

TS**6**/**7** (Chart 5-11), however, shows some interesting features. ^{6}TS**6**/**7** is located at E_{rel} = 24.4 kcal/mol, way above the entrance channel, with an imaginary frequency of i1148 cm^{-1}, corresponding mainly to the hydrogen-atom transfer from iron to sulfur. The situation is quite different in the quartet state. Despite numerous attempts to locate ^{4}TS**6**/**7** at the B3LYP/6-311+G* level of theory, no TS is found. The input structures collapse during optimization to give minimum ^{4}**6** or sometimes return to ^{4}**7**, thus pointing to a very flat PES in this region. Vertical excitation from the ^{6}TS**6**/**7** geometry to the quartet surface yields a relative energy for the quartet TS of only -0.8 kcal/mol; note, that this value actually lies below the corresponding minimum ^{4}**7**. In order to get more information about the quartet region, the basis set of the calculations is reduced to the 6-311G basis. At this level of theory, a stationary point ^{4}TS**6**/**7** is indeed found (Chart 5-11). The frequency calculation on this geometry at the B3LYP/6-311G level of theory shows a single imaginary frequency of i393 cm^{-1}, corresponding to the migration of the iron-bound hydrogen atom to the sulfur. Using the B3LYP/6-311+G* approach, a single-point calculation reveals the TS to be located at E_{rel} = 0.6 kcal/mol, i.e., only 0.3 kcal/mol above minimum ^{4}**7**. Note, however, that a frequency calculation at this higher level of theory shows two imaginary frequencies (i557 cm^{-1} and i139 cm^{-1}), of which the larger corresponds to hydrogen migration from iron to sulfur, while the smaller one represents a rotation of the methyl group around the putative Fe–C axis. Further optimization of this point using the B3LYP/6-311+G* level of theory leads to a continuous decrease of both imaginary frequencies and stopped at product complex ^{4}**6**. The close energies of ^{4}TS**6**/**7** and ^{4}**7** easily explain the difficulties encountered during localization of ^{4}TS**6**/**7** at the B3LYP/6-311+G* level of theory. It therefore deemed unnecessary to further explore this part of the PES, as the barrier associated with ^{4}TS**6**/**7** seems to be small anyhow and not very different from that found with the B3LYP/6-311G approach. Similar phenomena were already

observed in the theoretical investigations of the FeS^+/H_2 and ScS^+/H_2-systems,[42,52] in which the low-spin insertion intermediates do not represent true minima.

Products. Experimentally, Fe^+ and $FeSH^+$ are formed as major ionic products in the reaction of FeS^+ with CH_4, Equation 5–7 and Equation 5–8; minor ionic products are $FeCH_3^+$, $FeSCH_3^+$, and $FeSCH^+$, according to the reactions in Equation 5–9, 5–10, and 5–11 of deuterated methane. Three processes by which the different products may be formed are considered, i.e., (i) dissociation of insertion structure **5**, $CH_3–Fe–SH^+$ into either $FeCH_3^+$ + SH or $FeSH^+$ + CH_3, (ii) dissociation of **7**, $H–Fe–SCH_3^+$, to yield FeH^+ + CH_3S or $FeSCH_3^+$ + H, and (iii) dissociation of product complex **6**, $Fe(CH_3SH)^+$, to form methanethiol and Fe^+, $FeSH^+$ + CH_3, or $FeSCH_3^+$ + H. Thus, the investigation includes the experimentally observed ionic products together with their neutral counterparts as well as formation of FeH^+ and CH_3S. Note however, that because of the covalent nature of the sulfur-carbon and sulfur-hydrogen bonds in methanethiol loss of a methyl radical or hydrogen radical from **7**, $Fe(CH_3SH)^+$, is likely to be much less pronounced than loss of the whole methanethiol molecule.[53,54] Even more so, this holds true because the electrostatic nature of the bond between iron and methanethiol with a calculated bond energy of only 29.7 kcal/mol appears more easy to dissociate.

In the following, the products are presented in order of increasing molecular mass of the ionic species, starting with formation of $Fe^+(^6D)$ and methanethiol. Although at the B3LYP/6-311+G* level of theory the ground state of iron is calculated to be $Fe^+(^4F)$ with the $Fe^+(^6D)$ electronic state 6 kcal/mol above, the experimental state splitting is known to be 5.8 kcal/mol in favor of $Fe^+(^6D)$, see above.[34,35,52] To account for this, the experimental state splitting is used in the PES. Methanethiol as the neutral counterpart to Fe^+ exhibits C_1 symmetry and a carbon-sulfur bond length of r_{CS} = 1.84 Å. The energy of the $^6Fe^+$ + CH_3SH product channel is calculated as E_{rel} = 22.7 kcal/mol, and the corresponding quartet is corrected to the experimental state splitting 5.8 kcal/mol above the corresponding sextet.

The second feasible product is FeH^+ + CH_3S (E_{rel} = 48.0 kcal/mol), whose experimental counterpart FeD^+ is not observed however. The FeH^+ molecule has been described in detail in the chapter on the FeS^+/H_2-system and will therefore not be evaluated again. The corresponding neutral CH_3S radical is calculated in C_S symmetry and has a $^2A'$ ground state.

The next exit channel to be considered at E_{rel} = 37.1 kcal/mol corresponds to the SH radical and $FeCH_3^+$. In $FeCH_3^+$, the iron-carbon distance is r_{FeC} = 1.91 Å and the carbon-hydrogen bonds amount to r_{CH} = 1.10 Å each. The deuterated analog of this exit channel is indeed observed experimentally, although as a minor channel only.

$FeSH^+$ and CH_3 form another exit channel at E_{rel} = 24.5 kcal/mol, only slightly higher than the lowest energy channel, $Fe^+(^6D)$ and CH_3SH. The $FeSH^+$ product has been elucidated in detail earlier, in the product section of the FeS^+/H_2-system, while the methyl-radical shows the expected, umbrella-like geometry.

The last exit channel accessible via a one-step reaction is formation of $FeSCH_3^+ + H$ (E_{rel} = 35.9 kcal/mol). $FeSCH_3^+$ has a ^5A ground state in C_1 symmetry. The calculations predict a bond dissociation energy of $D_0(Fe^+\text{-}SCH_3)$ = 69.9 kcal/mol.[55] It is also conceivable to assume other structural isomers for this species, for instance with the connectivities $SFeCH_3^+$ or $(CH_2S)FeH^+$. While the $SFeCH_3^+$ isomer would be expected to emerge from dissociation of intermediate **5**, $CH_3–Fe–SH^+$, by breaking the hydrogen-sulfur bond, isomer $(CH_2S)FeH^+$ should arise from loss of a hydrogen atom from insertion intermediate **7**, $H–Fe–SCH_3^+$. Both isomers are somewhat unlikely to be formed as their formation involves breaking of quite strong covalent bonds (S–H[53] and C–H[56]) in the presence of bonds, whose cleavage is less demanding energetically (Fe^+–C and Fe^+–H). The calculations confirm this intuitive assignment, showing that the lowest-lying electronic states of the $SFeCH_3^+$ and $(CH_2S)FeH^+$ structural isomers are located 9.8 kcal/mol and 23.3 kcal/mol above the ground state $FeSCH_3^+$ isomer.

Experimentally, formation of the deuterated analog of $FeSCH^+$ is observed as another product. According to the mechanistic scheme presented in Figure 5-6, the $FeSCH^+$ product is assumed to form by loss of H_2 from $FeSCH_3^+$. In order to clarify the minimum structure of $FeSCH^+$, a global minimum search is carried out. The theoretical approach used here is different from the rest of this study. Geometry optimizations are generally known to be much more independent of the quality of the basis set and method used than the corresponding total and relative energetics of the calculated species; for example it is known, that even HF calculations with small basis sets can often yield reasonable geometries. Therefore, the geometry optimizations are carried out using B3LYP with a very small 3-21G basis, and the relative energies of the geometry optimized species are then determined by single-point calculations using the B3LYP/6-311+G* approach. Several structural isomers are conceivable for $FeSCH^+$. The results of the minimum-search are shown in Chart 5-12; the relative energies of the structures are displayed in Table 5-3.

Generally, the quintet and triplet states of the corresponding structural isomers are considered. The data in Table 5-3 reveal a tendency of the quintet species being less stable than their triplet counterparts. The most stable isomer is ^{3}**8**, in which iron, sulfur, and carbon form a three-membered ring and the hydrogen atom is attached to the carbon atom. The

symmetry of this isomer is C_1. The corresponding quintet isomer ^{5}**8** is located only 2.2 kcal/mol above the ground state, thus assignment of the ground state is ambiguous in this case.

Table 5-3: Total and relative energies of the $FeSCH^+$-species at the B3LYP/6-311+G*//B3LYP/3-21G level of theory. ZPVE corrections are not included.

species	spin state	energy (Hartree)	rel. energy (kcal/mol)
8	3	-1700.29646	0.0
	5	-1700.29289	2.2
9	3	-1700.25649	25.1
	5	-1700.24586	31.8
10	3	-1700.24951	29.5
	5	-1700.23116	41.0
11	3	-1700.21064	53.8
	5	-1700.19911	61.1
12	3	-1700.20302	58.6

All other structural isomers are much less favorable than ^{3}**8** (see Table 5-3 and Chart 5-12). Also note, that the assumption that the small 3-21G basis is sufficient to properly describe the geometry of the $FeSCH^+$ species is further verified by complete geometry optimization of the minimum species ^{3}**6** and the corresponding quintet ^{5}**6** at the B3LYP/6-311+G* level of theory, which resulted in only small and negligible geometry changes. The energetic difference between ^{3}**6** and ^{5}**6** decreases from 2.2 kcal/mol in the B3LYP/6-311+G*//B3LYP/3-21G approach by only 0.2 kcal/mol to 2.0 kcal/mol in favor of ^{3}**6** at the B3LYP/6-311+G*//B3LYP/6-311+G* level of theory. For the minimum structure, the calculations suggest $D_0(Fe^+\text{-SCH})$ = 67.3 kcal/mol. The question remains, why the 3-membered ring is the most stable structure for $FeSCH^+$ as compared to $FeSCH_3^+$, where the methyl group is bent away from iron with an Fe–S–C angle of 108°. The rationale for this structure seems to be the following: taking off two hydrogen atoms from $FeSCH_3^+$ leads to a carbene-like electronic structure on the carbon atom which requires further stabilization. Bending of the carbon atom towards iron and formation of an Fe–C bond will stabilize the structure in two ways: (i) Fe^+ is capable of accepting some of the electron density from the carbon due to its positive charge and (ii) as a result of the ring formation, additionally the positive charge is delocalized over the whole ring, as indicated by the Mullikan charge

analysis; note, that the integrated charge on the hydrogen atom is included in the charge of the carbon atom (q_{Fe}: +0.55; q_C: +0.12, q_S: + 0.33). The occurrence of charge delocalization is also supported by a comparison of the ionization energies (*IE*s) of iron (IE_{Fe} = 7.9 eV) and the thioformyl radical HCS (IE_{HCS} > 7.3 eV).[57] Therefore, formation of the ring structure after detachment of two hydrogen atoms from $FeSCH_3^+$ finds a rationale.

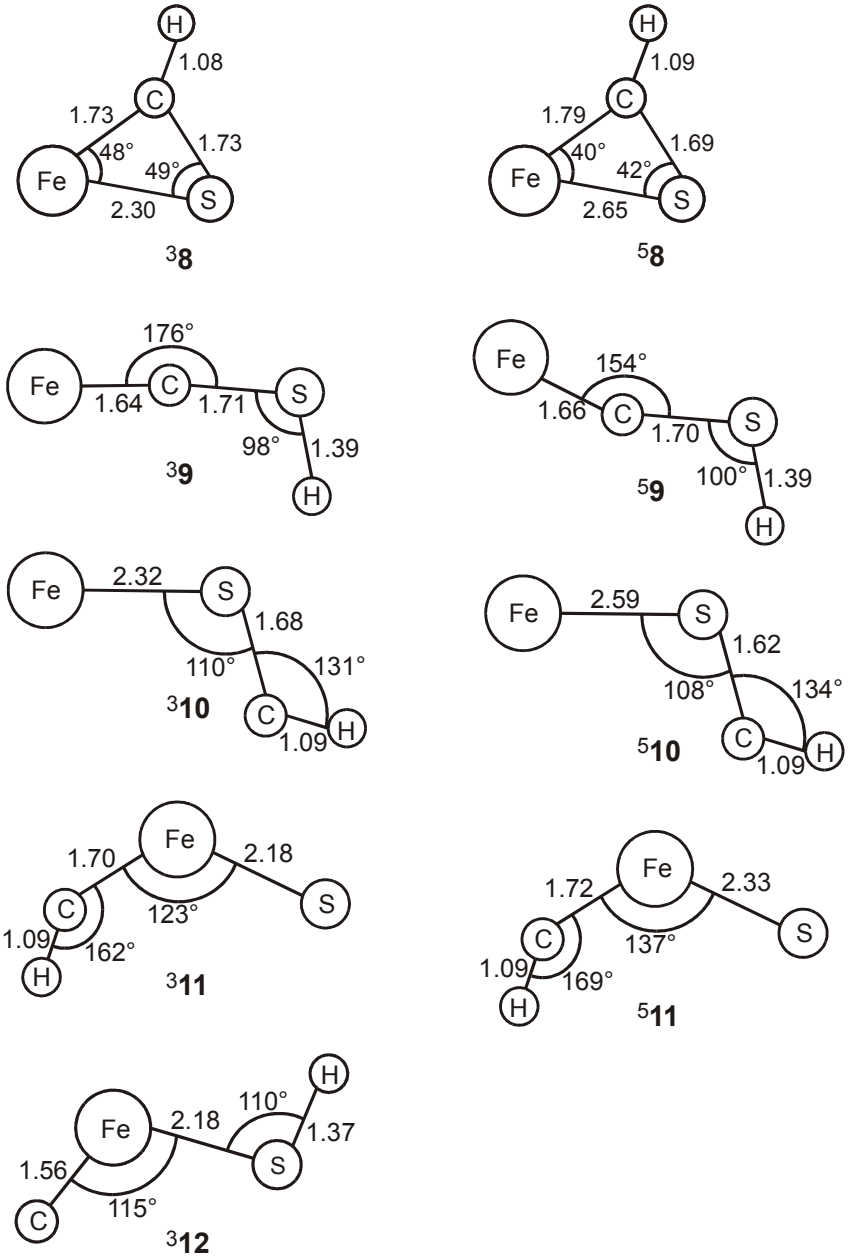

Chart 5-12: Structures of $FeSCH^+$, obtained using the B3LYP/6-311+G*//B3LYP/3-21G approach. Bond lengths are given in Å and angles in degree.

5.3.3 Discussion

Combination of the stationary points presented in the results section yields the potential-energy surfaces depicted in Figures 5–7 and 5–8. In the construction of the PES, only the most stable conformers are considered, because the barriers for the interconversion of the electrostatically bound conformers are assumed to be much lower than the barriers associated with the breaking and formation of covalent bonds. Also note, that the predicted barriers for the lowest-energy pathways are below the thermochemical threshold for all products, such that theory leads us to expect all products to be formed in the GIB at thermochemical threshold.

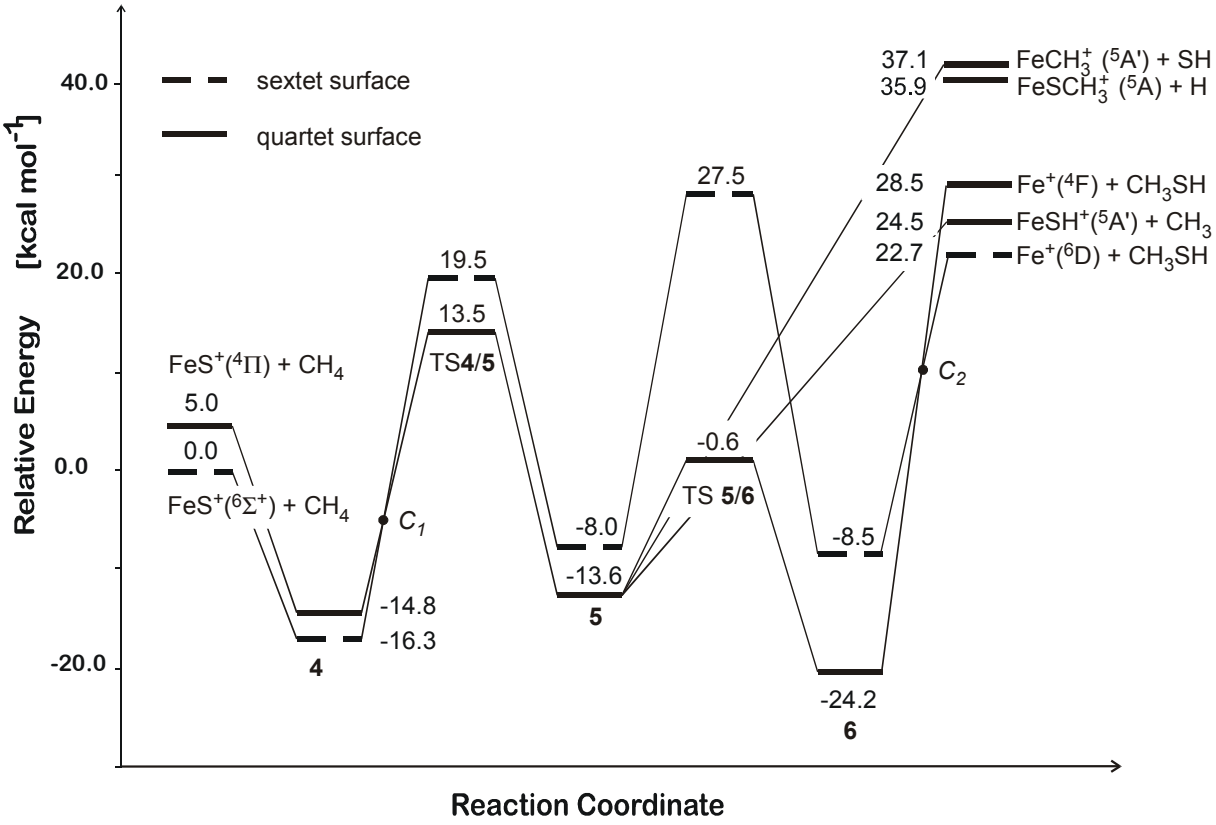

Figure 5-7: B3LYP/6-311+G* potential-energy surface for pathway ⓐ of the FeS^+/CH_4-system involving intermediate formation of CH_3-Fe-SH^+. All energies are given in kcal/mol relative to the entrance channel $FeS^+ + CH_4$ and include ZPVE contributions. C_1 and C_2 denote the tentative crossing points between the sextet and the quartet surfaces as discussed in the text.

Reaction via CH_3–Fe–SH^+ intermediate. (Figure 5-7) The calculated threshold of the overall reaction of formation of Fe^+ (22.7 kcal/mol = 0.98 eV) lies above the experimental (GIB) threshold of 0.65 ± 0.11 eV. However, considering the error of the PES of 8 kcal/mol

and further considering the problems of the B3LYP approach in the calculation of atoms and atomic ions, the deviation is acceptable. In addition, the threshold of 0.86 ± 0.12 eV obtained from literature thermochemistry fits smoothly into the above picture.

The formation of Fe^+ at threshold energies, however, cannot occur via the sextet surface alone because the barrier ^{6}TS**5**/**6** is significantly above the exit channel. Instead, the reaction may cross to the quartet surface at the putative crossing point C_1 between the encounter complex **4** and TS**4**/**5**.[58] The reaction then continues on the quartet surface from the low-lying TS ^{4}TS**4**/**5** (E_{rel} = 13.5 kcal/mol) to the insertion intermediate ^{4}**5**, CH_3–Fe–SH^+. The latter may then either dissociate into the products $FeCH_3^+$ and $FeSH^+$ or form the product complex ^{4}**6**, $Fe(CH_3SH)^+$, via ^{4}TS **5**/**6**. Note, that energetically ^{4}TS**4**/**5** lies much below the energies of the corresponding exit channels $FeSH^+$ + CH_3 at E_{rel} = 24.5 kcal/mol and $FeCH_3^+$ + SH at E_{rel} = 37.1 kcal/mol. Formation of product complex ^{4}**6** and further dissociation allows to access $Fe^+(^4F)$ + CH_3SH and provides pathways to form (i) $FeSH^+$ + CH_3 by breaking the carbon-sulfur bond, and (ii) $FeSCH_3^+$ + H by breaking the sulfur-hydrogen bond. Due to the weakness of the bond between Fe^+ and methanethiol as compared to the C–S or S–H bond energies, loss of CH_3SH under formation of Fe^+ is much more pronounced than loss of a H- or CH_3-radical from the methanethiol unit. Therefore, the major product expected at thermal threshold is formation of Fe^+ and methanethiol which agrees nicely with the experimental observations.

Some ambiguity remains about the details of the $FeSH^+$ channel. The calculated reaction endothermicity amounts to 24.5 kcal/mol (1.06 eV) in good agreement with literature thermochemistry. The calculations also reveal that product formation should not be hindered by barriers in excess of the reaction endothermicity. As shown in the results section, no quantitative experimental result are obtained for the $FeSH^+$ threshold, but rather in a more qualitative manner it is stated that this channel rises at approximately 2 eV and thus much too late as compared to both, theory and literature thermochemistry. Upon closer inspection of the PES and the experimental data, two explanations are possible.

(i) As discussed above, starting from ^{4}**5**, three possibilities are conceivable for the reaction to proceed, i.e. two dissociation pathways and reaction towards the product complex ^{4}**6**. In the following, the direct dissociation to access $FeSH^+$ + CH_3, and rearrangement via ^{4}TS**5**/**6** leading to formation of the product complex ^{4}**6** are evaluated in detail. The third possibility, i.e. direct dissociation of ^{4}**5** giving rise to formation of $FeCH_3^+$ and SH, is not considered because of the high energy demand which excludes involvement of this product channel in explaining the delayed threshold of the $FeSH^+$ product. Thermochemistry predicts direct

dissociation of insertion intermediate ^{4}**5** into $FeSH^+ + CH_3$ to be 25.1 kcal/mol energetically disfavored compared to formation of the product complex ^{4}**6** (Figure 5-7). More importantly, formation of ^{4}**6** is strongly exothermic while dissociation of ^{4}**5** to give $FeSH^+$ would require further energy input. These facts are likely to result in a strong competition between the two channels, with the $FeSH^+$ channel being almost absent at energies close to threshold, such that most particles are expected to move on along the PES to form ^{4}**6**. Once this ion is formed, it's dissociation to form Fe^+ or $FeSH^+$ competes with a preference for formation of Fe^+ due to the lower threshold of this channel. On the sextet PES, dissociation of ^{6}**5** may easily result in either dissociation or formation of ^{6}**6**, because ^{6}TS**5**/**6** along the way to form ^{6}**6** is energetically comparable to the dissociation exit channel. In contrast to the situation on the quartet surface, dissociation of ^{6}**5** should therefore not be suppressed but should rather effectively compete with the hydrogen migration to form ^{6}**6**. However, ^{6}**5** has only a low probability to be formed. The predicted relative energy of ^{6}TS**4**/**5** (E_{rel} = 19.5 kcal/mol) does not allow for formation of ^{6}**5** below this energy. As ^{4}TS**4**/**5** is located 6 kcal/mol below its sextet counterpart, most of the sextet species will flip spin along the reaction coordinate if an efficient crossing between the sextet and quartet surfaces is assumed at the arbitrarily drawn crossing point C_1. In the previous part of this chapter, it has been shown for the FeS^+/H_2-system that the assumption of an efficient crossing may well be justified. Thus, the probability for the reactant complex to traverse ^{6}TS**4**/**5** at low energies is strongly reduced and only a small percentage of reactant collisions will reach intermediate ^{6}**5**. At higher interaction energies the crossing probability decreases, as the motion of the reactants speeds up. Therefore, at higher interaction energies more particles will traverse ^{6}TS**4**/**5** and access ^{6}**5**, where they may form $FeSH^+$ effectively. The hindered formation of ^{6}TS**4**/**5** leads us therefore to expect a competition induced threshold delay for $FeSH^+$ formation.

(ii) Although the competition argument is able to bring about compatibility between the experimentally observed features and the calculated PES, shortcomings of the experiment need to be considered as well. As described above, due to the scattered and noisy experimental data no quantitative threshold fit for the $FeSH^+$ channel is obtained. Although the qualitative assignment leads to the conclusion that the $FeSH^+$ channel rises too late, the particular noise level in the low-energy regime may well hide a low-energy feature due to electronic or structural isomers. The calculations show for instance, that besides the quintet ground state of $FeSH^+$ there exists a corresponding $FeSH^+$ triplet isomer, for which the calculations resulted in an energy splitting $^5FeSH^+/^3FeSH^+$ of 0.77 eV (17.8 kcal/mol). Another structural isomer, $^5HFeS^+$, is also calculated 1.98 eV (45.7 kcal/mol) above $^5FeSH^+$.

Therefore, in a trial fit, the experimental data are reproduced using a bimodal behavior and a fixed threshold of 1.27 eV (29.3 kcal/mol) according to literature thermochemistry. The results are shown in Table 5-2. The experimental data are reproduced well by this approach. For the second feature an approximate threshold of E_0 = 3.1 eV is obtained, however the uncertainty in the data is too large to assign this value to a certain process.

In summarizing pathway ⓐ, the reaction via intermediate **5**, CH_3–Fe–SH^+, does explain formation of the experimentally observed products Fe^+, $FeCH_3^+$ and $FeSCH_3^+$ easily, while the delayed formation of $FeSH^+$ requires either (i) the consideration of competition arguments or (ii) one has to assume a bimodal behavior for the experimental data with the low-energy feature hidden in the noise.

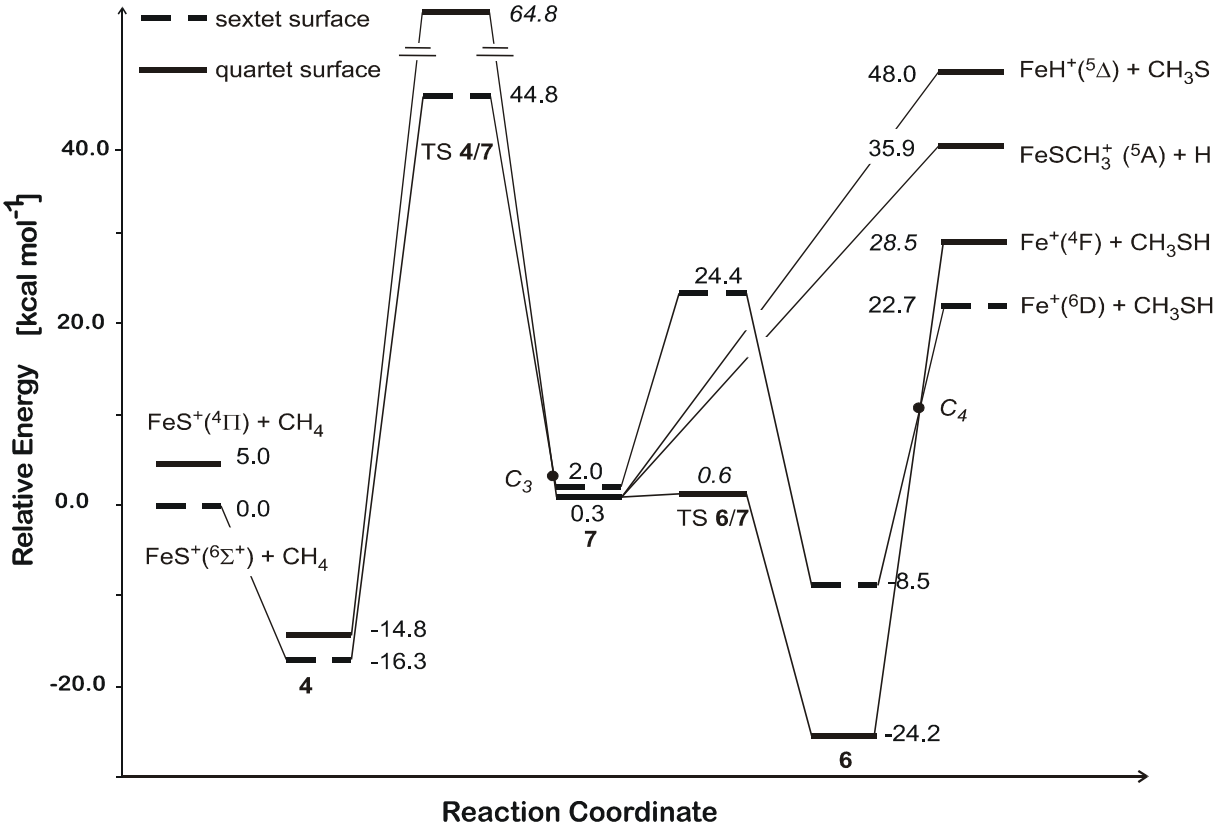

Figure 5-8: B3LYP/6-311+G* potential-energy surface for pathway ⓑ of the FeS^+/CH_4-system involving intermediate formation of H–Fe–SCH_3^+. All energies are given in kcal/mol relative to the entrance channel $FeS^+ + CH_4$ and include ZPVE contributions. C_3 and C_4 denote the tentative crossing points between the sextet and the quartet surfaces as discussed in the text.

Reaction via the intermediate H–Fe–SCH_3^+. (Figure 5-8) In analogy to the calculated behavior of the FeS^+/CH_4-system along path ⓐ, the occurrence of path ⓑ along intermediate **7**, H–Fe–SCH_3^+, on the sextet surface is excluded from further consideration due to the

substantially increased energy demands of ^{6}TS**4**/**7** and ^{6}TS**6**/**7**. Moreover, even reaction along the quartet surface is unlikely to occur due to the energy demand of ^{4}TS**4**/**7**. In good agreement with these calculations, formation of FeH^+, which is only conceivable via pathway ⓑ, is not observed at all in the experiments. Thus, the primary insertion reaction occurs regioselectively by exclusively forming intermediate **5**.

Before summarizing these data, another brief discussion of the formation of the $FeSCH^+$ product channel should be added. The latter is assumed not to be a primary product, but rather to stem from consecutive elimination of H_2 from $FeSCH_3^+$. It is also possible to think of $FeSCH^+$ being formed from primary loss of H_2, followed by loss of a H radical from the intermediate $FeSCH_2^+$. However, if the latter pathway holds true an intermediate product $FeSCH_2^+$ would be expected, which is not observed experimentally. The cross section of the putative $FeSCH_2^+$ intermediate may of course decrease at high interaction energies, when the reaction rate for the loss of the deuterium radical is expected to speed up. However, as formation of $FeSCH_2^+$ is not observed at all, formation of $FeSCH^+$ occurs most likely via primary loss of H and subsequent elimination of H_2 from the intermediate product $FeSCH_3^+$. This is in line with the experimental cross sections of $FeSCD_3^+$ and $FeSCD^+$, Figure 5-4. While the $FeSCD_3^+$ channel rises somewhat earlier, it decreases dramatically as soon as the $FeSCD^+$ product appears, and at higher interaction energies (>7.3 eV in the center-of-mass frame) only formation of $FeSCD^+$ is observed, pointing to an increased reaction rate for the deuterium loss and a corresponding decrease in the lifetime of the $FeSCD_3^+$ product.

5.3.4 Summary

In the seemingly simple reaction of FeS^+ with CH_4, several ionic product species are observed experimentally. The experimental threshold for formation of Fe^+ at 0.65 eV ± 0.11 eV (15.0 ± 2.5 kcal/mol) agrees with the thermochemistry calculated from the B3LYP/ 6-311+G* approach (22.7 ± 6 kcal/mol) as well as the literature thermochemistry (18.0 ± 2.7 kcal/mol). For the $FeSH^+$ product qualitatively a delayed experimental threshold is diagnosed, while the B3LYP/6-311+G* calculations in agreement with literature thermochemistry expect the product to be formed at threshold. Two possible explanations for the difference between theory and experiment are suggested, (i) that the delayed threshold may be due to competition between the dissociation of ^{4}**5**, CH_3–Fe–SH^+ and the rearrangement to give ^{4}**6**; or (ii) that due to the noise level of the data a small low-energy feature may exist but not be visible in the experimental data.

All results are in line with the occurrence of only one of the two theoretically investigated reaction mechanisms; i.e., the pathway via intermediate formation of $CH_3–Fe–SH^+$. The second pathway via intermediate formation of $H–Fe–SCH_3^+$ may be ruled out because of the high energy demand associated with the hydrogen migration to form the product complex $Fe(CH_3SH)^+$. In addition, along the operative pathway ⓐ even participation of the sextet surface may be ruled out due to the energy demands of the associated TSs. Loss of Fe^+ accompanied by formation of CH_3SH is calculated to be the thermodynamically favorite reaction; accordingly, this product dominates in the experiments. The experimentally observed product $FeSH^+$ is in line with either direct dissociation of **5** or formation of the product complex **6** and subsequent breakage of the carbon-sulfur bond. The $FeCH_3^+$ product is formed exclusively by direct dissociation of the intermediate $CH_3–Fe–SH^+$, and the experimental observation of $FeSCH_3^+$ can only be explained by breaking the sulfur-hydrogen bond in product complex **6**, $Fe(CH_3SH)^+$. The formation of $FeSCH^+$ is explained by the occurrence of a secondary H_2-loss reaction starting from $FeSCH_3^+$.

5.4 Conclusions

The two reactions of FeS^+ with H_2 and CH_4 show some general trends. (i) All product channels appear experimentally only at elevated energies. (ii) The major product in both reactions is formation of Fe^+ under incorporation of the sulfur atom into the activated σ-bond of the substrate. (iii) Although simple thermodynamics determines the formation of high-energy products, the formation of the major products is dominated by kinetic effects. (iv) The reactions follow similar patterns, i.e. primary 1,2-insertion of FeS^+ into a bond of the substrate and subsequent migration of a hydrogen- or methyl-group to yield the product complexes.

In principle, the same reaction pattern should apply for higher alkanes. For linear alkanes, reaction with iron results for the most part in loss of H_2S, but starting with butane, loss of two neutral molecules, i.e. H_2S and small carbon-hydrogen species is observed as well, although in minor amounts only.[9b] Some speculation about possible reaction mechanisms for the higher alkenes should now be allowed, although under careful consideration of the results of the FeS^+/H_2- and FeS^+/CH_4-systems. In linear alkanes, the FeS^+ unit is most likely going to activate the most easily accessible C–H bonds in the same manner as described for FeS^+/H_2 and FeS^+/CH_4. For steric reasons, these are assumed to be the terminal C–H bonds. Thus, 1,2-addition of FeS^+ yields species of the general structure $C_nH_{2n+1}FeSH$. As shown for the

FeS^+/CH_4 system, the direction of the 1,2-addition is "predefined" in that the hydrogen atom will attach to the sulfur side of the reagent. In the second reaction step, migrations of C_nH_{2n+1}-moieties become more and more unlikely with increasing n. Therefore, in contrast to methane, in higher alkanes migration of a second hydrogen atom to sulfur is likely to be preferred over C_nH_{2n+1}- migrations for $n \geq 2$. After dissociation of H_2S, formation of a iron-alkene product complexes occurs.

Thus, the mechanistic scenarios for small substrates may, although cautiously, be translated to their higher homologs and in the present case, they are well able to explain the as yet available experimental data.

References

[1] (a) B. Delman *Bull. Soc. Chim. Belg.* **1995**, *104*, 173. (b) K.-T. Li, M.-Y. Huang, W.-D. Cheng *Ind. Eng. Chem. Res.* **1996**, *35*, 621. (c) K.-T. Li, N.-S. Shyu *Ind. Eng. Chem. Res.* **1997**, *36*, 1480. (d) X. Zhang, C. A. Dullaghan, G. B. Carpenter, D. A. Sweigart, Q. Meng *J. Chem. Soc., Chem. Comm.* **1998**, 93. (e) T. Becue, J. Leglise, M. Manoli, C. Potvin, D. Cornet *J. Catal.* **1998**, *179*, 90.

[2] (a) R. Cammack *Adv. Inorg. Chem.* **1992**, *38*, 281. (b) R. Cammack, A. G. Sykes *Advances in Inorganic Chemistry*, Academic Press **1992**. (c) D. H. Flint, R. M. Allen *Chem. Rev.* **1996**, *96*, 2315. (d) H. Beinert, M. C. Kennedy, C. D. Stout *Chem. Rev.* **1996**, *96*, 2335. (e) P. J. Stephens, D. R. Jollie, A. Warshel *Chem. Rev.* **1996**, *96*, 2491. (f) I. Bertini, C. Luchinat, G. Mincione, A. Soriano *Inorg. Chem.* **1998**, *37*, 969.

[3] For Ni/Fe/S-reactive cores in enzymes, see: (a) R. Cammack *Adv. Inorg. Chem.* **1988**, *32*, 297. (b) M. J. Maroney Comments *Inorg. Chem.* **1995**, *17*, 347, and references cited therein.

[4] (a) R. R. Eady, R. L. Robson, T. H. Richardson, R. W. Miller, M. Hawkins *Biochem. J.* **1987**, *244*, 197. (b) Y. Deng, Q. Liu, Y. Yang, Y. Wang, Y. Cai, D. Wu, C. Chen, D. Liao, B. Kang, J. Lu *Inorg. Chem.* **1997**, *36*, 214.

[5] (a) W. Kaim, B. Schwederski *Bioanorganische Chemie*, Teubner, Stuttgart, **1991**. (b) S. J. Lippert, J. M. Berg *Principles of Bioinorganic Chemistry*, University Science Books, Mill Valley, **1994**. (c) H. Ogino, S. Inomata, H. Tobita *Chem. Rev.* **1998**, *98*, 2093.

[6] For investigations on model compounds of Ni/Fe/S-hydrogenase, see: (a) M. Cha, C. L. Gatlin, S. C. Critchlow, J. A. Kovacs *Inorg. Chem.* **1993**, *32*, 5868. (b) C. A. Marganian, H. Vazir, N. Baudya, M. M. Olmstead, P. K. Mascharak *J. Am. Chem. Soc.* **1995**, *117*, 1587. (c) G. Musie, P. J. Farmer, T. Tuntulani, J. H. Reibenspies, M. Y. Darensbourg *Inorg. Chem.* **1996**, *35*, 2176.

[7] (a) S. Harris *Chem. Phys.* **1982**, *67*, 229. (b) S. Harris, R. R. Chianelli *Chem. Phys. Lett.* **1983**, *101*, 603. (c) C. W. Bauschlicher, P. Maitre *Theor. Chim. Acta* **1995**, *90*, 189.

[8] A. Müller, E. Diemann, R. Jostes, H. Bögge *Angew. Chem.* **1981**, *93*, 957.

[9] (a) T. J. Carlin, M. B. Wise, B. S. Freiser *Inorg. Chem*. **1981**, *20*, 2745. (b) T. C. Jackson, T. J. Carlin, B. S. Freiser *Int. J. Mass Spectrom. Ion Processes* **1986**, *72*, 169. (c) T. J. McMahon, T. C. Jackson, B. S. Freiser *J. Am. Chem. Soc*. **1989**, *111*, 421. (d) I. G. Dance, K. J. Fisher, G. D. Willett *Angew. Chem., Int. Ed. Engl.* **1995**, *34*, 201. (e) I. G. Dance, K. J. Fisher, G. D. Willett *Inorg. Chem.* **1996**, *35*, 4177. (f) J. N. Harvey, C. Heinemann, A. Fiedler, D. Schröder, H. Schwarz *Chem. Eur. J.* **1996**, *2*, 1230. (g) I. Kretzschmar, A. Fiedler, J. N. Harvey, D. Schröder, H. Schwarz *J. Phys. Chem. A* **1997**, *101*, 6252. (h) I. Kretzschmar, D. Schröder, H. Schwarz *Int. J. Mass Spectrom. Ion Processes* **1997**, *167/168*, 103. (i) K. J. Fisher, I. G. Dance, G. D. Willett *J. C. S. Dalton Trans.* **1998**, 975. (k) I. Kretzschmar, D. Schröder, H. Schwarz, C. Rue, P. B. Armentrout *J. Phys. Chem. A* **1998**, *102*, 10060. (l) I. Kretzschmar *Energetics and Reactivity of the Binary Transition-Metal Sulfides of the 2nd and 3rd Row*, Ph.D. Thesis Technische Universität Berlin D83, Shaker-Verlag, Berlin, **1999**. (m) I. Kretzschmar, D. Schröder, H. Schwarz, P. B. Armentrout In: *Advances in Metal and Semiconductor Clusters – Metal-Ligand Bonding and Metal-Ion Solvation*, M. A. Duncan (Ed.), JAI PRESS Inc, Stanford, in press.

[10] For metal-sulfide clusters, see: (a) E. Ramli, T. B. Rauchfuss, C. L. Stern *J. Am. Chem. Soc.*, **1990**, *112*, 4043. (b) J. H. E. Nakat, I. G. Dance, K. J. Fisher, D. Rice, G. D. Willett *J. Am. Chem. Soc.*, **1991**, *113*, 5141. (c) S. Dehen, A. Schäfer, R. Ahlrichs, D. Fenske *Chem. Eur. J.* **1996**, *2*, 429. (d) K. J. Fisher, I. G. Dance, G. D. Willett, M. Yi *J. Chem. Soc., Dalton Trans.* **1996**, 709. (e) A. Nakajima, T. Hayase, F. Hayakawa, K. Kaya

Chem. Phys. Lett. **1997**, *280*, 381. (f) J. N. Harvey, D. Schröder, H. Schwarz *Inorg. Chim. Acta*, **1998**, *273*, 111.

[11] *Gaussian 94* (Revision A.1), M. J. Frisch, G. W. Trucks, H. B. Schlegel, P. M. W. Gill, B. G. Johnson, M. A. Robb, J. R. Cheeseman, T. A. Keith, G. A. Petersson, J. A. Montgomery, K. Raghavachari, M. A. Al-Laham, V. G. Zakrzewski, J. V. Ortiz, J. B. Foresman, J. Cioslowski, B. B. Stefanov, A. Nanayakkara, M. Challacombe, C. Y. Peng, P. Y. Ayala, W. Chen, M. W. Wong, J. L. Andres, E. S. Replogle, R. Gomperts, R. L. Martin, D. J. Fox, J. S. Binkley, D. J. Defrees, J. Baker, J. P. Stewart, M. Head-Gordon, C. Gonzalez, J. A. Pople, Gaussian Inc., Pittsburgh **1995**.

[12] A. D. McLean, G. S. Chandler *J. Chem. Phys.* **1980**, *72*, 5639.

[13] (a) A. H. J. Wachters *J. Chem. Phys.* **1972**, *52*, 1033. (b) P. J. Hay *J. Chem. Phys.* **1977**, *66*, 4377. (c) K. Raghavachari, G. W. Trucks *J. Chem. Phys.* **1989**, *91*, 1062.

[14] T. Clark, J. Chandrasekhar, G. W. Spitznagel, P. v. R. Schleyer *J. Comp. Chem.* **1983**, *4*, 294.

[15] S. Bärsch, I. Kretzschmar, D. Schröder, H. Schwarz, P. B. Armentrout *J. Chem. Phys. A* **1999**, *103*, 5925.

[16] M. W. Chase Jr., C. A. Davies, J. R. Downey Jr., D. J. Frurip, R. A. McDonald, A. N. Syverud *J. Phys. Chem. Ref. Data* **1985**, *14*, Suppl. 1 (JANAF Tables).

[17] (a) J. L. Elkind, P. B. Armentrout *J. Am. Chem. Soc.* **1986**, *108*, 2765. (b) J. L. Elkind, P. B. Armentrout *J. Phys. Chem.* **1986**, *90*, 5736.

[18] D. Schröder, I. Kretzschmar, H. Schwarz, C. Rue, P. B. Armentrout *Inorg. Chem.* **1999**, *38*, 3474.

[19] P. B. Armentrout, B. L. Kickel In: *Organometallic Ion Chemistry*, B. S. Freiser (Ed.), Kluwer, Dordrecht **1996**.

[20] M. Brönstrup, I. Kretzschmar, D. Schröder, H. Schwarz *Helv. Chim. Acta* **1998**, *81*, 2348.

[21] J. Berkowitz, G. B. Ellison, D. Gutman *J. Phys. Chem.* **1994**, *98*, 2744

[22] M. Brönstrup, D. Schröder, H. Schwarz *Chem. Eur. J.* **1999**, *5*, 1176.

[23] (a) E. R. Fisher, R. H. Schultz, P.B. Armentrout *J. Phys. Chem.* **1989**, *93*, 7382. (b) D. Schröder, J. Hrusak, H. Schwarz *Ber. Bunsenges. Phys. Chem.* **1993**, *97*, 1085.

[24] (a) D. L. Hildenbrand *J. Chem. Phys.* **1995**, *103*, 2634. (b) R. D. Bach, D. S. Shobe, H. B. Schlegel, C. J. Nagel *J. Phys. Chem*. **1996**, *100*, 8770.

[25] D. E. Clemmer, Y.-M. Chen, F. A. Khan, P. B. Armentrout *J. Phys. Chem.* **1994**, *98*, 6522.

[26] (a) M. M. Kappes, R. H. Staley *J. Phys. Chem.* **1981**, *85*, 942. (b) D. Schröder, A. Fiedler, M. F. Ryan, H. Schwarz *J. Phys. Chem.* **1994**, *98*, 68. (c) A. Fiedler, D. Schröder, S. Shaik, H. Schwarz *J. Am. Chem. Soc.* **1994**, *116*, 10734. (d) V. I. Baranov, G. Jahavery, A. C. Hopkinson, D. K. Böhme *J. Am. Chem. Soc.* **1995**, *117*, 12801. (e) A. Fiedler, Ph.D. Thesis, Technische Universität Berlin D83, 1996. (f) D. Schröder, H. Schwarz, D. E. Clemmer, Y.-M. Chen, P. B. Armentrout, V. I. Baranov, D. K. Böhme *Int. J. Mass Spectrom. Ion Processes* **1997**, *161*, 175.

[27] M. Filatov, S. Shaik *J. Phys. Chem. A* **1998**, *102*, 3835.

[28] The error is estimated from the average deviations of the calculated heats of reaction for several model processes from known literature values. The reactions employed in this procedure are: (a) $FeS^+ + H_2 \rightarrow Fe^+$ (^{4}F) + H_2S, (b) Fe^+ (^{6}D) $\rightarrow Fe^+$ (^{4}F), (c) FeS^+ ($^6\Sigma^+$) $\rightarrow FeS^+$ ($^4\Pi$), (d) $H_2S \rightarrow HS + H$, and (e) $FeH^+ + SH \rightarrow FeSH^+ + H$.

[29] See also: O. Hübner, V. Termath, A. Berning, J. Sauer *Chem. Phys. Lett.* **1998**, *294*, 37.

[30] S. Shaik, D. Danovich, A. Fiedler, D. Schröder, H. Schwarz *Helv. Chim. Acta* **1995**, *78*, 1393.

[31] J. Hrušak, D. Schröder, H. Schwarz *Chem. Phys. Lett.* **1994**, *225*, 416.

[32] S. Hoyan, G. Ohanessian *Chem. Phys. Lett.* **1997**, *280*, 266.

[33] (a) M. Newcomb, M.-H. Le Tadic-Biadetti, D. A. Putt, P. F. Hollenberg *J. Am. Chem. Soc.* **1995**, *117*, 3312. (b) M. Newcomb, M.-H. Le Tadic-Biadatti, D. L. Chestrey, E. S. Roberts, P. F. Hollenberg *J. Am. Chem. Soc.* **1995**, *117*, 12085.

[34] C. E. Moore *Atomic Energy Levels*, National Standard Ref. Data; National Bureau of Standards NSRDS-NBS 35: Washington D.C., *1971*.

[35] (a) O. Gunnarson, R. O. Jones *Phys. Rev. B* **1985**, *31*, 7588. (b) T. V. Russo, R. L. Martin, P. J. Hay *J. Chem. Phys.* **1994**, *101*, 7729. (c) M. C. Holthausen, C. Heinemann, H. H. Cornehl, W. Koch, H. Schwarz *J. Chem. Phys.* **1995**, *102*, 4931. (d) C. W. Bauschlicher Jr. *Chem. Phys.* **1996**, *211*, 163.

[36] As the nature of **3** is very much that of a simple electrostatic complex, the relative stabilities of **3** (^{4}A") and **3** (^{6}A") may well also be affected. This would place the sextet and quartet species very close in energy.

[37] (a) G. Ohanessian, W. A. Goddard III *Acc. Chem. Res.* **1990**, *23*, 386. (b) L. G. M. Petterson, C. W. Bauschlicher, S. R. Langhoff, H. Partridge, *J. Chem. Phys.* **1987**, *87*, 481. (c) E. A. Carter, W. A. Goddard III *J. Phys. Chem.* **1988**, *92*, 5679.

[38] M. L. McKee *J. Am. Chem. Soc.* **1990**, *112*, 2601.

[39] One may think of a third mechanism (see Ref. 27), where the dihydrogen approaches the FeS^+ in a colinear manner at the sulfur. Next, a hydrogen radical is transferred from the hydrogen molecule to the FeS^+ in a single step to yield $FeSH^+$ and H. In terms of the PES depicted in Figure 5-2**,** this is equivalent to entering the PES from the product side at the energy of $FeSH^+$ + H with no barrier in excess of the reaction endothermicity. Thus, although possible, this mechanism can not explain the delayed threshold observed for $FeSH^+$ and is therefore not considered any further.

[40] S. Shaik, M. Filatov, D. Schröder, H. Schwarz *Chem. Eur. J.* **1998**, *4*, 193.

[41] "Normal" refers to the default setting in Gaussian 94: Max. Force = 0.00045; RMS Force = 0.00030; Max. Displacement = 0.00180; RMS Displacement = 0.00120, whereas "tight" convergence criteria correspond to: Max. Force = 0.000015; RMS Force = 0.000010; Max. Displacement = 0.000060; RMS Displacement = 0.000040.

[42] (a) J. L. Tilson, J. F. Harrison *J. Phys. Chem.* **1991**, *95*, 5097. (b) J. L. Tilson, J. F. Harrison *J. Phys. Chem.* **1992**, *96*, 1667

[43] D. Danovich, S. Shaik *J. Am. Chem. Soc.* **1997**, *119*, 1773.

[44] (a) H. Schwarz *Angew. Chem.* **1991**, *102*, 837. (b) J. M. Fox *Catal. Rev. – Sci. Eng.* **1993**, *35*, 169. (c) F. D. Mango, J. W. Hightower, A. T. James *Nature* **1994**, *368*, 536. (d) R. H. Crabtree *Chem. Rev.* **1995**, *95*, 987. (e) G. Olah, A. Molnar *Hydrocarbon Chemistry*, Wiley, New York, 1995. (f) J. J. Schneider *Angew. Chem.* **1996**, *108*, 1133. (g) D. L. Strout, S. Zaric, S. Niu, M. B. Hall *J. Am. Chem. Soc.* **1996**, *118*, 6068.

[45] Chem. Eng. News **1993**, 31, 27.

[46] For transition-metal mediated CH_4 activation, see, for instance: (a) D. Schröder, H. Schwarz *Angew. Chem.* **1990**, *102*, 1468. (b) P. A. M. van Koppen, P. R. Kemper, J. E. Bushnell, M. T. Bowers *J. Am. Chem. Soc.* **1995**, *117*, 3294. (c) M. F. Ryan, A. Fiedler, D. Schröder, H. Schwarz *J. Am. Chem. Soc.* **1995**, *117*, 2033. (d) B. L. Tjelta, P. B. Armentrout *J. Am. Chem. Soc.* **1996**, *118*, 9652. (e) A. Fiedler, I. Kretzschmar, D. Schröder, H. Schwarz *J. Am. Chem. Soc.* **1996**, *118*, 9941.

[47] For CH_4 activation mediated by transition-metal complexes, see, for instance: (a) T. Böhme, Diploma Thesis, TU Berlin **1998**. (b) ref. 48.

[48] (a) K. Yoshizawa, Y. Shiota, T. Yamabe *Chem. Eur. J.* **1997**, *3*, 1160. (b) K. Yoshizawa, Y. Shiota, T. Yamabe *J. Am. Chem. Soc.* **1998**, *120*, 564. (c) K. Yoshizawa, Y. Shiota, T. Yamabe *Organometallics*, **1998**, *17*, 2825. (d) K. Yoshizawa, Y. Shiota, T. Yamabe *J. Chem. Phys.* **1999**, *111*, 538.

[49] Note, that FT-ICR experiments in the course of this Thesis reproduce these branching ratios quite well; however, additional formation of small amounts (< 3 %) of $FeCH_3^+$, $FeSH^+$, and $FeSCH_3^+$ is observed.

[50] (a) T. C. Jackson, D. B. Jacobson, B. S. Freiser *J. Am. Chem. Soc.* **1984**, *106*, 1252. (b) D. Schröder, A. Fiedler, J. Hrusak, H. Schwarz *J. Am. Chem. Soc.* **1992**, *114*, 1215.

[51] Note, that thresholds of CID processes depend on the collision gas. Most reliable thresholds are obtained with xenon as collision partner, while use of methane is known to give thresholds that are too high, thus agreeing nicely with the result for the second feature of the Fe^+ channel. For a discussion of several collision gases, see: Ref. 9k.

[52] S. Bärsch, I. Kretzschmar, D. Schröder, H. Schwarz, P. B. Armentrout *J. Chem. Phys. A* **1999**, *103*, 5925.

[53] The bond strengths of the S-H and C-S bonds are estimated to be on the order of 85 kcal/mol and 70 kcal/mol, according to S-H and C-S bond strengths of comparable molecules, tabulated in CRC-Handbook of Chemistry and Physics (Ref. 54). As references for the S-H bond strength H-SH, H-SCH_3, and H-SC_6H_5 are used, for the C-S bond strength the analogy with tert-C_4H_9-SH, C_6H_5-SH, and CH_3-SC_6H_5 species is used.

[54] R. C. Weast (Ed.) *CRC-Handbook of Chemistry and Physics*, CRC-Press Inc., Boca Raton, **1990**.

[55] This calculation is supported by a so far unpublished FT-ICR experiment where, under thermal conditions, ligand exchange is observed according to $FeCl^+ + CH_3SH \rightarrow FeSCH_3^+ + HCl$. The occurrence of this reaction leads to $D_0(Fe\text{-}SCH_3^+) \geq 65.9$ kcal/mol using literature thermochemistry.

[56] The C-H bond strength in a methyl group is given to 111.1 kcal/mol in (Ref. 54).

[57] Ionization energies are taken from: S. G. Lias, J. E. Bartmess, J. F. Liebman, J. L. Holmes, R. D. Levin, W. G. Mallard *Gas Phase Ion and Neutral Thermochemistry; J. Phys. Chem. Ref. Data, Suppl. 1* **1988,** *17*.

[58] The relevance of this type of crossing and the requirements for the violation of spin conservation have been discussed previously at great length; for details, see: (a) Ref. 27. (b) Ref. 30. (c) Ref. 40. (d) D. A. Plattner *Angew. Chem. Int. Ed.* **1999**, *38,* 86. (e) D. Schröder, S. Shaik, H. Schwarz *Acc. Chem. Res.* **2000**, *33*, 139.

6 Theoretical and Experimental Study on the Activation of Ethylsilane by 'Bare' Co^+ and Fe^+ Cations - A Comparison*

The activation of C–H and C–C bonds by transition-metal complexes has been a matter of interest in chemistry for at least the last three decades[1] both in solution,[2] and in the gas phase.[3] In recent years, theoretical approaches have gained more and more importance for the understanding of reaction mechanisms.[4] The gas-phase metal-ion mediated activation of several functionalized substrates, e.g. nitriles, ketones, and alcohols, just to mention a few substrates, has been elucidated in detail.[5] A particular case concerns the high regioselectivity observed in the remote functionalization of ω-silyl-substituted alkanenitriles,[6] for which also the corresponding monosubstituted compounds were studied in order to obtain more information about the underlying mechanisms.[7,8] As part of this mechanistic study, the reactions of *n*-propyltrimethylsilane with Fe^+ and Co^+ were investigated to determine the role of the metal ions' electronic structure in the activation process.[9] However, despite use of extensive labeling techniques, some questions remain unclear concerning the detailed mechanism of the metal-mediated bond activation, and theoretical studies are indicated. Albeit some significant progress, nowadays available theoretical methods can hardly be employed to answer these questions for open-shell systems of large size. In this context, even relatively small molecules such as *n*-propyltrimethylsilane are already too large a substrate to allow for a detailed and accurate theoretical treatment of the relevant potential-energy surfaces (PES) at a sufficient level of theory. Therefore, as a first-order approximation, a smaller model system is chosen which allows both, theoretical and experimental investigations. In the present study, the reactivity of the systems Co^+/ethylsilane and Fe^+/ethylsilane is examined by a B3LYP-approach, and some additional results from mass spectrometric FT-ICR and sector-MS experiments are presented for comparison. The knowledge of the two systems will hopefully allow a comparison of the electronic structure role in the activation behavior of these two important transition-metal ions.[3b,10]

* Published in part in: S. Bärsch, T. Böhme, D. Schröder, H. Schwarz *Int. J. Mass Spectrom. Ion Processes* in press.

6.1 Theoretical Procedure

Calculations are performed utilizing the program package Gaussian94.[11] As the system is of considerable size and requires large resources concerning computing time and memory requirements, the use of the resources of the CRAY-YMP supercomputer at the Konrad-Zuse-Zentrum Berlin is indicated. The B3LYP approach is employed for two reasons: (i) especially in recent years, the B3LYP approach is widely used for the description of transition metal mediated activation of organic substrates and has been shown to provide reasonably accurate energetics in the investigation of these reactions.[4a,8] (ii) Due to both, the limitation in computing resources and to the size of the investigated system DFT is a reasonable alternative as compared to the computational efforts associated with non-DFT, highly correlated *ab initio* methods.

The Ahlrichs valence double-zeta (VDZ) basis sets are used for Fe, Co, C, Si, and H.[12] Due to the small state splittings in iron, it is essential to achieve a good description of the valence space for this atom. Therefore, the original Ahlrichs basis for Fe is slightly modified, such that the coefficients remain the same, but the contractions for the d-functions are changed (instead using (5d) → (2d)/[32] from Ahlrichs et al. we used (5d) → (3d)/[311]). The complete basis set then consists of the following basis functions and contractions: H (10s7p)/[4s3p], C (7s4p)/[3s2p], Si (10s7p)/[4s3p], Co (14s8p5d)/[5s2p2d] and Fe (14s8p5d)/[5s2p3d]. This basis set is further denoted as BS1. To allow for a more direct comparison with experimental results, all energies are corrected for the zero-point vibrational energy (ZPVE) contributions.

For the Co^+/ethylsilane system, the effect of a larger basis set is evaluated by single-point calculations on the critical parts of the PES, e.g. the transition structures of the rearrangement, the entrance, and the exit channels. Here, the B3LYP approach is used with a basis set of approximately valence triple-zeta (VTZ) quality, i.e. Wachters+f for cobalt[13,14] and cc-pVTZ according to Dunning et al.[15] for Si, C, and H. The contractions for these basis sets read as follows: H (7s2p1d)/[3s2p1d], C (12s7p2d1f)/[4s3p2d1f], Si (15s9p2d1f)/[5s4p2d1f], and Co (14s11p6d3f)/[8s6p4d1f].

6.2 The Activation of Ethylsilane by Co^+

The activation of ethylsilane by Co^+ is presented first because, at a first glance, the theoretical treatment of this reaction seems to involve less problems than the corresponding

iron analog. Cobalt cations show a triplet ground-state, with the excited quintet and singlet states being much higher in energy. Therefore, although this assumptions needs to be verified, the singlet and quintet PES may not need to be considered, in contrast to the iron case where explicit consideration of the quartet and sextet PES is indicated because of the small quartet-sextet state-splitting in Fe^+. Starting with a presentation of the experimental results, this chapter will then be continued by the theoretical description of the Co^+/ethylsilane system.

6.2.1 Experimental Results

The Co^+/ethylsilane system is investigated by FT-ICR mass spectrometry[16] and metastable ion (MI) decay in the four-sector mass spectrometer.[17] These results are presented in Figure 6-1, where the intensities are normalized to $\Sigma_{products}$ = 100% with ion intensities < 1% being omitted. Both, sector-MS and FT-ICR show qualitative agreement in terms of prevailing losses of neutral SiH_4 from metastable $Co(C_2H_5SiH_3)^+$ and the $Co^+ + C_2H_5SiH_3$ couple, respectively. In the sector-MS, additionally a small Co^+ peak (< 1%) due to loss of the entire ligand is observed, which is distinguished from the isobaric hydride-transfer species CoH + $C_2H_5SiH_2^+$ by labeling experiments. For the structure assignment of $C_2H_5SiH_2^+$, see the detailed discussion of the labeling experiments.

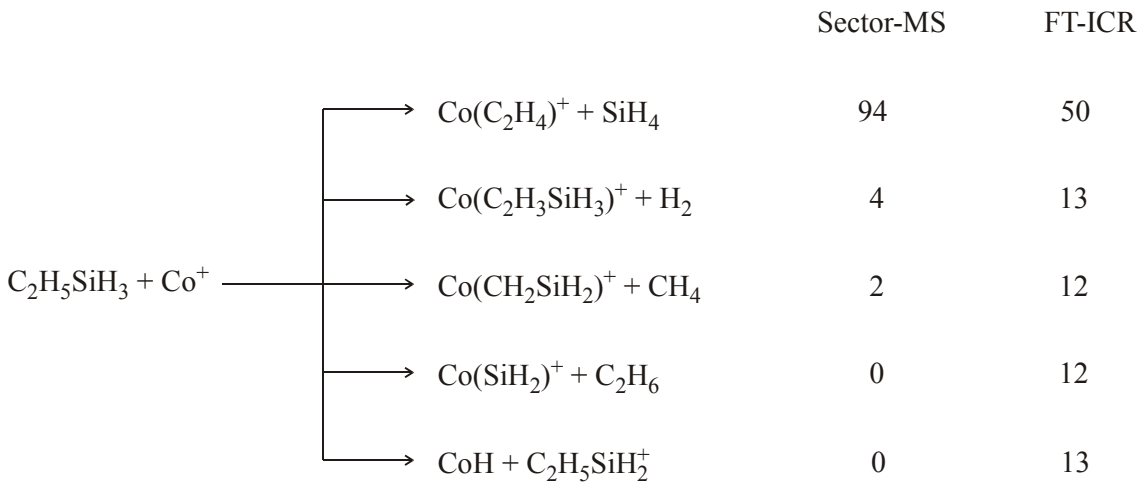

Figure 6-1: Product distribution for Co^+/ethylsilane in FT-ICR and sector-MS experiments.

While loss of SiH_4 is the dominating channel in the sector-MS experiment (94%), it accounts for only 50% of the products formed in the FT-ICR. Further products observed in both experimental setups are the losses of H_2 and CH_4. In the FT-ICR, additionally C_2H_6 and CoH are formed. According to the product distributions and the nature of the products

generated in the two experiments, MI studies with the sector-MS exhibit a higher selectivity than the FT-ICR experiments. This is attributed to a lower internal energy content of the metastable ions compared to the encounter complexes formed from the separated reactants in the FT-ICR.[18] This conjecture is further supported by the appearance of a $Co(SiH_2)^+$ fragment due to loss of neutral C_2H_6, which is generated upon collisional activation (CA) in the sector-MS.

In the labeling experiments utilizing the $Co^+/C_2H_5SiD_3$ couple, losses of SiD_3H (95%), CH_3D (2%), and D_2 (3%) are observed. Upon collisional activation, in addition to the above mentioned products small amounts of HD and H_2 as well as some neutral CoD are produced. While observation of all three isotopic species of molecular hydrogen complicates the assignment of a mechanism for this reaction, the loss of CoD with no indication for neutral CoH strongly suggests a silylium-structure for the hydride-transfer product as shown in Figure 6-1. The labeling experiments are in addition quite helpful in that the formation of SiD_3H suggests involvement of the C–Si and a C–H bond, while the generation of CH_3D points to C–C and Si–D bond activation. Further, formation of D_2 clearly demonstrates initial Si–D insertion.

In addition, the reaction of $Co(C_2H_4)^+$ with silane is considered under FT-ICR conditions, but no product formation at a reasonable rate constant is observed ($k < 2 \cdot 10^{-12}$ cm^3 molecule^{-1} s^{-1}), suggesting that $D_0(Co(SiH_4)^+) < D_0(Co(C_2H_4)^+) = 44.5 \pm 2.1$ kcal/mol.[19]

6.2.2 The PES of Co^+/Ethylsilane

The PES for the activation of ethylsilane **1** by "naked" Co^+ cations is calculated for five conceivable activation mechanisms, i.e. the initial insertions of the Co^+ ion into the C–Si, C(2) –H, C(1) –H, C–C, or Si–H bonds (Figure 6-2).

Only the triplet surface is considered for several reasons. (i) The experimentally determined, well established triplet-quintet splitting of Co^+ ($^3F \rightarrow {}^5F$) amounts to 8.3 kcal/mol,[20] while the corresponding triplet-singlet splitting is even more pronounced. (ii) Vanquickenborne and coworkers found the quintet surface to be of little importance for the activation of methane by Co^+.[21] (iii) Exploratory calculations on the quintet and singlet surfaces reveal a very strong preference of the Co^+-system towards a triplet spin state, as is illustrated by the following examples. For instance, the fully optimized structures for the encounter complexes on the singlet and quintet surfaces are located 16.1 kcal/mol and 19.1 kcal/mol, respectively, above the most stable conformer of the encounter complex on the

triplet surface. In addition, the primary product of C–Si bond insertion (see below) is also examined for all three spin states. Here, the singlet structure is 17.2 kcal/mol and the quintet structure is 20.0 kcal/mol higher in energy than the corresponding triplet species. Consequently, the singlet and quintet surfaces are unlikely to participate in the reaction, and consideration of the triplet PES alone should provide a sufficient description of the ground-state reactivity of the system.

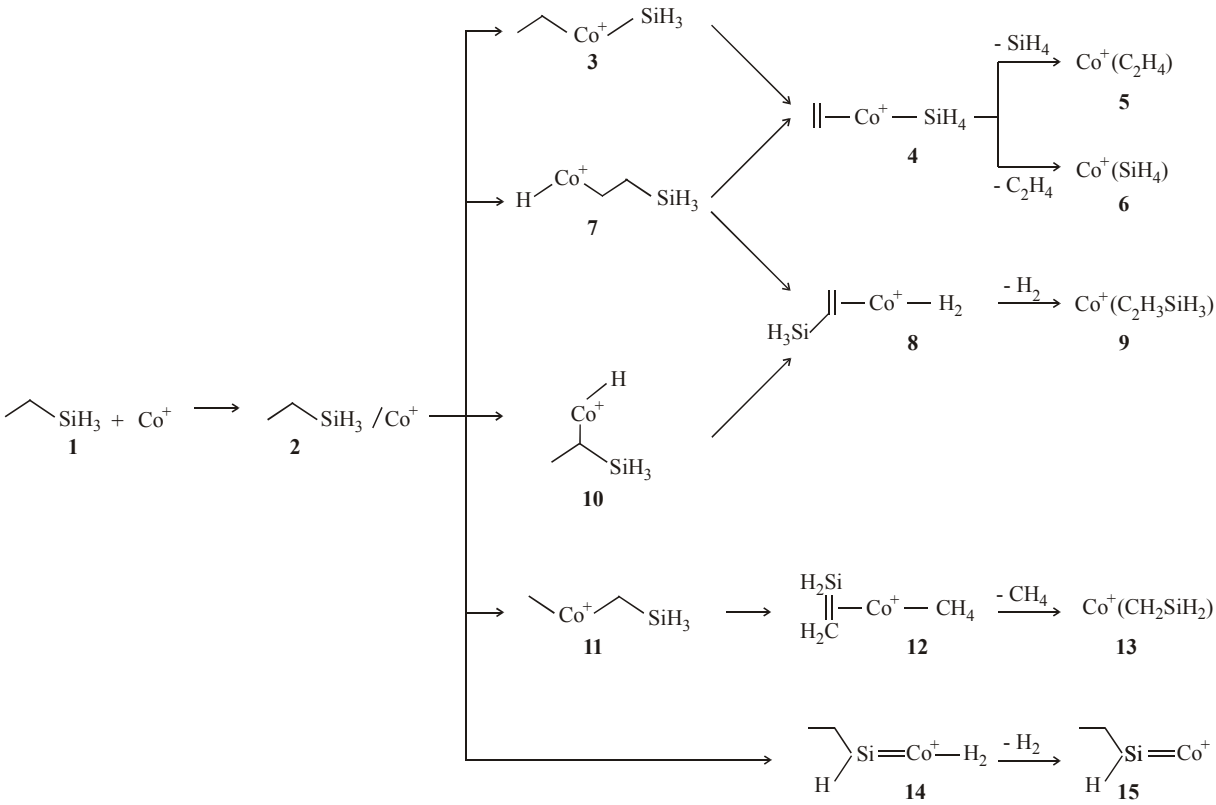

Figure 6-2: Schematic description of the five calculated reaction pathways of the Co^+/ethylsilane system. Note, that only the expected minima along the reaction coordinate are displayed. Transition structures connecting the respective minima are discussed in the text.

Because of the known deficiency of B3LYP to treat atoms accurately,[22] the theoretically predicted complexation energy of Co^+ and **1** is expected to be somewhat too large. Thus, the entrance channel is likely to be associated with a larger error than the remaining parts of the PES to which an average error of ± 6 kcal/mol is attributed. This uncertainty is based on the average deviations of some calculated bond-dissociation energies and heats of formation for model processes with known literature values[23] as well as comparison with B3LYP investigations of transition metal/hydrocarbon systems with basis sets of similar quality.[24]

In the following, first the reactants and the encounter complex are described because they are common to all five insertion pathways. Then the remaining minima and transition

structures of the five individual routes are discussed separately in the order of their appearance in Figure 6-2.

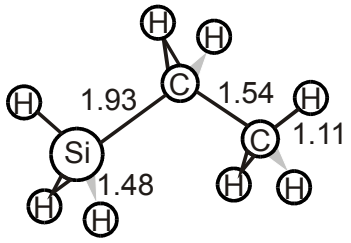

1

Chart 6-1: Geometrical features of ethylsilane, **1**. Bond lengths are given in Å and angles in degree.

Reactants. In agreement with the established electronic states,[20] the ground state of Co^+ is calculated to be ^3F. The corresponding quintet excited state is calculated only 2.5 kcal/mol above the ground state compared to the experimental value of 8.3 kcal/mol.[20] The deviation from the experimental state splitting highlights the known problem associated with the B3LYP approach in the calculation of atoms as mentioned above.[22] Ethylsilane, **1**, is optimized in C_S symmetry to yield a $^1A'$ state and is displayed in Chart 6-1. Note that throughout this chapter the two carbon atoms are referred to as C(1) and C(2), according to their positions in ethylsilane. The lengths of the Si–C, C–H, C–C, and Si–H bonds of **1** are further used as internal references for typical single bonds between these elements.

Encounter Complex. The η^4-coordinated encounter complex **2** is the most stable conformer localized and set to E_{rel} = 0.0 kcal/mol on the relative energy scale. In **2**, the Co^+ cation interacts with C(2), silicon, and two hydrogen atoms one from C(2) and the other from silicon, respectively; these hydrogen atoms are directed towards Co^+ in an agostic fashion.[25] The Co–Si distance of 2.77 Å (as compared to r_{CoSi} = 2.44 Å in **3**) indicates an electrostatic interaction, while the Co–C interaction is much weaker as displayed by the long Co–C distance of 2.50 Å.

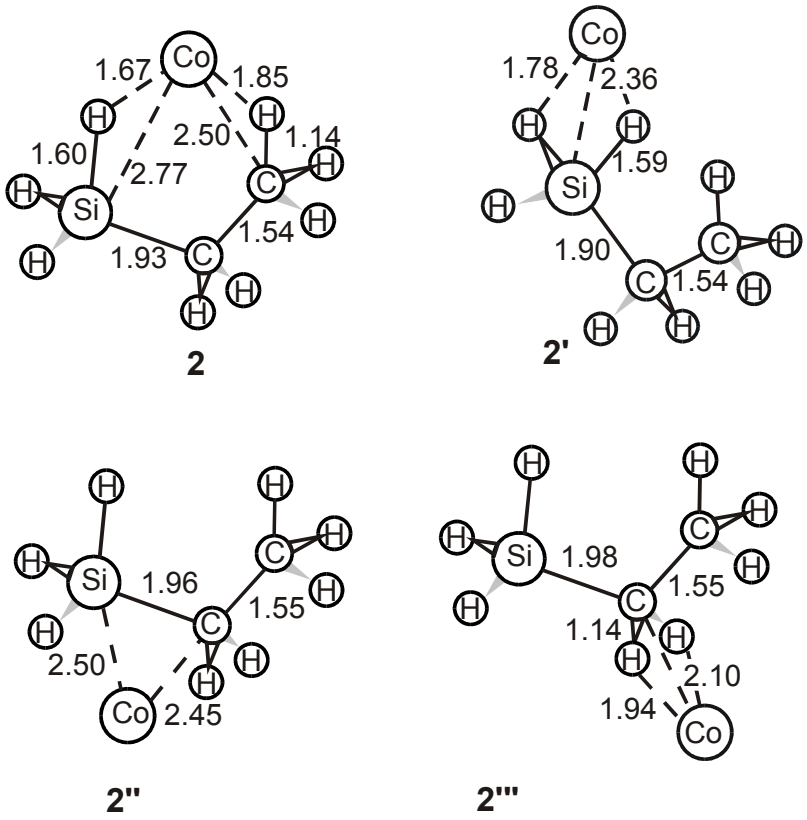

Chart 6-2: Encounter complexes located on the triplet surface of the system Co^+/ethylsilane. Bond lengths are given in Å and angles in degree.

Three other conformers of the encounter complex **2** are localized during the calculations, i.e. **2'**, **2"**, and **2'"**, all of which are less stable than **2** (see Chart 6-2). Briefly, the η^3-coordinated conformer **2'** is located only 0.8 kcal/mol above **2**. Here, interaction occurs between Co^+ and the silicon atom as well as two of the silylic hydrogen atoms. Another conformer, **2"** (E_{rel} = 4.1 kcal/mol), shows strong interactions between the silicon and Co^+ (r_{SiCo} = 2.50 Å) as well as C(1) and Co^+ ($r_{CoC(1)}$ = 2.45 Å). Finally, the η^3-complex **2'"** (E_{rel} = 8.9 kcal/mol) is characterized by the interaction of Co^+ with C(1) ($r_{CoC(1)}$ = 2.10 Å) and both hydrogen atoms on C(1) (r_{CoH} = 1.94 Å); in this conformer, no interaction with silicon is achieved. The fact that the silicon-bound conformers are at least 4.8 kcal/mol more stable than the carbon-only bound conformer indicates that coordination to the silyl-group is notably stronger than that to the alkyl moiety. Note that in the construction of the PESs only the most stable conformers are considered, because the barriers for the interconversion of the different conformers are assumed to be much lower than the barriers associated with cleavage and/or formation of covalent bonds.

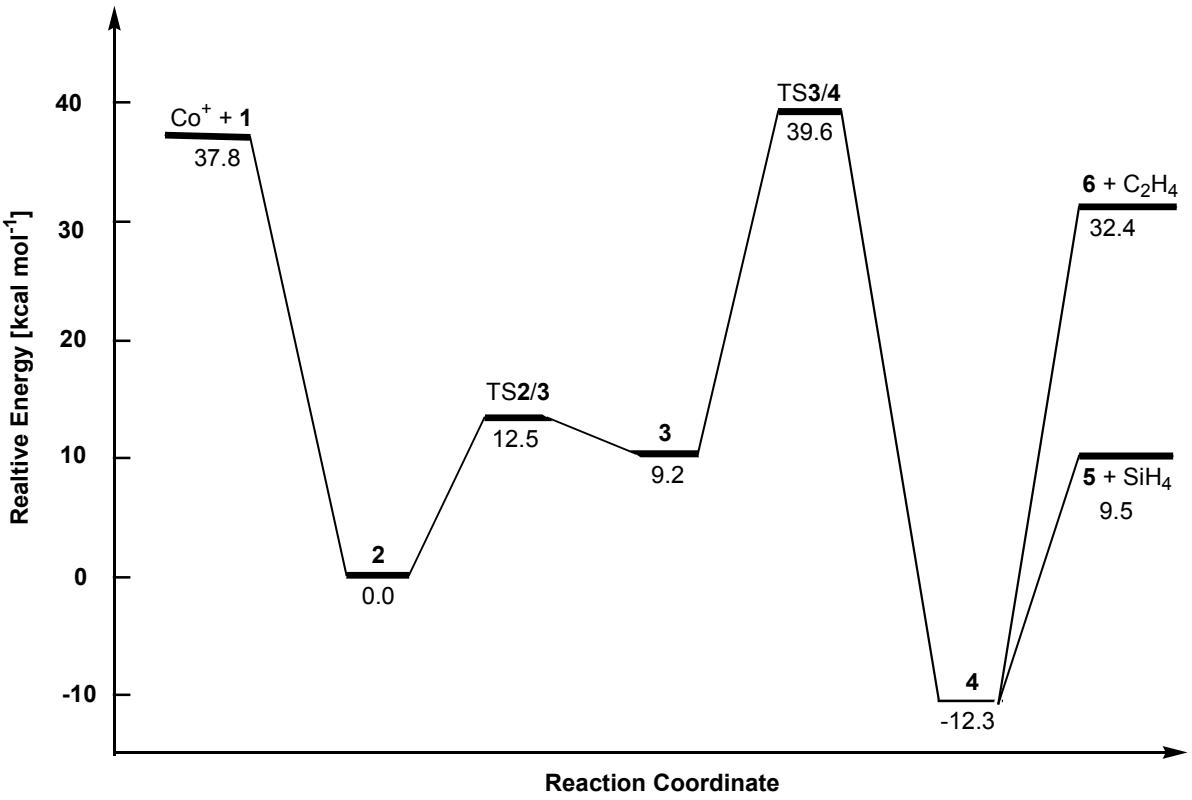

Figure 6-3: B3LYP/BS1 PES of the C–Si insertion pathway of $Co^+ + C_2H_5SiH_3$ relative to the lowest-lying encounter complex **2**; ZPVE corrections are included, and the relative energies are given in kcal/mol.

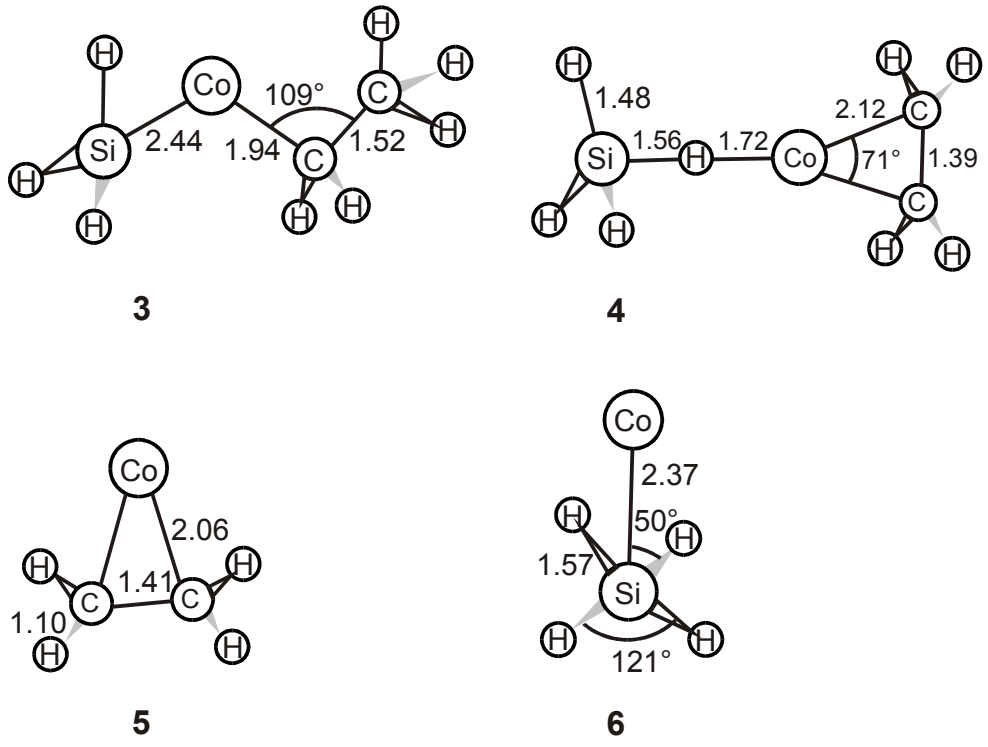

Chart 6-3: Minima along the C–Si insertion PES. Bond lengths are given in Å and angles in degree.

C-Si Bond Insertion, Figure 6-3. Minima along this pathway are displayed in Chart 6-3 and the respective TSs can be found in Chart 6-4. From the encounter complex **2**, the reaction commences via TS**2**/**3** towards **3**. In TS**2**/**3** (E_{rel} = 12.5 kcal/mol), the cobalt ion approaches the C-Si bond, which is elongated to 2.72 Å. The C_1-symmetric structure exhibits a single imaginary frequency (i240.8 cm^{-1}) which corresponds to the stretch of the C–Si bond together with a widening of the C(1) –Co–Si angle. The most stable conformer of the C–Si insertion complex **3** (E_{rel} = 9.2 kcal/mol) exhibits an eclipsed conformation with a dihedral angle $\theta_{SiCoC(1)C(2)}$ = 105° and Co–C(1) and Co–Si bond lengths of $r_{CoC(1)}$ = 1.94 and r_{CoSi} = 2.44 Å. Two other rotamers of **3** are located but not shown because they are energetically more demanding. The first one is located only 0.1 kcal/mol above **3**, showing an eclipsed conformation with $\theta_{SiCoC(1)C(2)}$ = 150°. The second structure (E_{rel} = 10.4 kcal/mol) has a gauche conformation with $\theta_{SiCoC(1)C(2)}$ = 52° only, thus causing a repulsive interaction between methyl- and silyl groups.

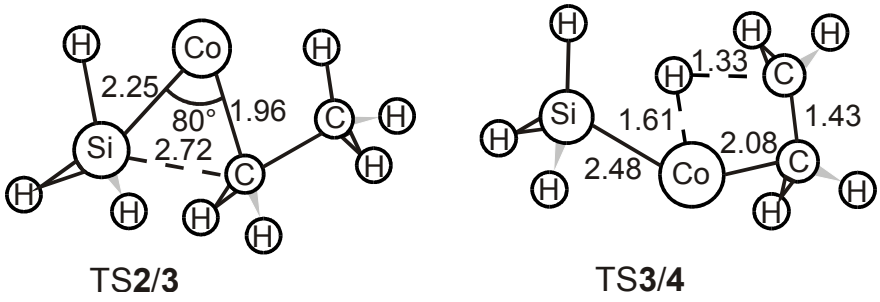

Chart 6-4: Transition structures along the C–Si- insertion PES. Bond lengths are given in Å and angles in degree.

From **3**, the reaction proceeds towards TS**3**/**4** (E_{rel} = 39.6 kcal/mol). The geometrical features of the transition structure describe a concerted process of (i) C–H bond cleavage at the methyl group (β-hydrogen transfer, r_{CH} = 1.33 Å) and (ii) transient formation of a Co–H bond (r_{CoH} = 1.61 Å). The imaginary frequency (i1184 cm^{-1}) of the multicentered[24] TS corresponds to the migration of the hydrogen from cobalt towards the silyl group, along with some rearrangement in the C_2H_4-moiety. Note, however, that in the TS the Co–C bonds are distinctly different ($r_{CoC(2)}$ = 2.22 vs $r_{CoC(1)}$ = 2.08 Å) such that the η^2-coordination of the ethylene ligand is not yet achieved.

Complex **4**, $Co(C_2H_4)(SiH_4)^+$, is formed after passing TS**3**/**4** and corresponds to the most stable structure along the C–Si bond insertion PES. In **4** (E_{rel} = -12.3 kcal/mol), the ethylene molecule is attached to one side of the Co^+ atom while the SiH_4 molecule is located on the

opposite side with one hydrogen atom pointing directly from silicon towards Co^+, forming a Co–H–Si angle of 180°. Thus, SiH_4 is connected to the metal ion only by a weak electrostatic Co···H···SiH_3 interaction, while ethylene is η^2-coordinated to the cobalt cation; the latter is indicated by two identical Co–C bonds of r_{CoC} = 2.12 Å and a C–C bond with r_{CC} = 1.39 Å, typical for C–C double bonds. In another conformer (not shown) at E_{rel} = -9.3 kcal/mol, the SiH_4 moiety is bound such that the silicon atom electrostatically interacts with Co^+, with the silicon-cobalt axis intersecting the angle of two of the hydrogen atoms while the bonding to the C_2H_4 moiety is alike in both conformers, as displayed by identical geometries of the $Co(C_2H_4)^+$ substructures.

From **4**, the product channels $Co(C_2H_4)^+ + SiH_4$ (E_{rel} = 9.5 kcal/mol) and $Co(SiH_4)^+ + C_2H_4$ (E_{rel} = 32.4 kcal/mol) can be reached by simple dissociation (Figure 6-3). Due to the calculated higher stability of $Co(C_2H_4)^+$ (D_0 = 50.6 kcal/mol) as compared to $Co(SiH_4)^+$ (D_0 = 27.7 kcal/mol), loss of silane from **4** is favored by 22.9 kcal/mol compared to elimination of ethylene. The cobalt-ethylene complex **5** exhibits a $^3A_2$ ground state in C_{2v} symmetry. The bond length of the C-C bond (r_{CC}) of 1.41 Å is slightly elongated as compared to free ethylene (r_{CC} = 1.34 Å) in accord with bond formation between Co^+ and ethylene and concomitant weakening of the C–C bond. The calculated bond dissociation energy of $D_0(Co(C_2H_4)^+)$ = 50.6 kcal/mol, however, has to be viewed with care, because (i) the error associated with the calculation of the metal cation is rather large as mentioned above,[22] and (ii) the bond dissociation energy of this complex is experimentally determined to be 44.5 ± 2.1 kcal/mol.[19] However, the qualitative view appears to be correct, e.g. the $Co(C_2H_4)^+$ complex is more strongly bound than $Co(SiH_4)^+$ which is consistent with the absence of ethylene loss in the experiment.

Note that neutral SiH_4 has been calculated in C_S symmetry with a $^1A'$ ground state, because the optimized structure shows slight deviations from tetrahedral symmetry. Attempts to optimize the structure in tetrahedral symmetry resulted in small imaginary modes during frequency analysis. In the $Co(SiH_4)^+$ complex **6**, the cobalt-silicon axis intersects the angle between two of the hydrogen atoms on silicon, forming Co–Si–H angles of 50°. The distance of r_{CoSi} = 2.37 Å points to a covalent bond with a bond length comparable to the cobalt-silicon distance in the insertion product **3**.

C-H Bond Insertion. Owing to its relationship to the C–Si bond insertion path shown in Figure 6-2, activation of the C(2) –H bond is considered first (see Figure 6-4). Minima and TSs of the C(2) –H insertion PES are displayed in Figures 6–5 and 6–6. Starting from the encounter complex **2**, initial insertion into the C(2) –H bond yields **7** via TS**2**/**7** (E_{rel} = 23.3

kcal/mol). This TS shows a product-like structure, the major structural difference between TS**2**/**7** and **7** concerns the length of the C–H bond into which the cobalt cation inserts (r_{CH} = 1.11 Å in **2**, r_{CH} = 1.84 Å in TS**2**/**7**, and r_{CH} = 2.35 Å in **7**). The imaginary frequency (i550 cm^{-1}) corresponds to a large extent to the motion of the hydrogen atom away from C(2), thus increasing the (C–Co–H) angle from 63° in the TS to 85° in **7**. In addition, the movement of C(2) towards C(1) accompanied with a slight shortening of the C–C bond (from 1.53 Å in TS**2**/**7** to 1.51 Å in **7**) contributes to the transition mode.

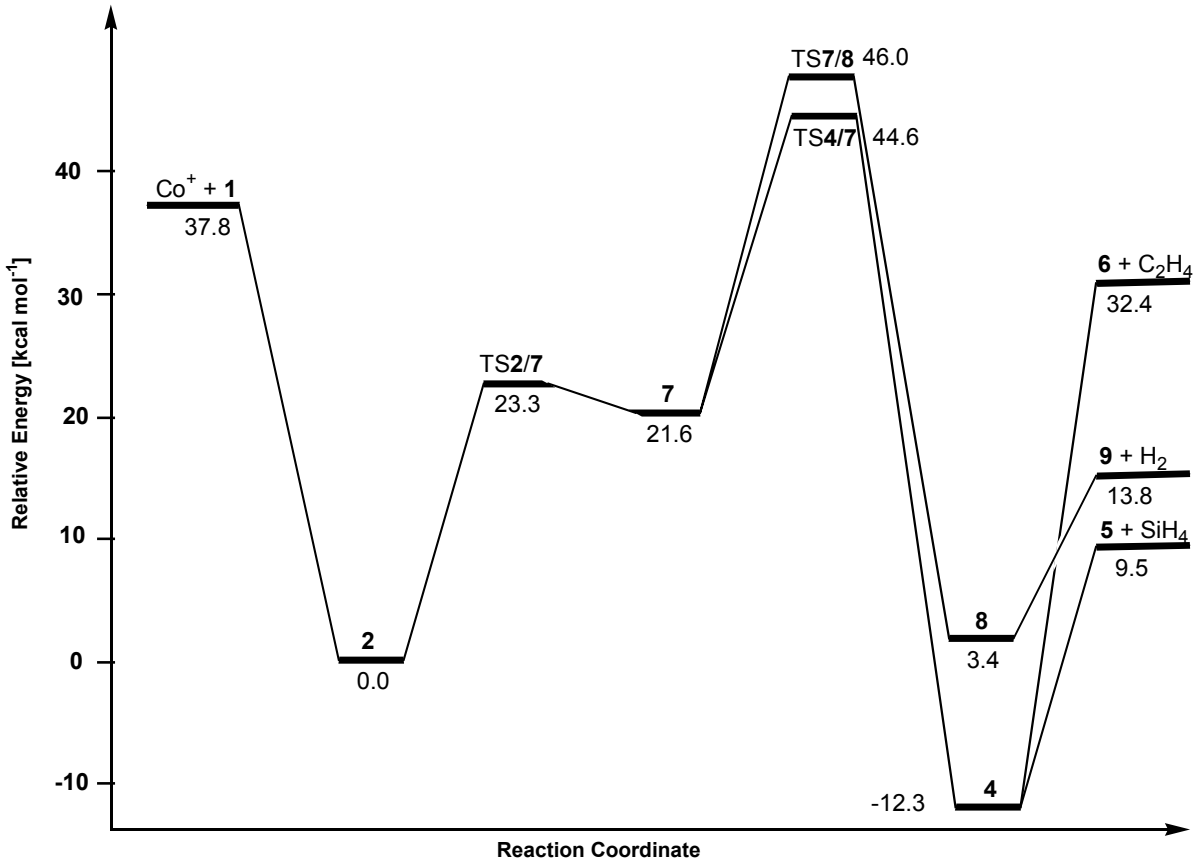

Figure 6-4: B3LYP/BS1 PES of the C(2)–H bond insertion pathway of $Co^+ + C_2H_5SiH_3$ relative to the lowest-lying encounter complex **2**; ZPVE corrections are included, and the relative energies are given in kcal/mol.

For the C(2) –H insertion structure three conformers are localized. The most stable species **7** (E_{rel} = 21.6 kcal/mol) corresponds to an anti-conformer with respect to the C–C bond. Two other conformers, **7'** and **7"** (not shown) are located at E_{rel} = 26.4 kcal/mol and E_{rel} = 30.3 kcal/mol, respectively. The former corresponds to an anti-conformer, with a different Co–C(2) bond length and C(2) –Co–H angle as compared to **7** ($r_{CoC(2)}$ = 1.99 Å and $\alpha_{C(2)CoH}$ = 102° vs $r_{CoC(2)}$ = 1.93 Å and $\alpha_{C(2)CoH}$ = 85° in **7**). These slight geometric deviations of the two

conformers are unlikely to account for an energetic difference of 4.8 kcal/mol between **7** and **7'** at E_{rel} = 26.4 kcal/mol; instead this rather points to a different electronic structure of **7'**. This conjecture is further supported by the NBO analysis of the two species, which shows different bonding orbitals for the two species in the insertion region. **7"** exhibits similar bond lengths as **7'**; in addition, the silyl group and the CoH unit are arranged in a gauche conformation with respect to the C–C bond (dihedral angle $\theta_{SiC(1)C(2)Co}$ = 45°). Therefore, it is readily understood that this conformer is disfavored by 8.7 kcal/mol compared to **7**, probably due to a joint action of electronic structure and conformational disadvantage. From **7**, the reaction may continue via two different pathways, either β-SiH_3 or β-H migration. First, the β-SiH_3 migration pathway is considered.

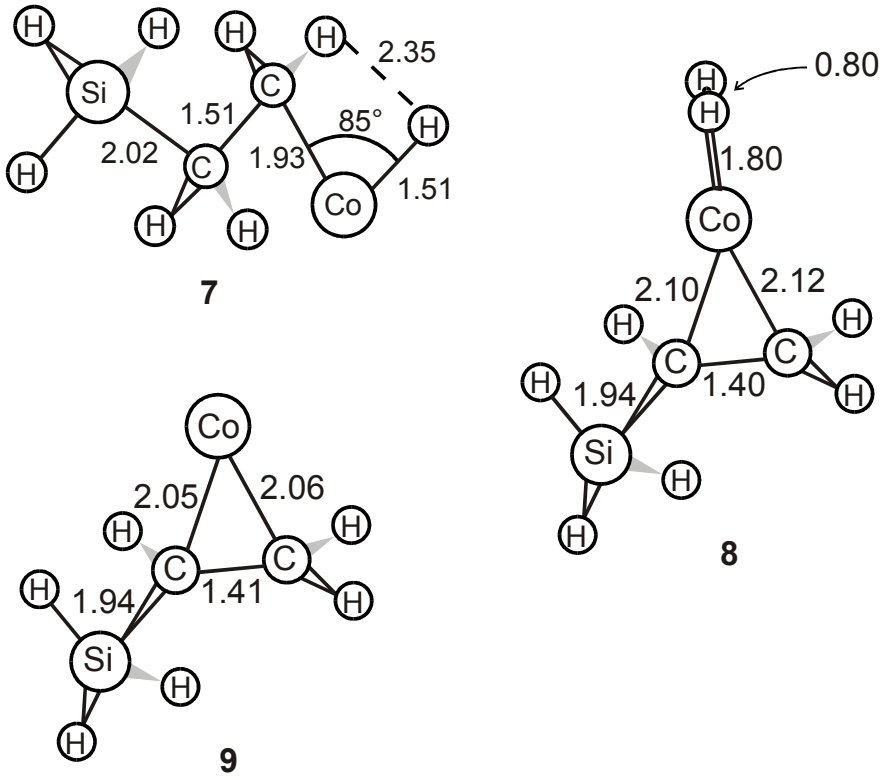

Chart 6-5: Minima along the C(2)–H insertion PES. Note, that only minima are displayed which have not been described before. Bond lengths are given in Å and angles in degree.

The transition from **7** to **4** proceeds via TS**4**/**7** (E_{rel} = 44.6 kcal/mol). Starting from **7**, rotation of the C–C bond and movement of the hydrogen atom on Co^+ towards the SiH_3-group leads to TS**4**/**7**. Both motions contribute to the imaginary frequency of i475 cm^{-1}. In the TS the C-Si bond is broken (r_{SiC} = 2.50 Å), and formation of the ethylene-ligand is in progress as is apparent from two features: (i) the change in the bond lengths of the two different Co–C bonds (**7**: $r_{CoC(1)}$ = 2.36 Å and $r_{CoC(2)}$ = 1.93 Å; TS: $r_{CoC(1)}$ = 2.34 Å and $r_{CoC(2)}$ = 2.08 Å), and

(ii) the planarization of the C_2H_4-moiety, going along with a change of hybridization from sp^3 in **7** to sp^2 in **4** as already discussed. Structure **4** can account for the losses of neutral silane and ethylene, respectively, resulting in the formation of product complexes **5** and **6**, which have been presented above.

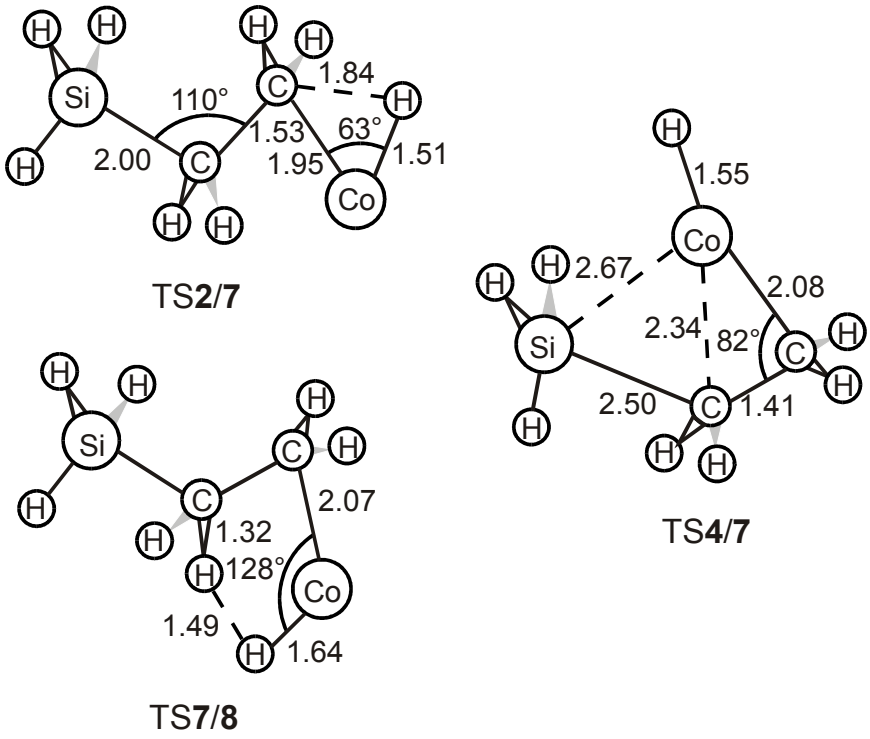

Chart 6-6: Transition structures along the C(2)–H bond insertion pathway. Bond lengths are given in Å and angles in degree.

Next, the pathway for the β-H migration is investigated. Starting from **7**, the product complex **8** is reached via TS**7**/**8** (E_{rel} = 46.0 kcal/mol) which involves a rotation of the Co–C(2) bond ($\alpha_{C(2)CoH}$ = 85° vs 128° in **7** and TS**7**/**8**, respectively) concomitant with elongation of a C(1) –H bond and assisted by an additional Co–H interaction in the TS ($r_{C(1)H}$ = 1.32 Å and r_{CoH} = 1.64 Å). The imaginary frequency of TS**7**/**8** (i972 cm^{-1}) corresponds to a motion of both hydrogen atoms on the cobalt atom approaching each other. The reaction continues towards **8** (E_{rel} = 3.4 kcal/mol), which consists of an intact H_2 molecule (r_{HH} = 0.80 Å), electrostatically interacting with the cobalt atom (r_{CoH} = 1.80 Å) to which a vinylsilane-moiety is bound on the opposite side of the complex. Similar to previous examples,[24] no indications for the existence of a dihydrido minimum are found; instead the reaction directly proceeds from **7** to **8** via the multicentered TS**7**/**8**. The C–C double bond (r_{CC} = 1.40 Å) of the vinylsilane-ligand binds in a π-type manner to the cobalt cation. The Co–C bond lengths of

$r_{CoC(1)}$ = 2.10 Å and $r_{CoC(2)}$ = 2.12 Å differ slightly, but are comparable to the corresponding r_{CoC} of the cobalt ethylene complex **5** (r_{CoC} = 2.06 Å) and to the Co–C bond length in **4**, r_{CoC} = 2.12 Å. From **8**, the reaction continues by loss of neutral H_2 to the dehydrogenation product **9**, $Co(C_2H_3SiH_3)^+$; the exit channel is located at E_{rel} = 13.8 kcal/mol. In **9**, the cobalt atom is located above the C–C bond (r_{CC} = 1.41 Å) with Co–C bond lengths of $r_{CoC(1)}$ = 2.05 Å and $r_{CoC(2)}$ = 2.06 Å. This indicates an almost symmetric π-type interaction between the C–C double bond and the cobalt cation. The influence of the silyl-moiety is rather small, in analogy to **8**, as both Co–C bonds exhibit approximately the same bond lengths. The Mulliken population analysis predicts the positive charge almost entirely on Co^+ (q_{Co^+} = +0.96); hence charge transfer is negligible.

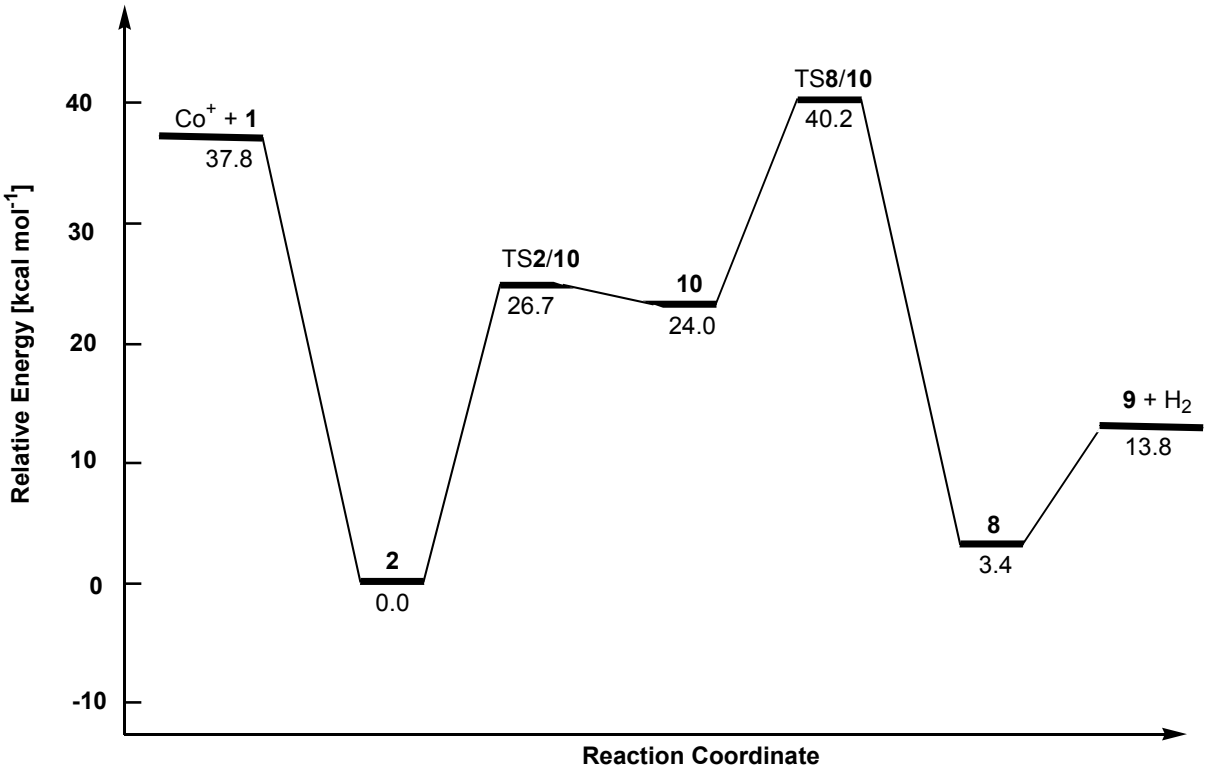

Figure 6-5: B3LYP/BS1 PES of the C(1)–H bond insertion pathway of $Co^+ + C_2H_5SiH_3$ relative to the lowest-lying encounter complex **2**; ZPVE corrections are included, and the relative energies are given in kcal/mol.

C(1) –H bond insertion (Figure 6-5) commences from the encounter complex via TS**2**/**10** (E_{rel} = 26.7 kcal/mol). Minima and TSs of this pathway are presented in Charts 6–7 and 6–8. In the TS, the C(1) –H bond elongates dramatically as compared to **2**, while the future Co–H and Co–C bonds are preformed (r_{CoH} = 1.50 Å and $r_{CoC(1)}$ = 1.93 Å).

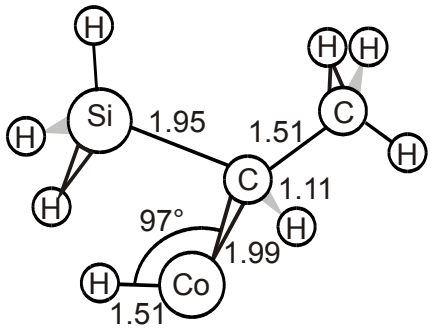

10

Chart 6-7: Minimum geometry of the C(1)–H bond inserted structure **10**. Note, that all other minima along the C(1)-H bond insertion PES have already been described above. Bond lengths are given in Å and angles in degree.

TS**2**/**10** is very much product-like, and the imaginary frequency of i407 cm^{-1} mainly corresponds to a movement of a hydrogen away from C(1), thus opening the C(1) –Co–H angle from 68° in the TS to 97° in **10**. Some coupling of rotational motions of the methyl- and silyl-groups also contributes to the imaginary frequency. The C_1 symmetric insertion structure **10** (E_{rel} = 24.0 kcal/mol) exhibits bond lengths of $r_{CoC(1)}$ = 1.99 Å and r_{CoH} = 1.51 Å.

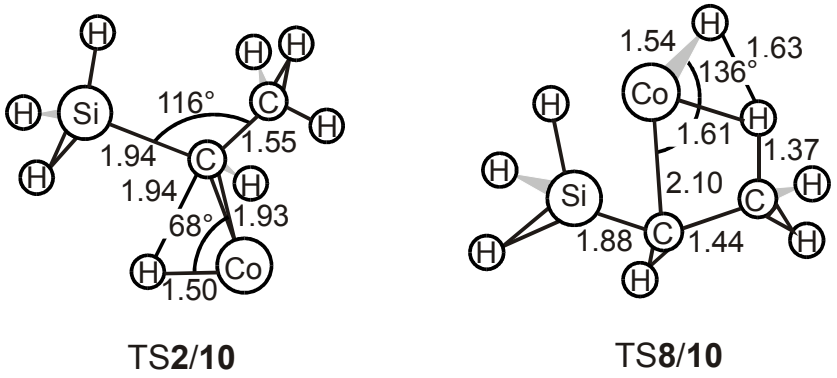

TS**2**/**10** TS**8**/**10**

Chart 6-8: Transition structures of the C(1)–H bond insertion PES. Bond lengths are given in Å and angles in degree.

Following the reaction path, TS**8**/**10** is localized at E_{rel} = 40.2 kcal/mol. The C(1) –Co–H angle in TS**8**/**10** is widened (from 97° in **10** to 136° in the TS) and one C(2) –H bond of the methyl group is elongated ($r_{C(2)H}$ = 1.37 Å) with the hydrogen atom moving towards the metal; thus, a second Co–H bond is formed (r_{CoH} = 1.61 Å). The H–H distance of r_{HH} = 1.63 Å is far from formation of a dihydrogen molecule. This points to an early TS on the reaction coordinate, in agreement with the structural similarity between TS**8**/**10** and **10**. Two major

motions contribute to the imaginary frequency of i810 cm^{-1}, i.e. the approach of the two hydrogen atoms towards each other and planarization of the two remaining hydrogen atoms on C(2). After traversing TS**8**/**10**, structure **8** is reached, which then may dissociate into product complex **9** and H_2. As these parts of the PES are common between the C(1) –H bond insertion and the C(2) –H bond insertion pathway, they need not to be discussed again.

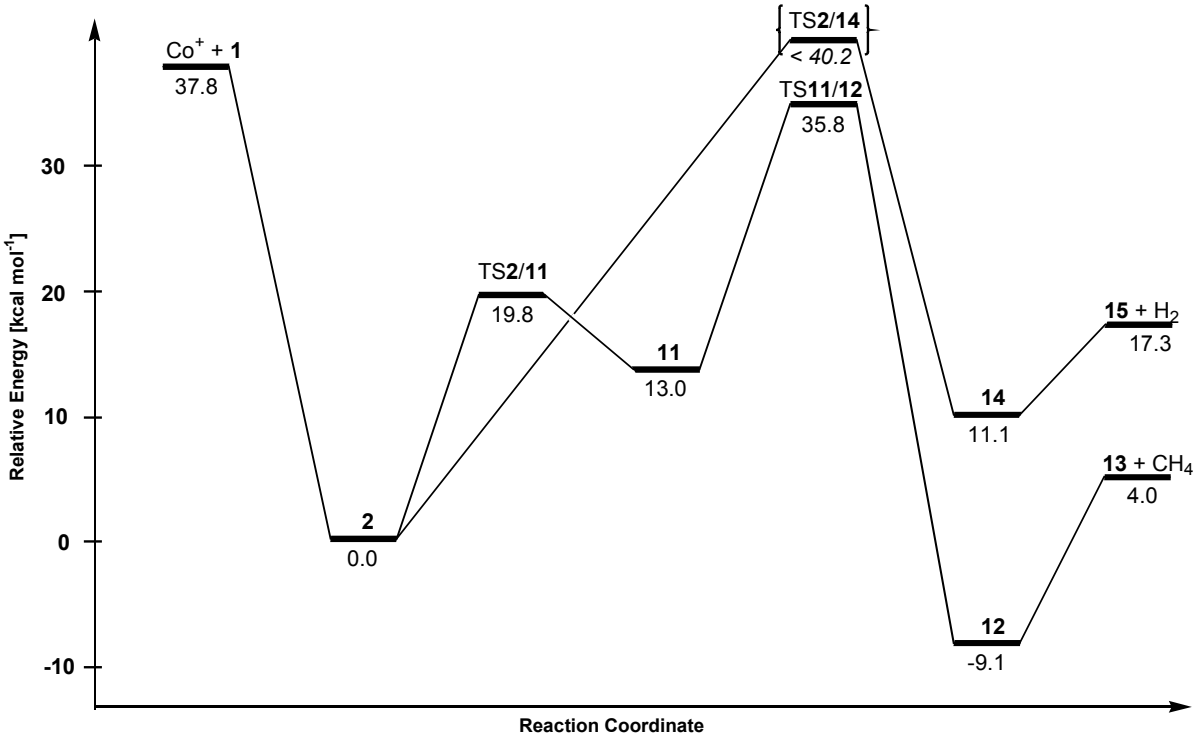

Figure 6-6: B3LYP/BS1 PES of the C–C and Si–H bond insertion pathway of $Co^+ + C_2H_5SiH_3$ relative to the lowest-lying encounter complex **2**; ZPVE corrections are included, and the relative energies are given in kcal/mol.

C–C Bond Insertion, Figure 6-6. Geometric features of the stationary points involved in this reaction pathway are found in Charts 6–9 and 6–10. Starting from the encounter complex **2**, C–C bond activation involves TS**2**/**11** (E_{rel} = 19.8 kcal/mol) en route to the insertion structure **11**. In the TS, the C–C bond is distinctly elongated as compared to the encounter complex **2**. The Co–C(2) distance decreases to 1.92 Å in TS**2**/**11** indicating an increased Co–C(2) interaction. The imaginary frequency (i305cm^{-1}) corresponds to an elongation of the C–C bond and subsequent insertion of the cobalt cation into the C–C bond. The insertion minimum **11** (E_{rel} = 13.0 kcal/mol) exhibits two almost equivalent Co–C bonds with r_{CoC} = 1.92 and 1.94 Å, respectively. The molecule shows an anti-conformation with respect to the Co–C(1) bond.

From **11**, the product complex **12** can be reached, which serves as a precursor for loss of methane. Interestingly, C–C bond activation via TS**11**/**12** has the lowest energy barrier (E_{rel} = 35.8 kcal/mol) of all activation pathways considered here. The motion of one hydrogen atom away from the silyl-moiety towards the methyl group is displayed by the elongated Si–H distance of the migrating hydrogen atom as compared to the two hydrogen atoms remaining on the silicon atom (r_{SiH} = 1.93 vs 1.48 Å). The TS can therefore be regarded as a cobalt cation, surrounded by three ligands, i.e. H, CH_3, and CH_2SiH_2. The angle between the two carbon atoms is 167°, such that the methyl moiety and CH_2SiH_2 are located almost exactly on opposite sides of the cobalt atom, thereby minimizing steric hindrance. The imaginary frequency of i578 cm^{-1} corresponds to the motion of the hydrogen atom away from the silyl- and towards the methyl group with minor contributions from the rotation of the two remaining hydrogen atoms on silicon.

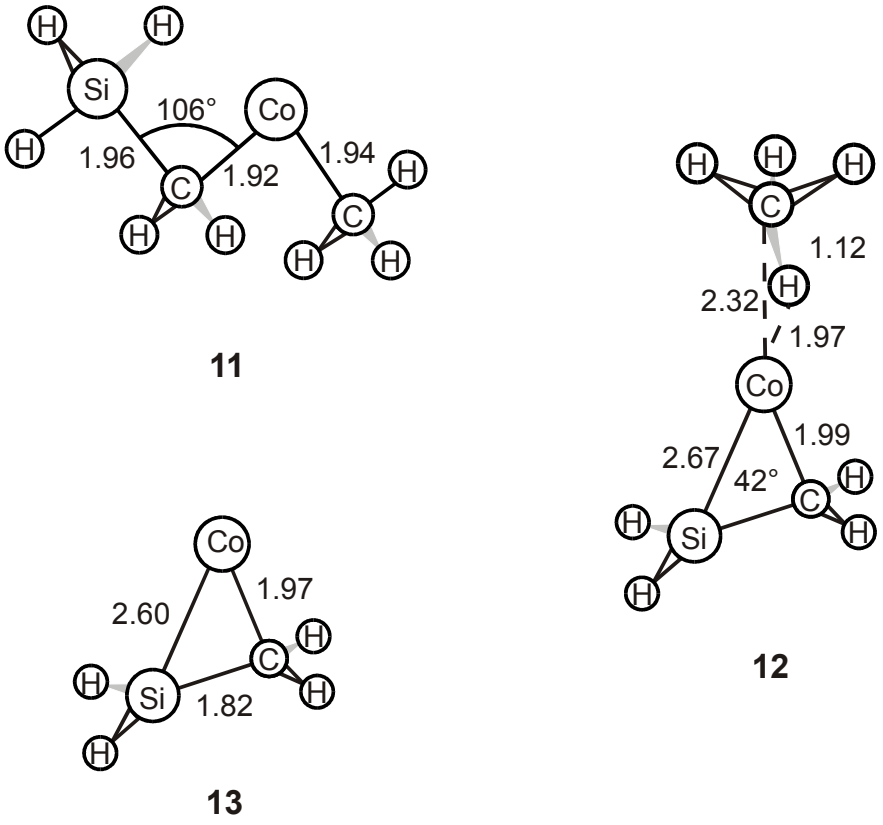

Chart 6-9: Minima along the C–C bond insertion PES. Note, that only structures are displayed which have not been mentioned before. Bond lengths are given in Å and angles in degree.

Structure **12** (E_{rel} = -9.1 kcal/mol) consists of a CH_4 molecule weakly interacting with the metal and a silaethene ligand attached to the opposite side of the Co^+. The structure of the

CH_4 subunit is slightly perturbed from tetrahedral symmetry because of the η^2-coordination of the ligand via two hydrogen atoms to Co^+.

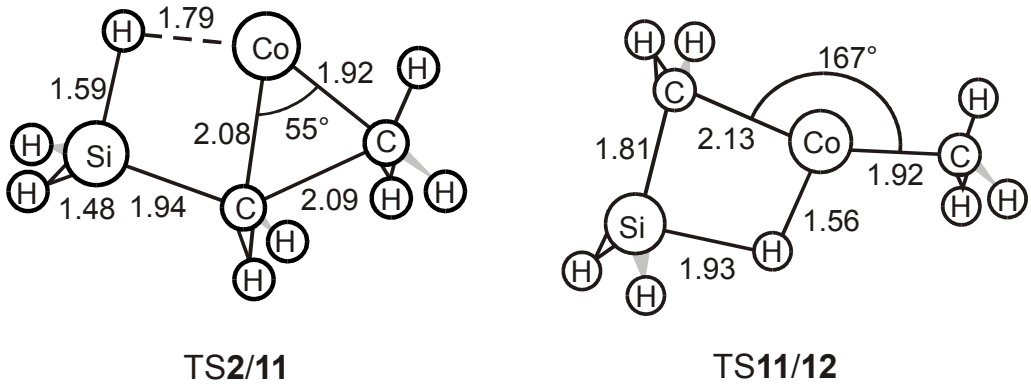

TS**2/11** TS**11/12**

Chart 6-10: Transition structures along the C–C bond insertion pathway. Bond lengths are given in Å and angles in degree.

This interaction causes a slight elongation of the coordinated C–H bonds as compared to the C–H bonds pointing away from Co^+ (r_{CH} = 1.12 vs 1.10 Å). The silaethene moiety is side-on coordinated to Co^+ with r_{CoC} = 1.99 Å and r_{CoSi} = 2.67 Å. **12** serves as a direct precursor for loss of methane concomitant with formation of $Co(CH_2SiH_2)^+$, **13**. This exit channel is predicted as the energetically most favoured of all product channels (E_{rel} = 4.0 kcal/mol). This observation is in agreement with the calculated reaction enthalpy of 15.5 kcal/mol for the ligand exchange reaction $Co(CH_2SiH_2)^+ + C_2H_4 \rightarrow Co(C_2H_4)^+ + CH_2SiH_2$. The increased stability of $Co(CH_2SiH_2)^+$ is not only rationalized by the higher polarizability of the CH_2SiH_2 ligand compared to C_2H_4, but also points to the involvement of mesomeric species, i.e. $Co^+–CH_2–SiH_2 \leftrightarrow Co–CH_2–SiH_2^+$. The latter is supported by the Mulliken population analysis (q_{Co^+} = +0.86, q_{Si} = +0.57, q_C = -0.43). In addition, structural features of product complex **13** assist this conjecture; the Co–C bond length of r_{CoC} = 1.97 Å is shorter than the corresponding Co–C bond length in the above described olefin complexes, whereas the Co–Si distance of r_{CoSi} = 2.60 Å is relatively long. This situation coincides with an asymmetric side-on coordination already discussed for **12**.

Si-H Bond Insertion. This mechanism seems to proceed in a different manner compared to the other insertion reactions described above (Figure 6-6). The geometries of the corresponding minima of this pathway are displayed in Chart 6-11. The expected pathway, i.e. primary insertion into only one Si–H bond, could not be confirmed. Moreover, not even

intermediate Si–H insertion structures could be located; any of the numerous inputs used in the geometry optimizations either converged to encounter complex **2** or product structure **14**.

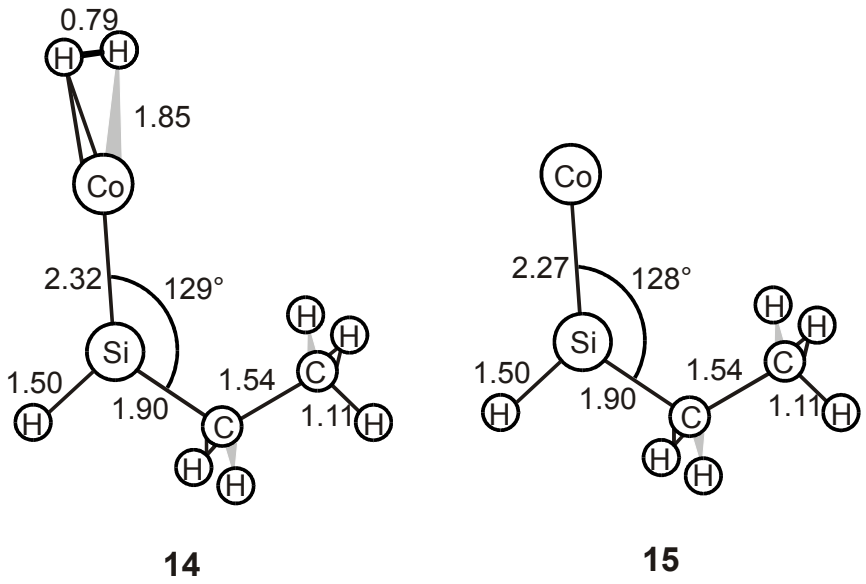

14 **15**

Chart 6-11: Minima of the Si–H bond insertion pathway. Bond lengths are given in Å and angles in degree.

Therefore, a genuine Si–H bond inserted structure may not even exist as a stationary point at the level of theory employed; instead the reaction is assumed to proceed via a four-centered transition structure directly from **2** to **14**, $(H_2)Co(SiHC_2H_5)^+$. To the best of our knowledge, no detailed calculations on the activation of silane by M^+ exist to corroborate this type of mechanism.[26,27] However, the insertion into two Si–H bonds would be in accord with quantum-chemical calculations of Morokuma and coworkers,[28] who investigated the reactions of late 3d-transition metals with CH_4. They too were unable to locate a species corresponding to $H–M–CH_3^+$, but found the reaction to proceed directly from $M(CH_4)^+$ to $(H_2)MCH_2^+$ for M = Co, Fe. As in the present system all attempts failed so far to locate the corresponding multicentered TS**2**/**14**, in analogy to the results of Morokuma et al.,[28] **2** and **14** are assumed to be connected by a single TS and the energetic location of this TS can be evaluated by comparison of experimental and computational data. The search for TS**2**/**14** included various plausible input structures as well as the LST (linear synchronous transit),[29] or QST2, and QST3 optimization methods[30] as implemented in Gaussian94.

Minimum **14** (E_{rel} = 11.1 kcal/mol) is characterized as a cobalt cation interacting with two ligands, i.e. a slightly distorted hydrogen molecule and an ethylsilylidene-unit; **14** thus serves as a precursor for loss of H_2 to afford product complex **15** (E_{rel} = 17.3 kcal/mol). The Co–Si bond lengths of r_{CoSi} = 2.32 Å and 2.27 Å in **14** and **15** are considerably shorter than the C–Si

bond in **3** (r_{CoSi} = 2.44 Å). This kind of bond shortening is in line with formal cobalt-silicon double bonds in the silylidene-complexes in **14** and **15**. The structure of the free cobalt silylidene **15** closely resembles the geometry of **14**. This is readily explained, because loss of the electrostatically bound H_2 ligand from **14** is not expected to induce major changes in the electronic and geometric structure of the silylidene unit.

6.2.3 Product Formation Pathways

Some more general features of the above described reaction paths need to be outlined first. (i) The calculated minima and transition structures of the C–Si, C(1) –H, and C–C bond insertion paths are lower in energy or in close vicinity of the entrance channel. These reactions are therefore expected to occur under thermal conditions, which is in agreement with the experimentally observed findings. The predicted barrier of the C(2) –H bond insertion pathway is more than 7 kcal/mol above the entrance channel; thus, this pathway should occur only at elevated energies and its role is therefore kept short in the further considerations. The activation of the Si–H bond is clearly exothermic from a thermochemical point of view, because all minima are located well below the entrance channel. As TS**2**/**14** could not be located, the barrier associated with this rearrangement remains uncertain. However, the significant loss of D_2 from the labeled substrate $C_2H_5SiD_3$ demands the inclusion of this pathway in the discussion. (ii) In general, the TSs of the initial oxidative additions are less energy demanding than the barriers associated with the further rearrangements and reductive elimination en route to the product complexes. Hence, the latter are rate determining for the Co^+/ethylsilane system; in contrast, initial bond insertion can be considered as facile and not rate determining. This finding is in accord with previous calculations on the activation of organic substrates by late transition-metal cations.[24] The following discussion therefore concentrates on the rate-determining TSs and the calculated thermochemistry of the products.

Loss of Silane. Elimination of silane is conceivable either via primary insertion in the C–Si bond (Figure 6-3) or via primary C(2) –H bond activation (Figure 6-4). On the C–Si insertion surface (Figure 6-3), the relevant TS is TS**3**/**4** at E_{rel} = 39.6 kcal/mol compared to the entrance channel at E_{rel} = 37.8 kcal/mol. Once this barrier is surmounted, **4** is formed and has enough internal energy to directly decompose into the products $Co(C_2H_4)^+$ and SiH_4 as well as $Co(SiH_4)^+$ and neutral ethylene. Due to the strong Co^+-ethylene bond, elimination of SiH_4 is thermochemically preferred over that of C_2H_4.

A second conceivable pathway for formation of **4** proceeds via initial C(2)–H bond insertion and consecutive reaction via TS**4**/**7** (Figure 6-4). Both pathways are strongly exothermic; however, while the C–Si bond insertion pathway remains below the entrance channel, the C(2)–H bond insertion pathway involves a barrier located 6.8 kcal/mol above separated Co^+ and $C_2H_5SiH_3$. Although the distinction is not unambiguous, because of the error bars of the calculations, initial activation of the C–Si bond is proposed as the energetically least demanding path for the formation of **4**.

Dehydrogenation. Elimination of molecular hydrogen may occur via two entirely different reaction pathways involving isomeric product species, i.e. the silene **9** and the silylidene **15**. Both types of species have been generated before, in the gas phase[31] as well as in solution.[32]

Two possible pathways (primary C(1)–H or C(2)–H bond insertions as depicted in Figures 6–4 and 6–5, respectively) lead to formation of **8**, the precursor of the silene complex **9**. TS**8**/**10** of the C(1)–H bond insertion pathway is located at E_{rel} = 40.2 kcal/mol, thus only 2.4 kcal/mol above the entrance channel. After traversing TS**8**/**10**, formation of **8** and subsequent loss of H_2 is easily accomplished and not associated with any further energy demand. On the C(2)–H bond insertion PES, however, the pathway for formation of **8** proceeds via TS**7**/**8** at E_{rel} = 46.0 kcal/mol. Accordingly, the C(1)–H bond insertion pathway should be preferred for thermalized ions, while the route involving initial activation of the C(2)–H bond requires elevated energies. Thus, formation of **9** is expected to proceed via the C(1)–H bond insertion pathway.

Dehydrogenation may also lead to the isomeric product **15** (Figure 6-6). However, as TS**2**/**14** could not be located, a direct comparison to the route leading to **9** is impossible. Thermochemically, formation of **15** is disfavored by 3.5 kcal/mol compared to **9**. Nevertheless, the experimental data obtained with labeled compounds (see above) indicate that 1,1-dehydrogenation of the silyl group prevails. Thus, the conclusion is that the rate determining TS**2**/**14** en route to silylene formation must be lower in energy than TS**8**/**10** (E_{rel} = 40.2 kcal/mol) and because loss of H_2 is only a minor experimental product, TS**2**/**14** is assumed to lie close to the entrance channel (E_{rel} = 37.8 kcal/mol).

Loss of methane. Only one pathway for the formation of **13** is calculated, which consists of primary C–C bond insertion, subsequent β-hydrogen migration from the silyl- to the methyl group and final release of a methane molecule from **12** (Figure 6-6). The reverse sequence, i.e. Si-H bond activation followed by a β-methyl migration is not pursued because (i) previous studies have shown that migration of hydrogen is generally preferred over that of alkyl

groups,[24,33] and (ii) the investigation of the primary Si–H bond insertion on the dehydogenation pathway shows that the H–Co^+–$SiH_2C_2H_5$ species may not even exist but rather insertion occurs into two Si–H bonds, thus leading to formation of **14** and final release of molecular hydrogen. Compared to the other PES, the critical TS**11**/**12** (E_{rel} = 35.8 kcal/mol) is the lowest lying TS of all rate determining steps. The energetic location of TS**11**/**12** as well as the low-lying exit channel suggest C–C bond activation as the kinetically and thermodynamically most favored pathway for the reaction of **1** with Co^+. Notwithstanding, formation of CH_4 does not constitute the major route in the experimental studies.

Therefore, a closer inspection of the whole PESs (Figures 6–3 to 6–6) is advisable. As the C(2) –H bond insertion pathway is less likely to occur due to the high energy demands of TS**4**/**7** and TS**7**/**8**, only the four remaining mechanisms have to be considered. The rate determining transition structures TS**3**/**4** (C–Si), TS**8**/**10** (C(1) –H), TS**11**/**12** (C–C), and TS**2**/**14** (Si–H) are located at E_{rel} = 39.6, 40.2, 35.8, and <40.2 kcal/mol, respectively; they are comparable within the error bars. Along these routes, all products are energetically located well below the corresponding TS, resulting in their strong competition. However, it is important to stress in this context that even slight differences in the energetic location of the TS can dramatically change the product branching ratios because of the exponential behavior of Arrhenius-type expressions; in addition, the reaction rates may not depend on activation energies alone.

As mentioned above, while the rate determining TS among several surfaces cannot be unequivocally assigned within the error of the method, the calculations show a strong trend towards formation of CH_4 as the kinetically and thermodynamically preferred neutral product; this contrasts with the experimental findings (Figure 6-1). Several factors can be considered to explain this discrepancy. (i) Earlier calculations on the binding energies of M^+–CH_3 and $(H_3C)M^+$–CH_3[34,35] and comparison with existing experimental data[36] (Table 6-1) show a distinct overestimation of the sum of the bond dissociation energies [$D_0(M^+\text{-}CH_3)$ + $D_0(CH_3M^+\text{-}CH_3)$] in the B3LYP/BS1 approach for Fe^+. While no experimental data are available for $Co(CH_3)_2^+$, comparison with *ab initio* calculations[35] (see Table 6-1) suggests a similar effect. The $M(CH_3)_2^+$ species may be considered as a model system for a C–C inserted intermediates; therefore, a similar overestimation of M^+–C bond dissociation energies might result in an artificial stabilization of **11** and TS**11**/**12** as compared to the corresponding structures of the Si–H and C–H insertion PESs.[37] Further support arises from preliminary

calculations on Co–CH_3, Co–SiH_3, and Co–H binding energies. However, for the C–Si bond activation overbinding would be expected as well. According to Table 6-1, the error due to this phenomenon amounts to 6.0 kcal/mol for $Fe(CH_3)_2^+$. If, as a rough first estimate, the same error is assumed for the C–C bond insertion PES in the present system, **11** and TS**11**/**12** would have to be shifted to higher energies by some kcal/mol. This puts the C–C insertion PES into the same energy range as calculated for C–Si, C–H, and Si–H bond activations.

Another hint that the C–C bond insertion may be artificially stabilized in the present computational approach arises from single-point calculations on the critical parts of the PES, i.e. the transition structures of the rearrangement and the exit channels, using a larger basis set (B3LYP/BS2, see Table 6-2). These calculations reveal small, but important changes in the qualitative picture as compared to the B3LYP/BS1 approach. While the order of the exit channels remains more or less unchanged, small but crucial changes occur for the activation barriers. TS**11**/**12** of the C–C insertion PES corresponds in the B3LYP/BS2 picture no longer to the lowest transition state; rather this TS is located at the same relative energy as TS**8**/**10** and TS**3**/**4** within the error of the calculations, e.g. TS**11**/**12** is calculated 3.0 kcal/mol *above* TS**8**/**10** of the C(1) –H insertion PES and only 3.0 kcal/mol below the corresponding TS of the C–Si insertion pathway (TS**3**/**4**).

Table 6-1: Comparison of experimental, MCPF- and DFT-based bond dissociation energies (D_0) in kcal/mol of Co^+ and Fe^+ methyl- and dimethyl-complexes.

	$D_{0,\text{experimental}}$[a]	$D_{0,ab\ initio}$[b]	$D_{0,DFT}$	$D_{0,DFT}$[e]
Fe^+–CH_3	54.6 ± 1.1	50.9	64.9[c]	60.9
H_3CFe^+–CH_3	43.1 ± 2.5	33.0		42.5
ΣD_0	97.7 ± 2.7	83.9		103.4
Co^+–CH_3	48.5 ± 0.9	48.6	56.3[d]	57.5
H_3CCo^+–CH_3		39.1		51.2
ΣD_0		87.7		108.7

[a] Ref. 36. [b] Ref. 35. [c] Ref 34a. [d] Ref 34b. [e] This work, obtained using the B3LYP/BS1 approach.

Thus, the B3LYP/BS2 results imply that the different pathways strongly compete with each other under thermal conditions. Accordingly, the preference of C–C bond activation may no longer exist at higher levels of theory and may even disappear when higher levels of theory are used in geometry optimizations. It needs to be stressed again, however, that although

distinction of TS**11**/**12**, TS**3**/**4**, and TS**8**/**10** is not possible within the error of the calculations, differences of 2.6 kcal/mol (between TS**11**/**12** and TS**8**/**10**) and 2.3 kcal/mol (between TS**3**/**4** and TS**11**/**12**) do well matter in the experiment. The use of more sophisticated theoretical methods is therefore indicated and may be a possibility to more reliably distinguish between the different pathways. (ii) Statistical arguments could also disfavor the formation of CH_4 in the experiments. For instance, formation of product complex **5** can be achieved along two pathways (initial C–Si and C(2) –H bond insertion), both of which are feasible energetically within the error of the calculations, although one of them is more likely to occur due to an energetically less demanding TS. While the C–Si bond insertion pathway has only one possibility to evolve, C(2) –H bond insertion may occur at any of the three C–H bonds at C(2) atom, leaving a statistical weight of 3 for the C(2) –H bond insertion pathway and a statistical weight of 4 for both possible pathways the formation of **5**. A similar situation is found for the formation of the product complex **8**. Both pathways, C(1) –H and C(2) –H bond insertions are thermodynamically accessible, although C(1) –H bond insertion is favored because of the lower-lying TS. While C(1) –H bond insertion has a statistical weight of 2 because insertion may occur into each of the two C–H bonds at C(1), the C(2) –H bond insertion pathway has a statistical weight of 3, as explained above. For the formation of **8** via both conceivable pathways this yields an overall statistical weight of 5. Using analogous arguments, loss of H_2 under formation of **15** is associated with a statistical weight of 3. In contrast, **12** can only be formed via a single pathway, and thus has a statistical weight of 1. Therefore, C–C bond cleavage is statistically disfavored compared to all other types of bond activations in the present system. (iii) Finally, temperature effects need to be considered. The computational results presented up to this point always refer to 0 K energies. However, the internal temperature of the metastable Co^+/ethylsilane complexes examined in the sector-MS experiment is assumed as 500 K, while higher values have also been reported.[8] The internal temperature of the separated reactants in the FT-ICR experiments is assumed to be 298 K, whereas the internal energy content of the encounter complexes formed in the FT-ICR is expected to be much higher; as outlined above, the internal energy content of the encounter complexes in the FT-ICR is even larger than in the sector-MS. Inclusion of thermal and entropic corrections in terms of relative ΔG_{298} values (Table 6–2) is therefore necessary but results in small changes of the picture in terms of absolute numbers only. Because the relative energies of both TS**11**/**12** and TS**3**/**4** decrease, the advantage of the C–C activation remains approximately the same indicating similar entropic effects. The disadvantage of the pathways based on initial C(2) –H bond insertion is still distinct, such that all considerations lead to

exclusion of this pathway in $Co^+/C_2H_5SiH_3$. Obviously, thermal effects alone therefore cannot account for the underestimation of the C–C bond activation pathway.

Table 6-2: Calculated relative energies (kcal/mol) of the critical parts of the PES using B3LYP/BS1, B3LYP/BS2, and B3LYP/BS1 under incorporation of thermal corrections. All energies given refer to the lowest lying encounter complex **2** at $E_{rel} = 0$.

	$E_{rel,0K}$ (BS1)	$E_{rel,0K}$ (BS2)	G_{298K} (BS1)
Co^+ + **1**	37.8	41.7	30.2
TS**3**/**4**	39.6	40.7	39.0
TS**4**/**7**	44.6	46.3	44.3
TS**7**/**8**	46.0	46.4	46.2
TS**8**/**10**	40.2	34.7	41.2
TS**11**/**12**	35.8	37.7	34.7
5 + SiH_4	9.5	17.2	-0.7
9 + H_2	13.8	20.8	6.9
13 + CH_4	4.0	11.7	-6.4
14 + H_2	17.3	20.4	9.6

6.2.4 Summary

The reactions of Co^+ with $C_2H_5SiH_3$ are investigated using the DFT-approach B3LYP with a basis set of VDZ-quality. The calculations show qualitative agreement with the experiments in that all products observed in the experiments are calculated to be formed in reactions proceeding via exothermic or thermoneutral pathways relative to the isolated reactants. While SiH_4 is formed by primary C–Si bond activation, the favored pathways for the formation of neutral H_2 are found to proceed via primary C(1) –H and Si–H bond insertions, respectively. According to the calculations, C(2) –H bond insertion is less likely to occur due to the higher lying transition structures associated with the rearrangements along the C(2) –H bond insertion pathway compared to the existing alternatives on the C–Si, C(1) –H, C–C, and Si–H insertion PESs. For the formation of neutral CH_4, only one conceivable pathway is calculated, commencing with insertion in the C–C bond.

The quantitative consistency between experimental product branching ratios and calculations is less good. No clear-cut energetic distinction can be made between TS**3**/**4**, TS**8**/**10**, and TS**11**/**12**, such that some disagreement between experiment and theory remains unresolved. In particular, the experimentally observed preference for loss of SiH_4 concomitant with formation of the charged product species **5** does not find a conclusive rationale in the theoretical predictions. Statistical factors and temperature effects are considered as possible origins for this behavior, but the major source of disagreement is attributed to the partially unbalanced description of M–H, M–C, and M–Si bond strengths in the investigated cationic complexes by the applied B3LYP functional in conjunction with the VDZ basis set.

An important conclusion derived from this study concerns the performance of currently used theoretical methods for the description of reactions involving transition-metal compounds. Thus, nowadays levels of theory are capable of describing the potential-energy surfaces involved in these processes qualitatively correct. In fact, the accuracy of the predicted barrier heights may even suffice for a quantitative assessment of branching ratios when *similar* processes compete with each other. For example, a combination of *ab initio* methods and molecular modeling proved successful in describing the regioselectivity in the remote functionalization of C–H bonds of nonanitrile/M^+ (M = Fe, Co).[8] The agreement achieved between experiment and theory in this case is not to be considered as entirely fortuitous because in the context of regioselectivity the pathways do not fundamentally differ in nature but in subtle effects imposed by the substrate's backbone. Therefore, the gross systematic errors in describing certain bonding situations cancel in the evaluation of the branching for the activation of a certain site. In the present case, however, *dissimilar* channels are compared with respect to the nature of the bonds being activated, i.e. C–H, C–C, C–Si, and Si–H bonds which all bear similar activation parameters. In such a case, even minute errors in the quantitative description of the bonding situations - recall the above discussion of the C–C bond insertion intermediates - result in dramatic changes of the predicted branching ratios. In conclusion, the quantitative description of competing processes of different kind remains problematic.

6.3 The Activation of Ethylsilane by Fe^+

In the previous section, the reaction of cobalt cations with ethylsilane was investigated. In a recent experimental study on the activation of *n*-propyltrimethylsilane by Fe^+ and Co^+ dramatic differences in the reaction behavior were found, depending on which of the two

transition metals was used as activating reagent. Therefore, a concise discussion of the Fe^+/ethylsilane system is advisable.

6.3.1 Experimental Results

Prior to the theoretical treatment, the reaction of Fe^+ with $C_2H_5SiH_3$ was investigated by two mass spectrometric techniques; FT-ICR and sector-MS. As both experimental procedures have been outlined in Chapter 2, only a short overview over the data is given here. The results of the measurements are displayed in Figure 6-7.

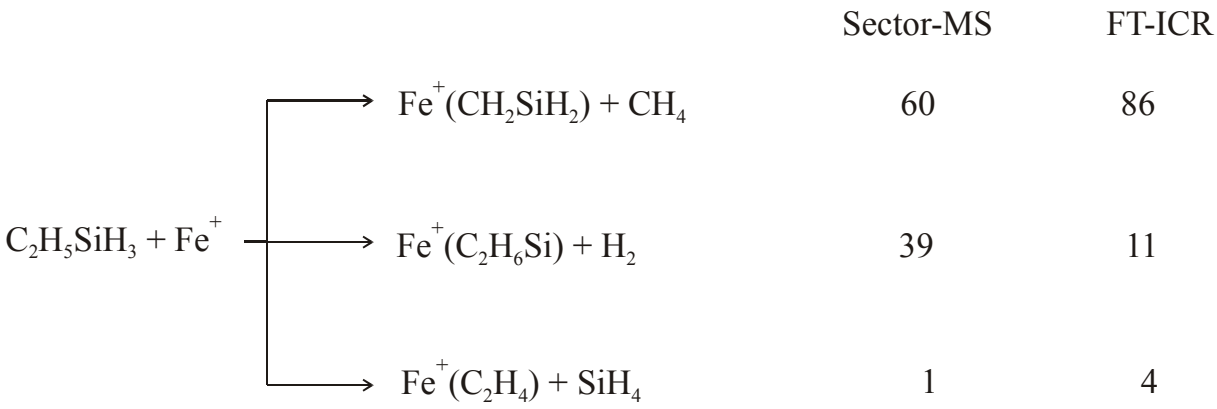

Figure 6-7: Product distribution for Fe^+/ethylsilane in FT-ICR and sector-MS experiments. Intensities are normalized to $\Sigma_{products}$ = 100%; and ion intensities < 1% are omitted.

Both, FT-ICR and sector-MS show a strong preference for loss of neutral CH_4 concomitant with formation of $Fe(CH_2SiH_2)^+$, and elimination of H_2 is clearly less pronounced. In contrast to the cobalt-system, formation of SiH_4 is only a very minor product channel for iron. Again, H_2 expulsion may occur from different positions within the molecule, resulting in the formation of the isomeric products $Fe(C_2H_3SiH_3)^+$ or $Fe(C_2H_5SiH)^+$. Some more insight is gained from labeling experiments using $Fe^+/C_2H_5SiD_3$. In the sector-MS, instead of CH_4 and SiH_4, the deuterated products CH_3D and SiD_3H are observed, consistent with primary C–C or Si–D bond insertions for methane formation and primary Si–C or C(2) –H bond insertions for formation of silane. However, no loss of D_2 or HD is observed in the labeling studies, even in CA experiments. Thus, the structure of the ionic product after dissociation of H_2 points to $Fe(C_2H_3SiH_3)^+$ rather than the silylidene-structure found in the corresponding reaction with Co^+.

6.3.2 The PES of Fe^+/Ethylsilane

Four different routes for the activation of ethylsilane by Fe^+ are calculated according to the conceivable primary insertion sites for the transition metal ion, e.g. C–Si, C(2) –H, C(1) –H, and C–C bond activation. Primary Si–H bond insertion is excluded because the labeling experiments show that it is not involved in the reaction. On each PES, the corresponding quartet and sextet states are considered. The following section is organized such that first the entrance channel and the encounter complexes are described. This is followed by a characterization of the remaining species along the four individual reaction pathways. The energetic and geometrical features of minima and transition structures for both, the quartet and the sextet states, are discussed in the order of their appearance in Figure 6-8.

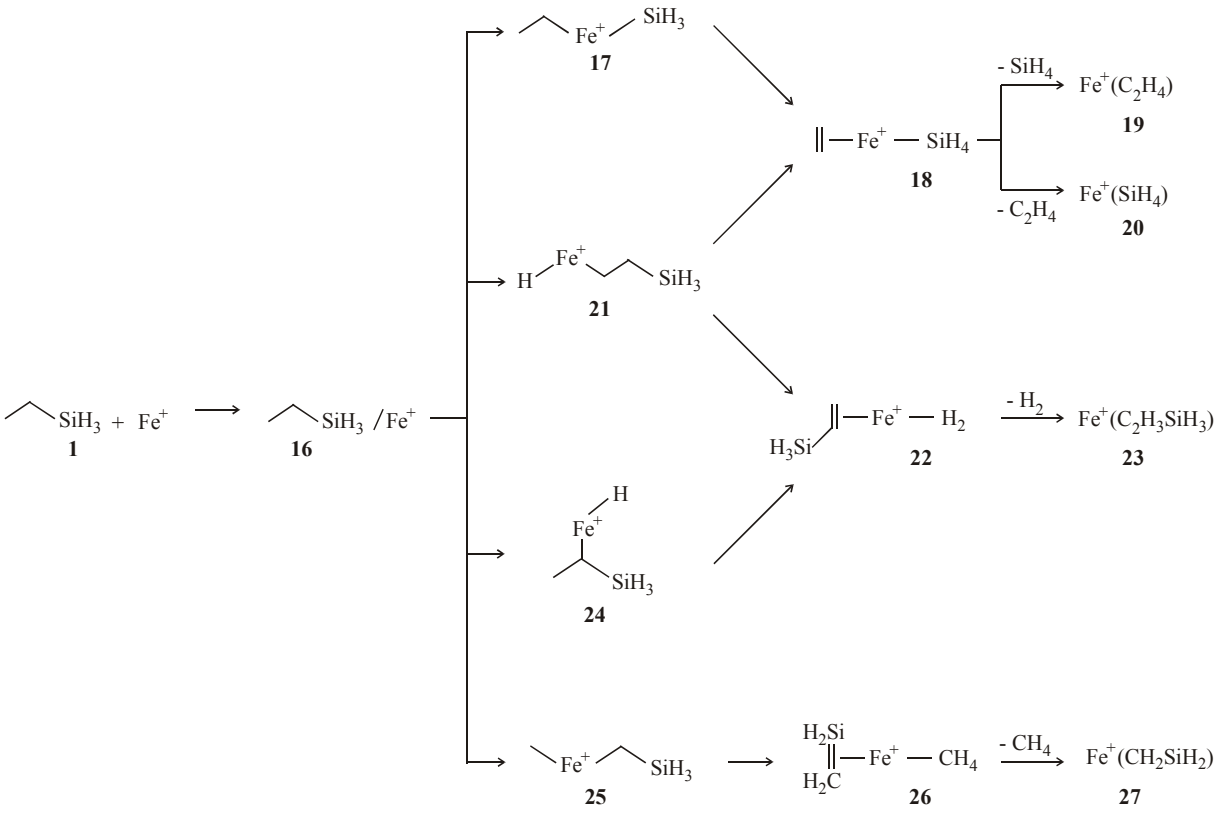

Figure 6-8: Schematic description of the calculated reaction pathways of the Fe^+/ethylsilane system. Only the expected minima along the reaction coordinate are displayed, while transition structures are discussed in the text.

Before starting with the evaluation of structures and geometries, some general remarks are indicated. (i) As described already for the Co^+/ethylsilane system, for the construction of the PES only the most stable conformers are used. (ii) In further analogy to Co^+/ethylsilane, the entrance channel ($Fe^+ + C_2H_5SiH_3$) is expected to be associated with a somewhat larger error

than the remaining parts of the PES; therefore, the encounter complex **16** is used as the reference point for the relative energy scale of the PES. The overall error of the calculations is estimated to be ± 6 kcal/mol, based on the average deviations of calculated bond dissociation energies and heats of formation of model processes with known literature thermochemistry as well as comparison with other B3LYP investigations on other transition-metal compounds (see Chapters 3 to 5).

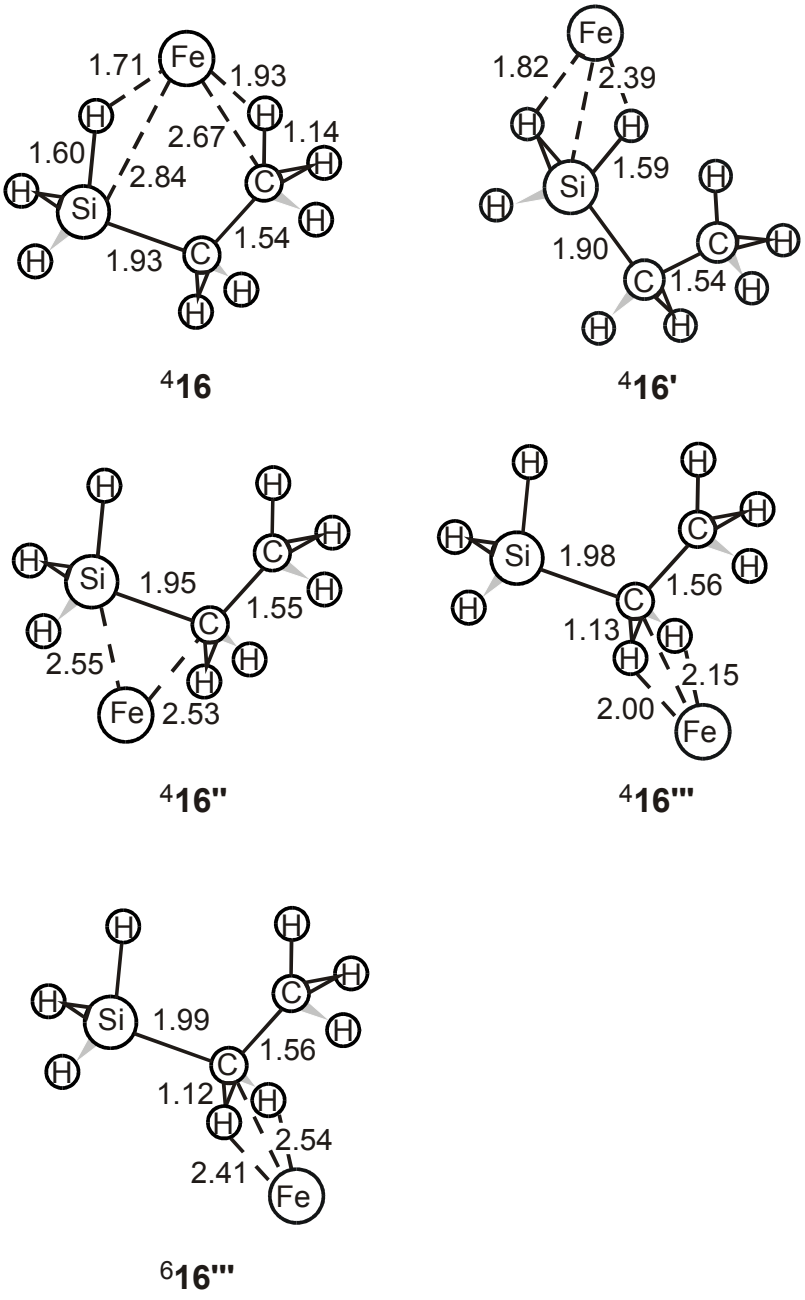

Chart 6-12: Encounter complexes of the Fe^+/ethylsilane system. Bond lengths are given in Å and angles in degree.

Reactants. Despite the preference of the B3LYP calculations for a ^{4}F ground-state of iron (see above), the experimental ^{6}D ground-state is used for the entrance channel. The structure of ethylsilane has already been depicted in Section 6.2, Chart 6-1. In analogy to the previous section on the Co^+/ethylsilane system, the carbon atoms in ethylsilane are referred to as C(1) and C(2), according to their connectivity in ethylsilane.

Encounter complexes. The lowest lying quartet encounter complex ^{4}**16** (see Chart 6-12) is assigned to E_{rel} = 0 kcal/mol on the relative energy scale. This η^4-complex is of C_1 symmetry and characterized by the interaction of the iron cation with the silicon atom, C(2) and two hydrogen atoms. In analogy to the Co^+/ethylsilane system, three other conformers of **16** are located on the quartet surface, at relative energies of 1.1, 4.8, and 7.5 kcal/mol, i.e ^{4}**16'**, ^{4}**16"**, and ^{4}**16'"**. While ^{4}**16'** is also a η^4-complex with interactions between iron and C(1), Si, and two hydrogen atoms, the η^3-complex ^{4}**16"** shows strong interaction only between the iron cation and silicon as well as two hydrogen atoms on silicon, respectively. These structures have a silicon-iron interaction in common, whereas in the least stable structure ^{4}**16'"** the iron cation interacts only with C(1) and the two hydrogen atoms on C(1). The lower stability of ^{4}**16'"** as compared to the other encounter complexes indicates a stronger interaction between the Fe^+ and silyl-group as compared to the less pronounced Fe^+-methyl interaction. On the sextet surface only one encounter complex ^{6}**16'"** (E_{rel} = 16.7 kcal/mol) is located, which structurally corresponds to ^{4}**16'"**. Due to the high relative energy further search for other encounter complexes along the sextet surface was not pursued.

C–Si-insertion, Figure 6-9. This pathway continues via TS**16**/**17** to the inserted structure **17**. The TS could not be located on either PES, however, previous experiences with these types of systems[4a,8,24] as well as the calculations on the Co^+/ethylsilane system show that the TS from the encounter complex to the primary insertion structure is generally lower in energy than the subsequent TS which is associated with migration processes. Therefore, TS**16**/**17** is likely not to play an important role in the overall reactivity of the system.

For the C–Si insertion structure (Chart 6-13), two conformers are located on the quartet surface, of which ^{4}**17**, the anti-conformer with respect to the Fe–C bond, is the minimum at E_{rel} = 5.7 kcal/mol. The second conformer, ^{4}**17'** (E_{rel} = 6.2 kcal/mol), shows an gauche-conformation. On the sextet surface, ^{6}**17** (E_{rel} = 21.7 kcal/mol) deviates from its quartet analog by an almost linear Si–Fe–C(1)-unit, a phenomenon which is observed on several occasions during this study and which can be attributed to the different electronic structure of $^6Fe^+$ compared to $^4Fe^+$. Because all orbitals in the 3d and 4s shells are occupied in Fe^+(^{6}D), formation of covalent bonds or donation of electron density into an empty orbital as in a π-

interaction is not possible, thus resulting in longer, electrostatic bonds formed by the sextet species as well as the observed linear arrangement of the fragments.

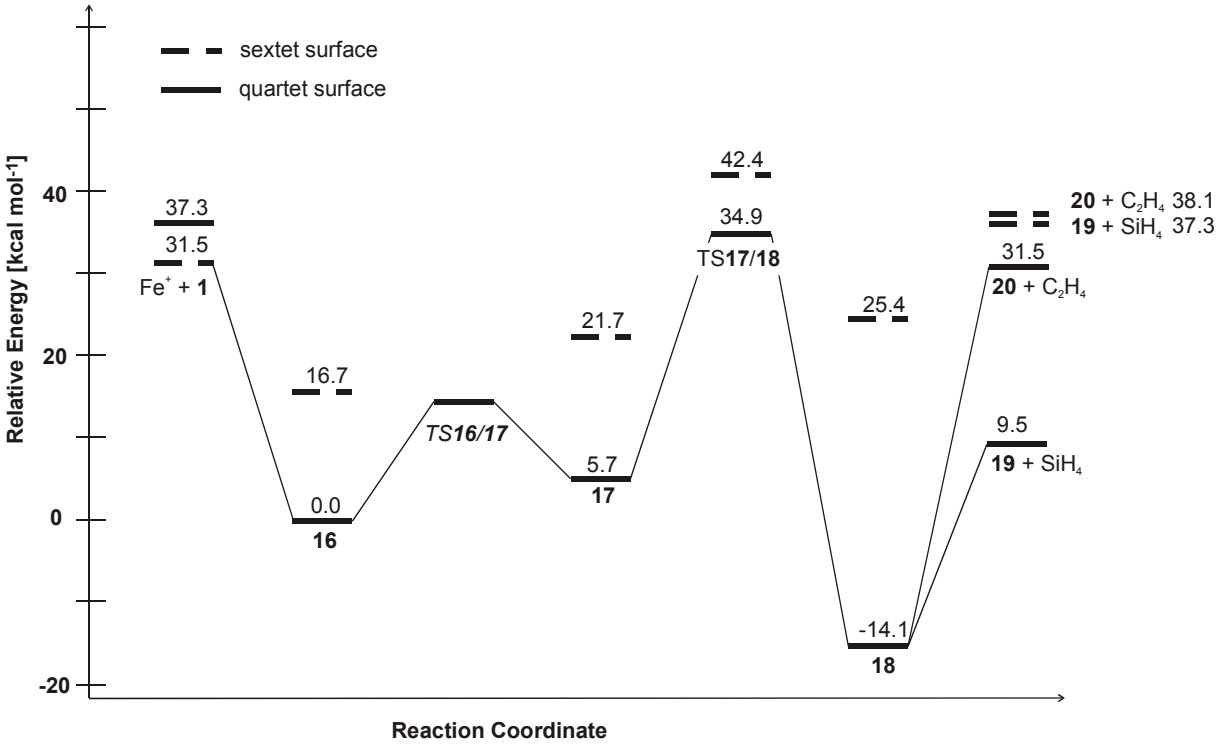

Figure 6-9: B3LYP/BS1 PES of the C–Si bond insertion pathway of Fe^+/ethylsilane relative to the lowest-lying encounter complex ^{4}**16**; ZPVE corrections are included, and the relative energies are given in kcal/mol. The solid lines refer to the quartet PES while the dashed lines are used to denote the sextet PES.

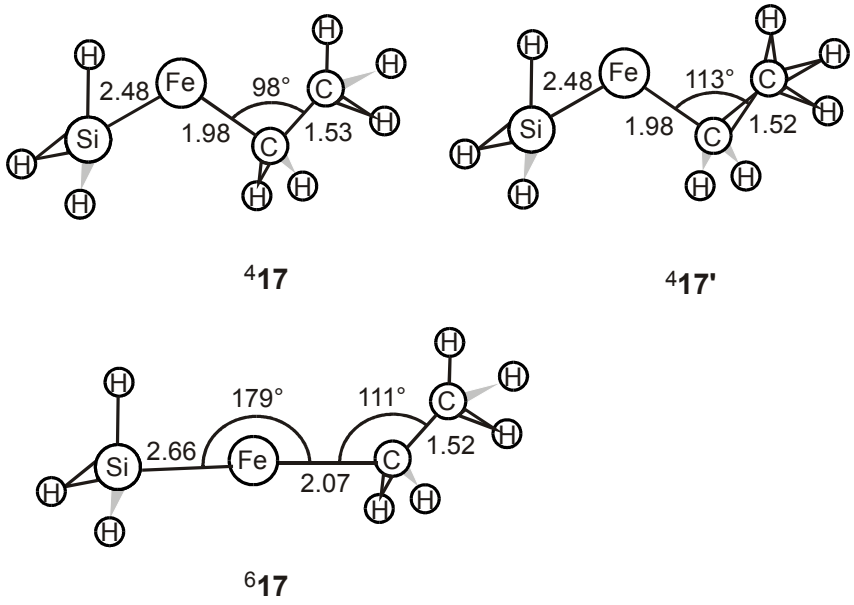

Chart 6-13: C–Si inserted structures on the quartet and sextet surface. Bond lengths in Å and angles in degree.

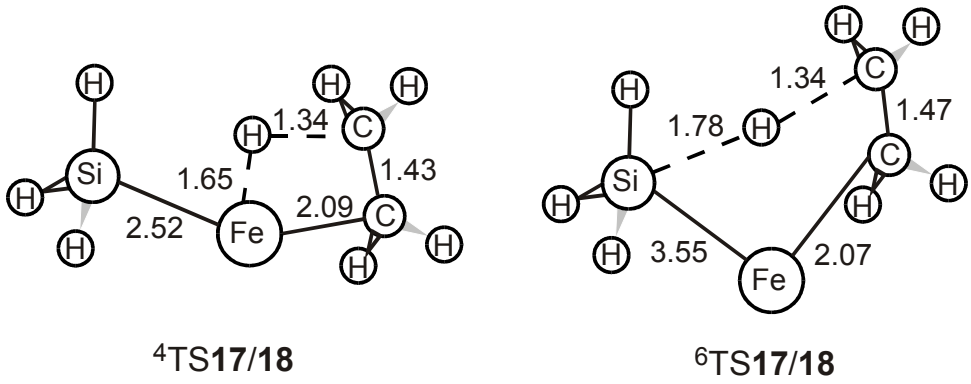

Chart 6-14: TS**17**/**18** of the Fe^+/ethylsilane system. Bond lengths are given in Å and angles in degree.

The reaction proceeds by β-H-migration via TS**17**/**18** to complex **18**. On the quartet surface, ^{4}TS**17**/**18** (E_{rel} = 34.9 kcal/mol) shows an elongated C(2)–H bond along with intermediate formation of a Fe–H bond (Chart 6-14). The imaginary frequency of i1040 cm^{-1} corresponds mainly to the motion of the hydrogen atom from C(2) to Si with smaller contributions due to the planarization of the remaining hydrogen atoms on C(1) and C(2). The structure of ^{6}TS**17**/**18** (E_{rel} = 42.4) differs from ^{4}TS**17**/**18** in that the Fe–Si bond is already very much elongated (r_{FeSi} = 3.55 Å) and the SiH_3 unit bend towards the C_2 unit (Chart 6-14). Thus, no intermediate Fe-H bond formation occurs in the sextet TS (r_{FeH} = 2.65 Å). The imaginary frequency of i804 cm^{-1} corresponds mainly to the motion of the hydrogen atom away from C(2) towards Si, accompanied by smaller contributions from the hydrogen atoms remaining at C(2).

Complex **18**, which is reached next, consists of the metal surrounded by two ligands, ethylene and silane (Chart 6-15). On the quartet surface, two conformers are located, i.e. ^{4}**18** and ^{4}**18'** (E_{rel} = -14.1 and -11.4 kcal/mol). In the energetically favorable conformer ^{4}**18**, the silane molecule is bound to Fe^+ through an electrostatic interaction of one hydrogen atom of the silane molecule with the iron cation, hence the hydrogen atom is pointing directly toward Fe^+, forming an Si–H–Fe^+ angle of 180°. ^{4}**18'** differs from ^{4}**18** only in the type of bonding of the silane molecule, which in ^{4}**18'** is bound by electrostatic interaction between the silicon atom and iron with the Fe–Si bond bisecting the H–Si–H angle. The sextet analog, ^{6}**18** (E_{rel} = 25.4 kcal/mol) shows a comparable bonding to SiH_4, but a totally different type of bonding to C_2H_4 compared to its quartet analogs. The ethylene ligand is not symmetrically bound, but rather an electrostatic interaction exists between C(1) and Fe^+, while C(2) is directed away from the metal. The silane ligand is also bound through electrostatic interaction, in the same manner as described for ^{4}**18**. Generally, the metal-ligand bond lengths in the sextet structures

are elongated as compared to the quartet structures, which is easily explained by the different bonding situation evoked by the electronic structure of $Fe^+(^6D)$ with its $3d^64s^1$-configuration.

From **18**, the reaction continues either to exit channel **19** + SiH_4, which is located at E_{rel} = 9.5 kcal/mol and E_{rel} = 37.3 kcal/mol on the quartet and sextet PES, respectively, or to exit channel **20** + C_2H_4, located at E_{rel} = 31.5 kcal/mol and E_{rel} = 38.1 kcal/mol on the respective quartet and sextet surfaces (Chart 6-16). In ^{4}**19**, the ethylene ligand shows a typical C–C bond length (r_{CC} = 1.41 Å), and Fe is symmetrically attached to the double bond with $r_{CoC(1),C(2)}$ = 2.09 Å. The structure obtained for ^{4}**19** agrees well with the geometrical features of this complex published in earlier calculations,[38] however, the calculated bond dissociation energy of D_0 = 51.2 kcal/mol deviates strongly from experimental data (D_0 = 34.6 ± 2.5).[19] The reason for this strong divergence between theory and experiment is most likely that B3LYP fails to adequately describe the π-bonding interaction between the metal center and the ligand. The sextet exit channels ^{6}**19** + SiH_4 and ^{6}**20** + C_2H_4 are not extensively discussed here, because they are energetically located well above the corresponding quartet states. The structure of ^{6}**19** resembles that of ^{4}**19**, with the already noted exception of elongated metal-ligand bond lengths in the sextet states.

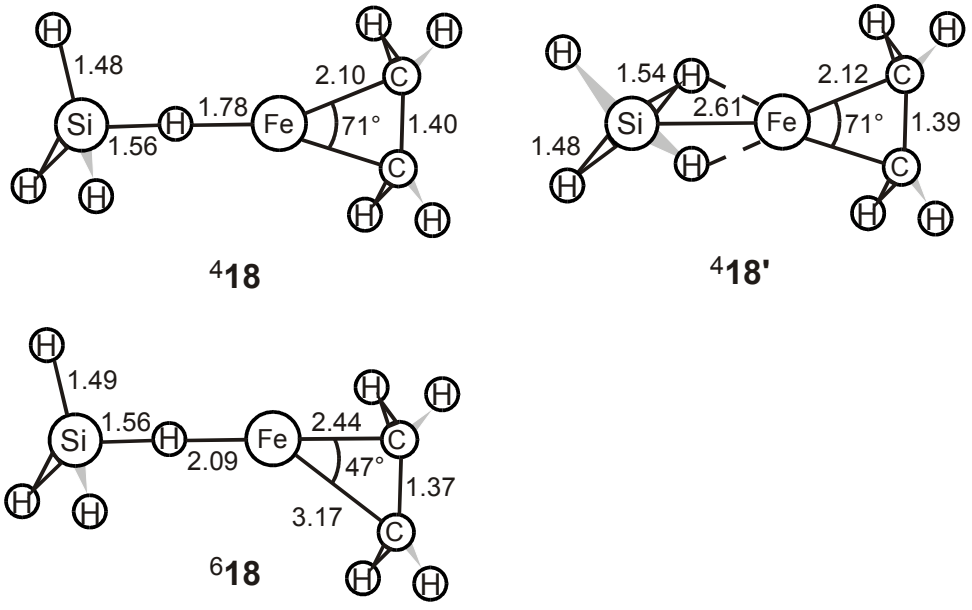

^{4}**18** ^{4}**18'** ^{6}**18**

Chart 6-15: Structures of minimum **18** on the quartet and sextet PES. Bond lengths are given in Å and angles in degree.

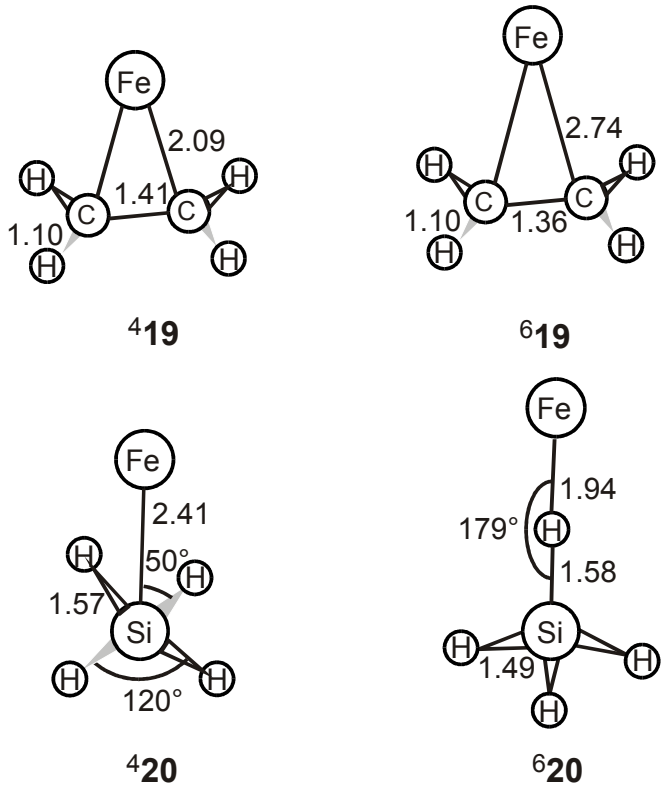

Chart 6-16: Products **19** and **20** of the Fe^+/ethylsilane system according to the B3LYP/BS1 calculations. Bond lengths are given in Å and angles in degree.

In complex ^{4}**20**, $FeSiH_4^+$, the silane ligand is bound through electrostatic Fe^+–Si interaction (r_{FeSi} = 2.41 Å), with the silicon-iron bond bisecting the H–Si–H angle. The bond energy $D_0(FeSiH_4^+)$ is calculated to 22.4 kcal/mol, which seems reasonable for the expected electrostatic interaction although no experimental values are available for comparison. The lower stability of ^{4}**20** as compared to ^{4}**19** accounts for the thermodynamic preference of the exit channel ^{4}**19** + SiH_4 of 22.0 kcal/mol. This theoretical result is supported by the experimental finding that no loss of C_2H_4 is observed in either mass spectrometric approach. In contrast to its quartet analog, the sextet $Fe(SiH_4)^+$ complex ^{6}**20** is bound through a single hydrogen-iron electrostatic interaction, causing a linear Si–H–Fe-unit (Chart 6-16).

C(2) –H bond insertion, Figure 6-10. On this PES, the reaction commences from **16** towards the inserted structure **21**. ^{4}TS**16**/**21** (E_{rel} = 24.2 kcal/mol) is a late TS, the structure already resembling the geometry of ^{4}**21** (Chart 6-17). The imaginary frequency of i680 cm^{-1} mainly accounts for the shift of the hydrogen atom from C(2) towards Fe^+, while the rotational motion of the two hydrogen atoms remaining at C(2) contributes less. While the sextet ^{6}TS**16**/**21** could not be located, a single point calculation of the optimized quartet structure shows a distinctly higher energy for the sextet, such that it is assumed not to

influence the lowest-energy path of the reaction, and a further search for ^{6}TS**16**/**21** is deemed unnecessary.

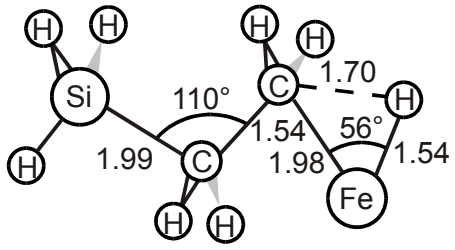

^{4}TS**16**/**21**

Chart 6-17: Structure of TS**16**/**21** of the Fe^+/ethylsilane system. Bond lengths are given in Å and angles in degree.

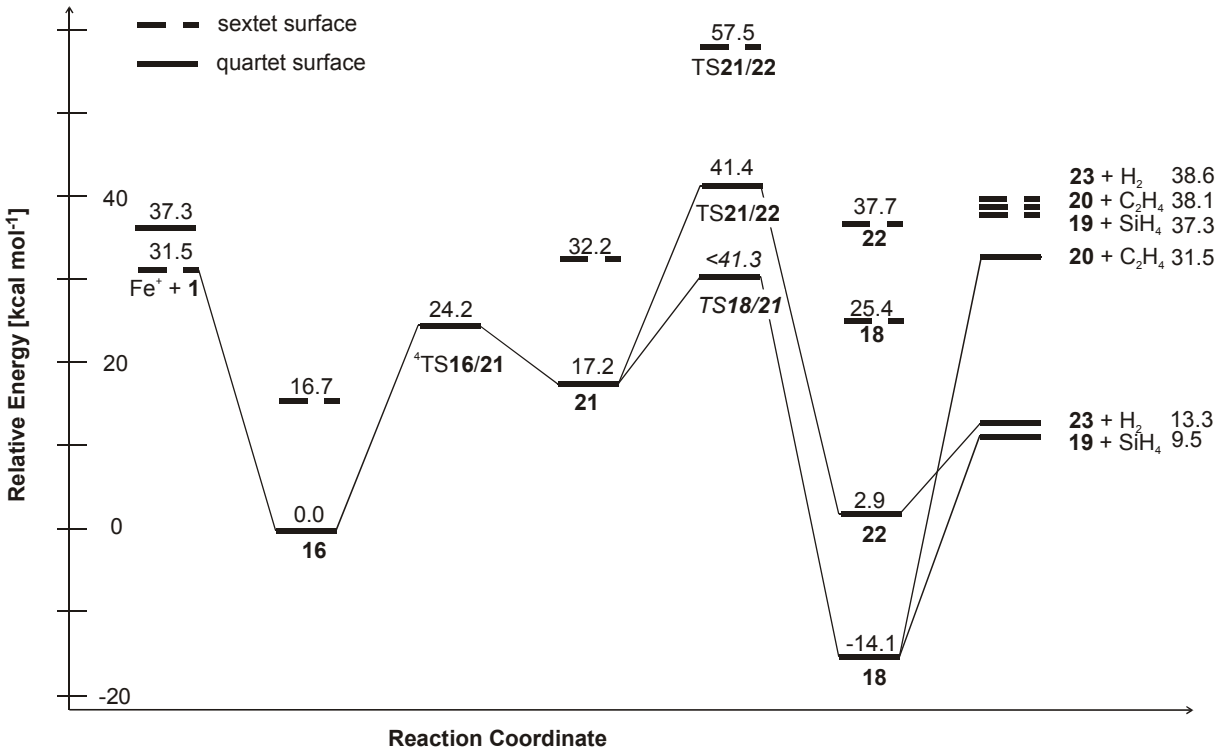

Figure 6-10: B3LYP/BS1 PES of the C(2)–H bond insertion pathway of Fe^+/ethylsilane relative to the lowest-lying encounter complex ^{4}**16**; ZPVE corrections are included, and the relative energetics are given in kcal/mol.The solid lines refer to the quartet PES while the dashed lines are used to denote the sextet PES.

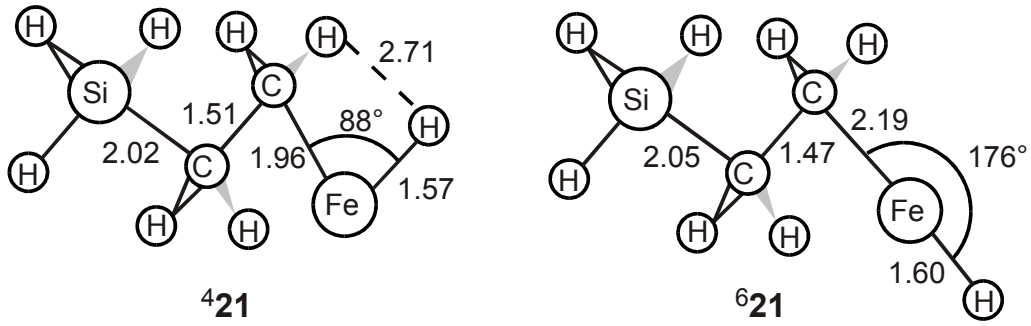

Chart 6-18: Structures of the C(2)–H inserted species **21** of the Fe^+/ethylsilane system. Bond lengths are given in Å and angles in degree.

The geometry of the quartet C(2) –H inserted structure, ^{4}**21** (E_{rel} = 17.2 kcal/mol) is shown in Chart 6-18; the major difference to ^{4}TS**16**/**21** is the distinctly widened C–Fe–H angle. In ^{6}**21** (E_{rel} = 32.2 kcal/mol), the C–Fe–H unit adopts an almost linear structure, thus clearly differing from the corresponding quartet minimum.

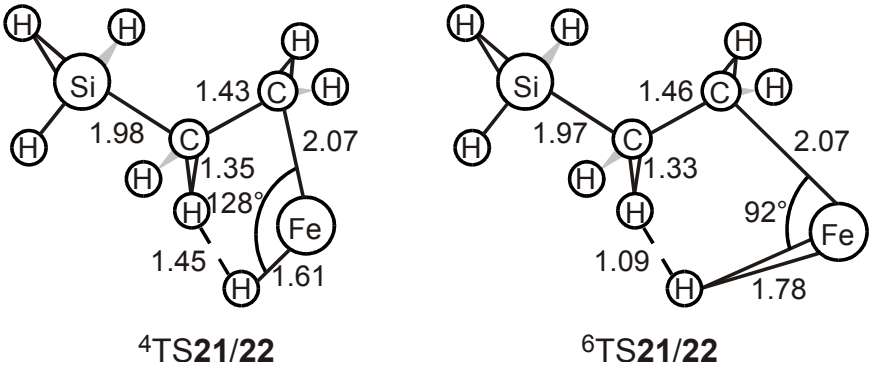

Chart 6-19: Structures of TS**21**/**22** of the Fe^+/ethylsilane system as obtained with the B3LYP/6-311+G* approach. Bond lengths are given in Å and angles in degree.

From **21**, the reaction may proceed by (i) β-SiH_3-migration via TS**18**/**21** to form complex **18** or by (ii) β-H-migration via TS**21**/**22** to form the bisligated complex $Fe^+(H_2)(C_2H_3SiH_3)$, denoted **22**. Along the first pathway, localization of TS**18**/**21** proved to be very difficult along both PES. Despite many different input structures and the attempts to localize a sufficiently well-guessed input structure using the LST (linear synchronous transit) and QST (quadratic synchronous transit) procedures, no transition structure is found. However, a single-point calculation on the optimized cobalt-analog yields an upper limit of E_{rel} < 41.3 kcal/mol for ^{4}TS**18**/**21**. As the single-point calculation for the corresponding sextet-TS is even higher in energy, it seems reasonable to neglect involvement of the sextet surface. The upper limit obtained from the cobalt-analog is well able to explain the experimentally observed features,

and although it is not satisfying to resign without locating this structure, due to limited computing resources further search for TS**18**/**21** is suspended and the given upper limit for ^{4}TS**18**/**21** is used instead. After passing TS**18**/**21**, the reaction continues toward minimum **18** and further to the products **19** and **20** (see above).

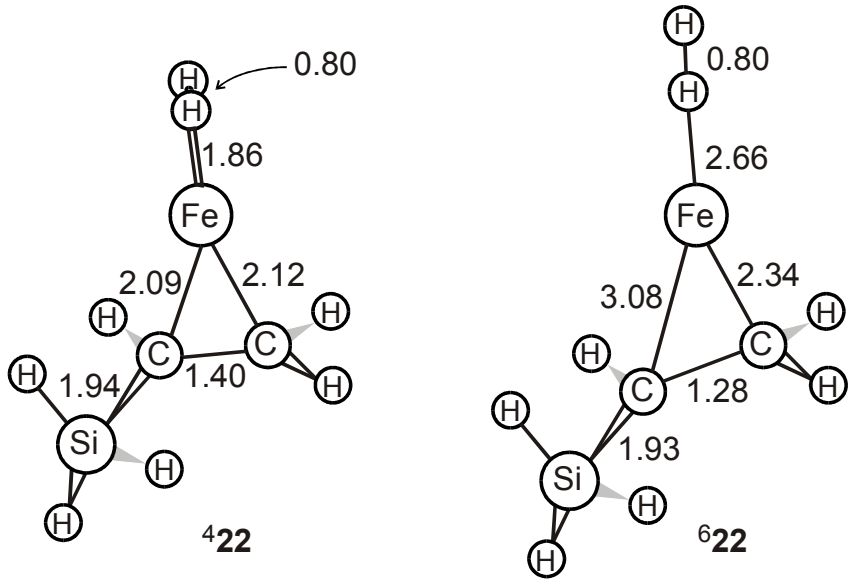

Chart 6-20: Minimum **22** of the Fe^+/ethylsilane system. Bond lengths are given in Å and angles in degree.

The second feasible pathway, i.e. the β-H migration starting from **21** passes via TS**21**/**22** toward minimum **22**. On the quartet surface, ^{4}TS**21**/**22** (E_{rel} = 41.4 kcal/mol) shows a distinctly elongated bond of $r_{C(1)H}$ = 1.35 Å pointing towards the Fe–H unit (Chart 6-19). Frequency analysis shows that the imaginary mode (i1053 cm^{-1}) corresponds mainly to the movement of the two hydrogen atoms approaching each other. Smaller contributions towards this strong negative frequency result from the shortening of the C–C bond. In analogy, in ^{6}TS**21**/**22** (E_{rel} = 57.5 kcal/mol) one C–H bond at C(1) is also distinctly elongated ($r_{C(1)H}$ = 1.35 Å) and the H–H distance amounts to only 1.09 Å (Chart 6-19); thus indicating that on the sextet PES the TS is even later on the reaction coordinate than in its quartet analog (r_{HH} = 1.45 Å). The strong imaginary frequency of i1332 cm^{-1} is mainly attributed to the approach of the two hydrogen atoms at Fe^+, with smaller contributions due to rotational rearrangement of the hydrogen atoms at C(1). Following TS**21**/**22**, complex **22** is reached, which consists of an iron cation surrounded by an H_2 ligand and a $C_2H_3SiH_3$-moiety. The corresponding quartet and sextet species are located 2.9 kcal/mol and 37.7 kcal/mol. In ^{4}**22**, the π-type bonding of the $C_2H_3SiH_3$-subunit to iron is demonstrated by almost symmetrical Fe–C bonds, $r_{FeC(1)}$ = 2.09 Å and $r_{FeC(2)}$ = 2.12 Å (Chart 6-20), in analogy to the iron-ethylene complex ^{4}**19**. The

slight distortion of the iron-ethylene unit from ideal symmetry can be attributed to the influence of the SiH_3-group on the C(1) atom. In contrast, in ^{6}**22** the $C_2H_3SiH_3$-unit is bound strongly asymmetric with $r_{FeC(1)}$ = 3.08 Å and $r_{FeC(2)}$ = 2.34 Å, such that the structure can be interpreted as a σ-type bonding between Fe^+ and C(2), an assignment which is also supported by the NBO-analysis. Again, the tendency is noticable that $Fe^+(^6D)$ arranges the fragments in a linear manner.

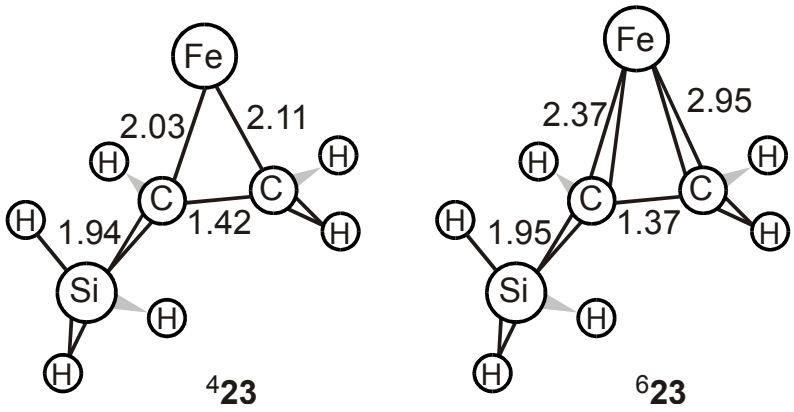

Chart 6-21: Product structures **23** of the Fe^+/ethylsilane system. Bond lengths are given in Å and angles in degree.

Dissociation of ^{4}**22** results in loss of H_2 and formation of the product **23**. The exit channels are located at E_{rel} = 13.3 kcal/mol and 38.6 kcal/mol on the respective quartet and sextet PES. In ^{4}**23**, the slightly asymmetric bonding in analogy to ^{4}**22** is again manifested ($r_{FeC(1)}$ = 2.03 Å and $r_{FeC(2)}$ = 2.11 Å), but r_{CC} = 1.42 Å still points to a carbon-carbon double bond (Chart 6-21). In contrast, the $C_2H_3SiH_3$-unit of complex ^{6}**23** is asymmetrically bound to iron, as it is already observed in ^{6}**22**. However, in contrast to ^{6}**22**, in ^{6}**23** the bond lengths are reversed, i.e. $r_{FeC(1)}$ = 2.37 Å and $r_{FeC(2)}$ = 2.95 Å. Although this effect is very interesting, because the H_2-ligand on iron seems to reverse the location of the electrophilic attack onto the double bond, the ground-state of this product channel is clearly the quartet analog, ^{4}**23** + H_2, such that investigation of its sextet analog was not pursued.

C(1) –H bond insertion, Figure 6-11. This pathway involves the following minima and transition states (in the order of their appearance): TS**16**/**24**, **24**, TS**22**/**24**, **22** and **23**. In ^{4}TS**16**/**24** (E_{rel} = 23.6 kcal/mol), the metal atom approaches the C–H bond to be activated which is already somewhat elongated (r_{CH} = 1.77 Å), see Chart 6-22. The imaginary frequency of the TS (i611 cm^{-1}) corresponds to widening the C(1) –Fe–H angle; in addition the rotational rearrangement of the atoms connected to C(1) adds to the imaginary frequency

to some extent. The sextet analog of ^{4}TS**16**/**24** could not be located despite many attempts. However, a single-point calculation onto the optimized quartet structure exhibited a much higher energy than ^{4}TS**16**/**24**, such that the assumption of a quartet ground-state for TS**16**/**24** seems justified.

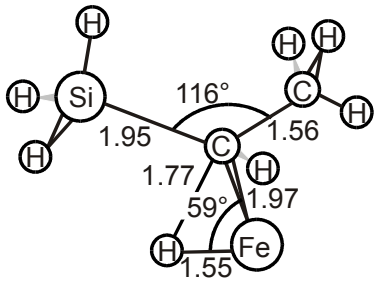

^{4}TS**16**/**24**

Chart 6-22: Structure of TS**16**/**24** of the Fe^+/ethylsilane system. Bond lengths are given in Å and angles in degree.

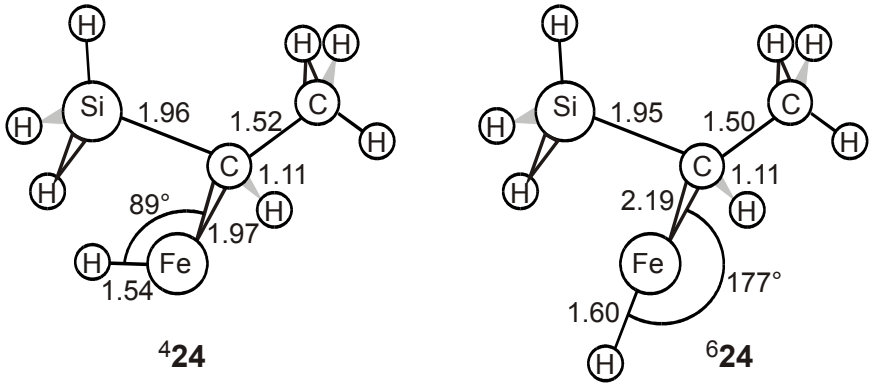

^{4}**24** ^{6}**24**

Chart 6-23: Structure of the C(1)–H inserted minimum **24** of the Fe^+/ethylsilane system. Bond lengths are given in Å and angles in degree.

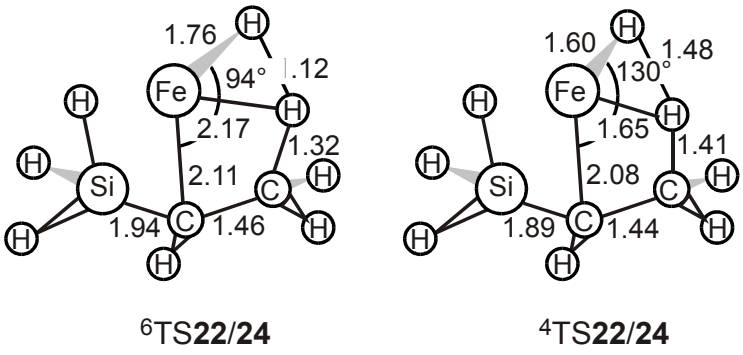

^{6}TS**22**/**24** ^{4}TS**22**/**24**

Chart 6-24: Structure of TS**22**/**24** of the Fe^+/ethylsilane system. Bond lengths are given in Å and angles in degree.

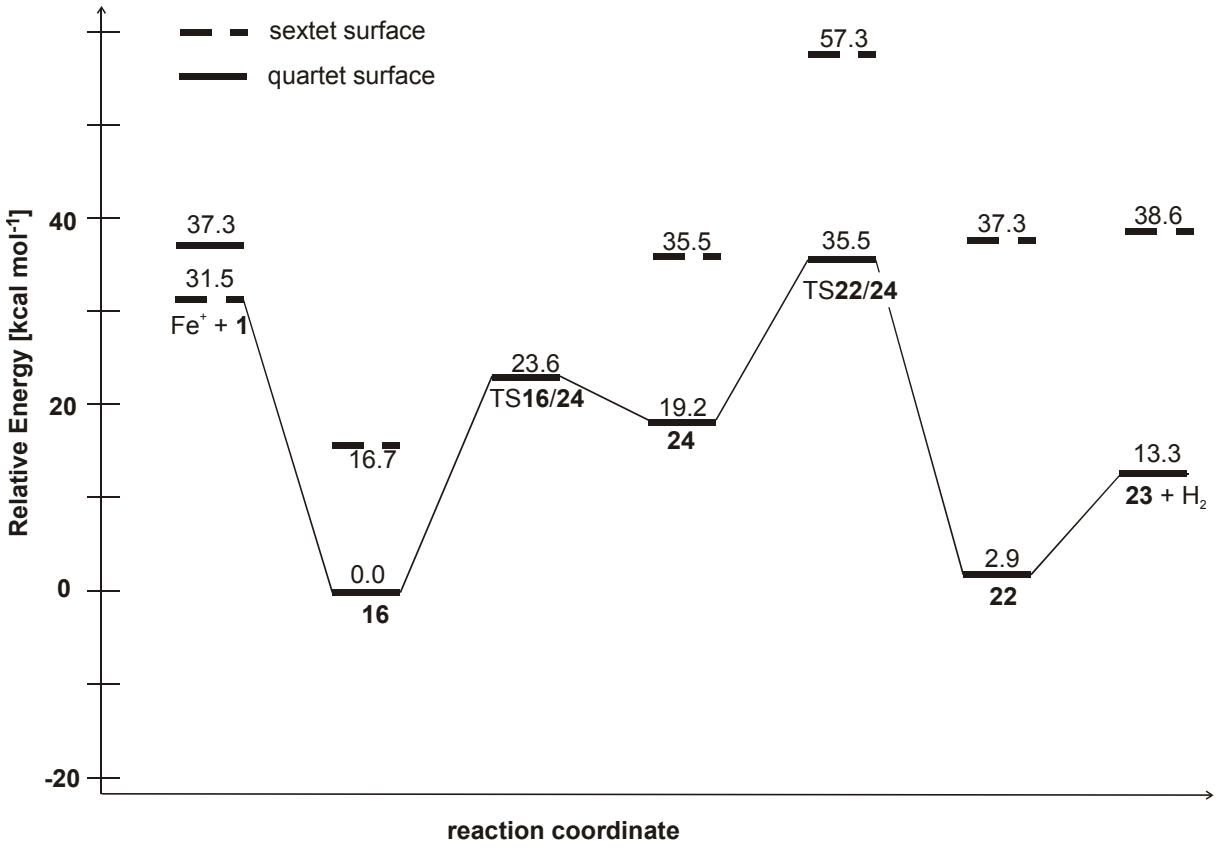

Figure 6-11: B3LYP/BS1 PES of the C(1)–H bond insertion pathway of Fe^+/ethylsilane relative to the lowest-lying encounter complex ^{4}**16**; ZPVE corrections are included, and the relative energies are given in kcal/mol. The solid lines refer to the quartet PES while the dashed lines are used to denote the sextet PES.

Minimum **24** is located at E_{rel} = 19.2 kcal/mol and E_{rel} = 35.5 kcal/mol on the quartet and sextet surfaces. While the structure of ^{4}**24** resembles very much its corresponding TS, ^{6}**24** exhibits a almost linear C–Fe–H unit (Chart 6-23).

The following transition structure TS**22**/**24** again shows a distinctly lower energy for the quartet than for the sextet state (E_{rel} = 35.5 vs. 57.3 kcal/mol). ^{4}TS**22**/**24** shows a very elongated C(2) –H bond with the hydrogen atom pointing towards the metal-hydrogen unit (Chart 6-24). The H–H distance is 1.48 Å, much longer than a normal H–H bond, thus the TS appears early on the reaction coordinate. The imaginary frequency (i1084 cm^{-1}) is assigned to the motion of the two hydrogen atoms approaching each other with smaller contributions from the rotational rearrangement of the hydrogen atoms at C(2). In contrast to its quartet analog, ^{6}TS**22**/**24** is a late TS on the reaction coordinate as demonstrated by the small H–H distance of only 1.12 Å. In analogy to the quartet structure, one C(2) –H bond is elongated, pointing towards the metal; the motion of the two approaching hydrogen atoms accounts for

the imaginary frequency of i1418 cm^{-1}. Complex **22** may easily decompose by loosing molecular hydrogen and forming product **23**. These structures have been described above and are therefore not repeated.

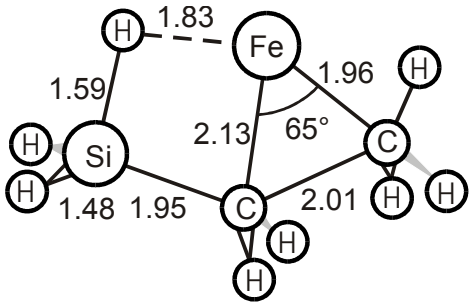

^{4}TS**16**/**25**

Chart 6-25: Structure of TS**16**/**25** of the Fe^+/ethylsilane system. Bond lengths are given in Å and angles in degree.

C–C bond insertion, Figure 6-12. The reaction on the quartet surface first traverses TS**16**/**25** to yield the C–C inserted structure **25**. In the quartet ^{4}TS**16**/**25** (E_{rel} = 24.2 kcal/mol), the metal ion approaches the C–C bond (Chart 6-25), and in the course of this motion the C–C bond is weakened and thus strongly elongated (from r_{CC} = 1.54 Å in ^{4}**16** to r_{CC} = 2.01 Å in ^{4}TS**16**/**25**). The imaginary frequency (i385 cm^{-1}) is attributed to the motion of the two C(1)- and C(2)-moieties away from each other. The sextet analog of this TS could not be localized despite many attempts; however, comparison with the other insertion pathways as well as with earlier work on the activation of ethane and propane by "bare" iron atoms allows the conclusion that the quartet TS is lower in energy than the sextet and thus further investigation of the sextet TS is not necessary.[8,24,34b]

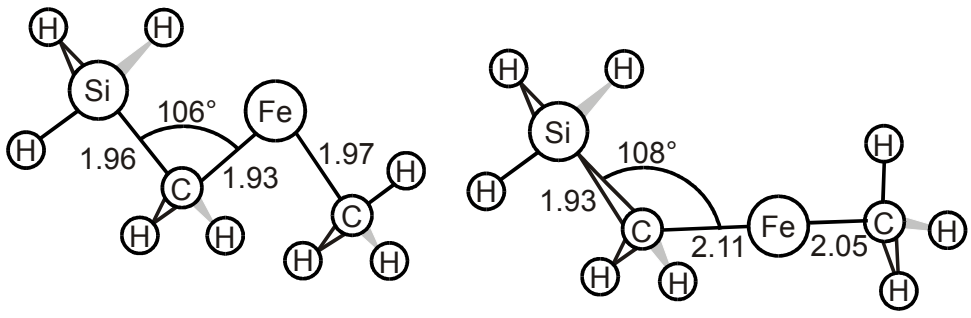

^{4}**25** ^{6}**25**

Chart 6-26: Structure of the C–C inserted minimum **25** of the Fe^+/ethylsilane system. Bond lengths are given in Å and angles in degree.

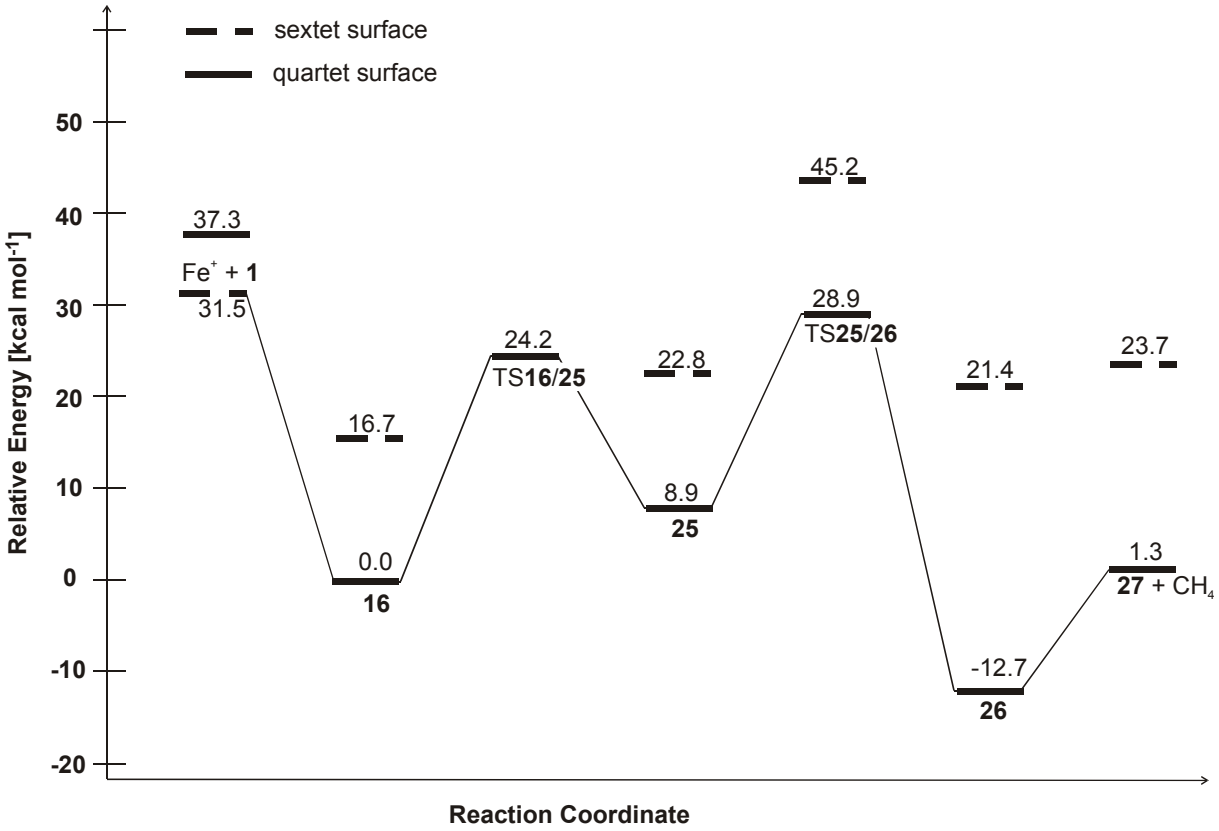

Figure 6-12: B3LYP/BS1 PES of the C–C bond insertion pathway of Fe^+/ethylsilane relative to the lowest-lying encounter complex ^{4}**16**; ZPVE corrections are included, and the relative energies are given in kcal/mol. The solid lines refer to the quartet PES while the dashed lines are used to denote the sextet PES.

The reaction then procedes towards the C–C inserted minimum **25**. The quartet isomer ^{4}**25** (E_{rel} = 8.9 kcal/mol) shows an anti-conformation with respect to the Fe–C(1) bond (Chart 6-26). The two metal-carbon bonds are almost symmetric ($r_{FeC(1)}$ = 1.93 Å and $r_{FeC(2)}$ = 1.97 Å); the shorter Fe–C(1) bond is attributed to the influence of the silyl-moiety. The sextet isomer, ^{6}**25** (E_{rel} = 22.8 kcal/mol), shows a linear C(1) –Fe–C(2) unit ($\alpha_{C(1)FeC(2)}$ = 179°) with both, Fe–C and Fe–H bonds elongated as compared to the corresponding quartet structure (Chart 6-26). Next along the reaction path is TS**25**/**26**, whose respective quartet and sextet isomers are located at E_{rel} = 28.9 kcal/mol and E_{rel} = 45.2 kcal/mol. ^{4}TS**25**/**26** shows a dramatically elongated Si–H bond in conjunction with a preformed iron-hydrogen bond (Chart 6-27). This suggests that the actual hydrogen migration occurs in two steps, the first one being the migration from the silyl-group to iron and the second step consisting of the hydrogen shift from iron to the methyl-moiety. However, the structure showing an iron-hydrogen bond is not a true minimum but a TS which is supported by the IRC calculations connecting ^{4}TS**25**/**26** with ^{4}**26**. ^{6}TS**25**/**26** is a very early TS, in which the Si–H bond is only slightly elongated and iron-hydrogen distance is quite large, see Chart 6-27. Here again, IRC

calculations prove the assigment of this TS to the migration of the hydrogen atom from the silyl- to the methyl-group. The rather small imaginary frequency of i317 cm^{-1} corresponds to the motion of the hydrogen atom away from SiH_3 toward the methyl as well as a rotation of the CH_3-group.

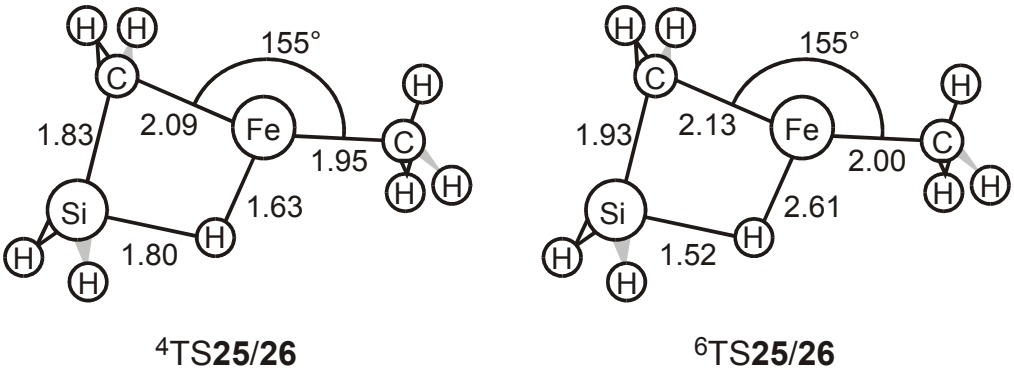

Chart 6-27: Structure of TS**25**/**26** of the Fe^+/ethylsilane system. Bond lengths are given in Å and angles in degree.

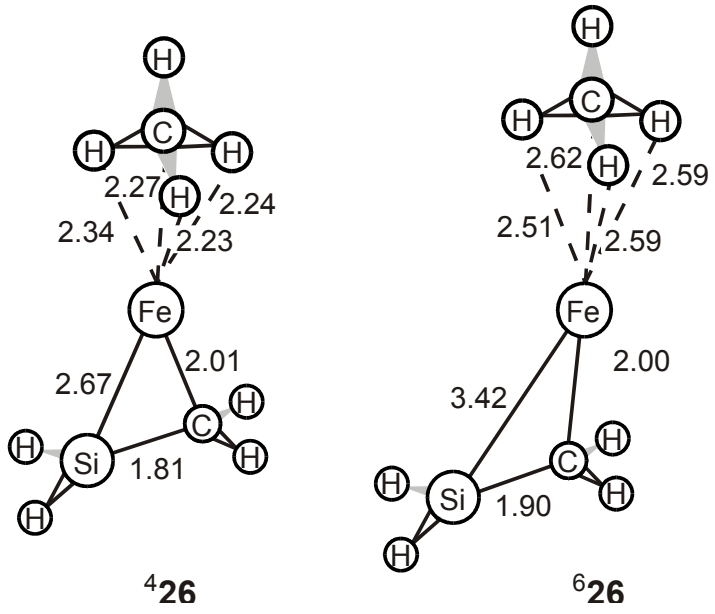

Chart 6-28: Structure of the C–C inserted minimum **26** of the Fe^+/ethylsilane system. Bond lengths are given in Å and angles in degree.

The reaction further continues to minimum **26**, whose quartet and sextet isomers are located at E_{rel} = -12.7 kcal/mol and 21.4 kcal/mol, respectively. These complexes consist of the metal ion surrounded by a methane and a silaethylene ligand (Chart 6-28). The methane is bound through electrostatic Fe^+–C interaction. In ^{4}**26**, the short Si–C bond of 1.81 Å in the silaethylene ligand points to the nominal formation of a C–Si double bond,[39] which then can bind through π-interaction to the metal center. The symmetric π-interaction is supported by

the Fe–C and Fe–Si bond lengths (r_{FeC} = 2.01 Å and r_{FeSi} = 2.67 Å), where the longer Fe–Si bond accounts for the larger volume of the silicon atom as compared to carbon. In contrast, the silaethylene ligand does not form a π-bond to the metal in minimum ^{6}**26**. Instead, electrostatic interaction occurs between Fe^+ and C(1) ($r_{FeC(1)}$ = 2.00 Å), while the SiH_3-group is pointing away from the metal (r_{FeSi} = 3.42 Å). From minimum **26**, the exit channel **27** + CH_4 (E_{rel} = 1.3 kcal/mol and E_{rel} = 23.7 kcal/mol for the quartet and sextet state) is easily reached by simple dissociation. The structure of ^{4}**27** is very close to that of ^{4}**26**, which is easily explained as no significant change in the electronic structure is expected from loss of the only weakly electrostatically bound methane molecule. The same holds true for the sextet analog ^{6}**27**.

6.3.3 Product Formation Pathways

Let us first outline the general features of the investigated PESs. (i) As evidenced from the energetic demand of the calculated sextet species, the sextet PES does not play a role for the ground-state reactivity of the system along all four primary insertion pathways. This is in good agreement with Holthausen et al.,[24] who found the low-spin PES to dominate the activation of ethane and propane by Fe^+. Although not all of the sextet transition structures have been located, there is no reason to doubt this conjecture. (ii) In analogy to the Co^+/ethylsilane system, the quartet minima are located well below the entrance channel. Thermochemically, formation of ^{4}**27** + CH_4 is the lowest lying exit channel at 1.3 kcal/mol, which is to the most part due to the stability of the neutral, but also because of the π-type interaction in $Fe(CH_2SiH_2)^+$ with $D_0(Fe^+\text{-}CH_2SiH_2)$ = 30.2 kcal/mol. (iii) On the quartet C–C bond insertion pathway, even all transition structures are calculated to lie below the entrance channel; the reaction exothermicity for formation of ^{4}**27** + CH_4 is calculated to be 2.6 kcal/mol. (iv) The pathways of primary C–Si and C(1) –H bond insertion are calculated to occur at only slightly elevated energies which may already be reached under thermal conditions. These results agree well with our experimental findings. For the C(2) –H bond insertion pathway, however, barriers of 9.9 and <9.8 kcal/mol in excess of the entrance-channel energy are calculated, thus rendering the progression of the reaction along this pathway unlikely. (v) In agreement with other calculations on the activation of non-polar organic substrates, the initial step of insertion into a bond of the substrate is not rate determining.

With regard to these general aspects, the following discussion concentrates on the quartet surface, with most attention being paid to the rate determining transition structures and the exit channels. The discussion follows the experimentally observed formation of individual products.

Demethanation. For the loss of CH_4 only the pathway of initial C–C bond insertion and subsequent β-hydrogen migration is calculated. The reverse pathway, i.e. primary Si–H bond insertion and subsequent methyl-migration, is not considered for two reasons. (i) Initial Si–H bond insertion would require formation of a stable species where Fe^+ is inserted into a Si–H bond. It was concluded above, however, that the reaction is likely to continue straight away by insertion into another Si–H bond and formation of the silylidene, ^{4}**14**. (ii) Generally it has been shown in earlier works, that migration of a alkyl group is energetically more demanding than migration of a hydrogen atom.[33,40]

The critical TS along the C–C bond insertion surface is ^{4}TS**11**/**12**, located 2.6 kcal/mol below the entrance channel. Together with the energetic location of the exit channel 30.2 kcal/mol below the entrance channel, this leads to the conclusion of a slightly exothermic reaction in good agreement with the experimental results.

Dehydrogenation. For loss of H_2, three different reaction pathways are in principle conceivable. However, based upon the experimental findings the Si–H insertion pathway concomitant with formation of a silylidene complex is excluded. The two remaining pathways for loss of hydrogen, i.e. initial C(1) –H and C(2) –H bond insertions, lead to $Fe(C_2H_3SiH_3)^+$ (^{4}**23**) as the ionic product complex. The critical TS along the C(1) –H and C(2) –H insertion pathways are ^{4}TS**22**/**24** and ^{4}TS**21**/**22** at 35.5 and 41.4 kcal/mol, respectively. These energies are 0 K values, and it is obvious that at thermal energies ^{4}TS**22**/**24** may be overcome while ^{4}TS**21**/**22** is too high in energy to allow this pathway to participate in the formation of H_2. Therefore it is easily concluded that (i) dehydrogenation occurs mainly via the C(1) –H bond insertion pathway and (ii) the energy of ^{4}TS**22**/**24** slightly above the entrance channel accounts for the experimentally observed small intensity of $Fe(C_2H_3SiH_3)^+$.

Loss of SiH_4. Two of the reaction pathways calculated lead to formation of the ionic product species $Fe(C_2H_4)^+$ concomitant with loss of neutral SiH_4, i.e. primary Si–H and C(2) –H bond insertions. In both pathways, $Fe(C_2H_4)(SiH_4)^+$ is the key intermediate which has in fact two obvious possibilities to dissociate by loss of silane or ethylene, respectively. However, the hypothetical formation of $Fe(SiH_4)^+$ is thermochemically handicapped due to the low stability of the $Fe(SiH_4)^+$-complex. Although this value seems to be too low given the fact that $Fe(SiH_4)^+$ can be produced as a stable complex in the FT-ICR, the general trend is

that $Fe(C_2H_4)^+$ is much stronger bound than $Fe(SiH_4)^+$. Thus, formation of $Fe(C_2H_4)^+$ is calculated to be the favorite dissociation channel of $Fe(C_2H_4)(SiH_4)^+$, which is indeed supported by the experiments. While small amounts of $Fe(C_2H_4)^+$ are observed in both, sector-MS and FT-ICR experiments, no indication for formation of $Fe(SiH_4)^+$ is found, even in collisional activation experiments. The critical TSs toward formation of $Fe(C_2H_4)(SiH_4)^+$ are ^{4}TS**17**/**18** and ^{4}TS**18**/**21** along the C–Si and C(2)–H bond insertion pathways, respectively. The former is located 3.4 kcal/mol above the ground-state entrance channel, while for the latter only a limit of <41.3 kcal/mol is known. Although ^{4}TS**17**/**18** is located slightly above the entrance channel, this is a 0 K energy and it is thus easily conceivable that at room temperature the reaction may indeed occur, although with a presumably low reaction rate. This is in good agreement with the experimental data which show only very minor intensities of the $Fe(C_2H_4)^+$ fragment (1 – 4%). As for the second conceivable pathway only an energy limit for ^{4}TS**18**/**21** is known, it cannot unambiguously be figured out whether the C(2)–H bond insertion pathway contributes to the observed $Fe(C_2H_4)^+$ fragment or not. However, a comparison to the related Co^+/ethylsilane system may shine some more light on this matter. In Co^+/ethylsilane, the TS for the C(2)–H bond insertion pathway is distinctly higher in energy than the TS of the C–Si bond insertion pathway, and thus, it is concluded that this pathway does not contribute to the formation of $Co(C_2H_4)^+$. Although comparison between both metals is somewhat difficult as is demonstrated by the different experimental results, the hitherto calculated reaction pathways show very similar features for iron and cobalt. It is therefore reasonable to assume that this similarity can be transferred to the C–Si bond insertion pathway, i.e. $Fe(C_2H_4)^+$ is preferentially formed via the C–Si bond insertion pathway.

Comparison of the Product Channels. For all four pathways, the migration TSs are much higher in energy than the respective product channels. In addition, the TSs of the C–Si, C(1)–H, and C–C bond insertion pathways are located in the same energy range, given the error of the calculations of ± 6 kcal/mol. Thus, strong competition can be expected between these routes. Although quantitative assessment of the branching ratios is difficult, demethanation is suggested as the dominating channel. Even if the argumentation in Chapter 6.2 is taken into account, i.e. that the C–C bond insertion channel is somewhat artificially stabilized due to an overestimation of M^+–C bond dissociation energies, the C–C bond insertion will continue to dominate the reaction. In contrast, dehydrogenation and loss of silane are minor products, but experimentally with a clear preference for dehydrogenation. The calculations find the corresponding TSs ^{4}TS**22**/**24** and ^{4}TS**17**/**18** at a very small energy

splitting of only 0.6 kcal/mol with a preference for ^{4}TS**17**/**18** of the silane loss. This energy splitting is clearly within the error of the calculations and several reasons are conceivable for the contradictory experimental results: (i) within the error of the calculations ^{4}TS**22**/**24** may be calculated too high in energy and ^{4}TS**17**/**18** too low, or (ii) as all energies are given at 0 K, entropy effects may reverse the sequence of the two TSs when going to experimental temperatures of 298 K.

Alltogether, a promising agreement between experiment and theory is reached. The quantitative agreement may, however, be somewhat fortuitous as shown from the error of the calculations and the comparison with the quantitatively somewhat more problematic $Co^+/C_2H_5SiH_3$ system.

6.3.4 Summary

The reaction of Fe^+ with ethylsilane is investigated at the B3LYP/BS1 level of theory. Qualitative and semi-quantitative agreement is reached between the experiments and the calculations in that all experimentally observed products are calculated to be formed along exothermic or slightly endothermic pathways at 0 K, the latter being so close in energy to the entrance channel that the barriers are surmountable at room temperature (298 K) when entropy effects are taken into account. Moreover, loss of CH_4 after primary C–C bond insertion is the dominating product both, experimentally and in the calculations. The favored pathways of the losses of H_2 and SiH_4 are the C(1) –H and Si–H bond insertions, respectively. Primary C(2) –H insertion is ruled out for the dehydrogenation product but may occur to some extent en route to the formation of $Fe(C_2H_4)^+$. Both, the C(1) –H and Si–H bond insertion pathways are associated with comparable energy demands such that unambiguous assignment of the computationally preferred product is not possible within the accuracy of the calculations.

6.4 Comparison Between Co^+/Ethylsilane and Fe^+/Ethylsilane

While Co^+ and Fe^+ show seemingly distinct differences in their experimental behavior towards ethylsilane, the quantitative reproduction of these results has proven to be very difficult. For both systems, the computational approach finds the primary C-C insertion pathway exothermic by 2.0 and 2.6 kcal/mol, respectively. However, the energy gap between

the C–C bond insertion and insertion into the C–Si and C(1) –H bonds is distinctly larger for the iron system. A more than semi-quantitative analysis of the system is hindered by several problems: (i) the error associated with the entrance channel is rather large, thus the location of the entrance channel relative to the critical transition structures and exit channels is uncertain within ± 6 kcal/mol, and (ii) the systematic error of the calculations cancels largely for the relative energies within one PES, but for the dissimilar channels with respect to the activated bond even small differences in the systematic errors for each PES result in distinct changes of the predicted product branching ratios.

Nevertheless, a qualitative explanation of the experimental behavior is reached for Co^+ and even semi-quantitative agreement is obtained in case of Fe^+. In order to explain the experimental differences *between* the two metals, it is necessary to recall of the Co^+/ethylsilane discussion. There, it is stated that the C–C insertion pathway is artificially stabilized by a few kcal/mol compared to the C–Si and C–H bond insertion pathways due to a computational overestimation of M^+–C bond strengths. As the C–Si, C(1) –H, and C–C bond insertion TSs are very close in the Co^+/ethylsilane system (within 4.4 kcal/mol) and somewhat more apart in the Fe^+/ethylsilane system (within 6.6 kcal/mol), an artificial stabilization of the C–C bond insertion pathway will effect the Co^+ system more than the Fe^+ system. Therefore, taking the extra stabilization for the C–C pathway into account, the computed sequence of the reactions may reverse for Co^+ while this is less likely to occur for Fe^+. However, note that this interpretation is somewhat precarious because the error of the calculations is to large to allow for definitive assignments.

In summary, both metals are a lot more alike than is expected from the experimental results. According to their neighborhood in the periodic system of the elements, both metals show similar reactivities with respect to the insertion sites. The observed differences are a result of small but yet important changes in the energetic location of the transition states, which can have huge effects because of the exponential behavior of the Arrhenius-like equations used for the determination of the branching ratio.

Some more conclusions concern the general performance of DFT calculations to interpret and/or predict the reactivity of transition-metal containing systems. As shown from the examples in this section, B3LYP does indeed allow to describe these systems qualitatively correctly. In fact, when competition of similar processes is to be described, even quantitative assessment of branching ratios may be possible because systematic errors cancel to a large extent. However, dissimilar channels may exhibit different systematic errors, and because of the exponential behavior of the Arrhenius-equation, even minute differences between the

dissimilar channels render a quantitative assessment of branching ratios very difficult. Thus, despite all progress in recent years, the quantitative description of competing processes with DFT remains difficult.[41] Nevertheless, at present even high-level *ab initio* theoretical approaches cannot guarantee a less erratic quantitative description of branching ratios, such that DFT still appears as a good compromise between the desired accuracy of the calculations and the existing computational resources.

References

[1] (a) A. E. Shilov *Activation of Saturated Hydrocarbons by Transition Metal Complexes*, Reidel, Boston, **1984**. (b) C. L. Hill *Activation and Functionalization of Alkanes*, Wiley, New York, **1989**. (c) J. A. Davies, P. L. Watson, J. F. Liebmann, A. Greenberg (Eds.) *Selective Hydrocarbon Activation*, VCH, Weinheim, **1990**.

[2] Selected reviews: (a) R. H. Crabtree *Chem. Rev.* **1985**, *85*, 245. (b) F. Garin, G. Maire *Acc. Chem. Res*. **1989**, *22*, 100. (c) B. A. Arndtsen, R. G. Bergmann, T. A. Mobley, T. H. Perterson *Acc. Chem. Res.* **1995**, *28*, 154. (d) A. E. Shilov, G. B. Shulpin *Chem. Rev.* **1997**, *97*, 2879. (e) B. Rybtchinski, D. Milstein *Angew. Chem.* **1999**, *38*, 870.

[3] Selected reviews on gas-phase chemisty: (a) K. Eller, H. Schwarz *Chem. Rev.* **1991**, *91*, 1121. (b) K. Eller *Coord. Chem. Rev.* **1993**, *126*, 93. (c) B. S. Freiser *Acc. Chem. Res.* **1994**, *27*, 353.

[4] (a) K. Morokuma, K. Ohta, N. Koga, S. Obara, E. R. Davidson *Faraday Symp. Chem. Soc.* **1984**, *19*, 84. (b) E. Folga, T. Ziegler *Can. J. Chem.* **1992**, *70*, 333. (c) P. E. M. Siegbahn, M. R. A. Blomberg, M. Svensson *J. Am. Chem. Soc.* **1993**, *115*, 1952. (d) J. J. Carroll, K. L. Haug, J. C. Weisshaar, M. R. A. Blomberg, P. E. M. Siegbahn, M. Svensson *J. Phys. Chem.* **1995**, *99*, 13955. (e) M. C. Holthausen, W. Koch *J. Am. Chem. Soc.* **1996**, *118*, 9932.

[5] (a) G. Czekay, T. Drewello, K. Eller, C. B. Lebrilla, T. Prüsse, C. Schulze, N. Steinrück, D. Sülzle, T. Weiske, H. Schwarz In: *Organometallics in Organic Synthesis*, H. Werner, G. Erker (Eds.), Springer, Heidelberg **1989**, Vol. 2, p 203. (b) H. Schwarz *Acc. Chem. Res.* **1989**, *22*, 282. (c) T. Prüsse, H. Schwarz *Organometallics* **1989**, *8*, 2856. (d) D. Schröder, H. Schwarz *J. Am. Chem. Soc.* **1990**, *112*, 5947. (e) T. Prüsse Ph.D. Thesis, TU Berlin D83, **1991**. (f) T. Prüsse, J. Allison, H. Schwarz *Int. J. Mass Spectrom. Ion Processes* **1991**, *107*, 553. (g) T. Prüsse, A. Fiedler, H. Schwarz *Helv. Chim. Acta* **1991**, *74*, 1127. (h) D. Schröder, W. Zummack, H. Schwarz *J. Am. Chem. Soc.* **1994**, *116*, 5857. (i) G. Hornung Ph.D. Thesis, TU Berlin D83, **1998**.

[6] (a) A. Hässelbarth, T. Prüsse, H. Schwarz *Chem. Ber.* **1990**, *123*, 209. (b) G. Hornung, D. Schröder, H. Schwarz *J. Am. Chem. Soc.* **1997**, *119*, 2273.

[7] A. Hässelbarth, T. Prüsse, H. Schwarz *Chem. Ber.* **1990**, *123*, 213.

[8] M. C. Holthausen, G. Hornung, D. Schröder, S. Sen, H. Schwarz, W. Koch *Organometallics* **1997**, *16*, 3135.

[9] G. Hornung, S. Bärsch, D. Schröder, H. Schwarz *Organometallics* **1998**, *17*, 2271.

[10] (a) B. L. Kickel, P. B. Armentrout *J. Am. Chem. Soc.* **1995**, *117*, 764. (b) C. L. Haynes, Y.-M. Chen, P. B. Armentrout *J. Phys. Chem.* **1995**, *99*, 9110. (c) C. L. Haynes, Y.-M. Chen, P. B. Armentrout *J. Phys. Chem.* **1996**, *100*, 111.

[11] *Gaussian 94* (Revision A.1), M. J. Frisch, G. W. Trucks, H. B. Schlegel, P. M. W. Gill, B. G. Johnson, M. A. Robb, J. R. Cheeseman, T. A. Keith, G. A. Petersson, J. A. Montgomery, K. Raghavachari, M. A. Al-Laham, V. G. Zakrzewski, J. V. Ortiz, J. B. Foresman, J. Cioslowski, B. B. Stefanov, A. Nanayakkara, M. Challacombe, C. Y. Peng, P. Y. Ayala, W. Chen, M. W. Wong, J. L. Andres, E. S. Replogle, R. Gomperts, R. L. Martin, D. J. Fox, J. S. Binkley, D. J. Defrees, J. Baker, J. P. Stewart, M. Head-Gordon, C. Gonzalez, J. A. Pople, Gaussian Inc., Pittsburgh **1995**.

[12] A. Schafer, H. Horn, R. Ahlrichs *J. Chem. Phys.* **1992**, *97*, 2571.

[13] (a) A. J. H. Wachters *IBM Tech. Rept.* RJ584, **1969**. (b) A. J. H. Wachters *J. Chem. Phys.* **1970**, *52*, 1033.

[14] f-Exponents are taken from: C. W. Bauschlicher, S. R. Langhoff, L. A. Barnes *J. Chem. Phys.* **1989**, *91*, 2399.

[15] (a) T. H. Dunning Jr. *J. Chem. Phys.* **1989**, *90*, 1007. (b) R. A. Kendall, T. H. Dunning, R. J. Harrison *J. Chem. Phys.* **1992**, *96*, 6796. (c) D. E. Woon, T. H. Dunning *J. Chem. Phys.* **1993**, *98*, 1358.

[16] (a) K. Eller, H. Schwarz *Int. J. Mass Spectrom. Ion Processes* **1989**, *93*, 243. (b) K. Eller, W. Zummack, H. Schwarz *J. Am. Chem. Soc.* **1990**, *112*, 621.

[17] (a) R. Srinivas, D. Sülzle, T. Weiske, H. Schwarz *Int. J. Mass Spectrom. Ion Processes* **1991**, *107*, 368. (b) R. Srinivas, D. Sülzle, W. Koch, C. H. DePuy, H. Schwarz *J. Am. Chem. Soc.* **1991**, *113*, 5970. (c) C. A. Schalley, D. Schröder, H. Schwarz *Int. J. Mass Spectrom. Ion Processes* **1996**, *153*, 173.

[18] (a) C. A. Schalley, R. Wesendrup, D. Schröder, T. Weiske, H. Schwarz *J. Am. Chem. Soc.* **1995**, *117*, 7711. (b) D. Schröder, H. Schwarz *J. Organomet. Chem.* **1995**, *504*, 123.

[19] M. R. Sievers, L. M. Jarvis, P. B. Armentrout *J. Am. Chem. Soc.* **1998**, *120*, 1891.

[20] C. E. Moore *Atomic Energy Levels*, National Standard Ref. Data; National Bureau of Standards NSRDS-NBS 35, Washington D.C., **1971**.

[21] M. Hendrickx, M. Ceulemans, L. Vanquickenborne *Chem. Phys. Lett.* **1996**, *254*, 307.

[22] (a) O. Gunnarson, R. O. Jones *Phys. Rev. B* **1985**, *31*, 7588. (b) T. Ziegler, J. Li *Can. J. Chem.* **1994**, *72*, 783. (c) T. V. Russo, R. L. Martin, P. J. Hay *J. Chem. Phys.* **1994**, *101*, 7729. (d) E. J. Baehrends, V. Branchadell, M. Sodupe *Chem. Phys. Lett.* **1997**, *265*, 481.

[23] The reactions employed in this procedure are: (a) $CoCH_3^+ \rightarrow Co^+ + CH_3$, (b) $2CH_4 \rightarrow C_2H_4 + 2H_2$, and (c) $CoC_2H_4^+ \rightarrow Co^+ + C_2H_4$.

[24] (a) M. C. Holthausen, A. Fiedler, H. Schwarz, W. Koch *Angew. Chem.* **1995**, *107*, 2430. (b) M. C. Holthausen, W. Koch *Helv. Chim. Acta* **1996**, *79*, 1939. (c) M. C. Holthausen, A. Fiedler, H. Schwarz, W. Koch *J. Phys. Chem.* **1996**, *100*, 6236.

[25] (a) M. Brookhart, M. L. H. Green, L.-T. Wong *Prog. Inorg. Chem.* **1988**, *36*, 1. (b) O. Eisenstein, Y. Jean *J. Am. Chem. Soc.* **1985**, *107*, 1177.

[26] For an example of a combined theoretical and experimental study on the activation of SiH_4 with tungsten cations, see: A. Ferhati, T. B. McMahon, G. Ohanessian *J. Am. Chem. Soc.* **1996**, *118*, 5997. Note, though, that the computational efforts do not include treatment of the full PES but rather concentrate on the structural assignment of experimentally observed products.

[27] For an example of an existing Si-H inserted structure, see: D. G. Musaev, K. Morokuma *J. Am. Chem. Soc.* **1995**, *117*, 799. Note, however, that the existence of the Si–H inserted structure may be attributed to the steric crowding in the activating Rh(Cp)(CO)-complex, which prevents formation of the sterically demanding four-centered transition state.

[28] (a) D. G. Musaev, K. Morokuma *J. Phys. Chem.* **1996**, *100*, 11600. (b) D. G. Musaev, K. Morokuma *J. Chem. Phys.* **1994**, *101*, 10697. (c) D. G. Musaev, K. Morokuma, N. Koga, K. A. Nguyen, M. S. Gordon, T. R. Cundari *J. Phys. Chem.* **1993**, *97*, 11435.

[29] T. A. Halgreen, W. N. Lipscomb *Chem. Phys. Lett.* **1977**, *49*, 225.

[30] C. Peng, H. B. Schlegel *Israel J. Chem.* **1993**, *33*, 449.

[31] (a) D. B. Jacobson, R. Bakhtiar *J. Am. Chem. Soc.* **1993**, *115*, 10830. (b) R. Bakhtiar, C. M. Holznagel, D. B. Jacobson *J. Am. Chem. Soc.* **1993**, *115*, 345. (c) H. Kang, D. B. Jacobson, S. K. Shin, J. L. Beauchamp, M. T. Bowers *J. Am. Chem. Soc.* **1986**, *108*, 5668.

[32] (a) B. K. Campion, R. H. Heyn, T. D. Tilley *J. Am. Chem. Soc.* **1988**, *110*, 7558. (b) D. H. Berry, L. J. Procopio *J. Am. Chem. Soc.* **1989**, *111*, 4099. (c) D. A. Straus, C. Zhang, N. Quimbita, S. D. Grumbine, R. H. Heyn, T. D. Tilley, A. L. Rheingold, S. J. Geib *J. Am. Chem. Soc.* **1990**, *112*, 2673. (d) H. Tobita, K. Ueno, M. Shimoi, H. Ogino *J. Am. Chem. Soc.* **1990**, *112*, 3415. (e) A. Jutzi, A. Mohrke *Angew. Chem.* **1990**, *29*, 893. (f)

B. K. Campion, R. H. Heyn, T. D. Tilley *J. Am. Chem. Soc.* **1990**, *112*, 4079. (g) T. S. Koloski, P. J. Carroll, D. H. Berry *J. Am. Chem. Soc.* **1990**, *112*, 6405. (h) L. J. Procopio, D. H. Berry *J. Am. Chem. Soc.* **1991**, *113*, 4039. (i) R. Probst, C. Leis, S. Gampers, W. E. Herdweck, C. Zybill, N. Auner *Angew. Chem.* **1991**, *30*, 1132.

[33] Note, however, that CH_3-migration is not impossible; for an example, see: S. Karraß, H. Schwarz, *Organometallics* **1990**, 9, 2409.

[34] (a) M. C. Holthausen, C. Heinemann, H. H. Cornehl, H. Schwarz, W. Koch *J. Chem. Phys.* **1995**, *102*, 4931. (b) M. C. Holthausen, Ph.D. Thesis, TU Berlin D83, **1996**.

[35] M. Rosi, C. W. Bauschlicher, S. R. Langhoff, H. Partridge *J. Chem. Phys.* **1990**, *94*, 8685.

[36] P. B. Armentrout, B. L. Kickel In: *Organometallic Ion Chemistry*, B. S. Freiser (Ed.), Kluwer Academic Publishers, Dordrecht, **1996**.

[37] S. Bärsch, H. Schwarz, unpublished work. $Co–H^+$: D_0 = 45.7 ± 1.4 kcal/mol (exp.) and 34.7 kcal/mol (B3LYP/VDZ); $Co–CH_3^+$: D_0 = 48.5 ± 0.9 kcal/mol (exp.) and 57.5 kcal/mol (B3LYP/VDZ); $Co–SiH_3^+$: D_0 = 45.2 ± 3.0 kcal/mol (exp.) and 54.0 kcal/mol (B3LYP/VDZ)

[38] D. Schröder, A. Fiedler, H. Schwarz *Int. J. Mass Spectrom. Ion Processes* **1994**, *134*, 239.

[39] (a) Y. Apeloig in *The Chemistry of Organic Silicon Compounds*, S. Patai, Z. Rappoport (Eds.), Wiley, New York, **1989**, p. 103. (b) Y. Apeloig, M. Karni, T. Müller in *Organosilicon Chemistry II. From Molecules to Materials*, N. Auner, J. Weiss (Eds.), VCH, Weinheim, **1996**, p.263.

[40] See, for example, ref. 24b and ref. 25.

[41] W. Koch, M. C. Holthausen *A Chemists Guide to Density-Functional Theory*, Wiley-VCH, Weinheim, **2000**.

7 Summary and Perspectives

This Thesis reports some selected examples from the manifold of chemical reactions of iron species in the gas-phase. The influence of the different ligands on the thermochemical and physical properties of iron, as well as the differences in the activation behavior for "bare" and ligated metal ions are investigated for several examples. In Chapter 6, the topic is even extended somewhat towards a comparison of the activation behavior of "bare" iron and cobalt cations.

The combined mass spectrometric and DFT-approaches as applied throughout this Thesis have convincingly demonstrated to provide valuable tools for both, the investigation of the reaction mechanisms of chemical model systems as well as the thermochemical characterization of organometallic species. In particular, the HF/DFT approach has shown its general applicability towards the qualitative and semi-quantitative description of transition-metal related problems. Even complicated binding situations as electrostatic bonds and π-bonds have been described reasonably well. While quantitative evaluations of potential-energy surfaces remain difficult, it is doubted that any of todays computational methods could provide quantitatively correct results for so many different systems and thus, B3LYP is considered a promising and at the same time cost-efficient approach which allows an analysis of reasonably large systems. Moreover, the energy-resolved measurements of electron-transfer collisions, although depending heavily on only few well established literature values as anchor points, have provided access to hitherto unknown thermochemical data of iron-oxides, -hydroxides, and -chlorides.

Transition-metal chemistry in the gas phase has been a field of very active research for quite some time. This Thesis contributes to the improvement of this picture in four different and yet somewhat related fields.

(i) The iron-oxide and -hydroxide cations are investigated, and the following conclusions are drawn.

- The degenerate oxygen-exchange of reaction does occur along a different pathway than previously speculated in the literature, interestingly, no spin inversions are involved, but rather kinetic effects seem to be responsible for the experimentally observed differences in reactivity between FeO^+ and $FeOH^+$.
- Three isomers are found to exist for $FeO_2H_2^{+/2+}$; the stability of the isomers is governed by the simple concept of redox-states, such that the iron-peroxide dication complex as a formal iron(II) compound is shown to be the most stable complex on

the dication-PES, more stable than the iron-dihydroxide and iron-oxo water dications which are formal Fe(IV)-complexes.

- The determined redox thermochemistry of these species provides a data base for future investigations of applied processes such as catalytic cycles involving reactive iron-oxo species or corrosion processes or others.

(ii) The investigation of the thermochemistry of iron-chloride cations for the first time provides a consistent data base of the redox properties of these species. The method of choice for this investigation includes the experimental determination of vertical ionization energies and the conversion into adiabatic ionization energies by means of a computational approach. The close cooperation of theory and experiment, which to a large extent determines the impetus of this work, is thus clearly demonstrated in Chapter 4.

(iii) The experimental and computational investigation of the activation of dihydrogen as well as one of the most challenging problems in contemporary chemistry, i.e. the activation of methane, by FeS^+ cations provides insight into interesting details of the mechanism of σ-bond activation by FeS^+.

- Both reaction pathways show many similarities, for example that the FeS^+ cation activates H–H or C–H bonds in a 1,2-insertion manner.
- In the heteronuclear bonds in methane, a distinct regioselectivity in the addition behavior across FeS^+ is observed, such that preferably S–H and Fe–C bonds are formed.
- The major product for both substrates involves incorporation of the sulfur-atom and oxidation of the substrate.

(iv) Different transition metals, i.e. iron and cobalt cations, activate ethylsilane under formation of similar products but show very different product branching ratios.

- The computational investigation in Chapter 6 shows that despite the large differences in experiment the same reaction pathways are operative for both metals and that only slight changes in the energetics of the barriers cause the different product branching ratios.
- The example of the activation of ethylsilane by Co^+, however, demonstrates part of the current limitations of the B3LYP approach. While similar activation channels are assumed to be described quite well, the quantitative description of dissimilar activation channels, i.e. C–H vs. C–C vs. C–Si bond activation and so forth, remains

difficult, especially when small energetic differences between the TSs of each channel determine the product branching ratio of the system.

The field of gas-phase organometallic chemistry currently undergoes strong conceptual changes. Besides the gathering of hitherto unknown data, the investigation of mechanistic details gains more and more importance. This Thesis represents these changes in that besides the collection of new experimental and theoretical data concerning the chemical properties of transition-metal species, it utilizes the cooperation of experiment and computational chemistry for a better understanding of reaction mechanisms and the development of more general concepts in transition-metal chemistry. Although the field of organometallic chemistry has been explored in many directions, there remain numerous fields to be explored, for instance (i) the investigation of the chemistry of 4^{th} and 5^{th} row transition metals, which is much less understood up to this point than the corresponding 3^{rd} row elements chemistry, (ii) activation of very inert substrates, for example dinitrogen, carbon dioxide, or methane; although another contribution to the latter is given in this Thesis, (iii) activation of more exotic substrates, for example bisfunctionalized alkanes, and the understanding of cooperative effects in the interactions of transition metals with more than one functional group, and (iv) the use of transition-metal clusters or highly ligated and thus less reactive transition metals as activating reagents. As for quite a few ion-molecule reactions a concise data base is available already, future challenges for organometallic chemists will include the application of these data for several purposes, i.e. (i) a defined and possibly reversible formation of new bonds in reactions of considerable interest for industrial applications, and (ii) the extension of the current data base toward solvated transition-metals as a first step in order to approach the solution phase mechanisms. The reactions of cationic transition-metal species given in this Thesis represent a contribution to this development and will hopefully stimulate further studies in this field.

Publication Index

1. Susanne Goebel, Chris L. Haynes, Farooq A. Khan, Peter B. Armentrout
Collision-Induced Dissociation Studies of $Co(CO)_x^+$, x = 1-5: Sequential Bond Dissociation Energies and the Heat of Formation of $Co(CO)_4$.
J. Am. Chem. Soc. **1995**, *117*, 6994.

2. Georg Hornung, Susanne Bärsch, Detlef Schröder, Helmut Schwarz
Ligand-Induced Selectivity Switch: The Gas-Phase Reactions of "Bare" and Ligated Iron(I) and Cobalt(I) Cations with *n*-Propyltrimethylsilane.
Organometallics **1998**, *17*, 2271.

3. Detlef Schröder, Susanne Bärsch, Helmut Schwarz
The Crucial Role of CO as a Ligand in the Formation of Long-Lived Neutral Complexes in the Gas Phase.
Chem. Phys. Lett. **1999**, *309*, 407.

4. Susanne Bärsch, Ilona Kretzschmar, Detlef Schröder, Helmut Schwarz
The activation of D_2 by FeS^+: Predominance of kinetic over thermodynamic control.
J. Phys. Chem. **1999**, *103*, 5925.

5. Detlef Schröder, Susanne Bärsch, Helmut Schwarz
Redox properties of charged and neutral iron chlorides $FeCl_m^n$ (m = 1 - 3; n = -1, 0, +1, and +2).
Int. J. Mass Spectrom. **1999**, *192*, 125.

6. Susanne Bärsch, Detlef Schröder, Helmut Schwarz
Extreme Differences in the Interactions of 'Bare' Fe^+ and Fe^{2+} with Hydrogen Peroxide: Fenton-Chemistry in the Gas Phase.
Helv. Chim. Acta **2000**, *83*, 827.

7. Susanne Bärsch, Thilo Böhme, Detlef Schröder, Helmut Schwarz
Theoretical Investigation of the Activation of Ethylsilane by "bare" Co^+ Cations.
Int. J. Mass Spectrom., in press.

8. Detlef Schröder, Susanne Bärsch, Helmut Schwarz
Second ionization energies of gaseous iron oxides and hydroxides: The $FeO_mH_n^{2+}$ dications (m = 1, 2; n ≤ 4).
J. Phys. Chem., in press.

9. Susanne Bärsch, Detlef Schröder, Helmut Schwarz
A DFT Based Study on the $^{16}O/^{18}O$-Exchange Reactions of the Prototype Iron-Oxygen Compounds FeO^+ and $FeOH^+$ with $H_2{}^{18}O$ in the Gas Phase.
Eur. J. Chem., in press.

10. Susanne Bärsch, Detlef Schröder, H. Schwarz, P. B. Armentrout
Methane to Methanethiol Conversion by FeS^+ - A Combined Experimental and Theoretical Study.
in preparation.

11. Susanne Bärsch, Detlef Schröder, H. Schwarz
How Does Fe^+ Activate Ethylsilane? A Theoretical Study in Comparison with Experiments.
in preparation.

Curriculum Vitae

Persönliche Angaben:

Geburtsdatum:	07.02.1972 in Dessau/Sachsen-Anhalt
Familienstand:	geschieden
Staatsangehörigkeit:	deutsch

Ausbildung:

Sept. 1978 - Sept. 1988	Polytechnische Oberschule in Magdeburg
Sept. 1988 - Sept. 1990	Spezialklassen für Chemie der TH Merseburg
Sept. 1990 - Sept. 1992	Grundstudium der Chemie an der Technischen Hochschule Merseburg
Okt. 1992 - Nov. 1996	Hauptstudium der Chemie an der Technischen Universität Braunschweig
Sept. 1993 - Sept.1994	Chemiestudium als DAAD-Stipendiatin an der University of Utah, Salt Lake City, USA.
Nov. 1995 - Nov. 1996	Diplomarbeit unter der Anleitung von Prof. K. Kerl am Institut für Physikalische Chemie der TU Braunschweig
Jan. 1997 - Juni 2000	wissenschaftliche Mitarbeiterin im Arbeitskreis von Prof. H. Schwarz an der TU Berlin und Promotion zum Thema "Reaktivität und Thermochemie verschiedener Eisen-Spezies in der Gasphase"
Feb. - April 1998	Forschungsaufenthalt in der Arbeitsgruppe von Prof. Armentrout an der University of Utah, Salt Lake City, USA.